

Control and imaging of excitons, spins and spin dynamics in Van der Waals semiconductors and superconductor-magnet hybrids

Borst, M.

DOI

[10.4233/uuid:51792b59-14a6-4125-9761-063f4a7140d7](https://doi.org/10.4233/uuid:51792b59-14a6-4125-9761-063f4a7140d7)

Publication date

2024

Document Version

Final published version

Citation (APA)

Borst, M. (2024). *Control and imaging of excitons, spins and spin dynamics in Van der Waals semiconductors and superconductor-magnet hybrids*. [Dissertation (TU Delft), Delft University of Technology]. <https://doi.org/10.4233/uuid:51792b59-14a6-4125-9761-063f4a7140d7>

Important note

To cite this publication, please use the final published version (if applicable). Please check the document version above.

Copyright

Other than for strictly personal use, it is not permitted to download, forward or distribute the text or part of it, without the consent of the author(s) and/or copyright holder(s), unless the work is under an open content license such as Creative Commons.

Takedown policy

Please contact us and provide details if you believe this document breaches copyrights. We will remove access to the work immediately and investigate your claim.

**CONTROL AND IMAGING OF EXCITONS, SPINS AND SPIN
DYNAMICS IN VAN DER WAALS SEMICONDUCTORS AND
SUPERCONDUCTOR-MAGNET HYBRIDS**

**CONTROL AND IMAGING OF EXCITONS, SPINS AND SPIN
DYNAMICS IN VAN DER WAALS SEMICONDUCTORS AND
SUPERCONDUCTOR-MAGNET HYBRIDS**

Dissertation

for the purpose of obtaining the degree of doctor
at Delft University of Technology,
by the authority of the Rector Magnificus, prof. dr. ir. T.H.J.J. van der Hagen,
chair of the Board for Doctorates,
to be defended publicly on
Thursday 12 September 2024, at 12:30 o'clock

by

Michael BORST

MSc Applied Physics
Delft University of Technology, The Netherlands
born in Rijpwetering, The Netherlands

This dissertation has been approved by the promotor.

Composition of the doctoral committee:

Rector Magnificus,	chairperson
Prof. dr. G.A. Steele,	TU Delft, <i>promotor</i>
Dr. ir. T. van der Sar,	TU Delft, <i>promotor</i>

Independent members:

Prof. dr. ir. H.S.J. van der Zant	TU Delft
Prof. dr. C. Degen,	ETH Zürich (Switzerland)
Dr. M.H. Guimaraes,	University of Groningen
Dr. S. Bhattacharyya,	Leiden University
Dr. C. Gonzalez-Ballester,	TU Wien (Austria)

Reserve member:

Prof. dr. A.F. Otte,	TU Delft
----------------------	----------



Keywords: Quantum sensing, diamond, magnetism, NV magnetometry, TMDs, excitons, van der Waals magnets, spintronics, superconductivity, spin waves

Printed by: Gildeprint, Enschede

Cover by: Michael Borst

Copyright © 2024 by M. Borst

ISBN 978-94-6496-187-4

An electronic copy of this dissertation is available at
<https://repository.tudelft.nl/>.

*Perfectionism is the belief
that if we live perfect,
look perfect,
and act perfect,
we can minimize or avoid
the pain of blame, judgement, and shame.*

*It's a shield.
It's a twenty-ton shield
that we lug around
thinking it will protect us when, in fact,
it's the thing that's really preventing us from flight.*

Brené Brown, *The Gifts of Imperfection*

CONTENTS

Summary	ix
Samenvatting	xi
1 Introduction	3
2 Theory and experiment	13
2.1 Magnetometry with spins in diamond	14
2.2 Probing low-dimensional magnetic phenomena	18
2.2.1 The valley magnetic moment	18
2.2.2 Two-dimensional magnets	23
2.2.3 Spin waves in magnetic thin films	25
2.3 Fabrication methods	32
2.3.1 Exfoliation, stamping, and nanofabrication	32
2.3.2 Diamond membranes for quantum sensing	36
2.4 Electronics and digital control	41
3 Exciton-to-trion-conversion driven valley polarization in monolayer WS₂	57
3.1 Introduction	58
3.2 Chemical doping of WS ₂ using anisole	58
3.3 Doping-controlled exciton-to-trion conversion	61
3.4 Conclusion	63
3.5 Supplementary information	66
4 Magnetic imaging of van der Waals interlayer antiferromagnet CrSBr	79
4.1 Introduction	80
4.2 Membrane-facilitated magnetometry of CrSBr	81
4.3 Extraction of $T_{\text{Néel}}$ and monolayer magnetization	83
4.4 Conclusion	85
5 Observation of hybrid spin-wave–Meissner-current transport modes	91
5.1 Introduction	92
5.2 Magnetic resonance imaging of hybridized SWMC transport modes	92
5.3 Field-tuning of the hybridized modes	96
5.4 Temperature-tuning of the hybridized modes	98
5.5 Spin-wave refraction at target sites	99
5.6 Conclusion	101
5.7 Supplementary Information	103

6 Outlook	117
6.1 Probing the valley magnetic moment in group-IV TMDs with NV centers in diamond	118
6.2 Detecting spin-wave excitations in van der Waals magnets with NV magnetometry	121
6.3 Creating spin-wave optics with superconductor-magnet heterostructures .	122
Acknowledgements	131
Curriculum Vitæ	143
List of Publications	145

SUMMARY

Magnetic phenomena are at the foundation of modern-day information storage and processing technologies. In this dissertation, we study three phenomena that hold promise for the next generation of information technology: excitons in two-dimensional semiconductors, two-dimensional magnets and magnetic excitations. First, we introduce the reader to magnetism, its role in society (Chapter 1) and how magnetic phenomena can be imaged with high resolution using the nitrogen vacancy (NV) center in diamond (Chapter 2). Before presenting research results, we introduce the aforementioned phenomena, along with two experimental setups that we constructed ground-up to probe them using spectroscopy and cryogenic NV magnetometry (Chapter 2).

Valleytronics aims to encode information using valleys in the band structure of crystalline solids. In group-IV transition metal dichalcogenides such as WS_2 , MoS_2 , WSe_2 and MoSe_2 , optical selection rules enable selective valley-excitation of excitons (electron-hole pairs), making them attractive for valleytronic applications. We use polarization sensitive spectroscopy to demonstrate that chemical doping of WS_2 using anisole changes the balance between neutral and charged excitons, and thereby the degree of valley polarization under optical excitation. We capture this behaviour by developing a rate equation model and show that optical quenching can increase valley polarization at the cost of exciton lifetimes (Chapter 3). These experiments are an important step towards NV-based detection of the magnetic moment associated with the valley index (Chapter 6).

A central challenge in NV magnetometry is minimizing the distance between sample and the sensor spins. We address this challenge by fabricating small $50 \times 50 \text{ }\mu\text{m}^2$ diamond membranes that facilitate direct contact between sample and sensor (Chapter 2). We demonstrate their sensing potential by imaging uncompensated monolayer stray fields of Van der Waals interlayer antiferromagnet CrSBr (Chapter 4). Using the quantitative nature of NV measurements, we extract the CrSBr monolayer magnetization and Néel temperature. These results are an important stepping stone towards detecting spin waves, oscillations of the magnetic order, in Van der Waals magnets (Chapter 6).

Spin waves and their quanta, magnons, are promising signal carriers for next generation information devices that exploit their wave nature, non-reciprocal transport properties, and low intrinsic damping. An outstanding challenge is the efficient gating of spin-wave transport, which might be achieved by shaping their magnetic environment using diamagnetism. We employ diamond membranes to image spin waves in an yttrium iron garnet thin film as they travel underneath an optically opaque superconductor, to reveal hybridization of Meissner currents and spin wave modes (Chapter 5). We show that the superconductor modulates the spin-wave dispersion, enabling tuning of spin-wave transport using temperature, magnetic field and lasers. Finally, we suggest the use of superconductors to create magnonic cavities, crystals and spin-wave optics (Chapter 6).

SAMENVATTING

Magnetische verschijnselen vormen de basis van moderne informatieopslag- en verwerkingstechnologieën. We bestuderen drie fenomenen die veelbelovend zijn voor de volgende generatie informatietechnologie: excitonen in tweedimensionale halfgeleiders, tweedimensionale magneten en magnetische excitaties. We introduceren de lezer in magnetisme en zijn rol in de samenleving (Hoofdstuk 1), en vertellen hoe magnetische verschijnselen met hoge resolutie kunnen worden afgebeeld met stikstof-gat (NV) centra in diamant (Hoofdstuk 2). Vervolgens introduceren we de eerder genoemde fenomenen, samen met twee huisgemaakte experimentele opstellingen voor spectroscopie en cryogene NV-magnetometrie, waarmee we ze bestuderen (Hoofdstuk 2).

Valleitronica draait om het encoderen van informatie in valleien van de bandstructuur van kristallijne vaste stoffen. In groep-IV overgangsmetaal-dichalcogeniden zoals WS_2 , MoS_2 , WSe_2 en $MoSe_2$, maken optische selectieregels selectieve valleiexcitatie van excitonen (elektron-gatparen) mogelijk, wat ze aantrekkelijk maakt voor valleitronische toepassingen. We gebruiken polarisatiegevoelige spectroscopie om aan te tonen dat chemische dotering van WS_2 met anisol de balans tussen neutrale en geladen excitonen verandert, en daarmee ook de valleipolarisatie. We verklaren dit gedrag met behulp van een model, dat tevens laat zien dat de valleipolarisatie vergroot kan worden ten koste van excitonlevensduur (Hoofdstuk 3). Deze experimenten zijn een belangrijke stap naar NV-detectie van het valleindex-afhankelijke magnetische moment (Hoofdstuk 6).

Een centrale uitdaging in NV-magnetometrie is het minimaliseren van de afstand tussen het specimen en de spinsensoren. We pakken deze uitdaging aan door kleine $50 \times 50 \mu\text{m}^2$ diamantmembranen te fabriceren die direct contact tussen specimen en sensor mogelijk maken (Hoofdstuk 2). We demonstreren hun potentieel voor magnetometrie door ongecompenseerde monolaag-strooivelden van de interlaag antiferromagneet CrSBr (Hoofdstuk 4) in kaart te brengen. Met de kwantitatieve aard van NV-metingen extraheren we de monolaagmagnetisatie en Néeltemperatuur. Deze resultaten zijn een belangrijke stap richting het detecteren van spingolven, oscillaties van de magnetische ordening, in Van der Waals magneten (Hoofdstuk 6).

Spingolven en hun kwanta, magnonen, zijn veelbelovende signaaldragers voor nieuwe informatietechnologie die gebruikmaakt van hun golfkarakter, niet-reciproke transporteigenschappen en lage intrinsieke demping. Een belangrijke uitdaging is het efficiënt controlen van spingolfransport, wat wellicht mogelijk is door hun magnetische omgeving met diamagnetisme te conrolleren. We gebruiken diamantmembranen om spingolven af te beelden in een dunne film van yttrium-ijzer-granaat terwijl ze onder een optisch ondoorzichtige supergeleider doorreizen. We onthullen een hybridisatie van Meissnerstromen en spingolformodi die kunnen worden afgestemd met temperatuur, magnetisch veld en lasers. Ten slotte suggereren we het gebruik van supergeleiders om magnonische resonatoren, kristallen en spingoloptica te creëren (Hoofdstuk 6).



1

INTRODUCTION

*The lodestone has soul
as it is able to move the iron.*

Thales of Miletus

In this chapter we provide a brief overview of the history of magnetism, its applications in modern day life, and its potential for future information technology.

Magnetism has fascinated humans for thousands of years. It was Thales of Miletus (600 BCE) who allegedly believed that lodestones, magnetized naturally formed iron oxides, had a soul - due to their 'invisible' attractive properties [1]. According to legend, these lodestones were first found in Magnesia, the Macedonic region from which the magnet derives its name in the Western world [2]. Though the intricate origin of magnetism would remain concealed for multiple millennia, applications were widespread - there are Chinese accounts of lodestones employed as a compass as far back as 2637 BCE [3]. The mysterious nature of magnets spoke to imagination, and throughout medieval times they were even employed in medicine for their "magic healing powers" [4].

Modern systematic investigation of magnetism is considered to have started with "*De Magnete, Magneticisque Corporibus, et de Magno Magnete Tellure*" by William Gilbert in 1600. This seminal work on "Magnets and magnetic bodies, and the grand magnet Earth" considers distinctions between electricity and magnetism, and the behaviour and origin of the Earth magnetic field [5]. Charles Coulomb found that the force between magnetic poles follows an inverse square law with distance [6]. More than 200 years later, in 1820, Johannes Christian Ørsted discovered an electric current displaces a magnetic needle, hinting at a fundamental relationship between electricity and magnetism [7]. In the same year, Biot and Savart managed to express the magnetic field generated by a current quantitatively through the now well-known Biot-Savart law. Together with insights by Ampère, Gauss and Faraday, these findings were unified by James Clerk Maxwell between 1861 and 1865 into what are now called Maxwell's equations of electromagnetism [8, 9]. Though this electromagnetic revolution found its way into society through electromagnets in motors and generators, materials that displayed intrinsic ferromagnetism were still not properly explained by classical physics. Electrodynamics implied continuous circulating surface current densities on the order of a million Ampère per meter to be present on the surface of iron-like magnets, in order to account for the observed magnetic moment. Only when quantum mechanics was established, an adequate microscopic description of ferromagnetism was formed.

The key to understanding ferromagnetism was the discovery of the electron's intrinsic angular momentum, or its *spin*. In 1896, Zeeman observed the splitting of one spectral emission line into multiple, when placing the emission source in a static magnetic field [10]. In 1925, Uhlenbeck and Goudsmit found that a "spinning" electron model with quantized angular momentum resolved inconsistencies between experiments and theory of the emission spectrum of hydrogen [11, 12], simultaneously explaining Zeeman's observations as well as the quantization of angular momentum that was observed in the Stern-Gerlach experiment a few years prior in 1921 [13]. Now that a quantized magnetic moment of the electron was established, Heisenberg showed it was the interaction between these spins that gives rise to ferromagnetism [14]. A so-called exchange interaction between two neighbouring spins \mathbf{S}_i and \mathbf{S}_j arises from Coulomb repulsion in conjunction with the Pauli exclusion principle. This causes an energy splitting between parallel and anti-parallel spin states, captured by the Hamiltonian [15]

$$\mathcal{H} = -2J\hat{\mathbf{S}}_i \cdot \hat{\mathbf{S}}_j. \quad (1.1)$$

Here, J is the exchange integral, which takes different values for the type of atoms, orbitals and configurations considered. For $J > 0$, energy is minimized when spins are parallel and a ground state with ferromagnetic ordering arises. For $J < 0$, the ground state is formed by anti-ferromagnetic ordering with antiparallel spins, as predicted by Landau in 1933 [16] and Néel in 1948 [17]. When temperature T is sufficiently high ($|J| < k_B T$), magnetic ordering vanishes at the so-called Curie temperature T_C for ferromagnets and Néel temperature T_N for antiferromagnets. These insights gave birth to a microscopic understanding of intrinsically magnetic materials and their behaviour as a function of temperature.

Magnetism is a perfect example of the paradigm "*you don't have to understand how something works in order to do something useful with it*". From compasses for navigation, to electromotors, generators and the magnetic tape recorder - all were developed before Heisenberg's theory of ferromagnetism. Since then, magnetism has synergized with semiconductors to underpin modern information technology, for example through memory storage via magnetized domain structures in hard disk drives, whose information density has increased from 0.001 bits/ μm^2 in 1970 to 1000 bits/ μm^2 in 2010 [18]. Another critical milestone was the 1988 discovery of giant magnetoresistance in magnetic tunnel junctions, which exploit both the electron charge and its spin [19, 20], which found applications in magnetic sensors, hard disk drive read heads and magnetic random access memory. The field of *spintronics*, a portmanteau of *spin* and *electronics*, where spin and charge of the electron are employed for novel device functionalities, holds promise for miniaturization and energy efficiency in information technology [21].

While spintronic devices typically rely on the charge and spin of uncorrelated particles, more recently coherent many-body spin phenomena have gathered interest for device applications. One such phenomenon is the spin wave - a collective oscillation of the magnetic order in a magnetic material, whose quanta are known as magnons. Spin waves in magnetic insulators do not suffer Ohmic losses and are therefore attractive for energy efficient and wave-based computing purposes [22–24]. Spin wave excitations in magnets were predicted in 1930 by Bloch [25] and the ferromagnetic resonance mode, characterized by zero wavevector and a uniform in-phase oscillations of all spins, was observed by Griffiths in 1946 [26]. Propagating spin waves with non-zero wavevector were observed in yttrium iron garnet (YIG) by Eshbach in 1962 [27]. To this day, the ferrimagnetic insulator YIG remains a prominent material for spin wave applications due to its low spin-wave damping and macroscopic propagation distances of several millimeters [28]. In Chapter 5 we demonstrate that superconductors can be used to modulate and control spin wave propagation in YIG thin films, and propose that superconductors can realize the spin-wave analogues of optical devices such as magnonic crystals, cavities, beam splitters, mirrors and waveguides.

The minimization of magnetic devices entered a new era with the advent two-dimensional Van der Waals materials, heralded by the isolation of graphene through mechanical exfoliation in 2004 [29, 30] and the consequent discovery of two-dimensional magnets in 2017 [31–33]. The reduced dimensionality of Van der Waals materials enables strong interactions, which together with the ability

to combine many types of materials into hybrid heterostructures have made van der Waals materials a rich testbed for the exploration of novel physics [34]. In this dissertation, we explore magnetic phenomena in two Van der Waals materials. In Chapter 4 we image the weak magnetic fields of Van der Waals interlayer antiferromagnet CrSBr, and in Chapter 3 we detect polarization of the electronic valley degree of freedom in two-dimensional semiconductor WS₂, in order to pave the way for detecting its associated magnetic signature.

The quest to detect weak magnetic phenomena at the nanoscale has pushed the development of new magnetic sensing techniques. Among them are magnetic force microscopy [35], magnetic resonance force microscopy [36, 37], superconducting quantum interference devices on scanning tips [38–40], and color centers in solid state crystals and molecules [41–44]. One such color center is the nitrogen-vacancy center in diamond, a point-like defect with a field-sensitive spin that can be optically initialized and read out. By bringing such defects in close proximity to a sample its magnetic stray fields can be detected. The NV center has been integrated in atomic force microscopes to image weak nanoscale vector magnetic fields with a spatial resolution below the diffraction limit [45, 46]. Additionally, the NV center is sensitive to oscillating magnetic fields that are resonant with its spin transitions, enabling the detection and imaging of oscillations of the magnetic order in magnets [47–49]. A wide temperature operability from 300 mK [50] up to 600 K [51] has been demonstrated, making the NV center an attractive sensor for a wide variety of condensed matter systems.

In this dissertation, we explore magnetism in a van der Waals magnet (Chapter 4) and magnetic excitations in a superconductor-magnet hybrid (Chapter 5) with the nitrogen vacancy center in diamond as magnetic field sensor. Additionally, we explore polarization of the valley degree of freedom of excitons in an atomically thin semiconductor (Chapter 3), to set the stage for probing valley magnetism with NV magnetometry. Therefore, in the next Chapter we introduce sensing with the NV centers in diamond followed by an introduction of the magnetic phenomena we investigate.

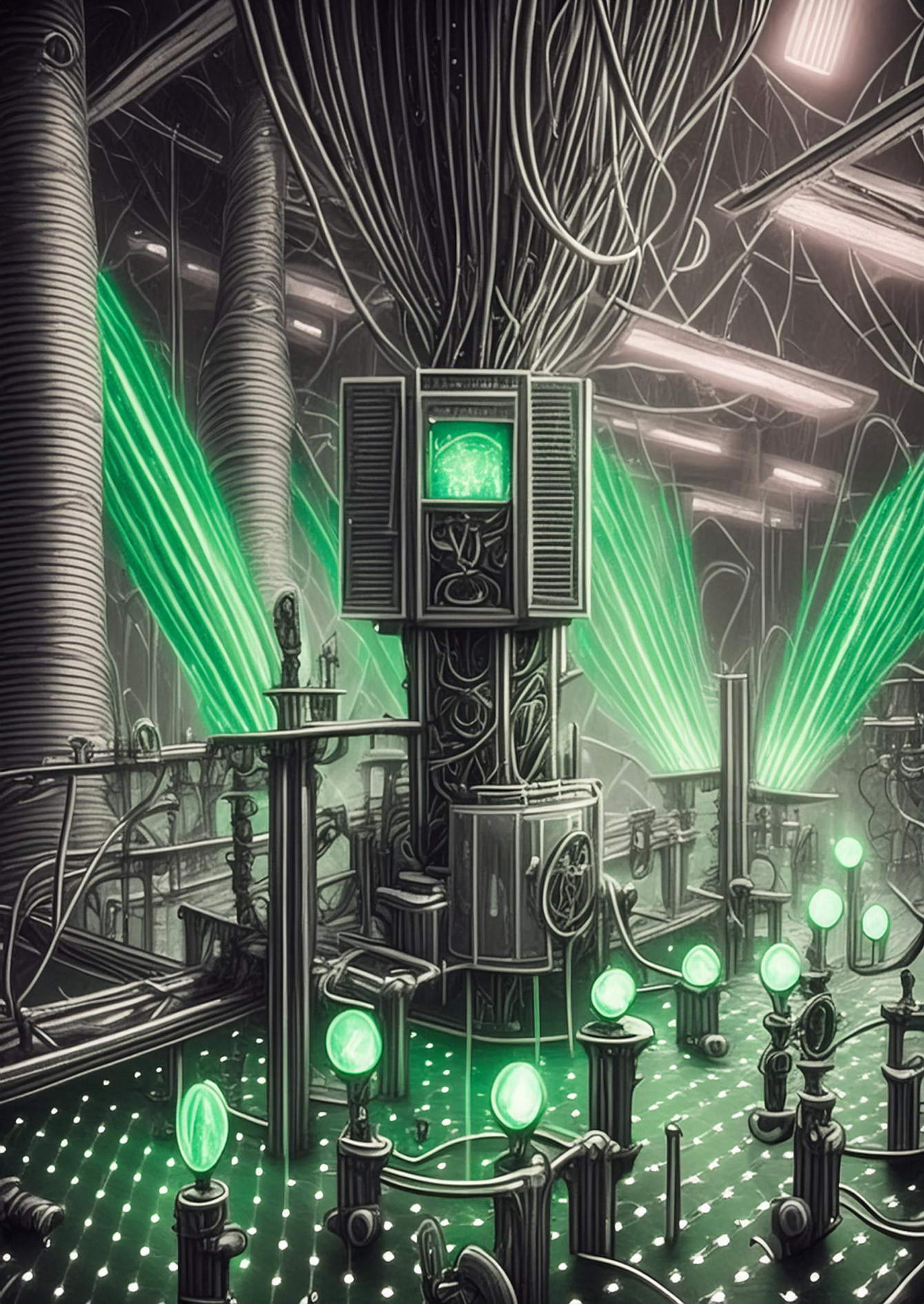
REFERENCES

- [1] P. O'Grady. *Thales of Miletus*.
- [2] Pliny *et al.* "The Magnet: Three remedies". *The Natural History of Plini*. London: Henry G. Bohn, 1855, p. 355.
- [3] N. Ida. *Engineering Electromagnetics*. Springer Nature Switzerland, 2015, p. 28. ISBN: 9780849373633.
- [4] J. Boutaric. "Les applications médicales de l'aimant de l'Antiquité au XIXe siècle". *Hist Sci Med* 28.3 (1994), pp. 255–263.
- [5] W. Gilbert. *De Magnete*. London: Peter Short, 1600.
- [6] C. Coulomb. "Premier mémoire sur l'électricité et le magnétisme". *Histoire de l'Académie Royale des Sciences* (1785), pp. 569–577.
- [7] J. Oersted. "Experiments on the effect of a current of electricity on the magnetic needle". *Annals of Philosophy; or, Magazine of Chemistry, Mineralogy, Mechanics, Natural History, Agriculture, and the Arts*. XVI (1820), pp. 273–276.
- [8] J. Maxwell. "On Physical Lines of Force". *Philosophical Magazine* 21.139 (1861), pp. 161–175.
- [9] J. Maxwell. "A dynamical theory of the electromagnetic field". *Royal Society* 155.155 (1865), pp. 459–512.
- [10] P. Zeeman. "On the Influence of Magnetism on the Nature of the Light Emitted by a Substance". *Communications from the Physical Laboratory of the University of Leiden* 33 (1896).
- [11] S. Goudsmit *et al.* "Over Het Roteerende Electron En de Structuur der Spectra". *Physica* 6 (1926), pp. 273–290.
- [12] G. Uhlenbeck *et al.* "Spinning Electrons and the Structure of Spectra". *Nature* 117 (1925), pp. 264/265. ISSN: 1660-8151. DOI: [10.1159/000182390](https://doi.org/10.1159/000182390).
- [13] W. Gerlach *et al.* "Der experimentelle Nachweis der Richtungsquantelung im Magnetfeld". *Zeitschrift für Physik* 9 (1922), pp. 349–352.
- [14] W. Heisenberg. "Zur Theorie des Ferromagnetismus". *Zeitschrift für Physik* 49 (1928), pp. 619–636.
- [15] J. Coey. "Exchange interactions". *Magnetism and Magnetic Materials*. 2010, pp. 135–143.
- [16] L. Landau. "A possible explanation of the field dependence of the susceptibility at low temperatures". *Phys. Z. Sowjet* 4 (1933), p. 675.

- [17] L. Néel. “Propriétés magnétiques des ferrites ; ferrimagnétisme et antiferromagnétisme”. *Annales De Physique* 12.3 (1948), pp. 137–198.
- [18] J. Coey. *Magnetism and Magnetic Materials*. 1st. Cambridge University Press, 2010.
- [19] M. N. Baibich *et al.* “Giant magnetoresistance of (001)Fe/(001)Cr magnetic superlattices”. *Physical Review Letters* 61.21 (1988), pp. 2472–2475. ISSN: 00319007. DOI: [10.1103/PhysRevLett.61.2472](https://doi.org/10.1103/PhysRevLett.61.2472).
- [20] G. Binasch *et al.* “Enhanced magnetoresistance in layered magnetic structures with antiferromagnetic interlayer exchange”. *Physical Review B* 39.7 (1989), pp. 4828–4830. ISSN: 01631829. DOI: [10.1103/PhysRevB.39.4828](https://doi.org/10.1103/PhysRevB.39.4828).
- [21] A. Hirohata *et al.* “Review on spintronics: Principles and device applications”. *Journal of Magnetism and Magnetic Materials* 509.March (2020). ISSN: 03048853. DOI: [10.1016/j.jmmm.2020.166711](https://doi.org/10.1016/j.jmmm.2020.166711).
- [22] V. V. Kruglyak *et al.* “Magnonics”. *Journal of Physics D: Applied Physics* 43.26 (2010). ISSN: 00223727. DOI: [10.1088/0022-3727/43/26/264001](https://doi.org/10.1088/0022-3727/43/26/264001).
- [23] A. V. Chumak *et al.* “Magnon spintronics”. *Nature Physics* 11.6 (2015), pp. 453–461. ISSN: 17452481. DOI: [10.1038/nphys3347](https://doi.org/10.1038/nphys3347).
- [24] P. Pirro *et al.* “Advances in coherent magnonics”. *Nature Reviews Materials* 6.12 (2021), pp. 1114–1135. ISSN: 20588437. DOI: [10.1038/s41578-021-00332-w](https://doi.org/10.1038/s41578-021-00332-w).
- [25] F. Bloch. “Zur Theorie des Ferromagnetismus”. *Zeitschrift für Physik* 61.11-12 (1930), pp. 206–209. ISSN: 14346001. DOI: [10.1007/BF01330417](https://doi.org/10.1007/BF01330417).
- [26] Griffiths J. H. E. “Anomalous High-frequency Resistance of Ferromagnetic Metals”. *Nature* 158 (1946), pp. 670–671.
- [27] J. R. Eshbach. “Spin-wave propagation and the magnetoelastic interaction in yttrium iron garnet”. *Physical Review Letters* 8.9 (1962), pp. 357–359.
- [28] A. A. Serga *et al.* “YIG magnonics”. *Journal of Physics D: Applied Physics* 43.26 (2010). ISSN: 00223727. DOI: [10.1088/0022-3727/43/26/264002](https://doi.org/10.1088/0022-3727/43/26/264002).
- [29] K. S. Novoselov *et al.* “Electric Field Effect in Atomically Thin Carbon Films”. *Science* 306.5696 (2004), pp. 666–669.
- [30] K. S. Novoselov *et al.* “Two-dimensional atomic crystals”. *Proceedings of the National Academy of Sciences of the United States of America* 102.30 (2005), pp. 10451–10453. ISSN: 00278424. DOI: [10.1073/pnas.0502848102](https://doi.org/10.1073/pnas.0502848102).
- [31] C. Gong *et al.* “Discovery of intrinsic ferromagnetism in two-dimensional van der Waals crystals”. *Nature* 546.7657 (2017), pp. 265–269. ISSN: 14764687. DOI: [10.1038/nature22060](https://doi.org/10.1038/nature22060).
- [32] B. Huang *et al.* “Layer-dependent ferromagnetism in a van der Waals crystal down to the monolayer limit”. *Nature* 546.7657 (2017), pp. 270–273. ISSN: 14764687. DOI: [10.1038/nature22391](https://doi.org/10.1038/nature22391). arXiv: [1703.05892](https://arxiv.org/abs/1703.05892).
- [33] Q. H. Wang *et al.* “The Magnetic Genome of Two-Dimensional van der Waals Materials”. *ACS Nano* (2021). ISSN: 1936086X. DOI: [10.1021/acsnano.1c09150](https://doi.org/10.1021/acsnano.1c09150).

- [34] Y. Liu *et al.* “Van der Waals heterostructures and devices”. *Nature Reviews Materials* 1.9 (2016). ISSN: 20588437. DOI: [10.1038/natrevmats.2016.42](https://doi.org/10.1038/natrevmats.2016.42).
- [35] O. Kazakova *et al.* “Frontiers of magnetic force microscopy”. *Journal of Applied Physics* 125.6 (2019). ISSN: 10897550. DOI: [10.1063/1.5050712](https://doi.org/10.1063/1.5050712).
- [36] J. Sidles *et al.* “Magnetic resonance microscopy”. *Reviews of Modern Physics* 67.1 (1995), pp. 259–266.
- [37] R. Winkler *et al.* *A Review of the Current State of Magnetic Force Microscopy to Unravel the Magnetic Properties of Nanomaterials Applied in Biological Systems and Future Directions for Quantum Technologies*. Vol. 13. 18. 2023. ISBN: 3487655535. DOI: [10.3390/nano13182585](https://doi.org/10.3390/nano13182585).
- [38] A. Finkler *et al.* “Scanning superconducting quantum interference device on a tip for magnetic imaging of nanoscale phenomena”. *Review of Scientific Instruments* 83.7 (2012). ISSN: 00346748. DOI: [10.1063/1.4731656](https://doi.org/10.1063/1.4731656). arXiv: [1206.2853](https://arxiv.org/abs/1206.2853).
- [39] D. Vasyukov *et al.* “A scanning superconducting quantum interference device with single electron spin sensitivity”. *Nature Nanotechnology* 8.9 (2013), pp. 639–644. ISSN: 17483395. DOI: [10.1038/nnano.2013.169](https://doi.org/10.1038/nnano.2013.169).
- [40] M. Wyss *et al.* “Magnetic, Thermal, and Topographic Imaging with a Nanometer-Scale SQUID-On-Lever Scanning Probe”. *Physical Review Applied* 17.3 (2022), p. 1. ISSN: 23317019. DOI: [10.1103/PhysRevApplied.17.034002](https://doi.org/10.1103/PhysRevApplied.17.034002). arXiv: [2109.06774](https://arxiv.org/abs/2109.06774).
- [41] L. Rondin *et al.* “Magnetometry with nitrogen-vacancy defects in diamond”. *Reports on Progress in Physics* 77.5 (2014). ISSN: 00344885. DOI: [10.1088/0034-4885/77/5/056503](https://doi.org/10.1088/0034-4885/77/5/056503). arXiv: [1311.5214](https://arxiv.org/abs/1311.5214).
- [42] M. Huang *et al.* “Wide field imaging of van der Waals ferromagnet Fe₃GeTe₂ by spin defects in hexagonal boron nitride”. *Nature Communications* 13.1 (2022), pp. 1–7. ISSN: 20411723. DOI: [10.1038/s41467-022-33016-2](https://doi.org/10.1038/s41467-022-33016-2). arXiv: [2112.13570](https://arxiv.org/abs/2112.13570).
- [43] P. Kumar *et al.* “Magnetic Imaging with Spin Defects in Hexagonal Boron Nitride”. *Physical Review Applied* 18.6 (2022), pp. 1–6. ISSN: 23317019. DOI: [10.1103/PhysRevApplied.18.L061002](https://doi.org/10.1103/PhysRevApplied.18.L061002). arXiv: [2207.10477](https://arxiv.org/abs/2207.10477).
- [44] K. R. Mullin *et al.* “Quantum sensing of magnetic fields with molecular color centers”. *Physical Review Research* 5.4 (2023), pp. 1–9. ISSN: 26431564. DOI: [10.1103/PhysRevResearch.5.L042023](https://doi.org/10.1103/PhysRevResearch.5.L042023). arXiv: [2302.04248](https://arxiv.org/abs/2302.04248).
- [45] F. Casola *et al.* “Probing condensed matter physics with magnetometry based on nitrogen-vacancy centres in diamond”. *Nature Reviews Materials* 3 (2018). ISSN: 20588437. DOI: [10.1038/natrevmats.2017.88](https://doi.org/10.1038/natrevmats.2017.88).
- [46] Y. Xu *et al.* “Recent advances on applications of NV magnetometry in condensed matter physics”. *Photonics Research* 11.3 (2023), p. 393. ISSN: 23279125. DOI: [10.1364/prj.471266](https://doi.org/10.1364/prj.471266).

- [47] T. Van Der Sar *et al.* “Nanometre-scale probing of spin waves using single-electron spins”. *Nature Communications* 6 (2015). ISSN: 20411723. DOI: [10.1038/ncomms8886](https://doi.org/10.1038/ncomms8886). arXiv: [1097326](https://arxiv.org/abs/1097326) [arXiv:submit].
- [48] T. X. Zhou *et al.* “A magnon scattering platform”. *Proceedings of the National Academy of Sciences of the United States of America* 118.25 (2021), pp. 1–6. ISSN: 10916490. DOI: [10.1073/pnas.2019473118](https://doi.org/10.1073/pnas.2019473118). arXiv: [2004.07763](https://arxiv.org/abs/2004.07763).
- [49] I. Bertelli *et al.* “Magnetic resonance imaging of spin-wave transport and interference in a magnetic insulator”. *Science Advances* 6.46 (2020), pp. 1–8. ISSN: 23752548. DOI: [10.1126/sciadv.abd3556](https://doi.org/10.1126/sciadv.abd3556). arXiv: [2004.07746](https://arxiv.org/abs/2004.07746).
- [50] P. J. Scheidegger *et al.* “Scanning nitrogen-vacancy magnetometry down to 350 mK”. *Applied Physics Letters* 120.22 (2022). ISSN: 00036951. DOI: [10.1063/5.0093548](https://doi.org/10.1063/5.0093548). arXiv: [2203.15527](https://arxiv.org/abs/2203.15527).
- [51] D. M. Toyli *et al.* “Measurement and control of single nitrogen-vacancy center spins above 600 K”. *Physical Review X* 2.3 (2012), pp. 1–7. ISSN: 21603308. DOI: [10.1103/PhysRevX.2.031001](https://doi.org/10.1103/PhysRevX.2.031001). arXiv: [1201.4420](https://arxiv.org/abs/1201.4420).



2

THEORY AND EXPERIMENT

*A journey of a thousand miles
begins with a single step.*

Lao Tzu

Here, we first introduce magnetometry with nitrogen vacancy centers in diamond, and discuss novel low-dimensional magnetic phenomena that we aim to detect with this technique. We discuss how we brought these ideas from paper into practice, such as the experimental setups that were constructed, the materials we studied, and the realization of suitable samples. Finally, we discuss electronics and measurements, providing a complete framework to understand the experimental research chapters of this dissertation.

Parts of this chapter have been published in *npj 2D Mater Appl* 7, 62 (2023) by T.S. Ghiasi, **M. Borst et al.** and in *Science* **382**, 430-434 (2023), by **M. Borst et al.**

Magnetism pervades modern information technology, and with the quest to improve performance, minimize device footprints and reduce energy consumption, novel magnetic phenomena in the smallest materials possible are of both fundamental interest and paramount technological importance. We highlight three such phenomena that hold promise for next generation information processing and storage: valley magnetism, two-dimensional magnets, and magnetic excitations. Within each topic we describe fundamental open questions, state long-term research goals, and set the stage for answering these questions with magnetometry based on the nitrogen vacancy center in diamond. We proceed to discuss the construction of experimental setups, the fabrication of samples, and the development and application of diamond membranes for quantum sensing of the magnetic phenomena described above. The research chapters in this dissertation can be understood as either stepping stones towards, or realization of the long term research goals.

2.1. MAGNETOMETRY WITH SPINS IN DIAMOND

The exploration of electronic transport and magnetism at the smallest scale has driven the development of new magnetic field sensors, capable of imaging weak magnetic fields with nanoscale spatial resolution and high sensitivity [1]. Superconducting quantum interference devices on the tip of a pulled fiber (SQUID-on-tip [2, 3]) have revealed hydrodynamic electron flow in WTe_2 [4] and exotic Berry-curvature magnetism in twisted bilayer graphene [5]. Magnetized nanowires have shown promise to sense even weak magnetic fields using magnetic force microscopy [6]. Finally, magnetometry based on the nitrogen vacancy (NV) center in diamond has been employed to image the weak magnetic fields of van der Waals magnets [7], magnetic and superconducting vortices [8, 9], and to detect and image spin-excitations in magnets [10–12]. Among these techniques, NV magnetometry stands out due to its capability to quantitatively measure vector magnetic fields over temperatures ranging from 350 mK to 600 K [13, 14]. In this dissertation, we employ NV magnetometry for quantum sensing of a Van der Waals magnet (Chapter 4) and spin waves in a hybrid superconductor-magnet system (Chapter 5). Therefore, we next introduce the NV center and discuss in detail how it can be used to sense magnetic fields.

The nitrogen vacancy (NV) center in diamond is formed by a lattice vacancy with an adjacent nitrogen substitution (Fig. 2.1a). By symmetry, eight NV orientations are possible along the [111]-family of lattice vectors in the diamond crystal. The NV center has two optically active charge states: a neutral (NV^0) state and a negatively charged (NV^-) state. The NV^0 state comprises five electrons: three from dangling carbon atom bonds, and two from the dangling nitrogen atom bond. NV^- is formed through the capture of an additional electron at the defect site [15]. NV^- and NV^0 are optically active single photon emitters (SPE), with a zero phonon line (ZPL) and phonon sideband (Fig. 2.1b), and interconversion between them is possible through manipulation of the charge environment of the defect [16]. The NV^- ground state is a spin-triplet that can be spin-polarized optically, shows spin-dependent photoluminescence, and is long-lived even at room temperature, making it an attractive defect for quantum information and quantum sensing [15, 17–19].

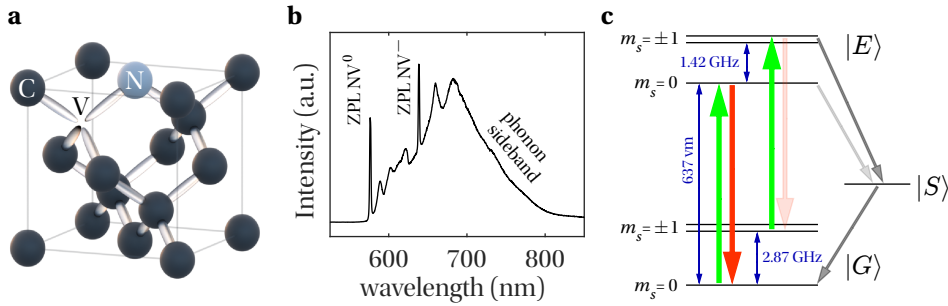


Figure 2.1. **The nitrogen vacancy center in diamond.** (a) A nitrogen vacancy (NV) center defect in the diamond lattice. One carbon atom is substituted with a nitrogen atom, and a neighbouring carbon atom is removed, leaving a vacancy. The eight possible orientations of the NV defect are degenerate in absence of magnetic field. (b) Photoluminescence spectrum of a diamond filled with an ensemble of near-surface NV centers, under off-resonant excitation with a green laser (520 nm), taken at $T = 5$ K. The many NV centers are in a distribution of neutral (NV^0) and negatively charged (NV^-) states, which luminesce either directly in their zero phonon lines (ZPL) at 575 nm (NV^0) and 637 nm (NV^-), or through phonon-assisted processes in the so-called phonon sideband. (c) Schematic of the NV energy level structure, and optical spin-readout and initialization. Spin-preserved excitation from the ground state $|G\rangle$ to the excited state $|E\rangle$ in $m_s = 0$ leads to optically bright relaxation, while the same process for $m_s = \pm 1$ yields mostly optically dark relaxation via the singlet state $|S\rangle$ back to $m_s = 0$, enabling both optical readout of the spin, and initialization in $m_s = 0$ through optical cycling.

OPTICAL SPIN POLARIZATION AND READOUT

To understand how the NV^- spin can be polarized and read out optically, we inspect the energy level structure of the defect [20]. As shown in Fig. 2.1c, the level structure is characterized by a spin triplet ground state $|G\rangle$ with a zero field splitting of $D = 2.87$ GHz separating the $m_s = \pm 1$ levels from $m_s = 0$. At room temperature, the excited state $|E\rangle$ can be described as a spin-triplet state with zero field splitting $D_e = 1.42$ GHz. The excited and ground states reside within the diamond band gap, and in between them lies a metastable singlet state $|S\rangle$. Non-resonant optical excitation (using e.g. a green laser) drives NV^- from $|G\rangle$ to $|E\rangle$ in a spin-conserved fashion [21]. While $|E, m_s = 0\rangle$ mostly undergoes fast radiative decay back to $|G, m_s = 0\rangle$, the excited state $|E, m_s = \pm 1\rangle$ has a larger probability to decay via the dark metastable state $|S\rangle$, leading to a contrast in luminescence between $m_s = 0$ and $m_s = \pm 1$, enabling optical readout of the spin state. Additionally, decay via $|S\rangle$ predominantly returns the NV center to $|G, m_s = 0\rangle$ [22]. Continuous wave cycling will thus spin-polarize the ground state, enabling high-fidelity initialization of a quantum system even at temperatures much larger than the spin-splitting $\sim \hbar D/k_B$.

OPTICALLY DETECTED MAGNETIC RESONANCE

As described above, optical excitation polarizes the NV center into the $m_s = 0$ state. The presence of a microwave magnetic field resonant with the electron spin transition from $|G, m_s = 0\rangle$ to $|G, m_s = \pm 1\rangle$ will drive the spin into $m_s = \pm 1$, leading to a reduction in photoluminescence as was first demonstrated in 1997 [23]. This is known as optically

detected magnetic resonance (ODMR), which is typically performed by sweeping the microwave frequency over the electron spin resonance (ESR) while monitoring the photoluminescence under continuous wave excitation, as shown in Fig. 2.2a. Here, the reduction in photoluminescence at the resonance frequency is the ESR contrast, defined as

$$C = \frac{PL_0 - PL_{\text{drive}}}{PL_0}, \quad (2.1)$$

where PL_0 is the photoluminescence without microwaves present and PL_{drive} is the photoluminescence while driving ESR. The ESR contrast depends on the microwave power and optical driving power [24],

$$C = C_0 \frac{\Omega_R^2}{\Omega_R^2 + \Gamma_p^\infty \Gamma_c^\infty \left(\frac{s}{1+s} \right)^2}. \quad (2.2)$$

Here, C_0 is the maximum attainable ESR contrast, which is set by the different spin-dependent transition rates between the NV levels and the background photoluminescence, and is typically 20% for single NV centers and 2% for NV ensembles. Ω_R is the Rabi frequency, i.e. the microwave field strength at the NV center location. The parameter $s = P/P_{\text{sat}}$ is the optical power P normalized by the saturation power P_{sat} . Γ_p^∞ is the maximum spin-polarization rate of the ground state, set by the lifetime of the metastable singlet state, roughly 200 ns at room temperature [25] ($\Gamma_p^\infty = 5 \times 10^6 \text{ s}^{-1}$). Γ_c^∞ is the maximum optical cycling rate, set by the excited state radiative lifetime of approximately 13 ns [26] ($\Gamma_c^\infty = 7.7 \times 10^7 \text{ s}^{-1}$). The ESR contrast saturates with both optical and microwave power, and tuning of these parameters is required if spatial variations in the microwave field strength can be revealed through measuring the contrast C . Optical detection of the microwave field strength is the basis for imaging spin waves through their stray fields as presented in Chapter 5 [11].

MAGNETIC FIELD SENSING WITH NV CENTRES

The NV center can be employed as a sensor of the local static magnetic field. To understand how we can use ODMR to detect magnetic fields, we investigate the Hamiltonian of the NV center ground state, in which we neglect contributions due to electric field and hyperfine coupling to various nuclear spins in the environment [28],

$$\frac{\hat{\mathcal{H}}}{\hbar} = D\hat{S}_z^2 + \gamma\mathbf{B} \cdot \hat{\mathbf{S}}, \quad (2.3)$$

where

$$\mathbf{B} = \begin{bmatrix} B_x \\ B_y \\ B_z \end{bmatrix}, \quad \hat{\mathbf{S}} = \begin{bmatrix} \hat{S}_x \\ \hat{S}_y \\ \hat{S}_z \end{bmatrix}, \quad (2.4)$$

$D = 2.87 \text{ GHz}$ is the zero field splitting, and $\gamma = 28.024 \text{ GHz/T}$ is electron gyromagnetic ratio. It is common to define the NV spin quantization axis along $\hat{\mathbf{z}}$, thus we write the

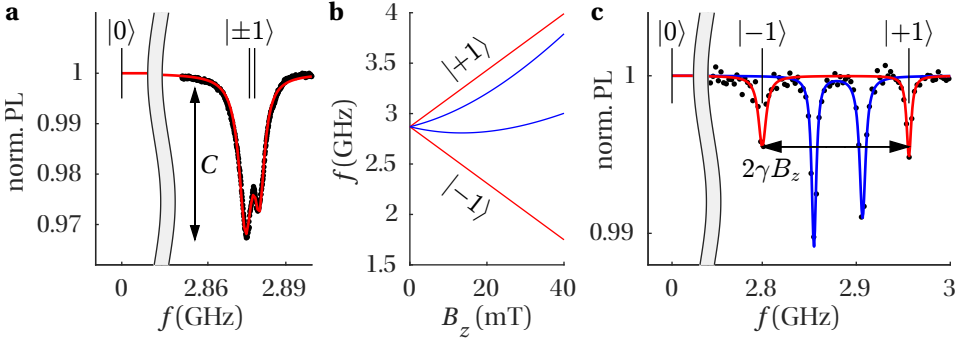


Figure 2.2. **Optically detected magnetic resonance.** (a) Electron spin resonance (ESR) of a nitrogen vacancy (NV) center ensemble near zero magnetic field. The photoluminescence (PL) is reduced when the microwaves drive the transition from $m_s = 0$ to $m_s = \pm 1$, parametrized by the ESR contrast C . A small few MHz splitting is visible, attributed to hyperfine coupling with the ^{15}N nuclear spin and a small but finite magnetic field [27]. (b) Energy level diagram of an NV ensemble in presence of a magnetic field B_z aligned with one of the four crystallographic NV axes. The $m_s = \pm 1$ states of the aligned NV family split linearly with the applied field (red), while the other families are degenerate due to symmetric projection of the misaligned field on their quantization axes (blue). (c) Electron spin resonance measurement of an NV ensemble with magnetic field $B_z = 2.8$ mT along the axis of one family. The $|\pm 1\rangle$ states of the aligned family split by an amount $2\gamma B_z$. Measurements were taken at room temperature, with the setup detailed in 2.6, by monitoring PL under non-resonant excitation with a 520 nm laser, while sweeping the microwave frequency.

Pauli spin matrices in the z basis as

$$\hat{S}_x = \frac{1}{\sqrt{2}} \begin{bmatrix} 0 & 1 & 0 \\ 1 & 0 & 1 \\ 0 & 1 & 0 \end{bmatrix}, \quad \hat{S}_y = \frac{1}{\sqrt{2}} \begin{bmatrix} 0 & -i & 0 \\ i & 0 & -i \\ 0 & i & 0 \end{bmatrix} \quad \text{and} \quad \hat{S}_z = \begin{bmatrix} 1 & 0 & 0 \\ 0 & 0 & 0 \\ 0 & 0 & -1 \end{bmatrix}. \quad (2.5)$$

The zero field splitting D predominantly arises from spin interactions with electrons on neighbouring carbon atoms, and thus depends on the crystal topology and changes with pressure, strain and temperature [29]. We consider the case where the magnetic field is aligned with the quantization axis of one NV family, i.e. $\mathbf{B} = B_z \hat{\mathbf{z}}$ where $\hat{\mathbf{z}} \in \{111\}$. The $m_s = \pm 1$ states split linearly and oppositely with the applied field,

$$\hat{\mathcal{H}} |\pm 1\rangle = (D \pm \gamma B_z) |\pm 1\rangle, \quad (2.6)$$

as calculated in Fig. 2.2b (red lines) and observed experimentally in Fig. 2.2c (red ODMR fits). By fitting ODMR spectra to find the ESR frequencies f^\pm corresponding to transitions from $|0\rangle$ to $|\pm 1\rangle$, we extract the magnetic field along the NV axis,

$$B_z = \frac{f^+ - f^-}{2\gamma}, \quad \text{or} \quad B_z = \frac{|D - f^\pm|}{\gamma}. \quad (2.7)$$

Typically, the first expression is preferred because it does not rely on knowledge of the zero field splitting, which can vary as a function of temperature and position through

change in the above mentioned quantities. The above demonstrated extraction of static field is used in Chapter 4 to measure the stray fields of a Van der Waals magnet.

When the field is aligned along the axis of a single family within the NV ensemble, by symmetry the remaining families have identical field projection on their quantization axes. This makes them energetically degenerate as evidenced by a total of only four resonance dips in the ESR spectrum (Fig. 2.2b-c, blue). The aligned family and the degenerate misaligned families are used for probing different parts of the spin-wave spectrum underneath a superconductor in Chapter 5. For arbitrary magnetic fields with a unique projection for every NV family, a total of eight resonance dips are present: a distinct transition to $|+1\rangle$ and $|−1\rangle$ for each NV orientation. Fitting ESR data with the above described Hamiltonian allows determining the vector magnetic field.

NV sensing is most efficient and sensitive with magnetic bias fields along its quantization axis \hat{z} , since the ESR contrast is quenched by fields perpendicular to its quantization axis [30], and the vector field \mathbf{B} can be reconstructed by measuring only a single magnetic field component [19]. Therefore, all NV measurements presented in Chapter 4 and 5 are performed with an external bias field along the NV quantization axis, unless otherwise mentioned.

2.2. PROBING LOW-DIMENSIONAL MAGNETIC PHENOMENA

Having discussed the concept of magnetic field sensing with nitrogen vacancy (NV) centers in diamond, we now shift our focus to exploration of three magnetic phenomena that hold promise for next generation magnetic information technology: valley magnetism in two-dimensional semiconductors, two-dimensional van der Waals magnets, and oscillations in the magnetic order of thin magnets. We set the stage towards probing these phenomena with nitrogen vacancy centers by introducing each topic and elaborating on the newly constructed experimental setups we used to study these material systems.

2.2.1. THE VALLEY MAGNETIC MOMENT

Information encoding and processing using the charge and spin degree of freedom of electrons is the foundation for electronics and spintronics [31]. Electrons in crystalline solids also possess a valley degree of freedom, which refers to the conduction band minimum or valence band maximum in which the electron resides. The idea to use the valley degree of freedom to encode, process and store information has brought forth the concept of valleytronics [32]. However, since long-lived and highly polarized valley states are difficult to generate and control, widespread application and manipulation of the valley degree of freedom has remained elusive compared to its spin and charge counterparts. The recent emergence of two-dimensional materials with hexagonal structures has shown great promise to realize functional valleytronic devices.

Valleytronics relies on the ability to create valley polarization, the selective population of a single valley. The first proposal to create valley polarization in 2D materials was through the so-called valley filter in graphene [33]. Though this idea proved difficult to realize because it required atomically clean graphene edges, it paved the way for further theoretical investigations. Shortly afterwards, theory by Xiao *et al.* [34] showed that

when inversion symmetry in graphene is broken, the pseudospin associated with the valley index carries an intrinsic magnetic moment akin to the electron spin and its associated Bohr magneton, opening the door for *magnetic* detection of valley polarization. As such, graphene-like materials in which inversion symmetry is intrinsically broken instead of externally imposed became natural candidates for further investigation of valley magnetism.

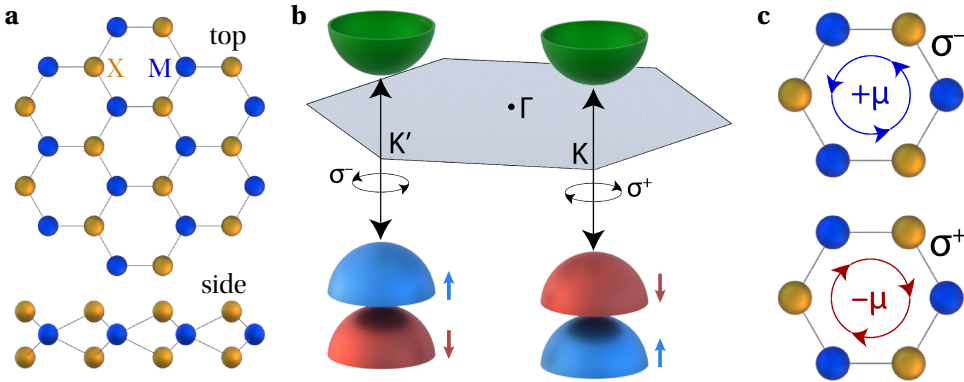


Figure 2.3. Valley magnetism in transition metal dichalcogenide monolayers. (a) Top and side view of the hexagonal structure of a monolayer transition metal dichalcogenide (TMD), in which no inversion center is present. It is comprised of the chemical formula MX_2 , where M is a transition metal and X a chalcogen. (b) Schematic of the band structure in the hexagonal Brillouin zone of TMDs, with direct-bandgap valleys at the K and K' points, enabling efficient optical excitation and emission. Strong spin-orbit coupling splits the valence band oppositely in K and K', while the breaking of inversion symmetry leads to valley-dependent circular dichroism: selective excitation of K (K') with right (left) circularly polarized light. (c) Schematic of self-rotating wavepackets with valley magnetic moment. The wavefunction of quasiparticles excited by right (σ^+) and left (σ^-) circularly polarized light have opposite self-rotation, arising from Berry curvature and orbital angular momentum, leading to a valley-magnetic moment μ that is opposite in sign.

One such promising class of materials are group-VI transition metal dichalcogenides (TMDs) of the formula MX_2 , where M = W, Mo and X = S, Se, of which the atomic structure is shown in Fig. 2.3a. In monolayers of these van der Waals materials, spin- and valley-physics were shown to be coupled due to the lack of an inversion center and strong spin-orbit coupling from the heavy metal atoms [35]. Additionally, optical polarization dependent selection rules enable selective photo-excitation of quasiparticles with spin- and valley indices, providing a straightforward method to optically induce valley polarization in the K- and K'-valley with left- and right-handed circularly polarized light, as was demonstrated shortly after [36–39], and schematically shown in Fig. 2.3b.

The existence of the accompanying valley magnetic moment was demonstrated from the coupling of pseudospin to external magnetic fields through the so-dubbed valley Zeeman effect [40–42]. The observation of the valley Zeeman effect in optically excited quasiparticles is evidence of electron-hole symmetry breaking, i.e. a different magnetic moment for the conduction and valence band, and thus of the ability to optically induce a valley magnetic moment [43], as schematically shown in Fig. 2.1c. However, the net

magnetic moment upon photoexcitation remains unclear for two reasons. Firstly, the Valley Zeeman experiments only detect the magnetic moments of quasiparticles that recombine radiatively. Secondly, it was shown that a picture of non-interacting optically excited quasiparticles can not explain the magnetic moments measured [40], implying the net magnetic moment depends on the quasiparticle distribution, which is in turn determined by doping, scattering mechanisms, and (non-)radiative recombination rates.

The ability to locally detect and image the valley magnetic moment would provide insight into its magnitude, and enable a local study of transport properties of valley-polarized states, such as their diffusion length and lifetime. The use of NV magnetometry forms a potential avenue to realizing magnetic imaging of valley states. However, recent experiments have demonstrated that the photoexcitation necessary for creating valley polarized states also induces a thermal gradient, which in the presence of a perpendicular magnetic field leads to formation of circulating Nernst currents around the optical spot [44], the magnetic field of which could obscure that of the valley magnetic moment. The direction of photo-Nernst currents is set by the thermal gradient induced by the laser and the direction of the external magnetic field, and is therefore independent of the polarization of the laser. Since the laser polarization sets the sign of the valley magnetic moment, it might be used to distinguish between magnetic signatures of photocurrents and valley states. A potential way to realize this is the use of an AC magnetometry protocol in which the valley magnetic moment repeatedly changes sign in unison with the NV spin, through fast polarization switching of the TMD excitation laser and simultaneous phase-locked microwave π -pulsing of the NV center spin. In Chapter 6, we discuss this idea in more detail.

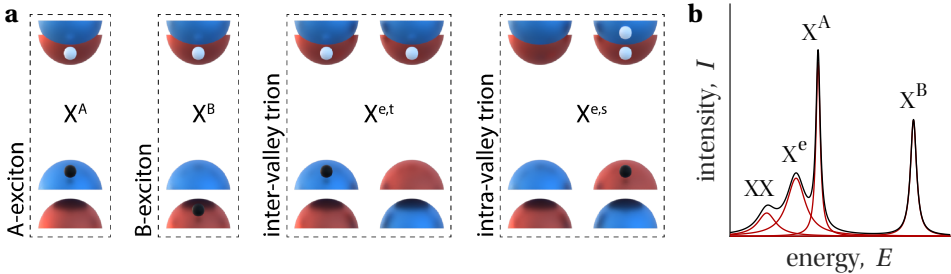


Figure 2.4. **Excitonic complexes and their optical footprints in neutral and doped TMD monolayers** (a) Schematic depictions of various excitonic complexes in the band structure of transition metal dichalcogenide monolayers. Optical excitation over the direct bandgap leads to formation of various excitonic complexes, bound states consisting of combinations of electrons and holes held together by strong Coulomb interaction. (b) Sketch of a typical optical emission profile of monolayer group IV transition metal dichalcogenides, upon non-resonant laser excitation. The optically bright A-exciton is separated by the valence band spin-orbit splitting from the B-exciton X^B . Darker charged trionic complexes ($X^{e(h)}$) or neutral biexcitons (XX) are characterized by additional binding energies.

The first step towards detecting the optically induced valley magnetic moment in group-IV TMDs is to understand their behaviour under optical excitation. A multitude of studies on the optical properties of TMDs have established that excitonic bound states form

upon near-resonant photoexcitation of mono- and few-layer TMDs [45]. When an electron is excited across the bandgap, the strong Coulomb interaction in two-dimensional materials results in a tightly bound exciton with a typical lifetime on the picosecond timescale and a Bohr radius of 1-2 nm [32, 42]. The attraction between electrons and holes can result in many types of bound states, each of which contributes differently to the net valley magnetic moment depending on whether its comprising quasiparticles reside in the K- or K'-valley. Therefore, to understand valley polarization, we first need to discuss the various excitonic states that are typically formed in group-IV TMD monolayers.

The optically bright A-exciton (X^A) is formed by an electron in the conduction band and a hole in the upper spin-split valence band, whereas the B-exciton (X^B) has a hole in the lower spin-split valence band (Fig. 2.4a). Either exciton resides completely in the K- or K'-valley, and it can scatter between them through inter-valley scattering. Upon creation of an exciton, one of various scenarios can take place. Predominantly, the exciton recombines radiatively giving rise to bright spectral emission peaks (Fig. 2.4b). Alternatively, the exciton can undergo non-radiative recombination through scattering pathways. In the presence of free excess carriers, the A-exciton can capture an additional electron (hole) to form a negatively (positively) charged trion $X^{e(h)}$, with typical binding energies of 30 meV [32]. The excess particle can originate either from the same valley (singlet trion) or opposite valley (triplet trion) (Fig. 2.4a), each with different valley magnetic moments [40]. Besides radiative recombination of an electron and hole within the trion complex, trions have a significant chance to undergo non-radiative Auger-recombination [46], making them less bright than the exciton (Fig. 2.4b). For completeness, we note that excitons can intercombine with excitons or trions, to create a bi-exciton (XX, Fig. 2.4b) or exciton-trion, where binding energies increase with the amount of particles involved [47]. Keeping the valley degeneracy in mind, it is clear many types of bound states can form. Under non-resonant optical excitation, we may thus expect a distribution to form between excitons, trions and additional bound state complexes, where the equilibrium and net valley magnetic moment will be determined by doping, quasiparticle lifetimes, emission rates and scattering between valleys [48].

Having discussed how excitonic bound states are formed upon photoexcitation, we now discuss how their valley polarization can be measured optically. As mentioned earlier, polarization dependent selection rules enable valley-selective excitation of electrons. Inversely, radiative recombination yields a σ^+ -photon for a K-valley exciton and a σ^- -photon for a K'-valley exciton. Therefore, the optically induced valley polarization ρ of excitonic states can be measured through circular dichroism of its emission,

$$\rho_K = \frac{I_{\sigma^+} - I_{\sigma^-}}{I} \quad \text{and} \quad \rho_{K'} = \frac{I_{\sigma^-} - I_{\sigma^+}}{I}. \quad (2.8)$$

Here, the total emission intensity I is decomposed in a right-handed (I_{σ^+}) and left-handed (I_{σ^-}) component. Typically, there is symmetry between polarization induced in either valley, such that $\rho = \rho_K = \rho_{K'}$. In Chapter 3, we use the above described principle to detect the valley polarization ρ of excitons and trions in monolayer WS_2 , and develop a novel method for controlling the exciton-trion balance through doping, paving the way for detecting and controlling the valley magnetic moment in monolayer TMDs.

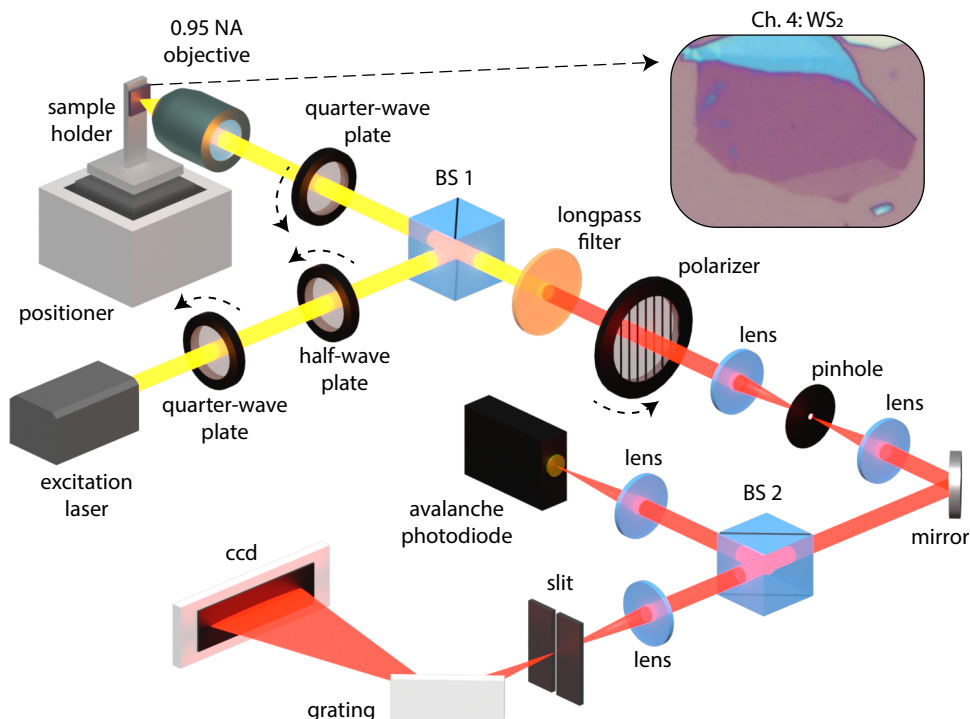


Figure 2.5. Home-built room temperature polarization-sensitive confocal microscopy setup. Schematic representation of the experimental setup constructed to perform confocal microscopy and spectroscopy on few-layer transition metal dichalcogenides at room temperature and ambient conditions, as presented in Chapter 4. Samples are excited by a low-pass filtered 594 nm laser (Coherent OBIS LS 594). The first quarter-wave plate ($\lambda/4$) corrects for imperfections in the laser polarization and makes it perfectly linear, such that the excitation polarization can be controlled by turning the half-wave plate ($\lambda/2$). A 10:90 (R:T) beam splitter separates the excitation and detection paths. A 0.95 NA objective (Olympus, 50x) focuses the laser on the sample and collects the photoluminescence. The sample position is fixed on a custom sample holder and positioned using an XYZ piezoelectric nano-positioner (Mad City Labs, Nano-3D200FT). The polarization of the detection is controlled by the relative orientations of the second quarter-wave plate and the polarizer. A longpass filter eliminates the excitation laser. The photoluminescence is filtered with a pinhole, after which it is detected by an avalanche photodiode (Excelitas SPCM-AQRG-13) and a spectrometer (Andor Kymera 193i) equipped with a 1600x200 pixel CCD (Andor iVac 324).

After conceptually demonstrating how valley polarization can be probed, we turn to its practical implementation by discussing a newly-built polarization sensitive confocal microscopy and spectroscopy setup (Fig. 2.5). A 594 nm laser is used to excite WS_2 close to the resonance of its A-exciton, after which we detect emission due to radiative recombination of the excitonic complexes. A combination of two quarter wave plates, a beam splitter and a polarizer is used to selectively excite with $\sigma+$ or $\sigma-$, and detect emission with $\sigma+$ or $\sigma-$ by projecting circularly polarized light from the sample on, or perpendic-

ular to, the polarizer transmission axis.

A longpass filter serves to separate the WS₂ luminescence from the excitation laser, while a pinhole spatially defines the detection volume, increasing the spatial resolution and the signal to background ratio of the detected signal. We decompose the luminescence in trion and exciton contributions by spectral analysis, and use an avalanche photodiode to count the total photons emitted by the sample. Four possible combinations of excitation and detection provide insights in the polarization induced in both valleys, commonly denoted $\sigma_1^{+/-}\sigma_2^{+/-}$, indicating excitation (1) and detection (2) of and from the K-valley (+) or K'-valley (-).

2.2.2. TWO-DIMENSIONAL MAGNETS

Having established a setup for spectral characterization of two-dimensional materials, we next developed the ability to detect and image the magnetic field of a two-dimensional material at cryogenic temperatures using NV centers in diamond. We expanded the experimental setup (Fig. 2.5) with a newly-arrived cryostat with optical access, and implemented microwave control and DC transport capabilities (Fig. 2.6). A central challenge in widefield NV-based sensing of weak evanescent magnetic fields is to reduce the distance between the sample and sensor spins. To address this, we developed the ability to place NV ensemble diamonds in contact with a sample, as shown in the sample insets in Fig. 2.6 and detailed in Section 2.3.2. As such, we established the ability to image weak magnetic fields from 2D materials. Combined with the spectral characterization capabilities, we created a versatile setup that enables spectral, electronic and magnetic probing of ultrathin materials over a temperature range of 4-300 K. In Chapter 4, we use these abilities to image the magnetic stray fields emanating from an uncompensated monolayer of Van der Waals magnet CrSBr. Therefore, we next briefly review the short history of van der Waals magnets and their magnetic excitations.

After the successful isolation of atomically thin graphene by mechanical exfoliation [50, 51], van der Waals materials have become one of the most exciting and versatile material systems in condensed matter physics. They owe this to rich physics in reduced dimensions and the virtually limitless possibilities for creating hybrid materials through stacking van der Waals materials in heterostructures. Yet, fifteen years after the birth of this exciting field, the word "magnet" remained surprisingly absent from reviews on Van der Waals materials [52]. Since the Mermin-Wagner theorem forbids long-range magnetic order in two dimensional systems without anisotropy [53], it was long unclear whether two-dimensional magnets are physically realisable, until intrinsic ferromagnetism was discovered in monolayers of Cr₂Ge₆Te₂ and CrI₃ through the magneto-optical Kerr effect [54, 55]. These materials have cryogenic Curie temperatures, and naturally a search for room-temperature van der Waals magnets began, with a demonstration of ionic gating pushing T_c of Fe₃GeTe₂ above room temperature soon to follow [56].

On the theoretical side, the study of interacting magnetic moments in 2D through e.g. the Ising-, XY-, and Heisenberg-models have long since led to novel concepts in the study of phase transitions and critical phenomena, such as scale invariance and renormalization. Consequent studies of phase transitions in van der Waals magnets demonstrated a large variety of critical exponents, many in between values corresponding to the known models, indicating more complex spin-spin interactions are at play [57].

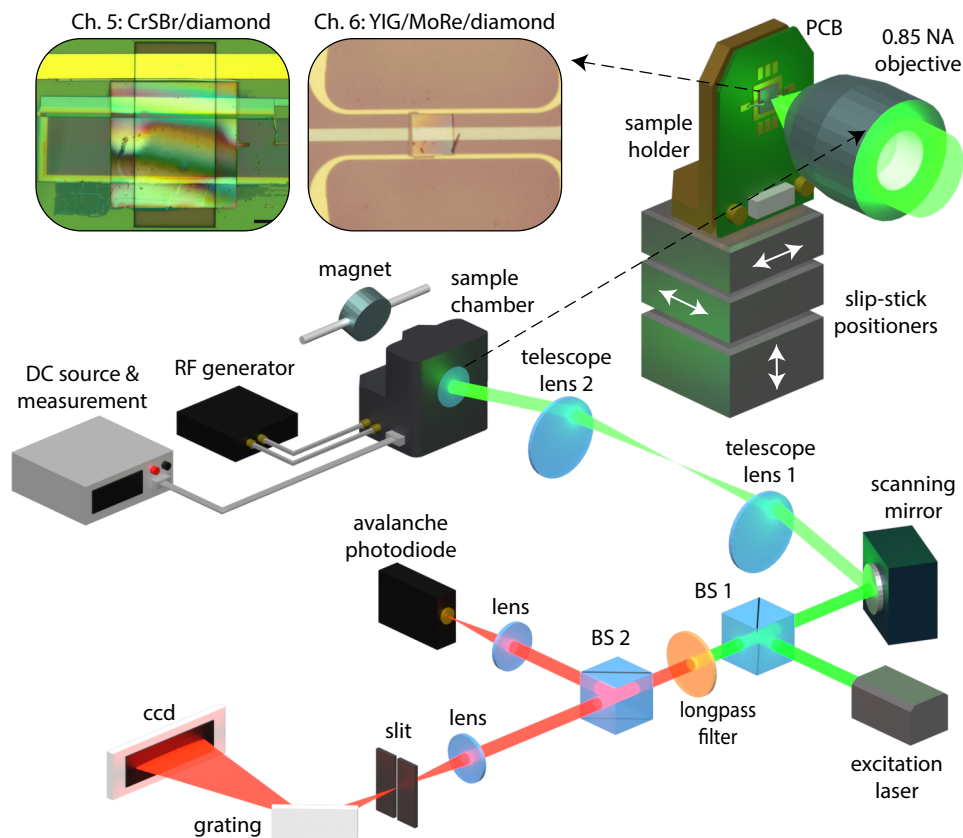


Figure 2.6. **Home-built low temperature photoluminescence microscopy setup.** Schematic representation of the experimental setup constructed to perform photoluminescence spectroscopy and optically detected magnetic resonance of nitrogen vacancy centers, used in research Chapters 4 and 5. Samples are placed on custom made sample holders and printed circuit boards, inside the vacuum sample chamber of a Montana Cryostation S100 with optical access through a 0.85 NA room-temperature objective (Zeiss, 100x, 0.87 mm WD) and base temperature of 4.5 K. The sample is positioned and brought into focus using slip-stick positioners (2x Attocube ANPx101/LT and 1x ANPx101/LT). A green 520 nm laser (Coherent OBIS LX 520) is scanned over the sample using a scanning mirror (Newport FSM300) to excite the NV centers, while microwaves are supplied using an RF generator (Windfreak SynthHD v2). In the detection path, a longpass filter (cut-on 600 nm) is used to filter out the excitation laser, after which the photoluminescence is detected by an avalanche photodiode (Excelitas SPCM-AQRG-13) and a spectrometer (Andor Kymera 193i) equipped with a 1600x200 pixel CCD (Andor iVac 324). A magnetic field is applied by a permanent cylindrical ND52-grade magnet outside the sample chamber with translational (Zaber X-LRT0250AL-E08C) and rotational (Zaber T-RS60) degrees of freedom. DC is sourced and measured using custom-built equipment (IVVI-DAC2-rack and Matrix rack [49]).

Besides enabling a study of fundamental magnetism at the smallest scale, two-dimensional

magnets hold promise for ultracompact spintronic device applications and novel functionalities through their integration in van der Waals heterostructures. Van der Waals magnets have (among others) been employed to control valley pseudospin in WSe_2 [58], create magnetic tunnel junctions [59, 60], and to induce magnetism and polarize spin-currents in graphene by proximity [61, 62].

Additionally, two-dimensional magnets offer a new paradigm for spin waves, the collective oscillations of magnetic order. The strong spin-spin interaction in two dimensions might enable access to new regimes of strongly interaction spin-wave transport, which is of both fundamental interest and promising for spintronic and magnonic devices with ultrasmall footprints. The presence of spin-wave excitations in van der Waals materials has been detected in CrI_3 through the magneto-optical Kerr effect [63], magneto-Raman spectroscopy [64], and magnon-assisted tunneling [65] and in both $CrCl_3$ and $Cr_2Ge_6Te_2$ through magnon-phonon coupling between a flake and resonator [66, 67]. However, the imaging of a coherent propagating spin-wave has remained elusive, with only a single recent report using X-ray microscopy on Fe_5GeTe_2 [68]. Directly probing the spin-wave spectrum would give access to magnetic parameters such as the exchange coupling, magnetic anisotropy and spin-wave lifetimes.

NV magnetometry has been a powerful tool for both quantitatively characterizing the small static magnetic fields of various van der Waals magnets [69–78] and the detection and imaging of coherent spin waves in thin film magnets [11, 79–82]. The central obstacle for detecting spin waves in van der Waals magnets with NV centers is a frequency mismatch between the NV ESR frequencies (few GHz) and the gap in the spin-wave dispersion of van der Waals magnets (10s of GHz to THz). A potential solution to this challenge might be down-conversion of the spin-wave frequency to the NV frequency [83]. In Chapter 4 we use NV magnetometry to image the static magnetic stray fields of uncompensated monolayers of 2D interlayer antiferromagnet $CrSBr$ and extract the monolayer magnetization, which is simultaneously of fundamental interest and an important first step towards the detection and imaging of spin waves in van der Waals magnets with the nitrogen vacancy center in diamond.

2.2.3. SPIN WAVES IN MAGNETIC THIN FILMS

The developed ability to perform cryogenic magnetic imaging measurements on 2D magnets using NV-diamond membranes, together with the spin-wave imaging techniques simultaneously developed by our lab [81, 84–87], put us in a prime position to study the interaction between excitations in thin-film magnets and superconductors. In Chapter 5 we describe how superconductors can be used to control spin waves in magnetic thin films. In this section, we introduce spin waves and magnonics, and set out the theoretical background necessary for understanding the NV measurements on spin waves in Chapter 5.

Exploiting both the electron charge and its *spin* for the purpose of information processing and storage has birthed the concept of spintronics [88]. While spintronic devices typically rely on transport of uncorrelated particles, more recently coherent many-body spin phenomena have gathered attraction for spintronic and magnonic applications. One such phenomenon is the spin wave - an oscillation in the magnetic order of a magnetic material, which is an attractive candidate for low dissipation information tech-

nology, non-reciprocal transport and wave based computing [89, 90]. A key objective towards realizing functional spin wave devices is to efficiently control their propagation, which is thought to be possible by interfacing a thin film magnet with a superconducting gate electrode [91–94]. In Chapter 5, we directly image the effect of a superconducting gate electrode on spin waves travelling underneath, employing NV magnetometry as a powerful tool for phase-sensitive imaging of spin waves [84], even through optically opaque metals [81]. As spin waves travel underneath the superconductor their dispersive behaviour is altered. Therefore, we next derive and discuss the dispersion of spin waves in a magnetic thin film, and explain how to image coherent spin waves with NV centers.

DISPERSION OF SPIN WAVES IN AN IN-PLANE MAGNETIZED THIN FILM

We consider a magnetic film infinite in y and z , located at $0 < x < t$, where x points out of plane, and t is the film thickness. We apply a small ($B_0 \ll \mu_0 M_s$) external magnetic field $\mathbf{B}_0 = B_{0,x}\hat{\mathbf{x}} + B_{0,z}\hat{\mathbf{z}}$, which allows us to assume the magnetization \mathbf{m} lies purely in-plane along $\hat{\mathbf{z}}$. We assume the magnetization to be homogeneous along $\hat{\mathbf{z}}$. The response $\delta\mathbf{m}$ of this magnetization \mathbf{m} to an oscillating magnetic field \mathbf{B}_{AC} is described by the magnetic susceptibility χ via

$$\delta\mathbf{m} = \chi\mathbf{B}_{AC}. \quad (2.9)$$

Finding the poles of the susceptibility tensor χ allows to find the resonant modes of the magnetization \mathbf{m} . We construct the susceptibility tensor by considering the Landau-Lifshitz-Gilbert (LLG) equation, which describes the dynamics of magnetization \mathbf{m} in the presence of magnetic fields, and reads

$$\dot{\mathbf{m}} = -\gamma\mathbf{m} \times \mathbf{B} - \alpha\dot{\mathbf{m}} \times \mathbf{m}. \quad (2.10)$$

Here, γ is the electron gyromagnetic ratio, α is the phenomenological Gilbert damping parameter, and \mathbf{B} is the effective magnetic field,

$$\mathbf{B} = \mathbf{B}_Z + \mathbf{B}_D + \mathbf{B}_E. \quad (2.11)$$

The effective magnetic field comprises the Zeeman contribution \mathbf{B}_Z due to static external magnetic fields, the demagnetizing field \mathbf{B}_D generated by the magnetic film itself, and the exchange field \mathbf{B}_E arising from exchange interactions between spins in the magnet. Next, we introduce the contributions, of which a detailed derivation is presented in [95]. In the following, it is convenient to express the magnetic fields as frequency ω over γ . The projection of the externally applied field \mathbf{B}_0 on the magnetization forms the Zeeman contribution,

$$\mathbf{B}_Z = \frac{\omega_B}{\gamma}\hat{\mathbf{z}}, \quad \text{with } \omega_B = \gamma B_{0,z}. \quad (2.12)$$

The demagnetizing field is the dipolar field experienced by a spin due to all other spins in the system, and thus involves integrating the magnetization and the field it produces over space,

$$\mathbf{B}_D = \mu_0 M_s \int \Gamma(\mathbf{r} - \mathbf{r}')\mathbf{m}(\mathbf{r}') d\mathbf{r}'. \quad (2.13)$$

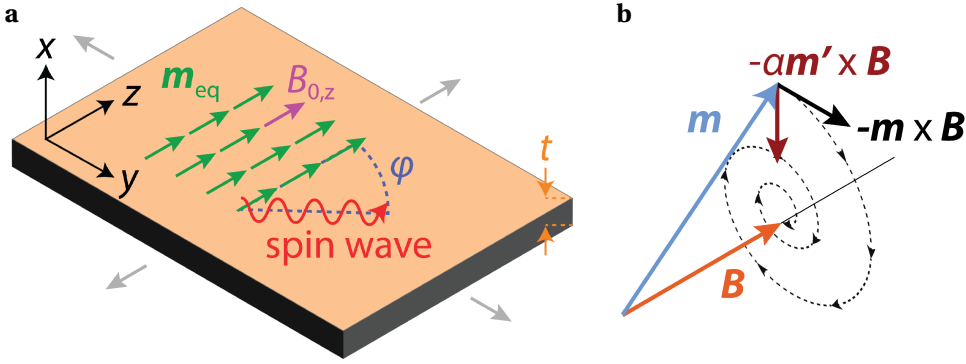


Figure 2.7. **Schematic of an in-plane magnetized thin film and magnetization dynamics.** (a) Schematic of the model magnet for which the spin-wave dispersion is derived. We consider a magnetic film of thickness t , infinite in the y, z -plane. An external magnetic field \mathbf{B}_0 aligns the equilibrium magnetization \mathbf{m}_{eq} in-plane along \hat{z} . Spin waves travel at an angle φ with respect to \mathbf{m}_{eq} . (b) Magnetization dynamics of the Landau-Lifshitz-Gilbert equation. The magnetization \mathbf{m} Larmor precesses around the effective field \mathbf{B} that it experiences, which depends on exchange- and dipolar-interactions between spins, and the externally applied field \mathbf{B}_0 . The phenomenological Gilbert damping α describes the inward damping motion of the precession. In our derivation, an oscillating field \mathbf{B}_{AC} causes \mathbf{B} to precess around \hat{z} , which drags \mathbf{m} along in a rotation around \mathbf{m}_{eq} . We assume this to be a small perturbation, such that the magnetization along \hat{z} remains constant.

Here $\Gamma(\mathbf{r} - \mathbf{r}')$ is the dipolar tensor which describes the magnetic field \mathbf{B} at location \mathbf{r} due to the magnetization \mathbf{m} at location \mathbf{r}' and is given by derivatives of the Coulomb kernel [95–97],

$$\Gamma(\mathbf{r} - \mathbf{r}') = -\nabla\nabla' \frac{1}{|\mathbf{r} - \mathbf{r}'|}. \quad (2.14)$$

In Cartesian coordinates, its components are given by

$$\Gamma_{\alpha\beta}(\mathbf{r} - \mathbf{r}') = -\frac{\partial^2}{\partial\alpha\partial\beta'} \frac{1}{4\pi|\mathbf{r} - \mathbf{r}'|}, \quad \text{with } \alpha, \beta = \{x, y, z\}. \quad (2.15)$$

We will be looking at plane waves in the y, z -plane with wavevector $\mathbf{k} = k_y\hat{y} + k_z\hat{z}$, therefore it is convenient to 2D Fourier transform Eq. 2.13 with respect to y and z ,

$$\mathbf{B}_D = \mu_0 M_s \int \Gamma(\mathbf{k}, x - x') \mathbf{m}(\mathbf{k}, x') dx'. \quad (2.16)$$

The 2D Fourier integral representation of the Coulomb kernel is [98]

$$\frac{1}{|\mathbf{r} - \mathbf{r}'|} = \frac{1}{2\pi} \int \frac{e^{-k|x-x'|}}{k} e^{i\mathbf{k}(\boldsymbol{\rho} - \boldsymbol{\rho}')} d\mathbf{k}, \quad (2.17)$$

where $\boldsymbol{\rho} = y\hat{y} + z\hat{z}$. We use the identity for the Laplacian of the Coulomb kernel [98]

$$\nabla^2 \frac{1}{|\mathbf{r} - \mathbf{r}'|} = -4\pi\delta(\mathbf{r} - \mathbf{r}') \quad (2.18)$$

together with Eq. 2.17 to calculate the components of the dipolar tensor where $\alpha, \beta = \{y, z\}$,

$$\begin{aligned}\Gamma_{xx}(\mathbf{k}, x - x') &= 2\delta(x - x') - ke^{-k|x-x'|}, \\ \Gamma_{\alpha\beta}(\mathbf{k}, x - x') &= \frac{k_\alpha k_\beta}{k} e^{-k|x-x'|}, \\ \Gamma_{\alpha x}(\mathbf{k}, x - x') &= i \operatorname{sgn}(x - x') k_\alpha e^{-k|x-x'|},\end{aligned}\quad (2.19)$$

with $\Gamma_{x\alpha} = \Gamma_{\alpha x}$. To find the demagnetizing field in the film, we integrate Eq. 2.16 with the dipolar tensor components in Eq. 2.19 over the film thickness t , and assume the magnetization is homogeneous along $\hat{\mathbf{x}}$, to find

$$\mathbf{B}_D = \mu_0 M_s \int_{-t}^0 \Gamma(\mathbf{k}, x - x') \mathbf{m}(\mathbf{k}, x') dx' = -\frac{\omega_D}{\gamma} \bar{\Gamma}(\mathbf{k}) \mathbf{m}(\mathbf{k}) \quad (2.20)$$

with

$$\bar{\Gamma}(\mathbf{k}) = \begin{bmatrix} 1 - f_t & 0 & 0 \\ 0 & f_t \sin^2(\phi) & f_t \sin(\phi) \cos(\phi) \\ 0 & f_t \sin(\phi) \cos(\phi) & f_t \cos^2(\phi) \end{bmatrix}, \quad (2.21)$$

where we have expressed the dipolar tensor in terms of the angle ϕ between \mathbf{m} and \mathbf{k} , such that $k_y/k = \sin(\phi)$ and $k_z/k = \cos(\phi)$, and we have defined $\omega_D = \gamma \mu_0 M_s$. The term f_t arises from integrating over the film thickness and is given by

$$f_t = 1 - \frac{1 - e^{kt}}{kt}. \quad (2.22)$$

Next, the effective field introduced by the isotropic exchange interaction is given by

$$\mathbf{B}_E = -\frac{\omega_E}{\gamma} k^2 \mathbf{m}(\mathbf{k}), \quad \text{with } \omega_E = \frac{\gamma D}{M_s}, \quad (2.23)$$

where M_s is the saturation magnetization and D the spin stiffness.

Having defined all contributions to the magnetic field, we next use them to find the dispersion relation of spin waves. We start by introducing a small AC drive field

$$\mathbf{B}_{AC} = B_{AC,x} \hat{\mathbf{x}} + B_{AC,y} \hat{\mathbf{y}}, \quad (2.24)$$

which causes the spins to rotate transversely in the x, y -plane around their equilibrium along $\hat{\mathbf{z}}$,

$$\mathbf{m} = \mathbf{m}_{\text{eq}} + \delta \mathbf{m}. \quad (2.25)$$

We assume this perturbation to be small,

$$m_{\text{eq},z} = \sqrt{1 - m_{\text{eq},x}^2 - m_{\text{eq},y}^2} \approx 1, \quad (2.26)$$

such that the static and dynamic parts of the magnetization are described by

$$\mathbf{m}_{\text{eq}} = \begin{bmatrix} 0 \\ 0 \\ 1 \end{bmatrix} \quad \text{and} \quad \delta \mathbf{m} = \begin{bmatrix} \delta m_x \\ \delta m_y \\ 0 \end{bmatrix}. \quad (2.27)$$

The deviations in the magnetization $\delta\mathbf{m}$ cause a deviation $\delta\mathbf{B}$ in the effective magnetic field. The total field is then given by the sum of the static equilibrium field, the change in field due to the change in magnetization, and the drive field itself,

$$\mathbf{B} = \mathbf{B}_{\text{eq}} + \delta\mathbf{B} + \mathbf{B}_{\text{AC}}. \quad (2.28)$$

The static field is simply the external field

$$\mathbf{B}_{\text{eq}} = \frac{\omega_B}{\gamma} \begin{bmatrix} 0 \\ 0 \\ 1 \end{bmatrix}. \quad (2.29)$$

The dynamic component $\delta\mathbf{m}$ of the magnetization induces a change in the exchange field (Eq. 2.23) and demagnetizing field (Eq. 2.20),

$$\delta\mathbf{B} = -\frac{\omega_E k^2}{\gamma} \begin{bmatrix} \delta m_x \\ \delta m_y \\ 0 \end{bmatrix} - \frac{\omega_D}{\gamma} \begin{bmatrix} (1-f_t)\delta m_x \\ f_t \sin^2(\phi)\delta m_y \\ f_t \sin(\phi)\cos(\phi)\delta m_y \end{bmatrix}. \quad (2.30)$$

Having found both the magnetic field \mathbf{B} and the magnetization \mathbf{m} , we fill these in the LLG equation (Eq. 2.10), linearize it and Fourier transform with respect to time, to find

$$-i\omega\delta\mathbf{m} = -\gamma\mathbf{m}_{\text{eq}} \times \delta\mathbf{B} - \gamma\delta\mathbf{m} \times \mathbf{B}_{\text{eq}} - \gamma\mathbf{m}_{\text{eq}} \times \mathbf{B}_{\text{AC}} - i\alpha\omega\mathbf{m}_{\text{eq}} \times \delta\mathbf{m}. \quad (2.31)$$

The linearization has reduced the dimensionality of our problem and only the static component of B_z is maintained,

$$-i\omega \begin{bmatrix} \delta m_x \\ \delta m_y \\ 0 \end{bmatrix} = -\gamma \begin{bmatrix} -\delta B_y \\ \delta B_x \\ 0 \end{bmatrix} - \omega_B \begin{bmatrix} \delta m_y \\ -\delta m_x \\ 0 \end{bmatrix} - \gamma \begin{bmatrix} -B_{\text{AC},y} \\ B_{\text{AC},x} \\ 0 \end{bmatrix} - i\alpha\omega \begin{bmatrix} -\delta m_y \\ \delta m_x \\ 0 \end{bmatrix} \quad (2.32)$$

Filling in the previous equation gives

$$\begin{aligned} i\omega\delta m_x &= (\omega_B + \omega_E k^2 + \omega_D f_t \sin^2(\phi) - i\alpha\omega)\delta m_y - \gamma B_{\text{AC},y} \\ i\omega\delta m_y &= -(\omega_B + \omega_E k^2 + \omega_D(1-f_t) - i\alpha\omega)\delta m_x + \gamma B_{\text{AC},x}. \end{aligned} \quad (2.33)$$

We introduce the shorthand notations

$$\begin{aligned} \omega_2 &= \omega_B + \omega_E k^2 + \omega_D(1-f_t) \\ \omega_3 &= \omega_B + \omega_E k^2 + \omega_D f_t \sin^2(\phi). \end{aligned} \quad (2.34)$$

We rewrite Eq. 2.33 into the form $\delta\mathbf{m} = \chi\mathbf{B}_{\text{AC}}$ to find the susceptibility,

$$\begin{bmatrix} \delta m_x \\ \delta m_y \end{bmatrix} = \frac{\gamma}{\Lambda} \begin{bmatrix} \omega_3 - i\alpha\omega & -i\omega \\ i\omega & \omega_2 - i\alpha\omega \end{bmatrix} \begin{bmatrix} B_{\text{AC},x} \\ B_{\text{AC},y} \end{bmatrix}, \quad (2.35)$$

with

$$\Lambda = (\omega_2 - i\alpha\omega)(\omega_3 - i\alpha\omega) - \omega^2. \quad (2.36)$$

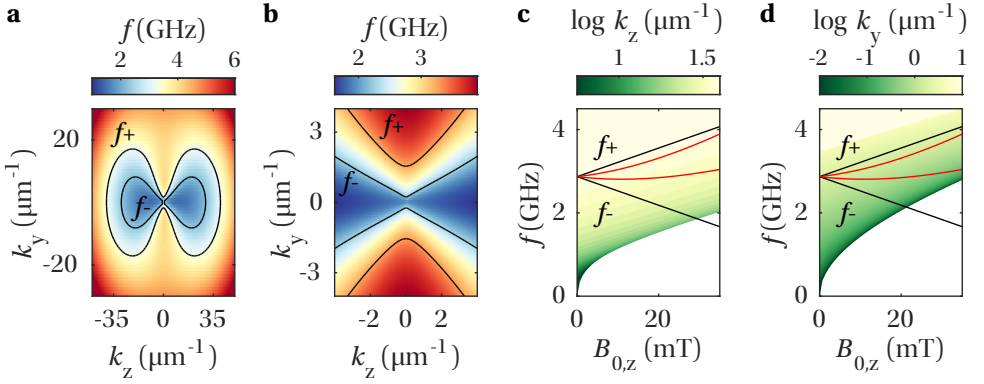


Figure 2.8. **Simulated spin-wave dispersion of yttrium iron garnet.** (a, b) Simulated dispersion for an in-plane magnetized yttrium iron garnet thin film with thickness $t = 245$ nm, with low-temperature saturation magnetization $M_s = 1.98 \times 10^5$ A/m, spin stiffness $D = 9.49 \cdot 10^{-6}$ rad s $^{-1}$ m $^{-2}$, and $B_{0,z} = 22$ mT. The out-of-plane component of the external field \mathbf{B}_0 is chosen such that the total field aligns with the axis of an NV-center in a diamond with crystal axis $[1, 1, 1] \parallel [(\hat{z} + \hat{y})/\sqrt{2}, (\hat{z} - \hat{y})/\sqrt{2}, \hat{x}]$. ESR frequencies of the NV center are overlaid in black for f_+ and f_- . (c) Dispersion for backward volume spin waves ($\mathbf{m} \parallel \mathbf{k}, \varphi = 0$) as function of magnetic field, with NV ESR transitions overlaid, including misaligned families in an NV ensemble (red) (d) Same as (c), but for Damon-Eshbach spin waves ($\mathbf{m} \perp \mathbf{k}, \varphi = \pi/2$).

The susceptibility is singular for $\Lambda = 0$, and as such we find the spin-wave dispersion in the limit of zero Gilbert damping ($\alpha = 0$) to be

$$\omega = \sqrt{\omega_2 \omega_3}. \quad (2.37)$$

We plot the obtained dispersion for yttrium iron garnet (YIG) in Fig. 2.8. To highlight which parts of the dispersion can be probed with nitrogen vacancy center magnetometry, we plot isofrequency lines of the NV ESR frequencies f^+ ($|0\rangle \rightarrow |+1\rangle$), f^- ($|0\rangle \rightarrow |-1\rangle$) in Fig. 2.8a-b. The $[111]$ -direction of the diamond crystal is aligned with $[(\hat{z} + \hat{y})/\sqrt{2}, (\hat{z} - \hat{y})/\sqrt{2}, \hat{x}]$ in the coordinate system of Fig. 2.7, and the external magnetic field \mathbf{B}_0 is aligned with $[111]$. The experimentally accessible part of the spin-wave dispersion is the intersecting slice of the NV ESR frequencies with the dispersion, plotted as a function of magnetic field in Fig. 2.8c for backward volume spin wave with $\mathbf{k} \parallel \mathbf{m}$ ($\mathbf{k} = k_z$ and $\varphi = 0$ in our coordinate system), and in Fig. 2.8d for Damon-Eshbach spin waves with $\mathbf{k} \perp \mathbf{m}$ ($\mathbf{k} = k_y$ and $\varphi = \pi/2$). By changing the magnetic field angle while keeping $B_{0,z}$ constant, we can slightly vary the NV ESR frequency while the dispersion remains the same, giving access to sensing of additional frequencies - though this comes at a loss of NV sensitivity.

PHASE SENSITIVE IMAGING OF SPIN WAVES WITH NV MAGNETOMETRY

Having discussed the spin-wave dispersion and which parts of it can be probed with NV magnetometry, we now conceptually introduce how NV magnetometry enables phase-sensitive detection and imaging of spin waves. The spin waves perturb the magnetization \mathbf{m} and generate a stray field \mathbf{B}_{SW} , which falls off as $\exp(-d/k)$, where d is the

distance between the magnetic film and the NV center. The spin-wave field \mathbf{B}_{SW} oscillates at frequency ω , and can drive the ESR transitions in nearby NV centers, enabling spin-wave detection [12, 84].

Having previously solved for $\omega(k)$, we recall that these are travelling spin waves characterized by their frequency f and wavevector \mathbf{k} . Detecting the presence of the field \mathbf{B}_{SW} is straightforward through presence or absence of ESR contrast, yet $|\mathbf{B}_{\text{SW}}|$ is spatially homogeneous and a typical ESR measurement takes seconds - retrieving phase information requires a trick. The key is to let the spin-wave field interfere with an auxiliary uniform phase-locked field, which is schematically displayed in Fig. 2.9. The driving field $\mathbf{B}_{\text{AC}} = B_{\text{AC},x}\hat{\mathbf{x}} + B_{\text{AC},y}\hat{\mathbf{y}}$ that excites spin waves is supplied to the thin film magnet by an RF generator connected to a microstrip. The microstrip excites spin waves perpendicular to it, which in the chosen configuration with $\mathbf{m} = m_z\hat{\mathbf{z}}$ are Damon-Eshbach spin waves with $\mathbf{k} = k_y\hat{\mathbf{y}}$, i.e. $\varphi = \pi/2$.

Besides excitation of spin waves, the microstrip field \mathbf{B}_{AC} serves to interfere with the local spin-wave stray field \mathbf{B}_{SW} . Since these fields are phase-locked, their interference results in a standing wave pattern that oscillates with the spin-wave frequency ω and periodicity $2\pi/k$. By spatially mapping the field strength using a diamond platelet with NV ensembles, e.g. through measuring the ESR contrast C or Rabi frequency Ω_R , the spin-wavefronts are revealed.

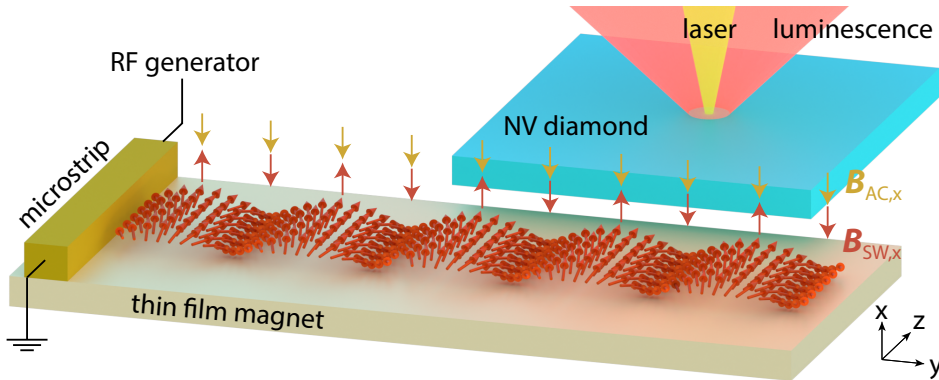


Figure 2.9. **Phase-sensitive imaging of spin waves with NV centers in diamond.** Schematic representation of phase-sensitive imaging of spin-waves in a thin film magnet with nitrogen vacancy centers in diamond. An RF generator connected to a microstrip along $\hat{\mathbf{x}}$ on the magnetic thin film supplies the field \mathbf{B}_{AC} that excites spin waves travelling along $\hat{\mathbf{y}}$. The field \mathbf{B}_{AC} emanating from the microstrip interferes with the local magnetic stray field \mathbf{B}_{SW} of the spin waves. Since these two fields are phase locked, they create a standing wave with a period equal to the wavelength of the spin wave. The difference in field strength at the nodes and antinodes of this pattern can be detected by nearby NV centers. A diamond platelet with an NV ensemble is positioned on the sample, and spatially scanning a laser over the NV ensemble while measuring the ESR contrast C through photoluminescence measurements allows for a spatial reconstruction of the spin-waves in the thin film magnet. This example shows Damon-Eshbach spin waves with $\mathbf{k} \perp \mathbf{m}$, with the external magnetic field \mathbf{B}_0 and magnetization \mathbf{m} along $\hat{\mathbf{z}}$.

2.3. FABRICATION METHODS

Here we discuss the fabrication of samples per research chapter - we discuss mechanical exfoliation methods, electron beam lithography recipes, and various deposition techniques such as evaporation and sputtering. We then highlight how to fabricate thin $50 \times 50 \mu\text{m}^2$ diamond membranes for quantum sensing, and two methods to interface these with the fabricated samples.

2.3.1. EXFOLIATION, STAMPING, AND NANOFABRICATION

To study magnetic phenomena in van der Waals materials, we cleave few-layer flakes from their bulk crystal by mechanical exfoliation, and stamp them on substrates (Chapter 3 and 4). For the study of van der Waals materials with NV centres, we pattern microwave lines on the substrate for driving their electron spin resonance (Chapter 4). Finally, for studying the effect of a superconducting gate on spin waves in magnetic thin films (Chapter 5), we pattern microstrips for spin-wave excitation and sputter strips of superconductors. The next sections highlight all these processes in detail.

STAMPING TMDs ON Si/SiO₂

In Chapter 3, we study the luminescence of various tungsten disulfide (WS₂) mono- and bi-layer flakes. The assembly of these samples is straightforward since WS₂ is stable in ambient conditions [99].

Exfoliation and stamping:

- i. We prepare a silicon substrate capped with 285 nm silicon dioxide for stamping and exfoliation by sonicating in acetone (30 mins, $T = 20^\circ\text{C}$) and oxygen plasma cleaning (Tepla 300).
- ii. We place WS₂ crystal (HQ Graphene) on Scotch tape and disperse it by repeated folding of the tape piece. After exfoliation, we store this piece of tape in a desiccator, and it will serve as a "mother" for many following exfoliation sessions. We affix the mother Scotch tape with crystal side up to a clean surface. Next, we follow one of two methods denoted (1) or (2).
- iii. (1) We press a clean piece of Nitto tape in contact with the mother Scotch tape hosting the crystal, peel off the Nitto tape, press the Nitto tape onto a 4mm x 4mm viscoelastic polydimethylsiloxane (PDMS) stamp on a microscope slide, and peel off the Nitto tape. In both steps we press down with our thumb to exert moderate pressure for 2 seconds. We search the PDMS under a microscope (10x, 20x, 50x, 100x) for monolayers. Typically, 100x is necessary to find monolayers on PDMS, since the contrast between monolayer and PDMS is low (Fig. 2.10a).
- iv. (1) We affix the microscope slide PDMS-side down to an XYZ-micromanipulator, maneuver it above our Si/SiO₂ and press PDMS stamp against the substrate, which is held in place by a vacuum chuck. Peeling of very slowly releases the flake onto the substrate [100] (Fig. 2.10b).

- iii. (2) We press a clean piece of Scotch tape in contact with the mother Scotch tape hosting the crystal. We peel off this second Scotch tape from the first, transferring material. Next, we exfoliate directly onto the Si/SiO₂ substrate, and search for monolayers using an optical microscope (10x, 20x, 50x, 100x) (Fig. 2.10c). Typically, 20x or 50x is sufficient to spot monolayers on our Si/SiO₂ substrates.

Because the above process is hands-on, it is important to be patient, diligent and consistent while developing a technique that works for you. After the flakes are transferred to the Si/SiO₂ substrate, we either load the samples directly in the measurement setup, or store them in the desiccator. Each method has its advantages: method (1) burns through less Si/SiO₂ substrates since we only attempt stamping when we have found a monolayer, while in method (2) one relies on chance to find a monolayer on the substrate. Additionally, method (1) allows for positioning of the flake on the target substrate, which is beneficial when the substrate is larger than the scanning area of the measurement setup. However, monolayer flakes have better optical contrast on Si/SiO₂, so it is easier to find them with method (2). Additionally, it is common for monolayers to tear or fold during the transfer process from PDMS stamp to substrate of method (1) as seen when comparing Figs. 2.10a-b.

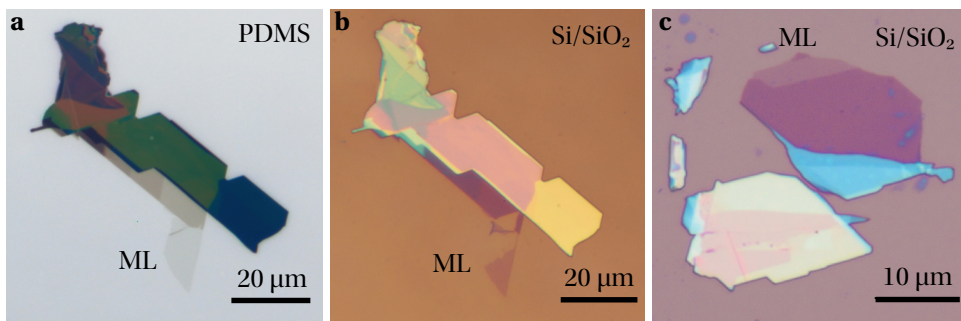


Figure 2.10. **Exfoliated tungsten disulfide flakes on polydimethylsiloxane and Si/SiO₂.** (a) Negative of an optical micrograph, showing a tungsten disulfide (WS₂) flake exfoliated on a polydimethylsiloxane (PDMS) stamp using Nitto tape, with monolayer region (ML) indicated. (b) Optical micrograph of the same flake as in (a) after stamping the PDMS on a silicon wafer capped with 285 nm SiO₂, transferring the flake. The monolayer part is torn and folded over, yet a significant area remains intact, suitable for study. (c) Optical micrograph of a WS₂ flake directly exfoliated on Si/SiO₂ using Scotch tape, with monolayer region indicated.

PATTERNING MICROSTRIPS AND STAMPING VAN DER WAALS MAGNETS ON Si/SiO₂

In Chapter 4, we use nitrogen vacancy magnetometry to image the stray fields of van der Waals magnet CrSBr. First, we pattern a microstrip on a Si/SiO₂ substrate through which we can supply microwaves for the NV measurements, and then stamp a CrSBr flake next to it. The detailed process is as follows:

Microstrip patterning and stamping:

- i. Preparation of silicon substrate capped with 285 nm silicon dioxide (sonicate in acetone for 30 mins at $T = 20^\circ\text{C}$, oxygen plasma cleaning in Tepla 300).
- ii. Spincoat bilayer polymethyl methacrylate (PMMA) e-beam resist (spincoat PMMA 495 A6 at 4000 RPM, bake 1 min at 175°C , spincoat PMMA 950 A3 @ 4000 RPM, bake 5 mins at 175°C)
- iii. E-beam lithography (Raith EBPG 5000+, 66 nm beam size, 50 nm beam step size, dose $1300 \mu\text{C}/\text{cm}^2$).
- iv. Developing (40 sec MIBK:IPA 1:3 while stirring with sample, 20 sec IPA while stirring with sample, nitrogen blowdry).
- v. Evaporation (short oxygen plasma clean in Tepla 300 beforehand, evaporation in Temescal FC2000, 5 nm Ti, 100 nm Au, liftoff using acetone).
- vi. We cleave CrSBr from the bulk crystal using Nitto tape, exfoliate it onto a PDMS layer on a microscope slide. Using an XYZ micromanipulator, we position the microscope slide such that the CrSBr flake is positioned next to the microstrip, and press the PDMS stamp on the substrate. Slowly retracting peels off the viscoelastic PDMS, while the flake remains on the substrate.

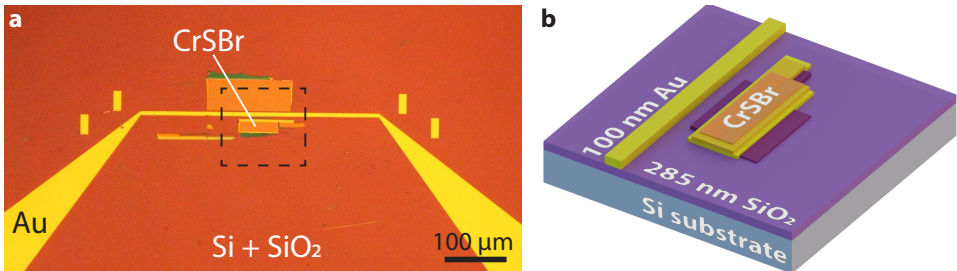


Figure 2.11. **CrSBr flakes next to a gold microstrip.** (a) Optical micrograph of the sample after fabricating the stripline and stamping the CrSBr using PDMS. (b) Schematic of the sample in the white box of (a), before receiving a diamond membrane. A CrSBr flake is stamped next to the microstrip, through which we supply microwaves for the NV measurements.

SPUTTERING AND EVAPORATION OF METALS ON GGG/YIG

In Chapter 5, we study the interaction between spin waves and a superconductor, therefore we here discuss fabrication methods for the sample. We use commercially available (Matesy GmbH) 245 nm thick yttrium iron garnet (YIG) films, grown on a gadolinium gallium garnet (GGG) substrate. To create the metal strips, we spincoat a positive PMMA e-beam resist and transfer our patterns to the chip with e-beam lithography.

Patterning of the superconducting strip:

- i. Carrier substrate and chip cleaning (acetone ultrasonication for 30 mins, plasma descum in Tepla 300 for 30 sec).
- ii. Spincoat trilayer resist (PMMA 495 A6 at 4000 RPM, ambient bake 1 min at 175 °C, PMMA 950 A3 at 4000 RPM, ambient bake 5 min at 175 °C, Electra 92 at 2000 rpm, ambient bake 2 min at 90 °C).
- iii. Glue 4 x 4 mm² on 2 x 1 cm² silicon carrier chip with a PMMA droplet for further processing. Bake 1 min at 90°C.
- iv. E-beam lithography (Raith EBPG 5000+, beam size 66 nm, beam step size 50 nm, dose 550 μC/cm²).
- v. Developing (H₂O dip for 60 sec, blowdry, MIBK:IPA 1:3 for 40 sec while stirring, IPA for 20 sec while stirring, blowdry)
- vi. Pre-deposition descum (Tepla 300, oxygen plasma, $P = 100$ W, $t = 30$ sec, oxygen flow = 200 sccm).
- vii. MoRe sputtering (Alliance Concept AC450, molybdenum rhenium, 140 nm).
- viii. Liftoff (acetone overnight, 2 hrs at 50°C, 12 hrs at 20 °C)

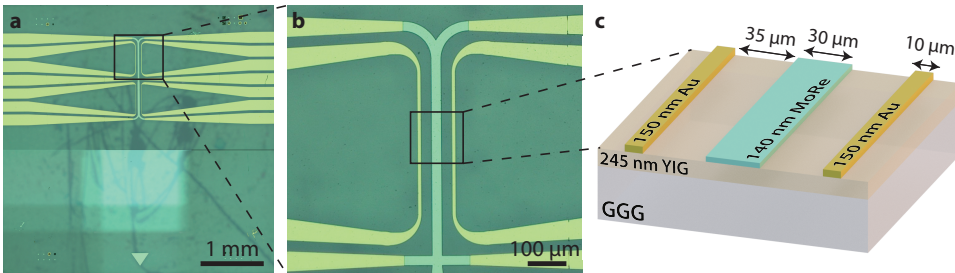


Figure 2.12. **Superconducting strips on a magnetic thin film.** (a) Optical micrograph of the structures fabricated to study the interaction between spin waves and a superconductor, on a 4x4 mm² substrate of gadolinium gallium garnet (GGG), with an epitaxial 245 nm thick film of yttrium iron garnet (YIG). (b) Zoom-in of the optical micrograph in (a), showing two parallel gold microstrips with a wider molybdenum rhenium (MoRe) superconducting strip in between. The diamond membrane is placed in the region outline with a square. (c) Schematic of the sample from the square region in (b), with geometric specifications.

In the above exposure and consequent sputtering, we have also patterned a 2x4 array (spacing is 100 μm) of square 20 × 20 μm² alignment markers near each corner of the chip, which we use to align the exposure of the gold microstrips with respect to the sputtered superconductor.

Patterning of the gold strips:

- i. Carrier substrate cleaning (acetone ultrasonication for 30 mins, plasma descum in Tepla)
- ii-vi. Repeat step ii. through vi. of the MoRe process.
- vii. Evaporation (Temescal FC2000, 10 nm of Ti at 0.5 Å/s, 140 nm of Au at 1.5 Å/s).
- viii. Liftoff (acetone overnight, 2 hrs at 50°C, 12 hrs at 20 °C).

Here, the titanium serves as a sticky layer to increase the adhesion of the gold film to the substrate. If this is not done, bonding wires will delaminate the gold from the substrate. The resulting structures on the chip are displayed in optical micrographs and a schematic in Fig. 2.12a-c.

When working with 4x4 mm² chips, we glue them on top of a larger 2x1 cm² silicon carrier substrate for further processing, using a tiny droplet of thick PMMA. This has a few benefits: 1) it reduces the chance of scratching the resist when handling the sample 2) it allows clamps required for e-beam and metal deposition to be placed on/against the silicon, preventing resist damage and unwanted deposition shadowing at the clamp location.

Since our GGG/YIG substrate is electrically insulating, we spincoat a layer of electrically conductive All-Resist AR-PC 5090 Electra 92 for dissipation of the electrons during lithography. This requires a short dip in water after e-beam exposure to dissolve the Electra 92, before the PMMA can be developed. After developing of the PMMA, we descum the chip to remove potentially leftover resist in the exposed area, promoting adhesion of the metals. After fabrication, the diamond membranes are placed on the sample as described in Section 2.3.2. Then, the sample is mounted on a PCB using silver conductive paint (RS PRO), wirebonded using a Westbond 4KE, and mounted in the setup displayed in Fig. 2.6.

2.3.2. DIAMOND MEMBRANES FOR QUANTUM SENSING

A central challenge in performing nitrogen vacancy magnetometry is to minimize the distance between the sample and the quantum sensor, which will benefit spatial resolution and enable sensing of evanescent fields that decay quickly with distance from the surface. Widefield magnetometry is typically performed by interfacing a few mm² diamond platelet hosting an ensemble of NV centers with a sample of interest, either through direct fabrication on the diamond surface, or placement of the diamond on the sample after fabrication. The latter method is simple, flexible, does not require development of new fabrication protocols, does not limit device fabrication, yet typically yields standoff distances of a few micron due to capturing of spurious particles [11, 101, 102]. Minimizing the surface area will reduce the chance to capture particles, and allows close proximity and even contact with the sample. Here, we discuss fabrication and application of small 50 × 50 μm² diamond membranes for quantum sensing purposes, which are applied for NV magnetometry in Chapter 4 and 5.

DIAMOND PREPARATION AND NITROGEN IMPLANTATION

We acquire electronic-grade nitrogen-free, isotopically purified diamond chips from Element 6 Inc., which are grown along the [001] crystal axis and have their surface parallel to the (001)-plane. The diamond is then cut and polished into $2\text{ mm} \times 2\text{ mm} \times 50\text{ }\mu\text{m}$ platelets by Almax easyLab. Next, we remove surface impurities and polishing marks on the diamond [87].

Removal of surface impurities and polishing marks:

- i. Fuming nitric acid dip (10 mins).
- ii. Rinse with H_2O and transfer diamond to beaker with H_2O .
- iii. Transfer diamond from H_2O to isopropyl-alcohol (IPA), and blow-dry with nitrogen (prevents drying stains).
- iv. Etch $\sim 2\text{ }\mu\text{m}$ of diamond surface with Ar/Cl plasma (30 mins, carrier substrate: quartz wafer, Oxford Plasmalab System 100, $T = 303\text{K}$, $P_{\text{RF}} = 200\text{ W}$, $P_{\text{ICP}} = 500\text{ W}$, Ar (Cl) flowrate = 20 (30) sccm, diamond etch rate $\sim 40\text{--}80\text{ nm/min}$).
- v. Etch $\sim 6\text{ }\mu\text{m}$ of diamond surface with O_2 plasma (20 mins, carrier substrate: Si/SiOx, Oxford Plasmalab System 100, $T = 293\text{ K}$, $P_{\text{RF}} = 90\text{ W}$, $P_{\text{ICP}} = 1100\text{ W}$, O_2 flowrate = 50 sccm, diamond etch rate $\sim 200\text{--}300\text{ nm/min}$).

Here, a quartz carrier wafer is used to prevent micromasking due to Si-redeposition of typical Si/SiOx-wafers, and the oxygen plasma is used to remove potential chlorine contaminants introduced during step iv [103–106]. We note that the later introduced "quantum polishing" option by Almax easyLab reduces surface roughness to nearly identical levels as the above process [87, 107]. Next, we glue the diamond platelets on a Si/SiOx wafer with polymethylmethacrylate (PMMA), send them out for nitrogen implantation, clean it, anneal it to create nitrogen-vacancy centers, and remove the graphite layer introduced during annealing with a mixture of acids.

Nitrogen implantation, annealing, and graphite removal:

- i. Nitrogen ion implantation by INNOViON (energy = 54 keV, density = $10^{13}/\text{cm}^2$, estimated implantation depth = $70 \pm 10\text{ nm}$ [108]).
- ii. Tri-acid cleaning in 1:1:1 mixture of 95% H_2SO_4 : 65% HNO_3 : 60% HClO_4 (2 hr, $120\text{ }^\circ\text{C}$ [104]).
- iii. Vacuum annealing (Nabertherm, $P = 3 \times 10^{-6}\text{ mBar}$, 6 hr ramp from to $400\text{ }^\circ\text{C}$, 4 hr hold, 6 hr ramp to $800\text{ }^\circ\text{C}$, 2 hr hold, cool-down to 300 K, expected NV density = $10^3\text{ }\mu\text{m}^2$ [108]).
- iv. Repeat step ii.

During the annealing, the vacancies in the diamond lattice pair up with the implanted nitrogen ions to form nitrogen-vacancy centers [109]. We note that a tri-acid cleaning temperature of $>150\text{ }^\circ\text{C}$ is desired for complete removal of the graphite layer that is introduced in step ii [110], which we are unable to attain due to hardware limitations.

MEMBRANE FABRICATION

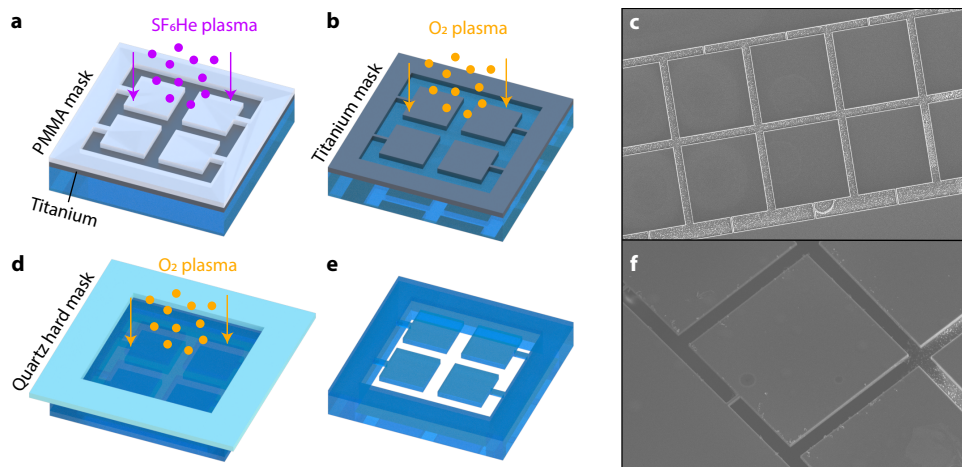


Figure 2.13. **Diamond membrane fabrication process.** (a) The membrane pattern is defined in a polymethyl methacrylate (PMMA) layer using e-beam lithography, after which an SF₆/He plasma etch transfers the pattern to a titanium layer that was sputtered on the diamond. (b) After the PMMA is removed, the membrane pattern is etched into the diamond using cycled O₂- and SF₆/He-plasma etching. (c) scanning electron microscope (SEM) image of the etched membrane pattern, showing 50 × 50 μm² squares and holding bars. (d) The titanium is removed, and the diamond is flipped and etched with first an Ar/Cl-plasma and then an O₂-plasma until the membranes are free-standing. (e) Diamond after fabrication with free-standing membranes. (f) SEM image of a 50 × 50 μm² diamond after fabrication.

Having obtained a 2 mm × 2 mm × 50 μm diamond platelet with a shallow surface ensemble of nitrogen vacancy centers, we shape it into smaller membranes. To do so, we perform three etching steps to define masks and create free-standing membranes attached to the original diamond frame through holding bars [87].

Membrane etching process:

- i. Sputter 50 nm titanium on diamond surface (Alliance Concept 450).
- ii. Spincoat polymethyl methacrylate (PMMA) (950 A8, 4k rpm, ambient bake 3 mins at 175 °C).
- iii. Define membrane pattern in PMMA (e-beam lithography, Raith EBPG5000+, 1600 μC/cm², 90 sec development in MIBK:IPA 1:3, IPA rinse).
- iv. Titanium etch with SF₆/He-plasma (Fig. 2.13a, carrier substrate: Si/SiO_x, Oxford Plasmalab System 100, $T = 20\text{ }^{\circ}\text{C}$, $P_{\text{RF}} = 40\text{ W}$, $P_{\text{ICP}} = 0\text{ W}$, SF₆ (He) flowrate = 12.5 (10) sccm, titanium etch rate ~20 nm/min, PMMA etch rate ~240 nm/min).
- v. Diamond pattern etch (Fig. 2.13b-c., 4x cycle of O₂-plasma (2 min) and intermittent SF₆/He (10s) plasma, carrier substrate: Si/SiO_x, Oxford Plasmalab

System 100, $P_{\text{RF}} = 70 \text{ W}$, $P_{\text{ICP}} = 1000 \text{ W}$, O_2 flowrate = 50 sccm, diamond etch rate $\sim 200\text{-}300 \text{ nm/min}$, SF_6/He recipe as in step iv, except $P_{\text{RF}} = 30 \text{ W}$.

- vi. Remove titanium mask with hydrofluoric acid dip
- vii. Diamond deep etch (Fig. 2.13d, carrier substrate: Si/SiO_x, Oxford Plasmalab System 100, diamond upside down with quartz hard mask, 90 min Ar/Cl-plasma with recipe as in surface etch, 2.5-3 hrs O₂-plasma with recipe as in step v).
- viii. Overnight acetone and inspection (Fig. 2.13e-f).

The intermittent SF_6/He -plasma in step iv serves to eliminate redeposited titanium which can micromask and lead to rough sidewalls [87]. Near the end of the diamond deep etch, we take the diamond out of the chamber and inspect whether the membranes are free-standing. If not, we continue etching with oxygen plasma in small steps, inspect, and repeat until ready.

MEMBRANE PLACEMENT

To place these diamond membranes on a sample of interest, we develop two different approaches. In the first method, which is used in Chapter 5, we glue the side of the carrier diamond to an elastic metal holding bar using a $\sim 0.25 \text{ mm}$ -diameter droplet of UV-curing glue (Norland Optical Adhesive) and mount it to an XYZ-manipulator, so that it can be positioned above the sample with $\sim \mu\text{m}$ accuracy. Next, we use a thin metal needle, attached to another XYZ-manipulator, to push the membrane on the sample by breaking its holding bar. This process is displayed in Fig. 2.14 by a series of images. The membranes we placed on samples did not displace under typical mechanical disturbances such as wire bonding, vertical mounting in our cryostat, and slip-stick positioning of the sample.

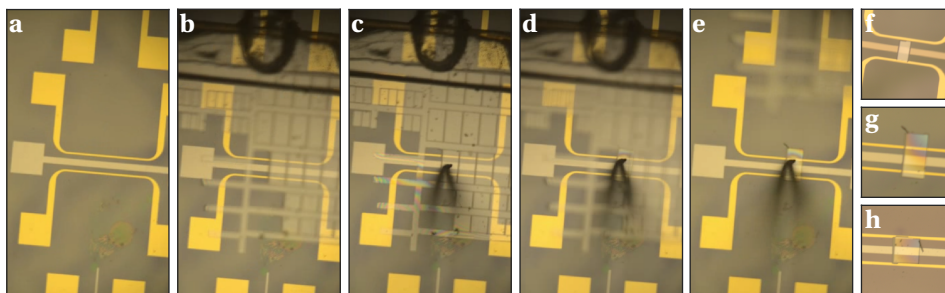


Figure 2.14. **Diamond membrane tipping process for NV magnetometry.** (a) The sample region of interest is selected and brought into optical focus. (b) A carrier diamond hosting many NV sensing membranes is positioned above the sample area. The carrier diamond is glued to an elastic metallic spring, which is attached to an XYZ-micromanipulator for positioning. (c) A thin metallic needle, attached to a second XYZ-micromanipulator, is positioned above the selected membrane. (d) The membrane is tipped out with the needle. (e) After tipping, the membrane is brought into its final position by careful manipulation with the needle. (f-h) Various tipped-out membranes on top of devices of interest.

The second approach we developed allows better control over placement and rotation of the membrane, is more robust against potential dislocation of the membrane, yet is quite a bit more work. This approach, used in Chapter 4, is a diamond membrane dry transfer method, akin to assembly of two-dimensional materials. The process is schematically depicted in Fig. 2.15. As in the other methods, we attach the carrier diamond to a metallic needle, and fasten it to an XYZ-micromanipulator for movement control. Next, we position the carrier diamond above, and nearly into contact with a substrate covered with a flexible, 0.5 mm-thick polydimethylsiloxane (PDMS) layer. A metallic needle attached to another XYZ-micromanipulator is used to press a membrane in contact with the PDMS through bending of its holding bar, exploiting the flexibility of the thin diamond (Fig. 2.15a). Finally, we break this holding bar by lifting the carrier diamond up. In this way, we prevent unwanted flipping of membranes, which can occur when breaking the membranes' holding bar too far above the substrate surface.

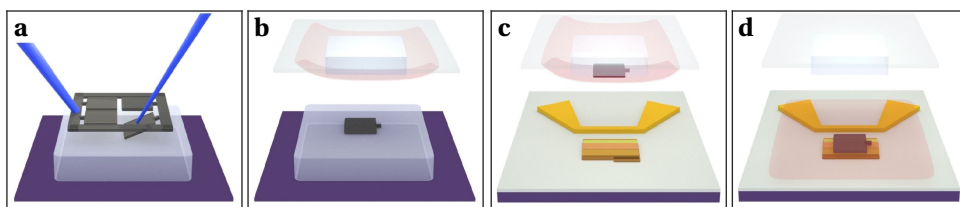


Figure 2.15. **Dry-transfer of diamond membranes for sensing 2D materials.** (a) A metallic needle is used to tip out a diamond membrane onto a PDMS layer affixed to a substrate. (b) A PMMA-PDMS stamp on a glass slide picks up the membrane. (c) The stamp with membrane is positioned above a CrSBr flake and brought into contact. (d) Heating to 180 °C release the PMMA from the PDMS, placing the membrane onto the targeted flake of van der Waals material with $\sim \mu\text{m}$ precision.

We continue by preparing a stamp to pick up and transfer the diamond membrane, consisting of a PDMS / polymethyl methacrylate (PMMA) bilayer, similar to methods in [111]. On a Si/SiO₂ substrate, we spincoat a layer of water-soluble polymer (Electra 92, 3 min at 1000 rpm) and bake it (1 min at 100 °C). On top of this, we spincoat a layer PMMA 950K (3 min at 1000 rpm) and bake it shortly (45 sec at 180 °C), and repeat this process to form a second PMMA layer, yielding a total thickness of $\sim 1 \mu\text{m}$.

We prepare a piece of Scotch tape, from which we cut a $7 \times 7 \text{ mm}^2$ window, and place the tape sticky-side-down on the PMMA-covered substrate. To delaminate the Scotch tape with PMMA from the substrate, we dissolve the Electra 92 by placing our Scotch tape with sample-facing-down in a beaker of water. We remove the Scotch tape with PMMA from the beaker and let it dry in air (10 min). We finish the stamp by placing the Scotch tape / PMMA structure sticky-side-down on a PDMS stamp held on a glass slide.

The PDMS-PMMA stamp is positioned above the diamond membrane using micromanipulators (Fig. 2.15b), and brought into contact. PMMA-diamond adhesion is promoted by heating to 80 °C, and the membrane is picked up by lifting the glass slide, ready for deposition on a sample of interest. Next, we position the membrane above the region of interest, and rotate it to match the NV quantization axis to any desired direction within the sample plane (Fig. 2.15c). We bring the stamp and membrane into contact with our

sample while heating 100 °C. After cooling to 30 °C and retracting the PDMS, the PMMA and diamond locally detach from the PDMS. Then, we melt the PMMA by heating the sample to 180 °C, which causes it to fully detach from the PDMS carrier onto the sample (Fig. 2.15d). As a precautionary measure, to potentially improve optical readout of the NV centers, we partially remove the PMMA covering the NV membrane using e-beam lithography and acetone.

2.4. ELECTRONICS AND DIGITAL CONTROL

The registration and transfer of knowledge is of paramount importance in starting labs with newly constructed experimental setups. To this end, we here provide a detailed account of the electronic devices in the constructed experimental setups, their interconnections, and functionalities, hoping that it will prove insightful and useful for its next caretakers. Since the room-temperature setup (Fig. 2.5) was rearranged and expanded into the low-temperature setup (Fig. 2.6) their electronics and operating protocols are the same, thus we limit our discussion to the latter. To illustrate how the low-temperature setup for NV magnetometry and DC transport is operated, we show a connection diagram in Fig. 2.16 (power supply lines are not drawn). The left hand side shows hardware and software within a desktop computer, while the right hand side shows the cryostat chamber and its connections. All electronic devices and their connection chains are displayed in the middle. We highlight the functionalities of the setup through a point-by-point description.

Desktop computer: We use the desktop ethernet and USB terminals for control and communication of all electronic devices and auxiliary computers systems. Two peripheral component interconnect (PCI) cards are used for high-throughput signal processing: a configurable pulse generator (PulseBlaster ESR-PRO) that provides transistor-transistor logic (TTL) pulses with a minimum pulse length of 2 ns, and a multipurpose I/O card (National Instruments PCI-6221) that hosts two click counter channels, analog ± 10 V in/outputs, and configurable I/O-channels (e.g. TTL). MATLAB is used to communicate with the USB-, ethernet- and PCI-peripherals.

RF generation, pulsing and amplification: Microwaves between 10 MHz and 15 GHz are generated with 0.1 Hz resolution by a USB-controlled RF source (Windfreak SynthHDv2) with two output channels. The RF signal is fed through an RF switch (Mini-Circuits ZASWA-2-50DRA+), which routes the signals to output 1 (2) when the TTL signal is low (high), effectively creating an on/off switch. In the schematic in Fig. 2.16, the TTL signal is provided by a configurable output of the NI PCI-6221 card, routed through a breakout box (NI BNC-2110). To deliver fast microwave pulse sequences, an output of the PulseBlaster ESR-PRO can be routed to the TTL gating channel of the RF switch. The signal is routed through an amplifier (Mini-Circuits ZX60-83LN-S+), which boosts signals between 500 MHz and 8 GHz by ~ 20 dB, and then enters an SMA-connector on the cryostat sample chamber panel.

Laser modulation and scanning: Four lasers are integrated in the setup, with wavelengths of 520 nm (OBIS LX520 40 mW), 594 nm (OBIS LS594 60 mW), 637 nm (OBIS LX637 140 mW) and 730 nm (OBIS LX730 30 mW), and are operated through a central USB-connected driver hub (Obis LX/LS Scientific Remote).

The 520 nm laser is used for NV excitation in Chapters 4 and 5. The 594 nm laser is used for creating excitons in WS₂ in Chapter 3, and to induce a scattering site for spin waves underneath a superconductor in Chapter 5. The LX637 can be used for resonant readout of the NV centers [112], while the 730 nm laser can be used for creating excitons in WSe₂ [113] without interfering with nearby NV centers. The 637 nm and 730 nm lasers are not used for experiments included in this dissertation. The lasers can be pulsed through external digital (on/off) modulation, with TTL signals provided by the PulseBlaster. Here, pulse width is limited by the rise time of the lasers (LX520: 3 ns, LS594: 18 μs, LX637: 2 ns, LX730: 2 ns). Additionally, continuous (analog) modulation can be achieved by connecting analog outputs of the NI PCI-6221 card (not wired in the diagram). A scanning mirror (Newport FSM300) is used to scan these lasers over the sample, via two analog outputs of the NI BNC-2110, denoted V_x and V_y in the schematic of Fig. 2.16.

Photoluminescence detection: An avalanche photodiode (APD, Excelitas SPCM-AQRH-13) generates 10 ns wide electrical pulses upon detection of an incoming photon, which are detected by one of two counter channels on the NI BNC-2110 breakout box. The APD generates 250 dark counts per second, and after a photon count there is a 24 ns dead time. Our spectrometer (Andor Kymera 193i) is equipped with a cooled 1650 x 200 CCD (Andor iVac 316) with 16 x 16 μm² pixels, that allows for hardware binning into superpixels, reducing read-out noise. A maximum of 269 full vertical binned (FVB) spectra per second can be communicated over USB to the desktop.

DC transport: Electronic transport measurements are performed with in-house constructed source- and measurement-unit (SMU) modules in the modular IVVI-DAC2 rack [49]. The IVVI-DAC2 is galvanically isolated from the desktop computer and relies on sourcing-communications through an optical fiber that is interfaced with a USB interconnect. Fiber-communications sets voltage values V_{set} on selected channels of the summing module, which are routed to the modular voltage- and current-sourcing modules through a large printed circuit board (PCB) in the back, in which the modules are inserted in plug-and-play fashion. For example, a voltage module outputs $\alpha V_{\text{out}}/V_{\text{set}}$, and a current module outputs $\beta I_{\text{out}}/V_{\text{set}}$, where α and β are selectable gain parameters. The output is routed to 1 of 24 channels in a matrix module, which forms the user-interface with the sample, and allows channel-selective electrical grounding, opening, and shorting (used for measuring) to the sample. The 24 channels are routed, through a 24-pin Fischer cable, to a custom-designed breakout box which converts the form factor to the required 26-pin 3M MDR of the cryostat sample chamber. Voltages and currents are analyzed by connecting the desired channels on the matrix module to voltage- and current-measurement modules in the IVVI-DAC2, which similarly to sourcing output a certain $V_{\text{out}}/V_{\text{measured}}$ or $V_{\text{out}}/I_{\text{measured}}$. The output voltages of the measurement modules are read out using a Keithley DMM6500 digital multimeter over USB.

Nanopositioner movement: The cryostat houses 2x ANP101x/RES/LT and 1x ANP101z/RES/LT slip-stick nanopositioners, for which we supply the driving signal for open-loop positioning using the Attocube ANC300 controller via USB. The output signals of the controller are routed to the same matrix module described above, and is supplied to the cryostat "user" 3M MDR-panel. The piezoelectric constants of the positioners decrease with temperature, leading to typical low temperature operating voltages that are beyond the room-temperature dielectric breakdown voltage. As such, caution is re-

quired to lower the operating limits when warming up, otherwise irreversible damage to the positioners is easily caused. Safe limits are 70 V for room temperature, 150 V for 4 K.

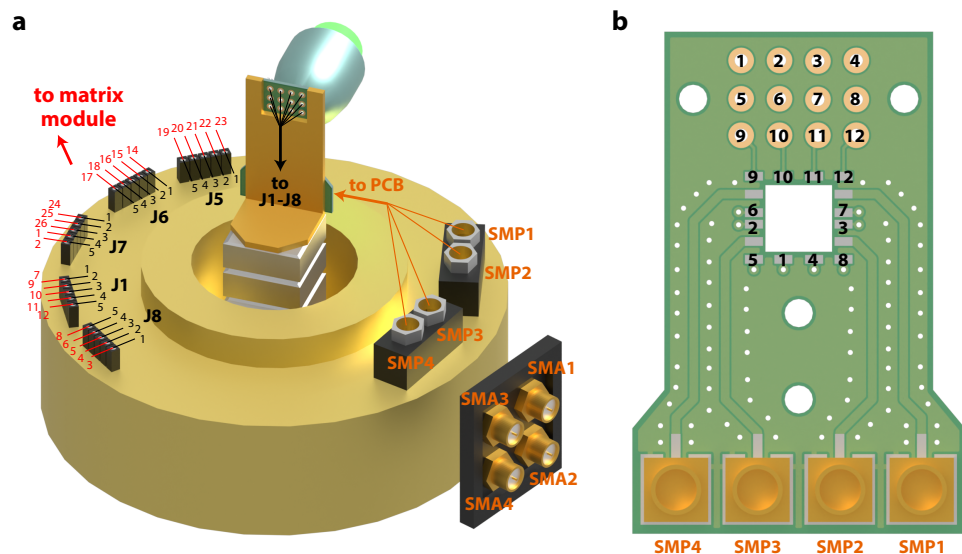


Figure 2.17. **Wiring schematic of sample chamber and printed circuit board.** (a) Overview of DC and RF connections inside the cryostat sample chamber. A custom high-purity copper sample holder placed on the positioner stack holds a custom-designed printed circuit board, with 12 soldered DC lines that are routed to five-pin connectors J1, J5, J6, J7 and J8 via a flexible braided cable. The five-pin connectors are internally routed to the 3M MDR connector (seen top-right in Fig. 2.16) on the outside of the sample chamber, which connects to the matrix module via a break-out box. The mapping of the five-pin connector channels (black numbering) to the matrix module channels (red numbering) is indicated with color coded numbers. RF signals are supplied to the SMA connector panel outside the sample chamber (bottom right), which are routed to four female SMP female sockets inside the chamber. Flexible SM 50 cables carry the signal to the printed circuit board. (b) Schematic of custom-made four-layer printed circuit board (PCB) with 12 DC lines and 4 RF connections. The RF signal is supplied by the SM 50 cables to four female SMPM sockets, and is routed through 50 Ω impedance matched grounded coplanar waveguides to bonding pads adjacent to a cut-out in the PCB. The cut-out hosts the sample, which is directly mounted on the high-purity copper sample holder with conductive silver paint for optimal thermalization. The DC bonding pads are routed through various layers to holes on top of the PCB, in which the wiring shown in (a) is soldered directly. Labeling of the bondpads to solder-sockets is indicated by black numbers.

Cryostat temperature: Temperature control of the cryostat is regulated through an auxiliary dedicated laptop. Establishing a TCP/IP communication protocol over direct ethernet connection between laptop and desktop enables temperature control through MATLAB.

Having discussed the electronics interfacing the desktop with the cryostat, we next elaborate on the further routing of relevant signals on the inside of the cryostat sample chamber, through a schematic displayed in Fig. 2.17. A custom-made high-purity cop-

per sample holder, holding a printed circuit board (PCB) with RF and DC connections, is mounted on the Attocube positioner stack as shown in Fig. 2.17a. The transport lines are soldered directly onto the PCB and connect to various five-pin connectors, which are routed to the 3M-MDR connector in the cryochamber side-panel, ultimately connecting to the matrix module. A schematic overview of the PCB used for the experiments in Chapter 4 and 5 is shown in Fig. 2.17b, with labelling of the various RF and DC connections and bondpads. A cut-out in the PCB ensures the sample can be mounted directly on the copper sample holder, which is necessary for proper thermalization.

SUMMARY

In this Chapter, we have provided a theoretical background on magnetometry with spins in diamond, described three low-dimensional magnetic phenomena that we aim to study with this technique, and discussed the development of experimental setups, samples and thin diamond membranes towards this end. By ending the Chapter with a detailed overview of electronics and operation, we have set the stage for understanding the research Chapters that follow.

REFERENCES

- [1] E. Marchiori *et al.* “Nanoscale magnetic field imaging for 2D materials”. *Nature Reviews Physics* 4.1 (2022), pp. 49–60. ISSN: 25225820. DOI: [10.1038/s42254-021-00380-9](https://doi.org/10.1038/s42254-021-00380-9).
- [2] K. Bagani *et al.* “Sputtered Mo66Re34 SQUID-on-Tip for High-Field Magnetic and Thermal Nanoimaging”. *Physical Review Applied* 12.4 (2019), p. 1. ISSN: 23317019. DOI: [10.1103/PhysRevApplied.12.044062](https://doi.org/10.1103/PhysRevApplied.12.044062). arXiv: [1908.09305](https://arxiv.org/abs/1908.09305).
- [3] Y. Anahory *et al.* “SQUID-on-tip with single-electron spin sensitivity for high-field and ultra-low temperature nanomagnetic imaging”. *Nanoscale* 12.5 (2020), pp. 3174–3182. ISSN: 20403372. DOI: [10.1039/c9nr08578e](https://doi.org/10.1039/c9nr08578e).
- [4] A. Aharon-Steinberg *et al.* “Direct observation of vortices in an electron fluid”. *Nature* 607.7917 (2022), pp. 74–80. ISSN: 14764687. DOI: [10.1038/s41586-022-04794-y](https://doi.org/10.1038/s41586-022-04794-y). arXiv: [2202.02798](https://arxiv.org/abs/2202.02798).
- [5] S. Grover *et al.* “Chern mosaic and Berry-curvature magnetism in magic-angle graphene”. *Nature Physics* 18.8 (2022), pp. 885–892. ISSN: 17452481. DOI: [10.1038/s41567-022-01635-7](https://doi.org/10.1038/s41567-022-01635-7).
- [6] H. Mattiat *et al.* “Nanowire Magnetic Force Sensors Fabricated by Focused-Electron-Beam-Induced Deposition”. *Physical Review Applied* 13.4 (2020), p. 1. ISSN: 23317019. DOI: [10.1103/PhysRevApplied.13.044043](https://doi.org/10.1103/PhysRevApplied.13.044043). arXiv: [1911.00912](https://arxiv.org/abs/1911.00912).
- [7] L. Thiel *et al.* “Probing magnetism in 2D materials at the nanoscale with single-spin microscopy”. *Science* 364.6444 (2019), pp. 973–976. ISSN: 10959203. DOI: [10.1126/science.aav6926](https://doi.org/10.1126/science.aav6926). arXiv: [1902.01406](https://arxiv.org/abs/1902.01406).
- [8] L. Rondin *et al.* “Stray-field imaging of magnetic vortices with a single diamond spin”. *Nature Communications* 4.May (2013), pp. 1–5. ISSN: 20411723. DOI: [10.1038/ncomms3279](https://doi.org/10.1038/ncomms3279). arXiv: [1302.7307](https://arxiv.org/abs/1302.7307).
- [9] Y. Schlüssel *et al.* “Wide-Field Imaging of Superconductor Vortices with Electron Spins in Diamond”. *Physical Review Applied* 10.3 (2018), p. 1. ISSN: 23317019. DOI: [10.1103/PhysRevApplied.10.034032](https://doi.org/10.1103/PhysRevApplied.10.034032). arXiv: [1803.01957](https://arxiv.org/abs/1803.01957).
- [10] T. Van Der Sar *et al.* “Nanometre-scale probing of spin waves using single-electron spins”. *Nature Communications* 6 (2015), pp. 1–8. ISSN: 20411723. DOI: [10.1038/ncomms8886](https://doi.org/10.1038/ncomms8886). arXiv: [1410.6423](https://arxiv.org/abs/1410.6423).
- [11] I. Bertelli *et al.* “Magnetic resonance imaging of spin-wave transport and interference in a magnetic insulator”. *Science Advances* 6.46 (2020), pp. 1–8. ISSN: 23752548. DOI: [10.1126/sciadv.abd3556](https://doi.org/10.1126/sciadv.abd3556). arXiv: [2004.07746](https://arxiv.org/abs/2004.07746).

- [12] T. X. Zhou *et al.* “A magnon scattering platform”. *Proceedings of the National Academy of Sciences of the United States of America* 118.25 (2021), pp. 1–6. ISSN: 10916490. DOI: [10.1073/pnas.2019473118](https://doi.org/10.1073/pnas.2019473118). arXiv: [2004.07763](https://arxiv.org/abs/2004.07763).
- [13] P. J. Scheidegger *et al.* “Scanning nitrogen-vacancy magnetometry down to 350 mK”. *Applied Physics Letters* 120.22 (2022). ISSN: 00036951. DOI: [10.1063/5.0093548](https://doi.org/10.1063/5.0093548). arXiv: [2203.15527](https://arxiv.org/abs/2203.15527).
- [14] D. M. Toyli *et al.* “Measurement and control of single nitrogen-vacancy center spins above 600 K”. *Physical Review X* 2.3 (2012), pp. 1–7. ISSN: 21603308. DOI: [10.1103/PhysRevX.2.031001](https://doi.org/10.1103/PhysRevX.2.031001). arXiv: [1201.4420](https://arxiv.org/abs/1201.4420).
- [15] I. Aharonovich *et al.* “Diamond-based single-photon emitters”. *Reports on Progress in Physics* 74.7 (2011). ISSN: 00344885. DOI: [10.1088/0034-4885/74/7/076501](https://doi.org/10.1088/0034-4885/74/7/076501).
- [16] B. Grotz *et al.* “Charge state manipulation of qubits in diamond”. *Nature Communications* 3 (2012). ISSN: 20411723. DOI: [10.1038/ncomms1729](https://doi.org/10.1038/ncomms1729).
- [17] F. Jelezko *et al.* “Single defect centres in diamond: A review”. *Physica Status Solidi (A) Applications and Materials Science* 203.13 (2006), pp. 3207–3225. ISSN: 18626300. DOI: [10.1002/pssa.200671403](https://doi.org/10.1002/pssa.200671403).
- [18] B. Hensen *et al.* “Loophole-free Bell inequality violation using electron spins separated by 1.3 kilometres”. *Nature* 526.7575 (2015), pp. 682–686. ISSN: 14764687. DOI: [10.1038/nature15759](https://doi.org/10.1038/nature15759).
- [19] F. Casola *et al.* “Probing condensed matter physics with magnetometry based on nitrogen-vacancy centres in diamond”. *Nature Reviews Materials* 3 (2018). ISSN: 20588437. DOI: [10.1038/natrevmats.2017.88](https://doi.org/10.1038/natrevmats.2017.88).
- [20] M. W. Doherty *et al.* “The negatively charged nitrogen-vacancy centre in diamond: The electronic solution”. *New Journal of Physics* 13 (2011). ISSN: 13672630. DOI: [10.1088/1367-2630/13/2/025019](https://doi.org/10.1088/1367-2630/13/2/025019). arXiv: [1008.5224](https://arxiv.org/abs/1008.5224).
- [21] A. V. Zvyagin *et al.* *Optical and Spin Properties of Nitrogen-Vacancy Color Centers in Diamond Crystals, Nanodiamonds, and Proximity to Surfaces*. Second Edi. Elsevier Inc., 2012, pp. 327–354. ISBN: 9781437734652. DOI: [10.1016/B978-1-4377-3465-2.00010-4](https://doi.org/10.1016/B978-1-4377-3465-2.00010-4).
- [22] P. Delaney *et al.* “Spin-polarization mechanisms of the nitrogen-vacancy center in diamond”. *Nano Letters* 10.2 (2010), pp. 610–614. ISSN: 15306992. DOI: [10.1021/nl903646p](https://doi.org/10.1021/nl903646p).
- [23] A. Gruber *et al.* “Scanning confocal optical microscopy and magnetic resonance on single defect centers”. *Science* 276.5321 (1997), pp. 2012–2014. ISSN: 00368075. DOI: [10.1126/science.276.5321.2012](https://doi.org/10.1126/science.276.5321.2012).
- [24] A. Dréau *et al.* “Avoiding power broadening in optically detected magnetic resonance of single NV defects for enhanced dc magnetic field sensitivity”. *Physical Review B - Condensed Matter and Materials Physics* 84.19 (2011), pp. 1–8. ISSN: 1550235X. DOI: [10.1103/PhysRevB.84.195204](https://doi.org/10.1103/PhysRevB.84.195204).
- [25] L. Robledo *et al.* “Spin dynamics in the optical cycle of single nitrogen-vacancy centres in diamond”. *New Journal of Physics* 13 (2011). ISSN: 13672630. DOI: [10.1088/1367-2630/13/2/025013](https://doi.org/10.1088/1367-2630/13/2/025013). arXiv: [1010.1192](https://arxiv.org/abs/1010.1192).

- [26] N. B. Manson *et al.* “Nitrogen-vacancy center in diamond: Model of the electronic structure and associated dynamics”. *Physical Review B - Condensed Matter and Materials Physics* 74.10 (2006), pp. 1–11. ISSN: 10980121. DOI: [10.1103/PhysRevB.74.104303](https://doi.org/10.1103/PhysRevB.74.104303).
- [27] J. R. Rabeau *et al.* “Implantation of labelled single nitrogen vacancy centers in diamond using ^{15}N ”. *Applied Physics Letters* 88.2 (2006), pp. 1–3. ISSN: 00036951. DOI: [10.1063/1.2158700](https://doi.org/10.1063/1.2158700).
- [28] R. Schirhagl *et al.* “Nitrogen-vacancy centers in diamond: Nanoscale sensors for physics and biology”. *Annual Review of Physical Chemistry* 65 (2014), pp. 83–105. ISSN: 0066426X. DOI: [10.1146/annurev-physchem-040513-103659](https://doi.org/10.1146/annurev-physchem-040513-103659).
- [29] V. Ivády *et al.* “Pressure and temperature dependence of the zero-field splitting in the ground state of NV centers in diamond: A first-principles study”. *Physical Review B - Condensed Matter and Materials Physics* 90.23 (2014), pp. 1–8. ISSN: 1550235X. DOI: [10.1103/PhysRevB.90.235205](https://doi.org/10.1103/PhysRevB.90.235205).
- [30] J. P. Tetienne *et al.* “Magnetic-field-dependent photodynamics of single NV defects in diamond: An application to qualitative all-optical magnetic imaging”. *New Journal of Physics* 14 (2012). ISSN: 13672630. DOI: [10.1088/1367-2630/14/10/103033](https://doi.org/10.1088/1367-2630/14/10/103033). arXiv: [1206.1201](https://arxiv.org/abs/1206.1201).
- [31] A. Hirohata *et al.* “Review on spintronics: Principles and device applications”. *Journal of Magnetism and Magnetic Materials* 509.March (2020). ISSN: 03048853. DOI: [10.1016/j.jmmm.2020.166711](https://doi.org/10.1016/j.jmmm.2020.166711).
- [32] J. R. Schaibley *et al.* “Valleytronics in 2D materials”. *Nature Reviews Materials* 1.11 (2016). ISSN: 20588437. DOI: [10.1038/natrevmats.2016.55](https://doi.org/10.1038/natrevmats.2016.55).
- [33] A. Rycerz *et al.* “Valley filter and valley valve in graphene”. *Nature Physics* 3.3 (2007), pp. 172–175. ISSN: 17452481. DOI: [10.1038/nphys547](https://doi.org/10.1038/nphys547). arXiv: [0608533](https://arxiv.org/abs/0608533) [cond-mat].
- [34] D. Xiao *et al.* “Valley-contrasting physics in graphene: Magnetic moment and topological transport”. *Physical Review Letters* 99.23 (2007). ISSN: 00319007. DOI: [10.1103/PhysRevLett.99.236809](https://doi.org/10.1103/PhysRevLett.99.236809). arXiv: [0709.1274](https://arxiv.org/abs/0709.1274).
- [35] D. Xiao *et al.* “Coupled spin and valley physics in monolayers of MoS₂ and other group-VI dichalcogenides”. *Physical Review Letters* 108.19 (2012), p. 196802. ISSN: 00319007. DOI: [10.1103/PhysRevLett.108.196802](https://doi.org/10.1103/PhysRevLett.108.196802). arXiv: [1112.3144](https://arxiv.org/abs/1112.3144).
- [36] K. F. Mak *et al.* “Control of valley polarization in monolayer MoS₂ by optical helicity”. *Nature Nanotechnology* 7.8 (2012), pp. 494–498. ISSN: 17483395. DOI: [10.1038/nnano.2012.96](https://doi.org/10.1038/nnano.2012.96).
- [37] T. Cao *et al.* “Valley-selective circular dichroism of monolayer molybdenum disulphide”. *Nature Communications* 3.May (2012). ISSN: 20411723. DOI: [10.1038/ncomms1882](https://doi.org/10.1038/ncomms1882).
- [38] H. Zeng *et al.* “Valley polarization in MoS₂ monolayers by optical pumping”. *Nature Nanotechnology* 7.8 (2012), pp. 490–493. ISSN: 17483395. DOI: [10.1038/nnano.2012.95](https://doi.org/10.1038/nnano.2012.95). arXiv: [1202.1592](https://arxiv.org/abs/1202.1592).

- [39] A. M. Jones *et al.* “Optical generation of excitonic valley coherence in monolayer WSe₂”. *Nature Nanotechnology* 8.9 (2013), pp. 634–638. ISSN: 17483395. DOI: [10.1038/nnano.2013.151](https://doi.org/10.1038/nnano.2013.151).
- [40] A. Srivastava *et al.* “Valley Zeeman effect in elementary optical excitations of monolayer WSe₂”. *Nature Physics* 11.2 (2015), pp. 141–147. ISSN: 17452481. DOI: [10.1038/nphys3203](https://doi.org/10.1038/nphys3203). arXiv: [1407.2624](https://arxiv.org/abs/1407.2624).
- [41] G. Aivazian *et al.* “Magnetic control of valley pseudospin in monolayer WSe₂”. *Nature Physics* 11.2 (2015), pp. 148–152. ISSN: 17452481. DOI: [10.1038/nphys3201](https://doi.org/10.1038/nphys3201). arXiv: [1407.2645](https://arxiv.org/abs/1407.2645).
- [42] A. V. Stier *et al.* “Exciton diamagnetic shifts and valley Zeeman effects in monolayer WS₂ and MoS₂ to 65 Tesla”. *Nature Communications* 7 (2016), pp. 1–8. ISSN: 20411723. DOI: [10.1038/ncomms10643](https://doi.org/10.1038/ncomms10643). arXiv: [1510.07022](https://arxiv.org/abs/1510.07022).
- [43] H. Rostami *et al.* “Valley Zeeman effect and spin-valley polarized conductance in monolayer MoS₂ in a perpendicular magnetic field”. *Physical Review B - Condensed Matter and Materials Physics* 91.7 (2015), pp. 1–11. ISSN: 1550235X. DOI: [10.1103/PhysRevB.91.075433](https://doi.org/10.1103/PhysRevB.91.075433). arXiv: [1412.1459](https://arxiv.org/abs/1412.1459).
- [44] B. B. Zhou *et al.* “Spatiotemporal Mapping of a Photocurrent Vortex in Monolayer MoS₂ Using Diamond Quantum Sensors”. *Physical Review X* 10.1 (2020), p. 11003. ISSN: 21603308. DOI: [10.1103/PhysRevX.10.011003](https://doi.org/10.1103/PhysRevX.10.011003).
- [45] G. Wang *et al.* “Colloquium: Excitons in atomically thin transition metal dichalcogenides”. *Reviews of Modern Physics* 90.2 (2018), p. 21001. ISSN: 15390756. DOI: [10.1103/RevModPhys.90.021001](https://doi.org/10.1103/RevModPhys.90.021001).
- [46] M. Danovich *et al.* “Auger recombination of dark excitons in WS₂ and WSe₂ monolayers”. *2D Materials* 3.3 (2016), pp. 4–9. ISSN: 20531583. DOI: [10.1088/2053-1583/3/3/035011](https://doi.org/10.1088/2053-1583/3/3/035011).
- [47] Z. Li *et al.* “Revealing the biexciton and trion-exciton complexes in BN encapsulated WSe₂”. *Nature Communications* 9.1 (2018), pp. 1–7. ISSN: 20411723. DOI: [10.1038/s41467-018-05863-5](https://doi.org/10.1038/s41467-018-05863-5).
- [48] D. H. Lien *et al.* “Electrical suppression of all nonradiative recombination pathways in monolayer semiconductors”. *Science* 364.6439 (2019), pp. 468–471. ISSN: 10959203. DOI: [10.1126/science.aaw8053](https://doi.org/10.1126/science.aaw8053).
- [49] R. N. Schouten. *QT designed instrumentation*.
- [50] K. S. Novoselov *et al.* “Electric Field Effect in Atomically Thin Carbon Films”. *Science* 306.5696 (2004), pp. 666–669.
- [51] K. S. Novoselov *et al.* “Two-dimensional atomic crystals”. *Proceedings of the National Academy of Sciences of the United States of America* 102.30 (2005), pp. 10451–10453. ISSN: 00278424. DOI: [10.1073/pnas.0502848102](https://doi.org/10.1073/pnas.0502848102).
- [52] Y. Liu *et al.* “Van der Waals heterostructures and devices”. *Nature Reviews Materials* 1.9 (2016). ISSN: 20588437. DOI: [10.1038/natrevmats.2016.42](https://doi.org/10.1038/natrevmats.2016.42).
- [53] B. I. Halperin. “On the Hohenberg–Mermin–Wagner Theorem and Its Limitations”. *Journal of Statistical Physics* 175.3-4 (2019), pp. 521–529. ISSN: 00224715. DOI: [10.1007/s10955-018-2202-y](https://doi.org/10.1007/s10955-018-2202-y). arXiv: [1812.00220](https://arxiv.org/abs/1812.00220).

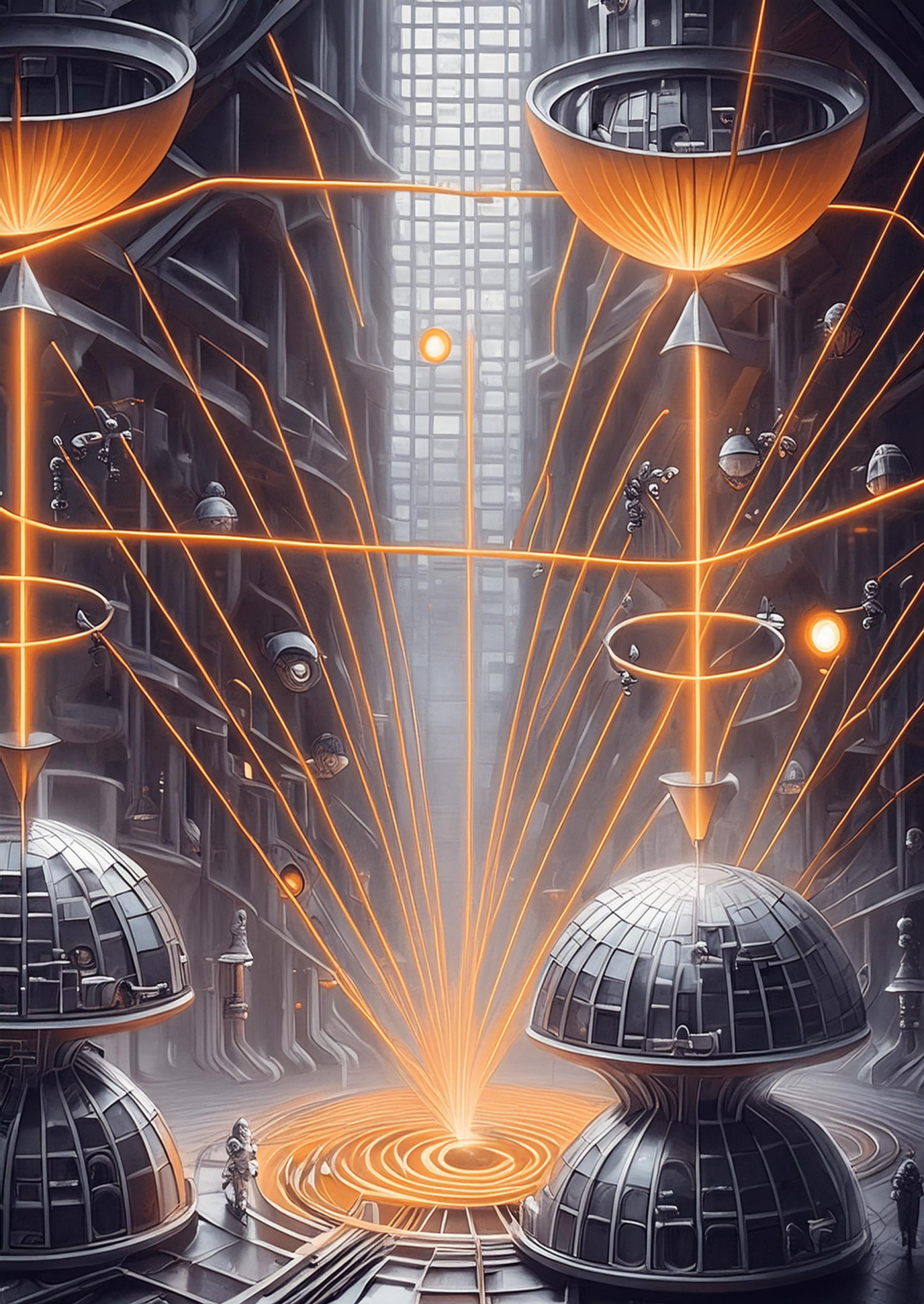
- [54] C. Gong *et al.* “Discovery of intrinsic ferromagnetism in two-dimensional van der Waals crystals”. *Nature* 546.7657 (2017), pp. 265–269. ISSN: 14764687. DOI: [10.1038/nature22060](https://doi.org/10.1038/nature22060).
- [55] B. Huang *et al.* “Layer-dependent ferromagnetism in a van der Waals crystal down to the monolayer limit”. *Nature* 546.7657 (2017), pp. 270–273. ISSN: 14764687. DOI: [10.1038/nature22391](https://doi.org/10.1038/nature22391). arXiv: [1703.05892](https://arxiv.org/abs/1703.05892).
- [56] Y. Deng *et al.* “Gate-tunable room-temperature ferromagnetism in two-dimensional Fe₃GeTe₂”. *Nature* 563.7729 (2018), pp. 94–99. ISSN: 14764687. DOI: [10.1038/s41586-018-0626-9](https://doi.org/10.1038/s41586-018-0626-9). arXiv: [1803.02038](https://arxiv.org/abs/1803.02038).
- [57] Q. H. Wang *et al.* “The Magnetic Genome of Two-Dimensional van der Waals Materials”. *ACS Nano* (2021). ISSN: 1936086X. DOI: [10.1021/acsnano.1c09150](https://doi.org/10.1021/acsnano.1c09150).
- [58] D. Zhong *et al.* “Van der Waals engineering of ferromagnetic semiconductor heterostructures for spin and valleytronics”. *Science Advances* 3.5 (2017), pp. 1–6. ISSN: 23752548. DOI: [10.1126/sciadv.1603113](https://doi.org/10.1126/sciadv.1603113). arXiv: [1704.00841](https://arxiv.org/abs/1704.00841).
- [59] Z. Wang *et al.* “Tunneling Spin Valves Based on Fe₃GeTe₂/hBN/Fe₃GeTe₂ van der Waals Heterostructures”. *Nano Letters* 18.7 (2018), pp. 4303–4308. ISSN: 15306992. DOI: [10.1021/acs.nanolett.8b01278](https://doi.org/10.1021/acs.nanolett.8b01278).
- [60] W. Zhu *et al.* “Large and tunable magnetoresistance in van der Waals ferromagnet/semiconductor junctions”. *Nature Communications* 14.1 (2023), pp. 1–7. ISSN: 20411723. DOI: [10.1038/s41467-023-41077-0](https://doi.org/10.1038/s41467-023-41077-0). arXiv: [2303.11596](https://arxiv.org/abs/2303.11596).
- [61] B. Karpiak *et al.* “Magnetic proximity in a van der Waals heterostructure of magnetic insulator and graphene”. *2D Materials* 7.1 (2020). ISSN: 20531583. DOI: [10.1088/2053-1583/ab5915](https://doi.org/10.1088/2053-1583/ab5915). arXiv: [1908.05524](https://arxiv.org/abs/1908.05524).
- [62] T. S. Ghiasi *et al.* “Electrical and thermal generation of spin currents by magnetic bilayer graphene”. *Nature Nanotechnology* 16.7 (2021), pp. 788–794. ISSN: 17483395. DOI: [10.1038/s41565-021-00887-3](https://doi.org/10.1038/s41565-021-00887-3).
- [63] X. X. Zhang *et al.* “Gate-tunable spin waves in antiferromagnetic atomic bilayers”. *Nature Materials* 19.8 (2020), pp. 838–842. ISSN: 14764660. DOI: [10.1038/s41563-020-0713-9](https://doi.org/10.1038/s41563-020-0713-9). arXiv: [2001.04044](https://arxiv.org/abs/2001.04044).
- [64] J. Cenker *et al.* “Direct observation of two-dimensional magnons in atomically thin CrI₃”. *Nature Physics* 17.1 (2021), pp. 20–25. ISSN: 17452481. DOI: [10.1038/s41567-020-0999-1](https://doi.org/10.1038/s41567-020-0999-1).
- [65] D. R. Klein *et al.* “Probing magnetism in 2D van der Waals crystalline insulators via electron tunneling”. *Science* 360.6394 (2018), pp. 1218–1222. ISSN: 10959203. DOI: [10.1126/science.aar3617](https://doi.org/10.1126/science.aar3617). arXiv: [1801.10075](https://arxiv.org/abs/1801.10075).
- [66] S. Mandal *et al.* “Coplanar cavity for strong coupling between photons and magnons in van der Waals antiferromagnet”. *Applied Physics Letters* 117.26 (2020). ISSN: 00036951. DOI: [10.1063/5.0029112](https://doi.org/10.1063/5.0029112). arXiv: [2002.00197](https://arxiv.org/abs/2002.00197).
- [67] Q. Zhang *et al.* “Zero-field magnon-photon coupling in antiferromagnet CrCl₃”. *Applied Physics Letters* 119.10 (2021). ISSN: 00036951. DOI: [10.1063/5.0063642](https://doi.org/10.1063/5.0063642).

- [68] F. Schulz *et al.* “Direct Observation of Propagating Spin Waves in the 2D van der Waals Ferromagnet Fe₅GeTe₂”. *Nano Letters* 23.22 (2023), pp. 10126–10131. ISSN: 15306992. DOI: [10.1021/acs.nanolett.3c02212](https://doi.org/10.1021/acs.nanolett.3c02212).
- [69] L. Thiel *et al.* “Probing magnetism in 2D materials at the nanoscale with single-spin microscopy”. *Science* 364.6444 (2019), pp. 973–976. ISSN: 10959203. DOI: [10.1126/science.aav6926](https://doi.org/10.1126/science.aav6926). arXiv: [1902.01406](https://arxiv.org/abs/1902.01406).
- [70] Q. C. Sun *et al.* “Magnetic domains and domain wall pinning in atomically thin CrBr₃ revealed by nanoscale imaging”. *Nature Communications* 12.1 (2021), pp. 1–7. ISSN: 20411723. DOI: [10.1038/s41467-021-22239-4](https://doi.org/10.1038/s41467-021-22239-4).
- [71] I. O. Robertson *et al.* “Imaging current control of magnetization in Fe₃GeTe₂ with a widefield nitrogen-vacancy microscope”. *2D Materials* 10.1 (2023). ISSN: 20531583. DOI: [10.1088/2053-1583/acab73](https://doi.org/10.1088/2053-1583/acab73). arXiv: [2207.10329](https://arxiv.org/abs/2207.10329).
- [72] T. Song *et al.* “Direct visualization of magnetic domains and moiré magnetism in twisted 2D magnets”. *Science* 374.6571 (2021), pp. 1140–1144. ISSN: 10959203. DOI: [10.1126/science.abj7478](https://doi.org/10.1126/science.abj7478).
- [73] H. Chen *et al.* “Above-Room-Temperature Ferromagnetism in Thin van der Waals Flakes of Cobalt-Substituted Fe₅GeTe₂”. *ACS Applied Materials and Interfaces* (2022). ISSN: 19448252. DOI: [10.1021/acsami.2c18028](https://doi.org/10.1021/acsami.2c18028).
- [74] G. Q. Yan *et al.* “Quantum Sensing and Imaging of Spin–Orbit–Torque–Driven Spin Dynamics in the Non-Collinear Antiferromagnet Mn₃Sn”. *Advanced Materials* 34.23 (2022), pp. 1–9. ISSN: 15214095. DOI: [10.1002/adma.202200327](https://doi.org/10.1002/adma.202200327). arXiv: [2203.11465](https://arxiv.org/abs/2203.11465).
- [75] D. A. Broadway *et al.* “Imaging Domain Reversal in an Ultrathin Van der Waals Ferromagnet”. *Advanced Materials* 32.39 (2020), pp. 1–6. ISSN: 15214095. DOI: [10.1002/adma.202003314](https://doi.org/10.1002/adma.202003314). arXiv: [2003.08470](https://arxiv.org/abs/2003.08470).
- [76] N. J. Mclaughlin *et al.* “Quantum Imaging of Magnetic Phase Transitions and Spin Fluctuations in Intrinsic Magnetic Topological Nanoflakes”. *Nano Letters* 22.14 (2022), pp. 5810–5817. ISSN: 15306992. DOI: [10.1021/acs.nanolett.2c01390](https://doi.org/10.1021/acs.nanolett.2c01390). arXiv: [2112.09863](https://arxiv.org/abs/2112.09863).
- [77] H. Chen *et al.* “Revealing room temperature ferromagnetism in exfoliated Fe₅GeTe₂ flakes with quantum magnetic imaging”. *2D Materials* 9.2 (2022). ISSN: 20531583. DOI: [10.1088/2053-1583/ac57a9](https://doi.org/10.1088/2053-1583/ac57a9). arXiv: [2110.05314](https://arxiv.org/abs/2110.05314).
- [78] X. Y. Zhang *et al.* “Ac Susceptometry of 2D van der Waals Magnets Enabled by the Coherent Control of Quantum Sensors”. *PRX Quantum* 2.3 (2021), p. 1. ISSN: 26913399. DOI: [10.1103/PRXQuantum.2.030352](https://doi.org/10.1103/PRXQuantum.2.030352). arXiv: [2105.08030](https://arxiv.org/abs/2105.08030).
- [79] T. Van Der Sar *et al.* “Nanometre-scale probing of spin waves using single-electron spins”. *Nature Communications* 6 (2015), pp. 1–7. ISSN: 20411723. DOI: [10.1038/ncomms8886](https://doi.org/10.1038/ncomms8886).
- [80] T. X. Zhou *et al.* “A magnon scattering platform”. *Proceedings of the National Academy of Sciences of the United States of America* 118.25 (2021), pp. 1–6. ISSN: 10916490. DOI: [10.1073/pnas.2019473118](https://doi.org/10.1073/pnas.2019473118). arXiv: [2004.07763](https://arxiv.org/abs/2004.07763).

- [81] I. Bertelli *et al.* “Imaging Spin-Wave Damping Underneath Metals Using Electron Spins in Diamond”. *Advanced Quantum Technologies* 4.12 (2021), pp. 1–6. ISSN: 25119044. DOI: [10.1002/qute.202100094](https://doi.org/10.1002/qute.202100094). arXiv: [2106.02508](https://arxiv.org/abs/2106.02508).
- [82] B. G. Simon *et al.* “Filtering and Imaging of Frequency-Degenerate Spin Waves Using Nanopositioning of a Single-Spin Sensor”. *Nano Letters* 22.22 (2022), pp. 9198–9204. ISSN: 15306992. DOI: [10.1021/acs.nanolett.2c02791](https://doi.org/10.1021/acs.nanolett.2c02791). arXiv: [2207.02798](https://arxiv.org/abs/2207.02798).
- [83] J. J. Carmiggelt *et al.* “Broadband microwave detection using electron spins in a hybrid diamond-magnet sensor chip”. *Nature Communications* 14.1 (2023), pp. 1–6. ISSN: 20411723. DOI: [10.1038/s41467-023-36146-3](https://doi.org/10.1038/s41467-023-36146-3). arXiv: [2206.07013](https://arxiv.org/abs/2206.07013).
- [84] I. Bertelli *et al.* “Magnetic resonance imaging of spin-wave transport and interference in a magnetic insulator”. *Science Advances* 6.46 (2020), pp. 2–8. ISSN: 23752548. DOI: [10.1126/sciadv.abd3556](https://doi.org/10.1126/sciadv.abd3556). arXiv: [2004.07746](https://arxiv.org/abs/2004.07746).
- [85] I. Bertelli. “Magnetic imaging of spin waves and magnetic phase transitions with nitrogen-vacancy centers in diamond”. PhD dissertation. Leiden University & Delft University of Technology, 2021. ISBN: 9789085935056.
- [86] J. J. Carmiggelt. “Spectroscopy and imaging of spin waves and valley excitons in two dimensions”. PhD thesis. Delft University of Technology, 2023, p. 173. ISBN: 9789085935513.
- [87] B. G. Simon. “Building a platform for magnetic imaging of spin waves”. PhD dissertation. Delft University of Technology, 2023. ISBN: 9789085935643.
- [88] S. A. Wolf *et al.* “Spintronics: A spin-based electronics vision for the future”. *Science* 294.5546 (2001), pp. 1488–1495. ISSN: 00368075. DOI: [10.1126/science.1065389](https://doi.org/10.1126/science.1065389).
- [89] V. Kruglyak *et al.* “Preface: Magnonics”. *Journal of Physics D: Applied Physics* 43.26 (2010), pp. 3–5. ISSN: 00223727. DOI: [10.1088/0022-3727/43/26/260301](https://doi.org/10.1088/0022-3727/43/26/260301).
- [90] A. Barman *et al.* “The 2021 Magnonics Roadmap”. *Journal of Physics Condensed Matter* 33.41 (2021). ISSN: 1361648X. DOI: [10.1088/1361-648X/abec1a](https://doi.org/10.1088/1361-648X/abec1a).
- [91] I. A. Golovchanskiy *et al.* “Ferromagnet/Superconductor Hybrid Magnonic Metamaterials”. *Advanced Science* 6.16 (2019), pp. 1–8. ISSN: 21983844. DOI: [10.1002/adv.201900435](https://doi.org/10.1002/adv.201900435).
- [92] I. A. Golovchanskiy *et al.* “Nonlinear spin waves in ferromagnetic/superconductor hybrids”. *Journal of Applied Physics* 127.9 (2020). ISSN: 10897550. DOI: [10.1063/1.5141793](https://doi.org/10.1063/1.5141793).
- [93] B. Niedzielski *et al.* “Magnon-Fluxon Interaction in Coupled Superconductor/Ferromagnet Hybrid Periodic Structures”. *Physical Review Applied* 19.2 (2023), p. 1. ISSN: 23317019. DOI: [10.1103/PhysRevApplied.19.024073](https://doi.org/10.1103/PhysRevApplied.19.024073).
- [94] T. Yu *et al.* “Efficient Gating of Magnons by Proximity Superconductors”. *Physical Review Letters* 129.11 (2022), p. 117201. ISSN: 10797114. DOI: [10.1103/PhysRevLett.129.117201](https://doi.org/10.1103/PhysRevLett.129.117201). arXiv: [2201.09532](https://arxiv.org/abs/2201.09532).

- [95] A. Rustagi *et al.* “Sensing chiral magnetic noise via quantum impurity relaxometry”. *Physical Review B* 102.22 (2020), pp. 1–6. ISSN: 24699969. DOI: [10.1103/PhysRevB.102.220403](https://doi.org/10.1103/PhysRevB.102.220403). arXiv: 2009.05060.
- [96] A. Gurevich *et al.* *Magnetic Oscillations and Waves*. CRC Press, Inc., 1996.
- [97] K. Y. Guslienko *et al.* “Magnetostatic Greens functions for the description of spin waves in finite rectangular magnetic dots and stripes”. *Journal of Magnetism and Magnetic Materials* 323.18-19 (2011), pp. 2418–2424. ISSN: 03048853. DOI: [10.1016/j.jmmm.2011.05.020](https://doi.org/10.1016/j.jmmm.2011.05.020).
- [98] J. D. Jackson. *Classical Electrodynamics*. New York: John Wiley & Sons, Inc., 1962, p. 625.
- [99] R. C. Longo *et al.* “Intrinsic air stability mechanisms of two-dimensional transition metal dichalcogenide surfaces: Basal versus edge oxidation”. *2D Materials* 4.2 (2017), pp. 0–21. ISSN: 20531583. DOI: [10.1088/2053-1583/aa636c](https://doi.org/10.1088/2053-1583/aa636c).
- [100] A. Castellanos-Gomez *et al.* “Deterministic transfer of two-dimensional materials by all-dry viscoelastic stamping”. *2D Materials* 1.1 (2014). ISSN: 20531583. DOI: [10.1088/2053-1583/1/1/011002](https://doi.org/10.1088/2053-1583/1/1/011002). arXiv: 1311.4829.
- [101] D. R. Glenn *et al.* “Micrometer-scale magnetic imaging of geological samples using a quantum diamond microscope”. *Geochemistry, Geophysics, Geosystems* 18.8 (2017), pp. 3254–3267. ISSN: 15252027. DOI: [10.1002/2017GC006946](https://doi.org/10.1002/2017GC006946). arXiv: 1707.06714.
- [102] S. C. Scholten *et al.* “Widefield quantum microscopy with nitrogen-vacancy centers in diamond: Strengths, limitations, and prospects”. *Journal of Applied Physics* 130.15 (2021). ISSN: 10897550. DOI: [10.1063/5.0066733](https://doi.org/10.1063/5.0066733). arXiv: 2108.06060.
- [103] P. Appel *et al.* “Fabrication of all diamond scanning probes for nanoscale magnetometry”. *Review of Scientific Instruments* 87.6 (2016). ISSN: 10897623. DOI: [10.1063/1.4952953](https://doi.org/10.1063/1.4952953). arXiv: 1604.00021.
- [104] Y. Chu *et al.* “Coherent optical transitions in implanted nitrogen vacancy centers”. *Nano Letters* 14.4 (2014), pp. 1982–1986. ISSN: 15306992. DOI: [10.1021/nl404836p](https://doi.org/10.1021/nl404836p).
- [105] Y. Tao *et al.* “Single-crystal diamond nanomechanical resonators with quality factors exceeding one million”. *Nature Communications* 5 (2014), pp. 1–8. ISSN: 20411723. DOI: [10.1038/ncomms4638](https://doi.org/10.1038/ncomms4638). arXiv: 1212.1347.
- [106] M. Ruf *et al.* “Optically Coherent Nitrogen-Vacancy Centers in Micrometer-Thin Etched Diamond Membranes”. *Nano Letters* 19.6 (2019), pp. 3987–3992. ISSN: 15306992. DOI: [10.1021/acs.nanolett.9b01316](https://doi.org/10.1021/acs.nanolett.9b01316). arXiv: 1904.00883.
- [107] *Quantum polishing by Almax easyLab*. 2023.
- [108] S. Pezzagna *et al.* “Creation efficiency of nitrogen-vacancy centres in diamond”. *New Journal of Physics* 12 (2010). ISSN: 13672630. DOI: [10.1088/1367-2630/12/6/065017](https://doi.org/10.1088/1367-2630/12/6/065017).
- [109] L. Allers *et al.* “The annealing of interstitial-related optical centres in type II natural and CVD diamond”. *Diamond and Related Materials* 7.2-5 (1998), pp. 228–232. ISSN: 09259635. DOI: [10.1016/s0925-9635\(97\)00161-1](https://doi.org/10.1016/s0925-9635(97)00161-1).

- [110] K. J. Brown *et al.* “Cleaning diamond surfaces using boiling acid treatment in a standard laboratory chemical hood”. *Journal of Chemical Health and Safety* 26.6 (2019), pp. 40–44. ISSN: 18715532. DOI: [10.1016/j.jchas.2019.06.001](https://doi.org/10.1016/j.jchas.2019.06.001).
- [111] A. A. Kaverzin *et al.* “Spin injection by spin-charge coupling in proximity induced magnetic graphene”. *2D Materials* 9.4 (2022). ISSN: 20531583. DOI: [10.1088/2053-1583/ac7881](https://doi.org/10.1088/2053-1583/ac7881).
- [112] R. Monge *et al.* “Resonant Versus Non-resonant Spin Readout of a Nitrogen-Vacancy Center in Diamond under Cryogenic Conditions”. *Physical Review Letters* 131.23 (2023), pp. 1–6. ISSN: 10797114. DOI: [10.1103/PhysRevLett.131.236901](https://doi.org/10.1103/PhysRevLett.131.236901).
- [113] J. Gusakova *et al.* “Electronic Properties of Bulk and Monolayer TMDs: Theoretical Study Within DFT Framework (GVJ-2e Method)”. *Physica Status Solidi (A) Applications and Materials Science* 214.12 (2017), pp. 1–7. ISSN: 18626319. DOI: [10.1002/pssa.201700218](https://doi.org/10.1002/pssa.201700218).



3

EXCITON-TO-TRION-CONVERSION DRIVEN VALLEY POLARIZATION IN MONOLAYER WS₂

*"When corner cutter and perfectionist unite
a diligent efficiency's in sight."*

Transition metal dichalcogenide (TMD) monolayers are two-dimensional semiconductors with two valleys in their band structure that can be selectively addressed using circularly polarized light. Their photoluminescence spectrum is characterized by neutral and charged excitons (trions) that form a chemical equilibrium governed by the net charge density. Here, we use chemical doping to drive the conversion of excitons into trions in WS₂ monolayers at room temperature, and study the resulting valley polarization via photoluminescence measurements under valley-selective optical excitation. We show that the doping causes the emission to become dominated by trions with a strong valley polarization associated with rapid non-radiative recombination. Simultaneously, the doping results in strongly quenched but highly valley-polarized exciton emission due to the enhanced conversion into trions. A rate equation model explains the observed valley polarization in terms of the doping-controlled exciton-trion equilibrium. Our results shed light on the important role of exciton-trion conversion on valley polarization in monolayer TMDs.

This chapter has been published in *Sci Rep* **10**, 17389 (2020), <https://doi.org/10.1038/s41598-020-74376-3>, by J.J. Carmiggelt*, **M. Borst*** and T. van der Sar. *These authors contributed equally.

3.1. INTRODUCTION

Transition metal dichalcogenide (TMD) monolayers are direct-bandgap semiconductors of which the conduction and valence band extrema consist of two valleys [1, 2]. The broken inversion symmetry of the lattice gives rise to optical selection rules that enable valley-selective, inter-band excitation of electrons using circularly polarized light [3–5]. A strong Coulomb interaction results in the subsequent formation of excitons [6], which maintain a valley polarization that is determined by the ratio between the intervalley scattering time and the exciton lifetime [3, 7]. Such valley-polarized excitons have been proposed as carriers of information and play a central role in the field of valleytronics [8, 9]. As such, understanding the processes that govern the exciton lifetime and associated valley polarization is important for assessing the potential applicability of valley-polarized excitons in devices.

Under optical excitation, a charge-density-controlled chemical equilibrium between neutral and charged excitons (trions) forms in a TMD monolayer [10–12]. The conversion into trions reduces the exciton lifetime [13] and may therefore be expected to lead to a large valley polarization of excitons that are created via valley-selective optical pumping, but demonstrating this effect has thus far remained elusive.

The charge density of TMD monolayers can be controlled via electrostatic gating or chemical doping [10, 11, 14–20]. While electrostatic gating is a flexible technique that allows a continuous change of the charge density [10, 11, 14], chemical doping provides a convenient alternative that requires no microfabrication and is well suited for achieving high doping levels [15–20]. Here, we study the valley polarization of excitons and trions in monolayer WS_2 and show that chemical doping via aromatic anisole (methoxybenzene) quenches the exciton photoluminescence and causes the spectrum to become dominated by trions with a strong valley polarization. A spatial study of the remaining exciton emission shows that also the excitons attain a strong valley polarization, which we attribute to the rapid doping-induced conversion into trions. We extend a rate equation model describing exciton-trion conversion [10] to include the two valleys and use it to explain the observed valley polarization in terms of the doping-controlled chemical equilibrium between excitons and trions.

3.2. CHEMICAL DOPING OF WS_2 USING ANISOLE

When doping a TMD monolayer using aromatic molecules such as anisole, Hard Soft Acid Base (HSAB) theory allows predicting whether the dopant will be n- or p-type [16]. Electrons hop between the adsorbed molecules (A) and the monolayer (B) to compensate for the difference in chemical potential μ between both systems [21]. The chemical hardness η of the materials determines how quickly an equilibrium is reached, leading to an average number of transferred electrons per molecule ΔN :

$$\Delta N = \frac{\mu_A - \mu_B}{\eta_A + \eta_B}. \quad (3.1)$$

For both anisole and monolayer WS_2 , the chemical potential and chemical hardness has been calculated using density functional theory [22, 23]. Using these values (Supplementary Section 3.5) we find $\Delta N = 0.22$, such that we expect the monolayer to be n-doped upon physisorption of anisole molecules (Fig. 3.1a).

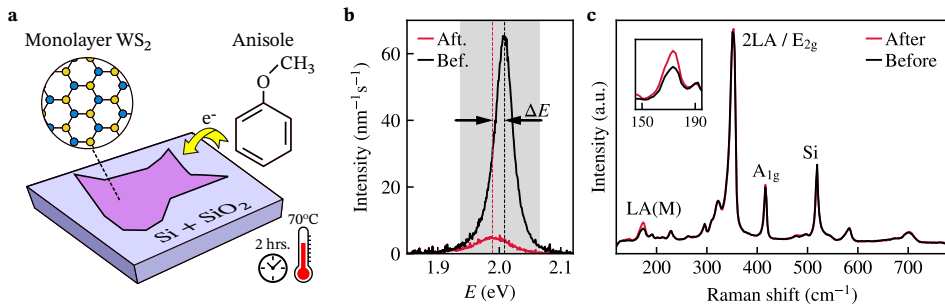


Figure 3.1. Controlling the photoluminescence properties of monolayer WS₂ via chemical doping. (a) WS₂ monolayers on Si/SiO₂ substrates become n-doped by treating them with anisole for 2 hours at 70 °C. The insets show the chemical structures of WS₂ and anisole. (b) Photoluminescence spectrum of a monolayer WS₂ before and after the anisole treatment. The treatment quenches the neutral exciton resonance, leading to the emergence of the trion resonance. The spectrum before (after) treatment was taken at 4 μW (40 μW) off-resonant laser excitation ($E = 2.331$ eV, $\lambda = 532$ nm). The shaded area indicates the transmission window of the bandpass filter used for the maps in Fig. 3.2. (c) Raman spectra before and after the treatment of the same monolayer as in (b), at 514 nm laser excitation. The inset shows the enhanced intensity of the longitudinal acoustic LA(M) phonon mode, attributed to the adsorption of the anisole molecules. Both spectra are averages over multiple positions of the flake, which all show the same mode enhancement.

To study the effect of chemical doping with anisole on the valley polarization properties of WS₂, we start by characterizing the photoluminescence of exfoliated WS₂ monolayers on 280 nm Si/SiO₂ substrates. The emission spectrum of an as-prepared monolayer shows the characteristic bright exciton resonance at 2.01 eV (Fig. 3.1b, black line) [24]. After chemical doping by a two-hour treatment in liquid anisole at 70 °C, the bright exciton resonance is strongly quenched and only a weak emission peak that is red-shifted by $\Delta E = 23$ meV remains (Fig. 3.1b, red line). Because the increased binding energy of trions compared to excitons should lead to such a red shift [14] and the expected n-type doping by the anisole molecules should favour trion formation, we attribute this peak to emission associated with trions. This conclusion is further supported by spatial studies of emission spectra showing both exciton and trion components that we will describe below. As expected, the trion emission is weak due to its long radiative lifetime and strong non-radiative decay attributed to Auger recombination [10, 25, 26].

Doping by adsorbed carbon-hydrogen groups [27] was previously shown to result in an increase of the longitudinal acoustic LA(M) and LA(K) modes in the Raman spectrum of WS₂ monolayers. Our treatment causes a similar increase of the LA(M) Raman mode (Fig. 3.1c), which we therefore attribute to the adsorption of anisole molecules. We do not observe an associated increase of the LA(K) mode at about 190 cm⁻¹, which may be due to the different nature of the adsorbates resulting in different lattice deformations and/or defects in the monolayer. We note that a similar behaviour was observed in previous work on WS₂ monolayers [7], which showed an increasing intensity of the LA(M) Raman mode without an associated increase in the LA(K) mode as a function of

the defect concentration. In addition, we find that the double-resonance 2LA(M) mode remains unaffected by the doping, indicating that our treatment does not significantly change the monolayer's electronic structure [28].

To study the valley polarization of chemically-doped WS₂ monolayers, we use near-resonant excitation with a 594 nm circularly polarized, continuous-wave laser that is focused to a diffraction-limited spot. The resulting photoluminescence is polarization filtered and collected using a home-built confocal microscope Chapter 2. Before detecting the emission with an avalanche photodiode (APD), we apply a spectral bandpass filter with a transmission window centered around the exciton and trion resonances (shaded area in Fig. 3.1b).

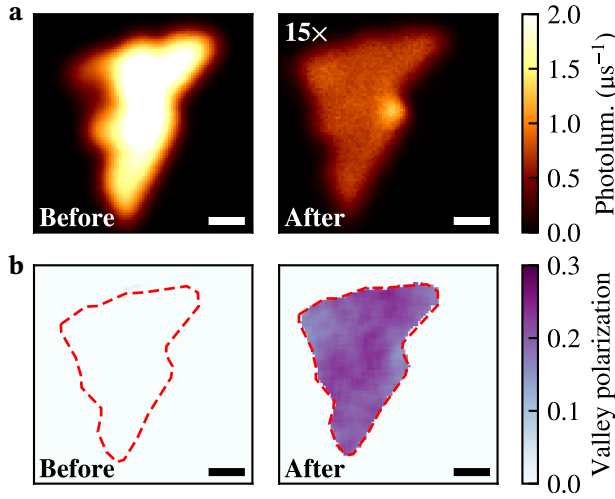


Figure 3.2. **Increasing valley polarization of WS₂ photo-emission through anisole doping.** (a) Spatial map of the photoluminescence of a monolayer WS₂ before and after chemical doping with anisole. The treatment quenches the brightness of the flake. (b) Spatial map of valley polarization before and after doping, with strongly valley-polarized emission post treatment. The flake was exfoliated on a Si/SiO₂ substrate and excited near the exciton resonance ($E = 2.087$ eV, $\lambda = 594$ nm, $4 \mu\text{W}$). Scale bar: $2 \mu\text{m}$.

We quantify the valley polarization ρ via polarization-resolved photoluminescence measurements according to

$$\rho = \frac{I_{\sigma^+} - I_{\sigma^-}}{I_{\sigma^+} + I_{\sigma^-}}. \quad (3.2)$$

Here, I_{σ^+} and I_{σ^-} represent the intensities of the right- and left-handed emission by the sample under σ^+ excitation and the total photoluminescence is given by $I = I_{\sigma^+} + I_{\sigma^-}$. By scanning the sample while detecting its emission using the APD, we make photoluminescence and valley-polarization maps of our flakes, before and after treating them. Before the anisole treatment, the photoluminescence is characterized by bright exciton emission (Fig. 3.2a, left panel) with no valley polarization (Fig. 3.2b, left panel). Strikingly, the trion emission that remains after chemical doping (Fig. 3.2a, right panel) has a valley polarization of about 25% (Fig. 3.2b, right panel). We consistently observe

the emergence of strong valley polarization after anisole treatment in multiple samples (Supplementary Section 3.5).

Next, we demonstrate the substrate independence of the effect of our treatment by repeating the measurements on an yttrium iron garnet (YIG) substrate. YIG is a magnetic insulator that was shown to effectively negatively dope MoS₂ monolayers at low temperatures, possibly due to dangling oxygen bonds at the YIG surface [29]. As such, the total level of doping could be larger for monolayers on YIG due to additional doping from the substrate. We exfoliated monolayers WS₂ onto polydimethylsiloxane (PDMS) stamps and deposited them onto the YIG substrates [30]. As before, the emission of the monolayers is strongly quenched after chemical doping and a valley polarization of about 20%-40% emerges (Fig. 3.3, Supplementary Section 3.5). Compared to the monolayers on Si/SiO₂ substrates we conclude that these data do not indicate significant additional doping from the YIG substrate.

3.3. DOPING-CONTROLLED EXCITON-TO-TRION CONVERSION

To assess the spatial homogeneity of the doping, we characterize the photoluminescence and valley polarization of a relatively large-area monolayer flake on YIG (Fig. 3.3a-b). In most parts of the flake, we observe a valley polarization of about 40%. In addition, at multiple spots in the monolayer, we observe an enhanced photoluminescence and reduced valley polarization. A comparison with an atomic force microscope topography image (Fig. 3.3c) shows that these spots are associated with wrinkles in the flake. Spectrally, the spots are characterized by the simultaneous presence of an exciton resonance and a trion resonance, with the exciton resonance rapidly vanishing as we move off the spot and the trion resonance remaining approximately constant (Fig. 3.3d). We extract the valley polarization and brightness of the exciton and trion resonances by fitting similar emission spectra near multiple wrinkles with an exciton and trion component (Supplementary Section 3.5). The extracted trion brightness and valley polarization is independent of the local exciton emission (Fig. 3.3e), highlighting their spatial homogeneity. In particular, the trion valley polarization of about 40% is similar to that in the flat areas of the flake (Fig. 3.3b,f). The stronger exciton emission at wrinkles indicates that the doping is less effective, possibly resulting from the restricted physical access to the monolayer at wrinkles or from a decreased substrate-induced doping due to the increased substrate-monolayer distance. In addition, the exciton and trion formation could be altered at the wrinkles as a result of local strain [32].

Strikingly, the excitons at the wrinkles also attained a strong valley polarization, as can be seen from the spectra in Fig. 3.3d. We extend an existing rate equation model [10] to argue that this is the result of the doping-induced conversion of excitons into trions (Fig. 3.4a). This conversion acts as a decay channel for the excitons, enhancing their valley polarization and quenching their photoluminescence. The model predicts that the excitonic valley polarization starts to increase strongly when the conversion rate into trions Γ_{T-X} becomes comparable to the intervalley scattering rate $\Gamma_{iv,X}$ (Fig. 3.4b, green line). Since Γ_{T-X} is proportional to the electron density as described by a law of mass-action [11, 12], indeed an emergent exciton polarization is expected when doping

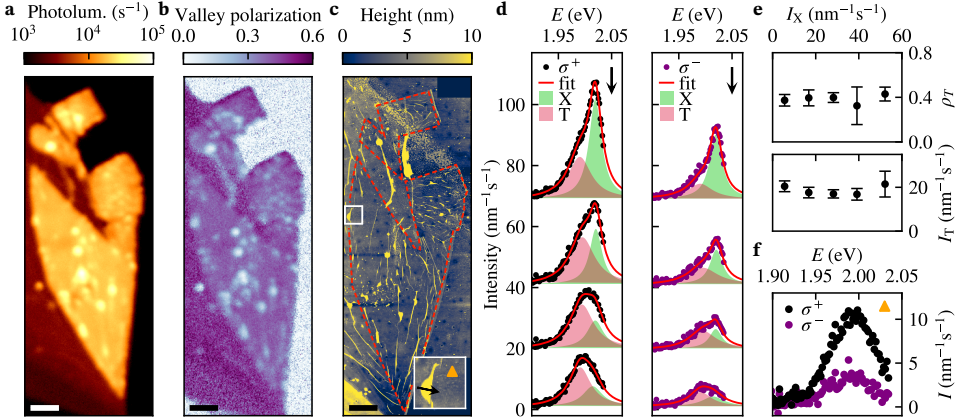


Figure 3.3. **Spatial characterization of the exciton and trion emission of a chemically-doped monolayer WS₂ on an yttrium iron garnet (YIG) substrate.** (a, b) Spatial maps of the photoluminescence (a) and valley polarization (b) under near-resonant excitation (594 nm, 200 μ W) after chemical doping. The sample was submerged in liquid anisole for 12 hours at room temperature and vacuum-annealed for 6 hours (400 $^{\circ}$ C, <1 mTorr) to remove contaminants. Multilayer areas of the flake surrounding the monolayer are identified by their low brightness due to their indirect bandgap [2] and large polarization [31]. (c) Atomic force microscope image of the sample. Comparison with (a, b) shows that spots with increased photoluminescence and reduced valley polarization occur at wrinkles of the monolayer. (d) Emission spectra at different locations close to a wrinkle indicated by the black arrow in the inset of (c). Lorentzian fits of the trion (red) and exciton (green) resonances reveal the simultaneous presence of trion and exciton emission at wrinkles. (e) Average trion brightness and valley polarization plotted against the local exciton photoluminescence at different wrinkles. (f) Typical σ^+ and σ^- emission spectra of trions in flat parts of the flake, obtained at the location indicated by the triangle in the inset of (c), corresponding to a valley polarization of about 40%. Scale bar: 5 μ m.

is strong.

Strongly valley-polarized excitons are expected in the limit of large doping (Fig. 3.4b). For our flakes, doping is strongest in the flat areas away from the wrinkles as reflected by the low photoluminescence in these areas. Because we are unable to spectrally distinguish the weak exciton emission from the dominant trion emission in these areas, we analyse the valley polarization of the integrated photoluminescence spectrum using our APD. When plotting the local valley polarization against the local photoluminescence (Fig. 3.4c), we observe a non-monotonous behaviour with a maximum at low photoluminescence. According to our model, this maximum occurs because the exciton valley polarization (green line in Fig. 3.4b) increases with doping while the exciton photoluminescence vanishes. As a result, the trion contribution (red line) starts to dominate the total signal (black line). These results highlight that the exciton valley polarization becomes large because of the rapid conversion into trions.

On wrinkles, we observe that the excitons have a lower valley polarization than the trions (Fig. 3.3d). In contrast, our model predicts that the local valley polarization of the trions cannot exceed that of the excitons even at low doping (Fig. 3.4b, Supplemen-

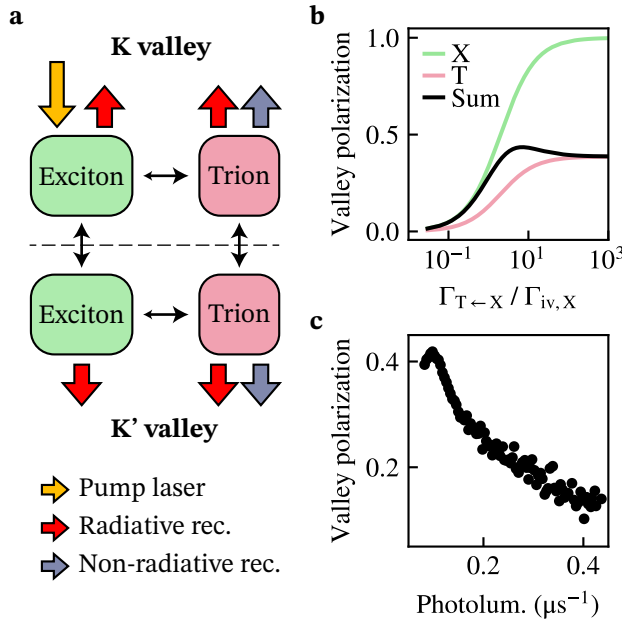


Figure 3.4. **Doping-controlled valley polarization of excitons and trions.** (a) Schematic depiction of the rate equation model used to describe the optically detected valley polarization. Excitons are created by valley-selective optical excitation, after which they can decay radiatively, scatter between the valleys at a rate $\Gamma_{iv,X}$, or change into trions at a doping-controlled rate Γ_{T-X} . The trions can scatter between the valleys, decay radiatively or non-radiatively, and change back into excitons. (b) Valley polarization of excitons, trions, and their photoluminescence-weighted average as a function of $\Gamma_{T-X}/\Gamma_{iv,X}$ calculated using the rate equation model shown in (a). (c) Valley polarization versus photoluminescence extracted by averaging data from individual pixels in the monolayer area of Fig. 3.3a-b.

tary Section 3.5). This indicates that the observed spectra on wrinkles are a result of spatial averaging over less-doped, wrinkled areas with a strong exciton contribution and strongly-doped surrounding areas with a dominant trion emission (Supplementary Section 3.5). Such averaging is expected from the diffraction-limited optical spotsize of our confocal microscope (diameter: ~ 500 nm).

3.4. CONCLUSION

In summary, we have demonstrated that chemical doping with anisole is an effective method to generate highly valley-polarized excitons and trions in monolayer WS₂ at room temperature. The emission spectrum of as-prepared monolayers is characterized by a bright exciton resonance that exhibits no valley polarization. After chemical doping, a trion resonance appears with a polarization up to 40%. The doping is less efficient at wrinkled areas, which are marked by the simultaneous presence of exciton and trion resonances. The excitons have a robust valley polarization, which we attribute to the

rapid conversion into trions induced by the doping. A rate equation model captures the quenching-induced valley polarization, indicating the presence of excitons with a higher polarization than trions in the limit of maximal quenching. Our results shed light on the effect of the doping-controlled conversion between excitons and trions on the valley polarization in single layers of WS_2 and highlight that valley polarization by itself does not necessarily reflect optovalleytronic potential, since a strongly-quenched carrier lifetime and emission may constrain its application in devices.

ACKNOWLEDGEMENTS

The authors thank N. Papadopoulos, M. Lee for their advice on fabrication and I. Komen, L. Kuipers for experimental help and discussions.

FUNDING

This work was supported by the Netherlands Organisation for Scientific Research (NWO / OCW), as part of the Frontiers of Nanoscience program, through the Startup grant 740.018.012, and by the Kavli Institute of Nanoscience Delft.

AUTHOR CONTRIBUTIONS STATEMENT

J.C. and **T.S.** conceived the experiment. **M.B.** fabricated the samples. **J.C.** and **M.B.** conducted the experiment and analysed the results. **M.B.** created the figures. **J.C.** and **T.S.** wrote the manuscript. All authors reviewed the manuscript. **T.S.** supervised the project.

3.5. SUPPLEMENTARY INFORMATION

EXPERIMENTAL SETUP.

A schematic overview of the setup is presented in Chapter 2. Our samples are excited by a lowpass-filtered 594 nm OBIS laser (Coherent) of which we control the polarization using achromatic half- and quarter-wave plates (Thorlabs). A 50X, NA=0.95 (Olympus) objective focuses the laser to a diffraction-limited spot and collects the emission from the sample. The emission is separated from the excitation by a 10:90 beam splitter (R:T, Thorlabs). The handedness of the excitation and detection is controlled by a second quarter-wave plate, which projects both circular polarizations of the photoluminescence onto two orthogonal linear polarizations of which we select one with the polarizer. The emission is longpass filtered (2x Semrock, BLP01-594R-25) to eliminate the laser reflection. We use a mirror on a computer-controlled flipmount to switch between a fiber-coupled spectrometer (Kymera 193 spectrograph with a cooled iVac 324 CCD detector) and an avalanche photodiode (APD, Laser Components) for the detection of the photoluminescence. Before the emission is detected by the APD, it is filtered with a pinhole and bandpass filter (Semrock, FF01-623/32-25). The sample is mounted on an xyz-piezo stage (Mad City Labs, Nano-3D200FT) to allow nanoscale positioning of the sample. An ADwin Gold II was used to control the piezo stage and read out the APD. The grating in the Raman microscope (Renishaw inVia Reflex, 514 nm laser) had 1600 lines per mm, giving a spectral resolution of $\sim 2 \text{ cm}^{-1}$ per pixel. All measurements were performed at room temperature.

SAMPLE FABRICATION.

The WS₂ monolayers were exfoliated from commercially-purchased bulk crystals (HQ Graphene) on PDMS stamps, and were transferred to Si/SiO₂ and YIG chips. The 245 nm thick YIG films were grown on a gadolinium gallium garnet (GGG) substrate via liquid phase epitaxy and were purchased at Matesy gmbh. YIG samples were sonicated in acetone and cleaned in IPA before stamping.

CHEMICAL POTENTIAL AND HARDNESS

	WS ₂ monolayer [23]	Anisole [22]
Chemical potential μ (eV)	-4.79	-3.17
Chemical hardness η (eV)	2.64	4.88

Table 3.1. **Chemical potential and chemical hardness of anisole and monolayer WS₂ calculated using density functional theory.**

SUPPORTING DATA

REPRODUCIBILITY OF QUENCHING-INDUCED VALLEY POLARIZATION

We repeat the anisole treatment as specified in the main text on five more WS₂ monolayer flakes, presented in Figure 3.5, all of which show a strong dimming and emergent

room-temperature valley polarization after doping. Of these, three have a Si/SiO₂ substrate and two an yttrium iron garnet (YIG) substrate. Variations in photoluminescence and valley polarization between the flakes are attributed to differences in defect density and unintentional doping prior to the treatment.

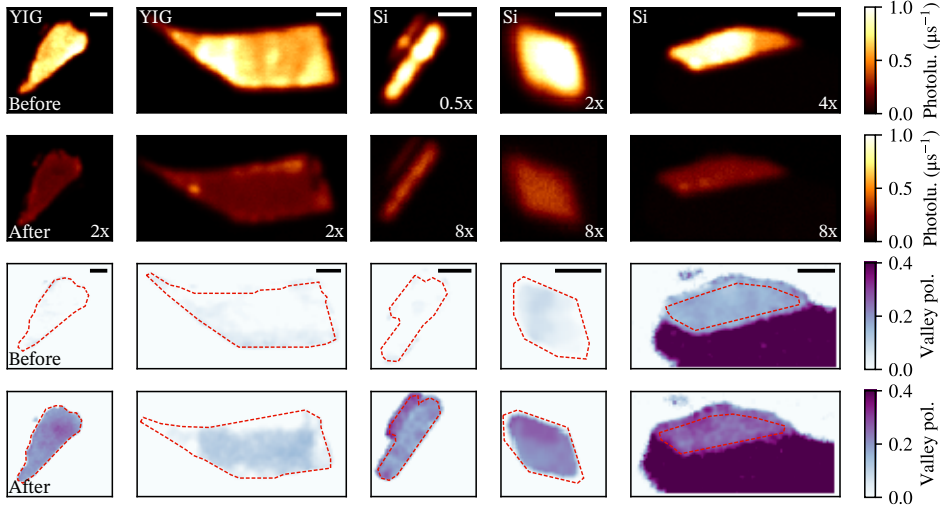


Figure 3.5. **Additional photoluminescence and valley polarization maps of WS₂ monolayer flakes before and after anisole treatment.** The first two monolayers were stamped on yttrium iron garnet (YIG) and the remaining three on Si/SiO₂. All maps were made using a 594 nm excitation laser at a power of 4 μ W before the doping and 40 μ W after doping. Scale bar: 2 μ m.

EMERGENCE OF EXCITON EMISSION AT WRINKLES

Here, we plot additional σ_+ emission spectra along spatial traces over wrinkles in the WS₂ flake presented in Fig. 3.3. As demonstrated in Figure 3.7, each trace is characterized by the emergence of a strong exciton resonance at the center of the wrinkle, highlighted by the asymmetry of the spectra. The central wavelength of both trions and excitons varies slightly over the different wrinkles, which we attribute to local variations in strain [32, 33] and doping [14]. From this, we extract spatially varying energy splittings between the excitons and trions within the range of 22 meV – 32 meV, in agreement with reported literature values [34]. Additional σ_- emission spectra were taken along the same spatial traces to determine the valley polarization and brightness of exciton and trion resonances in wrinkles, which were plotted in Fig. 3.3e of the main text.

MODELLING DOPING-CONTROLLED VALLEY DYNAMICS

MODEL OVERVIEW

To calculate the expected valley polarization as a function of doping level we extend the rate equation model of Lien *et al.* [10] by incorporating the valleys (Figure 3.8). The

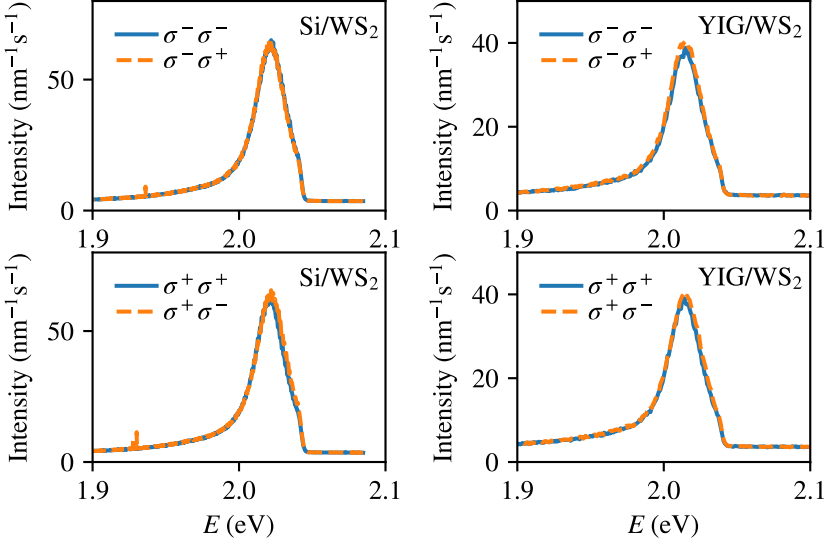


Figure 3.6. **Absence of valley polarization in untreated WS₂ monolayers.** $\sigma_{+(-)}$ emission spectra under circular near-resonant excitation ($E = 2.087$ eV, $\lambda = 594$ nm) of untreated WS₂ monolayers on Si/SiO₂ and YIG substrates. The overlapping spectra confirms the absence of valley polarization. A slight cut-off is visible at 2.04 eV due to longpass filtering of the excitation laser.

model assumes that excitons are excited in the K valley at a rate Γ_K , scatter to the K' valley at a rate $\Gamma_{iv,X}$, decay radiatively at a rate $\Gamma_{r,X}$, or decay to trions via Γ_{T-X} while preserving their valley. The trions then scatter between the valleys at a rate $\Gamma_{iv,T}$, decay radiatively via $\Gamma_{r,T}$, non-radiatively via Γ_{nr} , or back to excitons via Γ_{X-T} while preserving their valley. A law of mass-action states that Γ_{T-X} is linearly proportional to the electron density n_e , while Γ_{X-T} is fixed [10–12]. As described in the main text, we expect that Γ_{T-X} is spatially fluctuating due to local variations in doping level. Since the samples are strongly doped, we assume that Γ_{T-X} is much larger than any other non-radiative decay rate of the excitons, which we therefore neglect.

We define the probability for the system to be in the ground state as G , the probability to have formed an exciton in the K^(*v*) valley as $X_{K^{(v)}}$, and the probability to have formed a trion in the K^(*v*) valley as $T_{K^{(v)}}$. The time evolution of the system is then governed by the following master equations:

$$\frac{dG}{dt} = -\Gamma_K G + \Gamma_{r,X}(X_K + X_{K'}) + (\Gamma_{r,T} + \Gamma_{nr})(T_K + T_{K'}) = 0, \quad (3.3)$$

$$\frac{dX_K}{dt} = \Gamma_K G - (\Gamma_{iv,X} + \Gamma_{T-X} + \Gamma_{r,X})X_K + \Gamma_{iv,X}X_{K'} + \Gamma_{X-T}T_K = 0, \quad (3.4)$$

$$\frac{dX_{K'}}{dt} = -(\Gamma_{iv,X} + \Gamma_{T-X} + \Gamma_{r,X})X_{K'} + \Gamma_{iv,X}X_K + \Gamma_{X-T}T_{K'} = 0, \quad (3.5)$$

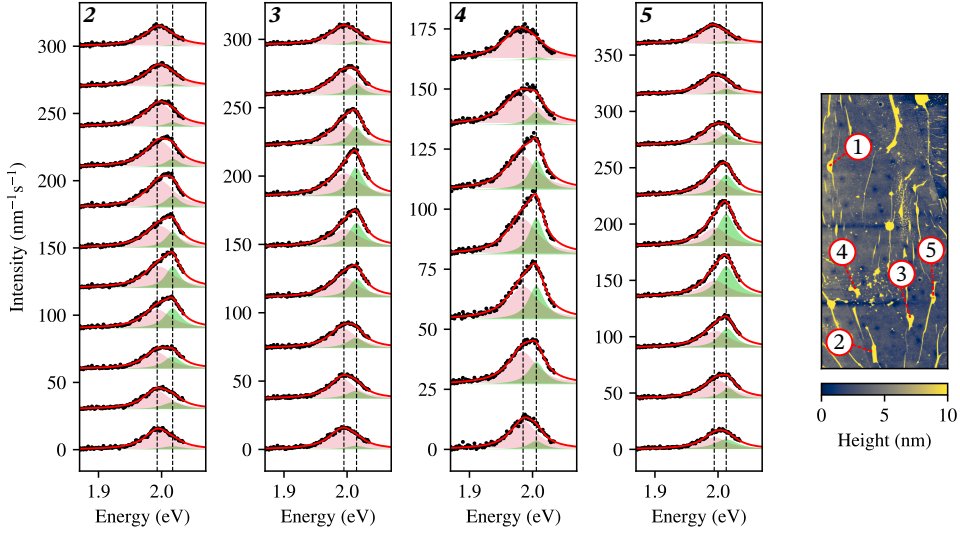


Figure 3.7. **Recurrent emergence of exciton emission at wrinkles.** σ_+ emission spectra are plotted along spatial traces over multiple wrinkles on the sample of Fig. 3.3 of the main text. Labels above the spectra correspond to wrinkles in the atomic force microscope map in the right panel. Emission spectra at label 1 are depicted in Fig. 3.3c of the main text. All spectra were taken at near-resonance excitation ($E = 2.087$ eV, $\lambda = 594$ nm, 40 μ W).

$$\frac{dT_K}{dt} = -(\Gamma_{iv,T} + \Gamma_{X \leftarrow T} + \Gamma_{nr} + \Gamma_{r,T})T_K + \Gamma_{iv,T}T_{K'} + \Gamma_{T \leftarrow X}X_K = 0, \quad (3.6)$$

$$\frac{dT_{K'}}{dt} = -(\Gamma_{iv,T} + \Gamma_{X \leftarrow T} + \Gamma_{nr} + \Gamma_{r,T})T_{K'} + \Gamma_{iv,T}T_K + \Gamma_{T \leftarrow X}X_{K'} = 0, \quad (3.7)$$

$$G + X_K + X_{K'} + T_K + T_{K'} = 1. \quad (3.8)$$

Here, we set the time derivatives to zero to consider a steady state and finally normalize the probabilities in the last line.

CALCULATION OF THE TRION AND EXCITON VALLEY POLARIZATION

The valley polarization of the exciton and trion are respectively denoted by ρ_X and ρ_T , and are defined as the normalized asymmetry in valley occupation,

$$\rho_X = \frac{X_K - X_{K'}}{X_K + X_{K'}}, \quad (3.9)$$

$$\rho_T = \frac{T_K - T_{K'}}{T_K + T_{K'}}.$$

By combining Eqs. 3.6-3.9 we derive a relation between ρ_X and ρ_T , demonstrating that the valley polarization of excitons is always larger than that of trions [35]

$$\rho_T = \frac{\Gamma_{X \leftarrow T} + \Gamma_{nr} + \Gamma_{r,T}}{2\Gamma_{iv,T} + \Gamma_{X \leftarrow T} + \Gamma_{nr} + \Gamma_{r,T}} \rho_X. \quad (3.10)$$

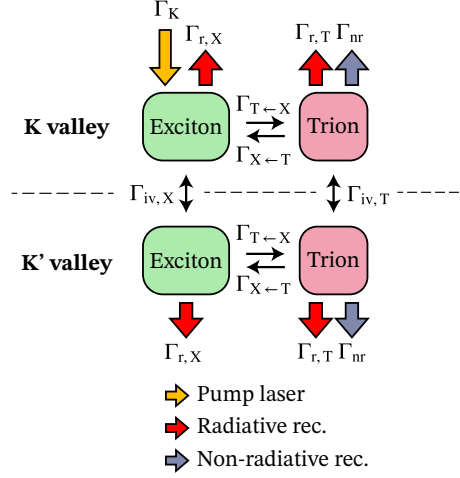


Figure 3.8. **Schematic overview of the rate equation model.** The closed system can either be in the ground state, or be an exciton or trion in the K or K' valley. By considering its steady state solutions, we model the valley polarization of excitons and trions under continuous-wave illumination.

We can express ρ_X in terms of the rates by combining Eqs. 3.3-3.8,

$$\rho_X = \frac{\frac{\Gamma_{r,X}}{2\Gamma_{iv,X}} + \frac{\Gamma_{r,T} + \Gamma_{nr}}{2(\Gamma_{X-T} + \Gamma_{nr} + \Gamma_{r,T})} \frac{\Gamma_{T-X}}{\Gamma_{iv,X}}}{1 + \frac{\Gamma_{r,X}}{2\Gamma_{iv,X}} + \frac{2\Gamma_{iv,T} + \Gamma_{nr} + \Gamma_{r,T}}{2(2\Gamma_{iv,T} + \Gamma_{X-T} + \Gamma_{nr} + \Gamma_{r,T})} \frac{\Gamma_{T-X}}{\Gamma_{iv,X}}} \approx \frac{\frac{\Gamma_{nr}}{2(\Gamma_{X-T} + \Gamma_{nr})} \frac{\Gamma_{T-X}}{\Gamma_{iv,X}}}{1 + \frac{2\Gamma_{iv,T} + \Gamma_{nr}}{2(2\Gamma_{iv,T} + \Gamma_{X-T} + \Gamma_{nr})} \frac{\Gamma_{T-X}}{\Gamma_{iv,X}}}. \quad (3.11)$$

Since the radiative decay rates are known to be low at room temperature [10, 36, 37], we assumed in the last step that $\Gamma_{iv,X} \gg \Gamma_{r,X}$ and $\Gamma_{nr} \gg \Gamma_{r,T}$. We thus conclude that the valley polarization of the excitons is parametrized by $\frac{\Gamma_{T-X}}{\Gamma_{iv,X}}$, and that it reaches a maximum ρ_X^{\max} when $\Gamma_{T-X} \gg \Gamma_{iv,X}$

$$\rho_X^{\max} = \frac{\Gamma_{nr}(2\Gamma_{iv,T} + \Gamma_{X-T} + \Gamma_{nr})}{(\Gamma_{nr} + 2\Gamma_{iv,T})(\Gamma_{nr} + \Gamma_{X-T})}. \quad (3.12)$$

ANALYSIS OF THE VALLEY POLARIZATION VERSUS PHOTOLUMINESCENCE

Using Eqs. 3.6, 3.7, and 3.11 we can calculate the valley polarization ρ as it is detected by the avalanche photodiode (APD) in the experiment, by summing the exciton and trion emission

$$\begin{aligned} \rho &= \frac{\Gamma_{r,T}(T_K - T_{K'}) + \Gamma_{r,X}(X_K - X_{K'})}{\Gamma_{r,T}(T_K + T_{K'}) + \Gamma_{r,X}(X_K + X_{K'})} \\ &= \frac{\frac{\Gamma_{r,T}}{\Gamma_{r,X}(2\Gamma_{iv,T} + \Gamma_{X-T} + \Gamma_{nr})} \Gamma_{T-X} + 1}{\frac{\Gamma_{r,T}}{\Gamma_{r,X}(2\Gamma_{iv,T} + \Gamma_{X-T} + \Gamma_{nr})} \Gamma_{T-X} + 1} \frac{\frac{\Gamma_{nr}}{2\Gamma_{iv,X}(\Gamma_{X-T} + \Gamma_{nr})} \Gamma_{T-X}}{\frac{2\Gamma_{iv,T} + \Gamma_{nr}}{2\Gamma_{iv,X}(2\Gamma_{iv,T} + \Gamma_{X-T} + \Gamma_{nr})} \Gamma_{T-X} + 1}. \end{aligned} \quad (3.13)$$

To find a relation between the valley polarization and total photoluminescence $I = I_T + I_X$, we express I in terms of the rates by combining Eqs 3.3, 3.6-3.8, and find that it is inversely related to $\Gamma_{T \rightarrow X}$,

$$I = \alpha N (\Gamma_{r,T}(T_K + T_{K'}) + \Gamma_{r,X}(X_K + X_{K'})) \approx \alpha N \Gamma_K \left(\frac{\Gamma_{r,T}}{\Gamma_{nr}} + \frac{\Gamma_{r,X} \left(\frac{\Gamma_{X \rightarrow T}}{\Gamma_{nr}} + 1 \right)}{\Gamma_{T \rightarrow X}} \right), \quad (3.14)$$

where $0 < \alpha < 1$ represents the finite detection efficiency of the confocal microscope and N is the number of electrons in the system. To simplify this expression, we made use of the previous assumptions, and assumed that the system is weakly excited and strongly doped, such that Γ_K is small and $\Gamma_{T \rightarrow X} \gg \Gamma_{r,X}$. By inverting this expression and substituting it into Eq. 3.13, we find ρ as a function of I for a sample with a varying doping level,

$$\rho = \frac{a_0 I + 1}{b_0 I^2 + c_0 I}. \quad (3.15)$$

Here, the constants are given by

$$\begin{aligned} a_0 &= -\frac{\Gamma_{nr}}{2\alpha N \Gamma_K \Gamma_{iv,T} \Gamma_{r,T}} (2\Gamma_{iv,T} + \Gamma_{X \rightarrow T} + \Gamma_{nr}), \\ b_0 &= -\frac{\Gamma_{nr} \Gamma_{iv,X}}{\alpha^2 N^2 \Gamma_K^2 \Gamma_{r,X} \Gamma_{r,T} \Gamma_{iv,T}} (2\Gamma_{iv,T} + \Gamma_{X \rightarrow T} + \Gamma_{nr}), \\ c_0 &= -\frac{1}{2\alpha N \Gamma_K \Gamma_{iv,T} \Gamma_{r,T}} (\Gamma_{X \rightarrow T} + \Gamma_{nr}) (2\Gamma_{iv,T} + \Gamma_{nr}) - \frac{2\Gamma_{iv,X} \Gamma_{r,T}}{\Gamma_{r,X} \Gamma_{nr}} a_0. \end{aligned} \quad (3.16)$$

In agreement to our data, the valley polarization should thus be inversely related to the photoluminescence at high I

$$\rho \approx \frac{a_0}{b_0 I + c_0}. \quad (3.17)$$

This inverse relation is reinforced by the spatial averaging of our diffraction-limited optical spot (Supplementary Section 3.5). At low I , a local maximum in the valley polarization is experimentally observed, only if

$$\frac{\Gamma_{nr}}{2\Gamma_{r,T}} \left(\frac{\Gamma_{r,X}}{\Gamma_{iv,X}} - \frac{\Gamma_{r,T}}{\Gamma_{iv,T}} \right) + \frac{\Gamma_{r,X} \Gamma_{iv,T}}{\Gamma_{iv,X} \Gamma_{r,T}} - \frac{\Gamma_{X \rightarrow T}}{2\Gamma_{iv,T}} > 1. \quad (3.18)$$

This is only true, if $\frac{\Gamma_{r,X}}{\Gamma_{iv,X}} > \frac{\Gamma_{r,T}}{\Gamma_{iv,T}}$, provided that $\Gamma_{iv,T} \gg \Gamma_{X \rightarrow T}$. We conclude that relatively bright excitons with a significantly higher polarization than trions are required for the observation of a local maximum in the total valley polarization versus photoluminescence.

COMPARISON BETWEEN MODEL AND EXPERIMENT

To better assess the correspondence between the model and the experimental data in Fig. 3.4c of the main text, we make a basic estimate of the valley polarization using MoS₂ literature values for the radiative and non-radiative rates [10] ($1/\Gamma_{r,X} = 8$ ns, $1/\Gamma_{r,T} = 110$

ns and $1/\Gamma_{nr} = 50$ ps). For a rough approximation, we assume that $\Gamma_{X \rightarrow T}$ is much smaller than the other rates. As a result, the exciton valley polarization approaches unity at strong doping via Eq. 3.12, while the trion polarization is parametrized by $\Gamma_{iv,T}$ via Eq. 3.10. Following the experimental results in Figure 4c, we tune the trion polarization at maximal doping to about 40%, which gives $1/\Gamma_{iv,T} = 60$ ps. At this stage only $\Gamma_{iv,X}$ remains as a free parameter and it determines whether the valley polarization has a local maximum as a function of photoluminescence via Eq. 3.18.

In Fig. 3.4b of the main text we demonstrate that for $1/\Gamma_{iv,X} = 10$ ps a small local maximum in valley polarization can be observed. In contrast, at an enhanced intervalley scattering of $1/\Gamma_{iv,X} = 2$ ps the local maximum disappears (Fig. 3.9, left panel), because $\frac{\Gamma_{r,X}}{\Gamma_{iv,X}} < \frac{\Gamma_{r,T}}{\Gamma_{iv,T}}$. To compare the model and experiment, we plot the valley polarization versus photoluminescence using equation 13 for different values of $\Gamma_{iv,X}$ (Fig. 3.9, right panel). We note that we obtain similar plots when increasing $\Gamma_{X \rightarrow T}$, which merely lowers the exciton valley polarization below unity at strong doping and decreases the difference between the trion and exciton polarization, making the presence of a local maximum less likely.

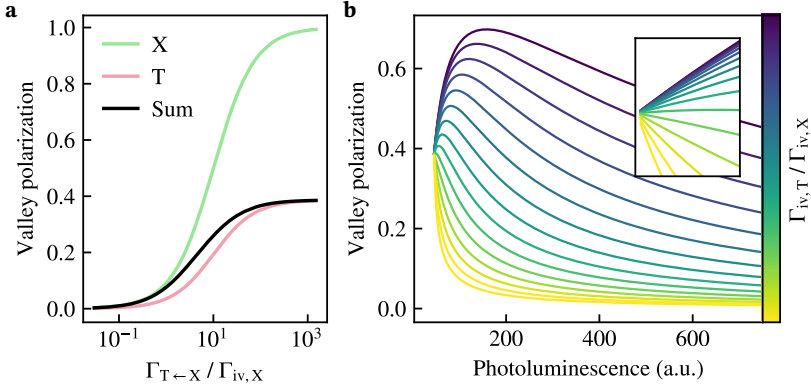


Figure 3.9. **Modelling valley polarization as a function of trion-to-exciton conversion and total luminescence.** (a) Modelled valley polarization versus $\Gamma_{T \leftarrow X} / \Gamma_{iv,X}$ using the same rates as in Fig. 3.4b of the main text, demonstrating that a different choice of $\Gamma_{iv,X}$ can yield absence of a local maximum. (b) Simulated valley polarization versus photoluminescence using the same rates as in (a), but with logarithmically spaced values for $1/\Gamma_{iv,X}$ ranging between 1 and 100 ps. The inset highlights the presence (absence) of a local maximum at low brightness for low (high) $\Gamma_{iv,X}$.

SPATIAL AVERAGING OF VALLEY POLARIZATION

In this section we calculate the valley polarization versus photoluminescence when averaging the emission of two regions with different doping levels. In particular, we consider a strongly-doped region with weak and highly polarized trion emission and a weakly-doped region with strong and weakly polarized exciton emission, similar to the emission detected on wrinkles in Fig. 3.3 of the main text. The emission from both regions is collected by our diffraction-limited optical spot, leading to a spatially-averaged valley

polarization of

$$\rho = \frac{\Gamma_{r,T}(T_K - T_{K'}) + \Gamma_{r,X}(X_K - X_{K'})}{\Gamma_{r,T}(T_K + T_{K'}) + \Gamma_{r,X}(X_K + X_{K'})} = \frac{\rho_T I_T + \rho_X I_X}{I_T + I_X}. \quad (3.19)$$

Here the valley polarization of the trions ρ_T and excitons ρ_X are constant and their intensities I_T and I_X vary with the area of the weakly-doped region compared to the optical spotsize ($0 \leq A \leq 1$), according to

$$\begin{aligned} I_X &= A \cdot I_{0,X}, \\ I_T &= (1 - A) \cdot I_{0,T}. \end{aligned} \quad (3.20)$$

Here $I_{0,T}$ and $I_{0,X}$ are constants that indicate the trion and exciton photoluminescence when their associated regions would fill an entire optical spot. The total photoluminescence is given by

$$I = I_T + I_X = I_{0,T} + A(I_{0,X} - I_{0,T}). \quad (3.21)$$

By substituting this expression into Eq. 3.19, we find that the ρ is inversely related to I for varying A

$$\rho = \frac{\rho_X I_{0,X} - \rho_T I_{0,T}}{I_{0,X} - I_{0,T}} + \frac{I_{0,X} I_{0,T} (\rho_T - \rho_X)}{I_{0,X} - I_{0,T}} \cdot \frac{1}{I}. \quad (3.22)$$

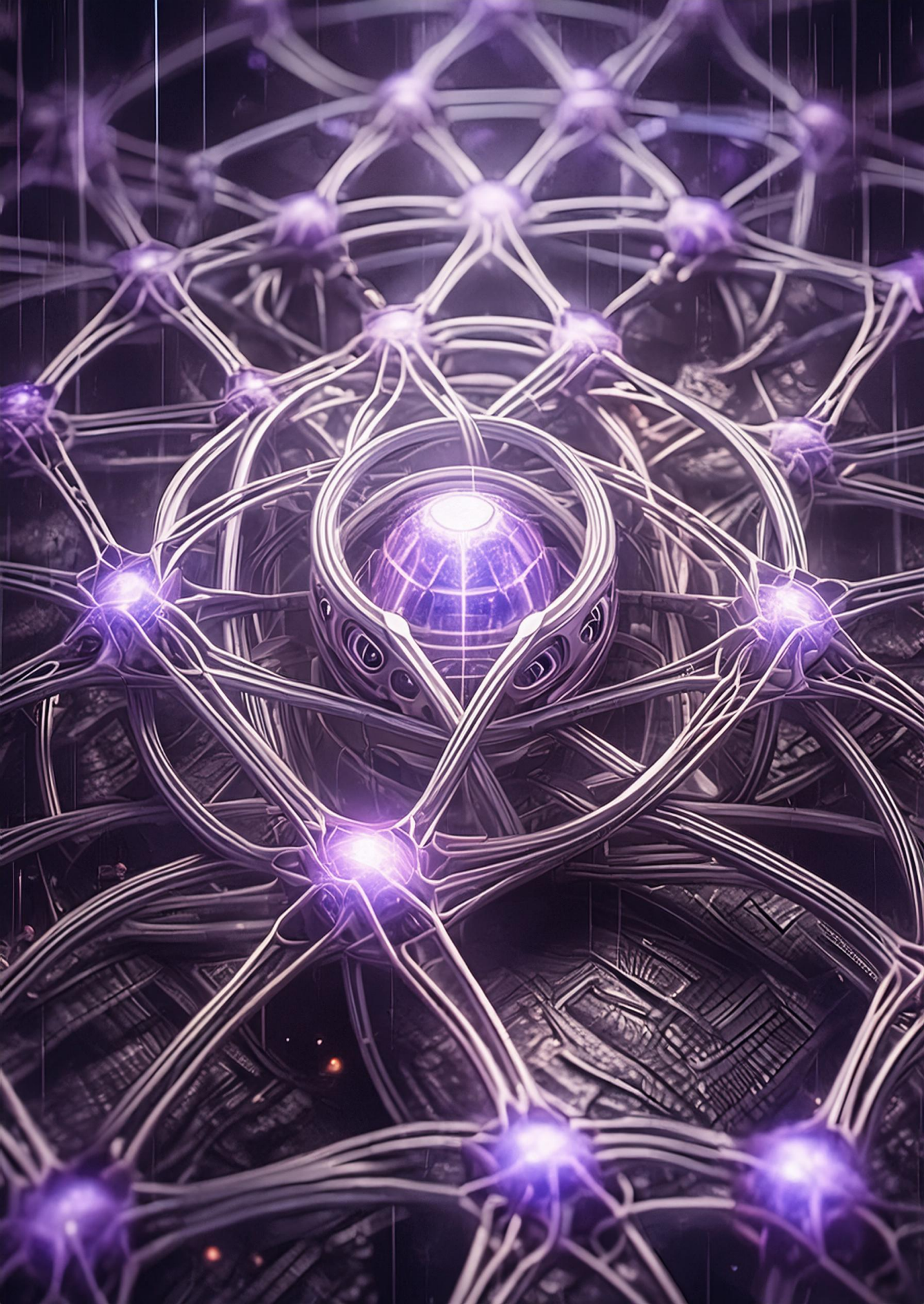
This is a similar inverse relation as the one in Eq. 3.17 for a varying doping level. Note that this relation is exclusively inverse, and cannot explain any local maximum. However, it is likely that the inverse decay of valley polarization in Fig. 3.4c of the main text is a combination of 1) spatial averaging due to a diffraction limited optical spot and 2) local variations in doping.

REFERENCES

- [1] K. F. Mak *et al.* “Atomically Thin MoS₂: A New Direct-Gap Semiconductor”. *Phys. Rev. Lett.* 105.13 (Sept. 2010), p. 136805. DOI: [10.1103/PhysRevLett.105.136805](https://doi.org/10.1103/PhysRevLett.105.136805).
- [2] A. Splendiani *et al.* “Emerging Photoluminescence in Monolayer MoS₂”. *Nano Letters* 10.4 (Apr. 2010), pp. 1271–1275. ISSN: 1530-6984. DOI: [10.1021/nl903868w](https://doi.org/10.1021/nl903868w).
- [3] K. F. Mak *et al.* “Control of valley polarization in monolayer MoS₂ by optical helicity”. *Nature Nanotechnology* 7.8 (2012), pp. 494–498. ISSN: 17483395. DOI: [10.1038/nnano.2012.96](https://doi.org/10.1038/nnano.2012.96).
- [4] T. Cao *et al.* “Valley-selective circular dichroism of monolayer molybdenum disulfide”. *Nature Communications* 3.May (2012). ISSN: 20411723. DOI: [10.1038/ncomms1882](https://doi.org/10.1038/ncomms1882).
- [5] H. Zeng *et al.* “Valley polarization in MoS₂ monolayers by optical pumping”. *Nature Nanotechnology* 7.8 (2012), pp. 490–493. ISSN: 1748-3395. DOI: [10.1038/nnano.2012.95](https://doi.org/10.1038/nnano.2012.95).
- [6] T. Mueller *et al.* “Exciton physics and device application of two-dimensional transition metal dichalcogenide semiconductors”. *npj 2D Materials and Applications* 2.1 (2018), p. 29. ISSN: 2397-7132. DOI: [10.1038/s41699-018-0074-2](https://doi.org/10.1038/s41699-018-0074-2).
- [7] K. M. McCreary *et al.* “Understanding Variations in Circularly Polarized Photoluminescence in Monolayer Transition Metal Dichalcogenides”. *ACS Nano* 11.8 (Aug. 2017), pp. 7988–7994. ISSN: 1936-0851. DOI: [10.1021/acsnano.7b02554](https://doi.org/10.1021/acsnano.7b02554).
- [8] K. F. Mak *et al.* “Light–valley interactions in 2D semiconductors”. *Nature Photonics* 12.8 (2018), pp. 451–460. ISSN: 1749-4893. DOI: [10.1038/s41566-018-0204-6](https://doi.org/10.1038/s41566-018-0204-6).
- [9] J. R. Schaibley *et al.* “Valleytronics in 2D materials”. *Nature Reviews Materials* 1.11 (2016). ISSN: 20588437. DOI: [10.1038/natrevmats.2016.55](https://doi.org/10.1038/natrevmats.2016.55).
- [10] D. H. Lien *et al.* “Electrical suppression of all nonradiative recombination pathways in monolayer semiconductors”. *Science* 364.6439 (2019), pp. 468–471. ISSN: 10959203. DOI: [10.1126/science.aaw8053](https://doi.org/10.1126/science.aaw8053).
- [11] J. S. Ross *et al.* “Electrical control of neutral and charged excitons in a monolayer semiconductor”. *Nature Communications* 4.1 (2013), p. 1474. ISSN: 2041-1723. DOI: [10.1038/ncomms2498](https://doi.org/10.1038/ncomms2498).
- [12] J. Siviniant *et al.* “Chemical equilibrium between excitons, electrons, and negatively charged excitons in semiconductor quantum wells”. *Phys. Rev. B* 59.3 (Jan. 1999), pp. 1602–1604. DOI: [10.1103/PhysRevB.59.1602](https://doi.org/10.1103/PhysRevB.59.1602).

- [13] P. H. L. *et al.* “Electrical and Chemical Tuning of Exciton Lifetime in Monolayer MoS₂ for Field-Effect Transistors”. *ACS Applied Nano Materials* 3.1 (Jan. 2020), pp. 641–647. DOI: [10.1021/acsanm.9b02170](https://doi.org/10.1021/acsanm.9b02170).
- [14] K. F. Mak *et al.* “Tightly bound trions in monolayer MoS₂”. *Nature Materials* 12.3 (2013), pp. 207–211. ISSN: 1476-4660. DOI: [10.1038/nmat3505](https://doi.org/10.1038/nmat3505).
- [15] A. O. A. Tanoh *et al.* “Enhancing Photoluminescence and Mobilities in WS₂ Monolayers with Oleic Acid Ligands”. *Nano Letters* 19.9 (Sept. 2019), pp. 6299–6307. ISSN: 1530-6984. DOI: [10.1021/acs.nanolett.9b02431](https://doi.org/10.1021/acs.nanolett.9b02431).
- [16] Y. Wang *et al.* “Doping of Monolayer Transition-Metal Dichalcogenides via Physisorption of Aromatic Solvent Molecules”. *The Journal of Physical Chemistry Letters* 10.3 (Feb. 2019), pp. 540–547. DOI: [10.1021/acs.jpcllett.8b03697](https://doi.org/10.1021/acs.jpcllett.8b03697).
- [17] M. Amani *et al.* “Near-unity photoluminescence quantum yield in MoS₂”. *Science* 350.6264 (2015), pp. 1065–1068. ISSN: 0036-8075. DOI: [10.1126/science.aad2114](https://doi.org/10.1126/science.aad2114).
- [18] N. Peimyoo *et al.* “Chemically Driven Tunable Light Emission of Charged and Neutral Excitons in Monolayer WS₂”. *ACS Nano* 8.11 (Nov. 2014), pp. 11320–11329. ISSN: 1936-0851. DOI: [10.1021/nn504196n](https://doi.org/10.1021/nn504196n).
- [19] S. Mouri *et al.* “Tunable Photoluminescence of Monolayer MoS₂ via Chemical Doping”. *Nano Letters* 13.12 (Dec. 2013), pp. 5944–5948. ISSN: 1530-6984. DOI: [10.1021/nl403036h](https://doi.org/10.1021/nl403036h).
- [20] S. Tongay *et al.* “Broad-Range Modulation of Light Emission in Two-Dimensional Semiconductors by Molecular Physisorption Gating”. *Nano Letters* 13.6 (June 2013), pp. 2831–2836. ISSN: 1530-6984. DOI: [10.1021/nl401117z](https://doi.org/10.1021/nl401117z).
- [21] R. G. Pearson. “The electronic chemical potential and chemical hardness”. *Journal of Molecular Structure: THEOCHEM* 255 (1992), pp. 261–270. ISSN: 0166-1280. DOI: [https://doi.org/10.1016/0166-1280\(92\)85014-C](https://doi.org/10.1016/0166-1280(92)85014-C).
- [22] R. L. Camacho-mendoza *et al.* “On the interaction of anisole and thioanisole derivatives with gold clusters studied by DFT”. *Computational and Theoretical Chemistry* 1126. February (2018), pp. 54–64. ISSN: 2210-271X. DOI: [10.1016/j.comptc.2018.01.017](https://doi.org/10.1016/j.comptc.2018.01.017).
- [23] H. L. Zhuang *et al.* “Computational Search for Single-Layer Transition-Metal Dichalcogenide Photocatalysts”. *The Journal of Physical Chemistry C* 117.40 (Oct. 2013), pp. 20440–20445. ISSN: 1932-7447. DOI: [10.1021/jp405808a](https://doi.org/10.1021/jp405808a).
- [24] K. M. McCreary *et al.* “The Effect of Preparation Conditions on Raman and Photoluminescence of Monolayer WS₂”. *Scientific Reports* 6.1 (2016), p. 35154. ISSN: 2045-2322. DOI: [10.1038/srep35154](https://doi.org/10.1038/srep35154).
- [25] A. T. Hanbicki *et al.* “Anomalous temperature-dependent spin-valley polarization in monolayer WS₂”. *Scientific Reports* 6.1 (2016), p. 18885. ISSN: 2045-2322. DOI: [10.1038/srep18885](https://doi.org/10.1038/srep18885).
- [26] A. Kurzmann *et al.* “Auger Recombination in Self-Assembled Quantum Dots: Quenching and Broadening of the Charged Exciton Transition”. *Nano Letters* 16.5 (May 2016), pp. 3367–3372. ISSN: 1530-6984. DOI: [10.1021/acs.nanolett.6b01082](https://doi.org/10.1021/acs.nanolett.6b01082).

- [27] F. Zhang *et al.* “Carbon doping of WS₂ monolayers: Bandgap reduction and p-type doping transport”. *Science Advances* 5.5 (2019). DOI: [10.1126/sciadv.aav5003](https://doi.org/10.1126/sciadv.aav5003).
- [28] A. Berkdemir *et al.* “Identification of individual and few layers of WS₂ using Raman Spectroscopy”. *Scientific Reports* 3.1 (2013), p. 1755. ISSN: 2045-2322. DOI: [10.1038/srep01755](https://doi.org/10.1038/srep01755).
- [29] B. Peng *et al.* “Valley Polarization of Trions and Magnetoresistance in Heterostructures of MoS₂ and Yttrium Iron Garnet”. *ACS Nano* 11.12 (Dec. 2017), pp. 12257–12265. ISSN: 1936-0851. DOI: [10.1021/acsnano.7b05743](https://doi.org/10.1021/acsnano.7b05743).
- [30] A. Castellanos-Gomez *et al.* “Deterministic transfer of two-dimensional materials by all-dry viscoelastic stamping”. *2D Materials* 1.1 (Apr. 2014), p. 011002. ISSN: 2053-1583. DOI: [10.1088/2053-1583/1/1/011002](https://doi.org/10.1088/2053-1583/1/1/011002).
- [31] H. Su *et al.* “Anomalous enhancement of valley polarization in multilayer WS₂ at room temperature”. *Nanoscale* 9.16 (2017), pp. 5148–5154. DOI: [10.1039/C7NR00554G](https://doi.org/10.1039/C7NR00554G).
- [32] M. G. Harats *et al.* “Dynamics and efficient conversion of excitons to trions in non-uniformly strained monolayer WS₂”. *Nature Photonics* 14.5 (2020), pp. 324–329. ISSN: 1749-4893. DOI: [10.1038/s41566-019-0581-5](https://doi.org/10.1038/s41566-019-0581-5).
- [33] A. Castellanos-Gomez *et al.* “Local Strain Engineering in Atomically Thin MoS₂”. *Nano Letters* 13.11 (Nov. 2013), pp. 5361–5366. ISSN: 1530-6984. DOI: [10.1021/nl402875m](https://doi.org/10.1021/nl402875m).
- [34] A. A. Mitioğlu *et al.* “Optical manipulation of the exciton charge state in single-layer tungsten disulfide”. *Phys. Rev. B* 88.24 (Dec. 2013), p. 245403. DOI: [10.1103/PhysRevB.88.245403](https://doi.org/10.1103/PhysRevB.88.245403).
- [35] X. X. Zhang *et al.* “Gate-tunable spin waves in antiferromagnetic atomic bilayers”. *Nature Materials* 19.8 (2020), pp. 838–842. ISSN: 14764660. DOI: [10.1038/s41563-020-0713-9](https://doi.org/10.1038/s41563-020-0713-9). arXiv: [2001.04044](https://arxiv.org/abs/2001.04044).
- [36] C. Robert *et al.* “Exciton radiative lifetime in transition metal dichalcogenide monolayers”. *Phys. Rev. B* 93.20 (2016), p. 205423. DOI: [10.1103/PhysRevB.93.205423](https://doi.org/10.1103/PhysRevB.93.205423).
- [37] C. R. Zhu *et al.* “Exciton valley dynamics probed by Kerr rotation in WSe₂ monolayers”. *Phys. Rev. B* 90.16 (2014), p. 161302. DOI: [10.1103/PhysRevB.90.161302](https://doi.org/10.1103/PhysRevB.90.161302).



4

MAGNETIC IMAGING OF VAN DER WAALS INTERLAYER ANTIFERROMAGNET CrSBr

*"If something looks like brass and feels like brass
it is likely gold plated copper."*

NV ensemble magnetometry holds potential for the detection of small magnetic fields produced by two-dimensional magnets. Achieving optimal sensitivity and spatial resolution hinges on minimizing the sample-to-NV distance. Here, we demonstrate the quantum sensing potential of our diamond membranes by using them to spatially resolve magnetic stray fields from the 2D interlayer antiferromagnet CrSBr and extracting its monolayer magnetization and Néel temperature. Our precision placement of NV-ensemble sensors in direct contact with target materials enables quantitative analysis of a wide range of 2D magnets on arbitrary target substrates.

Parts of this chapter have been published in *npj 2D Mater Appl* 7, 62 (2023) by T.S. Ghiasi, **M. Borst**, S. Kurdi, B.G. Simon, I. Bertelli, C. Boix-Constant, S. Mañas-Valero, H.S.J. van der Zant and T. van der Sar, <https://doi.org/10.1038/s41699-023-00423-y>.

4.1. INTRODUCTION

The genesis of two-dimensional magnets and their inclusion in Van der Waals heterostructures holds tremendous promise for new physical phenomena, unexplored magnetic order and novel functionalities [1]. Essential to this exploration is the ability to detect the subtle magnetic moments and stray fields that these atomically-thin magnets produce. Among the methods that have proven successful in this endeavour, there are potent optical techniques such as magnetic circular dichroism, the magneto-optical Kerr effect [2–4], second harmonic generation [5–7] and magnetometry based on nitrogen-vacancy (NV) centers in diamond [8–17]. Here, NV-based magnetometry boasts high sensitivity, nanoscale precision from cryogenic temperatures to 600 K, and quantitative measurement of magnetic stray fields [18, 19]. A central challenge for achieving high spatial resolution and sensitivity with NV-ensembles is to achieve a minimal, well-defined sample-to-NV distance. While direct placement of large ($> \text{mm}^2$) diamond plates on the sample surface enables contact, due trapping of spurious particles between diamond and sample it typically yields at best \sim few μm standoff distance [20]. While exfoliation and fabrication of complex, few-layer Van der Waals devices directly on the diamond surface yields a minimal NV-sample distance, this is challenging and limits flexibility in adding on-chip circuitry.

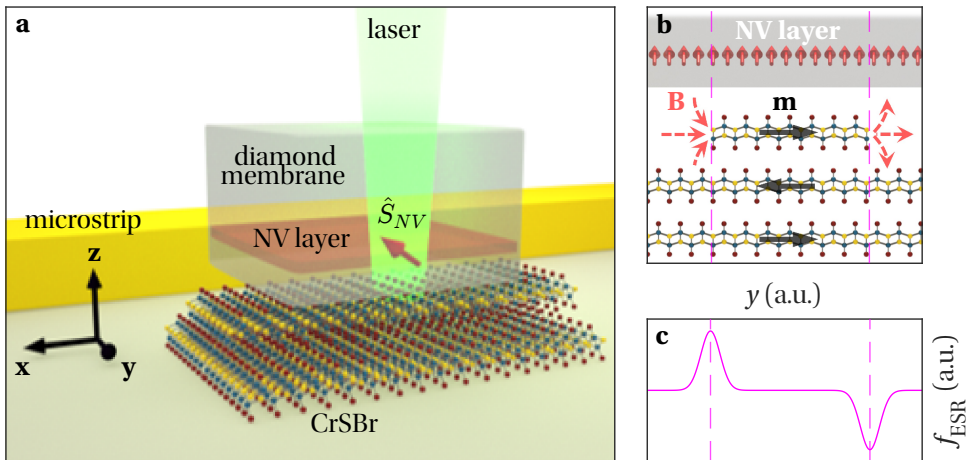


Figure 4.1. **Diamond membrane magnetometry of Van der Waals magnet CrSBr.** (a) Schematic overview of the experiment. A flake of CrSBr, with a diamond membrane with a shallow layer of NV ensembles on top, is placed next to a microstrip to drive the NV spins for sensing. A green laser is used to read out the sensor spins. (b) NV sensing schematic. Due to the interlayer antiferromagnetic coupling of CrSBr, odd-numbered steps in flake thickness will produce magnetic stray fields, detectable by the nearby NV layer. (c) The CrSBr stray field modulates the electron spin resonance frequency f_{ESR} , allowing a quantitative study of the CrSBr magnetization.

Here, we address these challenges by deterministically placing a small diamond membrane on a 2D material and substrate of choice, with micrometer lateral precision and rotational degree of freedom, by adapting commonly used 2D-assembly techniques [21]. By using small diamond membranes [22], we significantly reduce the probability to trap

unwanted particles between sample and diamond, facilitating direct contact. We demonstrate the utility of our membrane method by studying the two-dimensional Van der Waals magnet Chromium Sulfur Bromide (CrSBr), as schematically depicted in Fig. 4.1a. A flake of CrSBr is stamped near a microstrip that is used for driving NV spins in a small diamond membrane on top of the sample. Since CrSBr is a magnetic semiconductor with antiferromagnetic interlayer ordering [7], any step in material thickness with an odd number of atomic layers along a direction non-perpendicular to the magnetization \mathbf{m} produces magnetic stray fields (Fig. 4.1b). These stray fields locally shift the electron spin resonance frequency of nearby NV centers, enabling a quantitative study of magnetic properties of CrSBr (Fig. 4.1b-c).

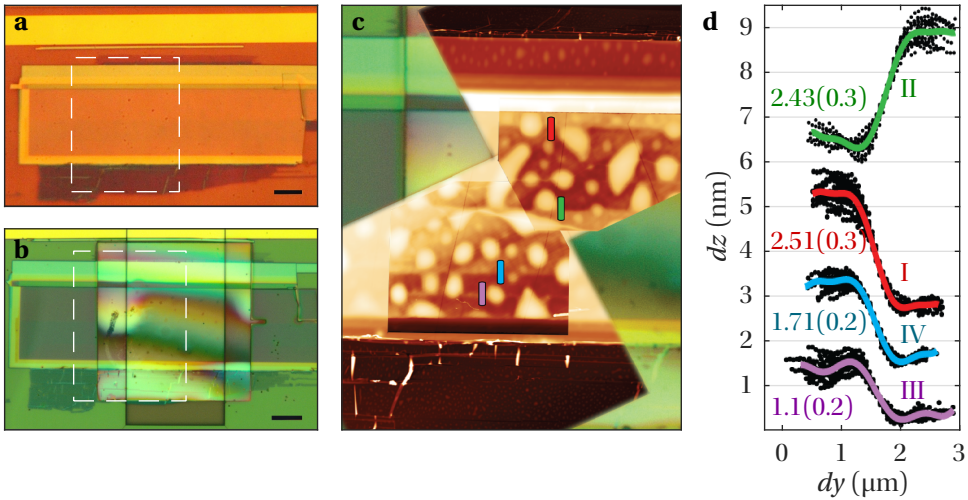


Figure 4.2. **Optical and atomic force microscopy of the CrSBr sample.** (a) Optical micrograph of the CrSBr flake next to the microstrip used for microwave driving of the NV spins. White box indicates the regions of interest displayed in (c). Scale bar: 10 μm . (b) Optical micrograph of the sample after membrane deposition, with a PMMA-removed window at its center. (c) Atomic force microscope map overlaid on the microscope image in (b). Bars indicate atomic steps in the CrSBr along \hat{y} underneath the diamond membrane. (d) Atomic force microscope traces along the bars in (c), revealing monolayer (III), bilayer (IV) and trilayer (I, II) steps in CrSBr thickness.

4.2. MEMBRANE-FACILITATED MAGNETOMETRY OF CrSBr

In order to identify regions of interest for NV measurements, we correlate the optical images of the CrSBr flake before (after) membrane deposition in Fig. 4.2a (Fig. 4.2b) with atomic force microscopy (AFM) maps (Fig. 4.2c). The CrSBr crystal is mostly uniform along \hat{x} , and has step-wise topography variations along \hat{y} . We identify four terrace-like steps along \hat{y} that are present underneath the diamond membrane, indicated by the dashes in Fig. 4.2c. AFM measurements reveal that these are monolayer (purple/III), bilayer (blue/IV), and trilayer (red/I, green/II) steps in flake thickness. As such, we investigate magnetic signatures at these locations. We first orient ourselves with a map

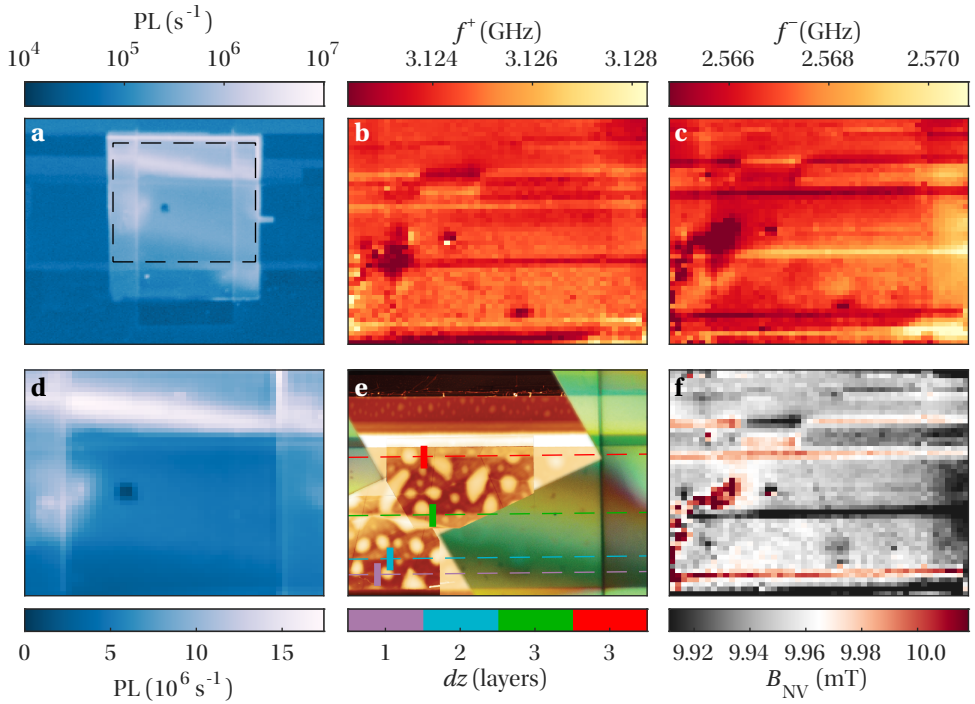


Figure 4.3. **Sensing of CrSBr magnetic stray fields.** (a) Photoluminescence map in the 600-800 nm band, showing the diamond membrane with holding bar. Black box indicates region of interest (ROI) displayed in panels (b-f). (b,c) Spatial maps of the measured NV electron spin resonance frequencies f^\pm for the transitions from $m_s = 0$ to $m_s = \pm 1$. (d) Photoluminescence map of the ROI. (e) Atomic force microscope map of the ROI, with guides to the eye for mono-, bi-, and trilayer steps. (f) The magnetic field B_{NV} along \hat{S}_{NV} , calculated from f^- and f^+ maps. Data in this figure are taken at $T = 80$ K.

of the photoluminescence of our sample in the NV-band of the spectrum (600-800 nm), as shown in Fig 4.3a. Here, we identify the membrane as the high-photoluminescence square with a small holding bar on the right. The black rectangle indicates the selected region for magnetometry, presented in the remaining panels.

To perform magnetometry, we cool down the sample to 80 K, and separate one family from the NV ensemble by applying a small bias field of $B_{\text{NV}} = 10.7$ mT along its quantization axis $\hat{S}_{\text{NV}} = \sin(\alpha)\hat{x} + \cos(\alpha)\hat{z}$, where $\alpha = 54.7$ deg. To understand how the field along this vector is modulated by the CrSBr stray fields, we notice that the CrSBr magnetization easy axis is defined by crystal cleaving and lies along \hat{y} [23]. As such, terrace-steps along \hat{y} will produce stray-field components along \hat{z} and \hat{y} . Since $\hat{S}_{\text{NV}} \cdot \hat{y} = 0$ and $\alpha \neq 0$, the selected NV family is insensitive to y -components, and sensitive to z -components of the CrSBr stray field, as shown schematically in Fig 4.1b-c. Next, we measure the electron spin resonance frequency of our NV family for the $m_s = 0$ to $m_s = \pm 1$ transitions, and a spatial map for f^+ and f^- , as shown in Fig. 4.3b and Fig. 4.3c. Horizontal stripes are apparent throughout the sample, indicating magnetic stray fields at thickness tran-

sitions of the CrSBr flake along \hat{y} . To better interpret these data, we show photoluminescence (Fig 4.3d) and atomic force microscope maps (Fig 4.3e) of the same region, and create a map of the NV-detected magnetic field $B_{\text{NV}} = (f^+ - f^-) / \gamma_{\text{NV}}$ (Fig. 4.3f), where $\gamma_{\text{NV}} \approx 28.024$ GHz/T is the gyromagnetic ratio. Four lines in the atomic force microscope map are drawn as a guide to the eye, and correspond to the thickness measurements presented in Fig. 4.2d. Notably, stray fields are present at the trilayer (red/I, green/III) and monolayer (purple/III) steps, yet we do not observe any magnetic signature for the bilayer (blue/IV) step. Additionally, the stray fields at the trilayer steps have similar magnitude but opposite sign, consistent with the AFM observation that these are steps at the edges of the same terrace, and hence have opposite stray field signatures. These findings lead us to conclude that we are indeed observing magnetic stray fields arising from uncompensated magnetic moments of the CrSBr, opening the way for a quantitative analysis of the stray field signatures and CrSBr single-layer-magnetization.

4.3. EXTRACTION OF $T_{\text{NÉEL}}$ AND MONOLAYER MAGNETIZATION

Here we extract the Néel temperature of CrSBr by investigating the temperature dependence of the detected stray fields across the magnetic phase transition. We do so by measuring $dB_{\text{NV}} = df_{\text{ESR}} / \gamma_{\text{NV}}$ along a line trace (across the step indicated by the green line in Fig. 4.3e), and varying the temperature as shown in Fig. 4.4a. The measured df_{ESR} is with respect to f_{ESR} at the center of the line trace. To highlight the temperature-induced change in magnetic stray field, the data are subtracted with dB_{NV} at $T = 160$ K. The magnetic signatures corresponding to the atomic steps disappear gradually between 120-130 K. Another seemingly global magnetic signature rises at the transition, and disappears above $T = 140$ K, which could be related to the reported intermediate ferromagnetic phase separating the paramagnetic and antiferromagnet phases in bulk CrSBr [7]. Importantly, we observe no dependence of these transitions on laser power nor microwave power. In order to quantitatively extract the phase transition temperature, we fit the dips and peaks in dB_{NV} with Gaussians (Fig. 4.4b). The fitted Gaussian amplitudes and fit errors are plotted as a function of temperature in Fig. 4.4c, normalized with respect to the low-temperature stray field $dB_{\text{NV}}|_{T=70\text{ K}}$, and fitted by a phenomenological model proportional to $1 - (T/T_c)^\delta$. The fit yields $\delta = 11(1)$ and $T_c = 130(1)$ K, in reasonable agreement with previously reported transition temperatures of 132 K [7, 24].

Next, we utilize the quantitative nature of NV magnetometry to extract the single layer magnetization of our CrSBr flake. To do so, we first model the CrSBr magnetic stray field originating from an odd-numbered step as that of an infinite array of magnetic monopoles along \hat{x} . This model is valid, when the following three conditions hold:

- i The NV-sample distance is negligible with respect to the distance along \hat{y} to the nearest step.
- ii The CrSBr stacking lattice constant is negligible compared to the NV-sample distance.
- iii The NV-sample distance is negligible compared to the terrace size along \hat{x} .

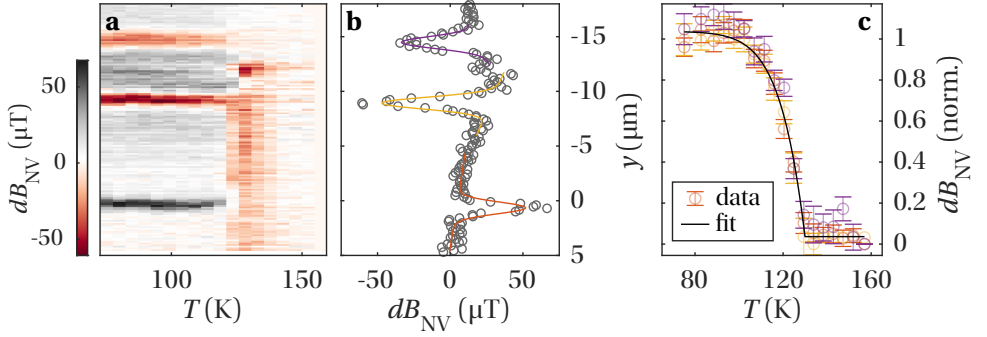


Figure 4.4. **Imaging of the magnetic phase transition in CrSBr.** (a) Change in magnetic field dB_{NV} along a line trace over the CrSBr flake as a function of temperature. Data is subtracted by dB_{NV} at 160 K. (b) Line trace of dB_{NV} at $T = 80$ K with Gaussian fits to three magnetic signatures. (c) Normalized amplitude of the Gaussian fits to dB_{NV} as a function of temperature, fitted by a phenomenological model $\propto 1 - (T/T_c)^\delta$. We extract $\delta = 11(1)$ and $T_c = 130(1)$ K.

4

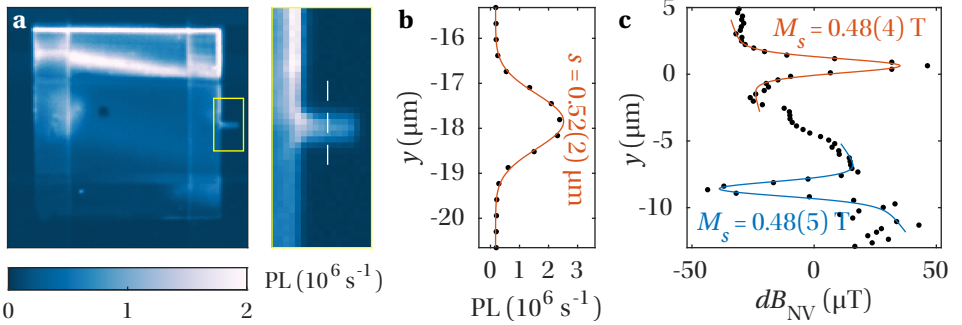


Figure 4.5. **Extraction of CrSBr single-layer magnetization.** (a) Photoluminescence map of the diamond membrane and its $1 \mu\text{m}$ -wide holding bar. (b) Photoluminescence trace over the holding bar. By convolving the holding bar width with a Gaussian, we extract an optical spot size of $\sigma = 0.52(2) \mu\text{m}$. (c) Spatial line trace of dB_{NV} at $T = 80$ K over the two tri-layer steps (I,II). By fitting the peaks with a Lorentzian, we extract a single-layer magnetization of $M_s = 0.48(5)$ T.

While condition i is likely satisfied at all locations investigated with AFM, we focus on the well-isolated steps I and II for our analysis. The interlayer lattice parameter of CrSBr is $c = 7.9 \text{ \AA}$, and our NV layer is roughly 70 nm below the diamond surface, as estimated by Stopping and Range of Ions in Matter (SRIM) calculations [25], so condition ii is satisfied. The CrSBr flake is homogeneous over multiple tens of microns along \hat{x} (Fig. 4.2a), satisfying condition iii. To proceed, we write the z -component of the field of a line of magnetic monopoles along \hat{x} at $y = y_0$ as

$$B_z(y) = \frac{M_s c}{2\pi} \frac{z_0}{z_0^2 + (y - y_0)^2}, \quad (4.1)$$

where z_0 is the height of the NV sensing layer. The projection of this field on the NV axis

causes a shift in ESR frequency, given by

$$df_{\text{ESR}}(y) = \gamma B_z(y) \cos(54.7^\circ). \quad (4.2)$$

We detect df_{ESR} by sweeping a detuned frequency df over the resonance frequency f_{ESR} while observing the NV photoluminescence. We model the normalized PL of an individual NV by a Lorentzian dip,

$$S_s(y, df) = 1 - \frac{1}{(df - df_{\text{ESR}}(y))^2 + w^2}, \quad (4.3)$$

where w is the ESR linewidth. Since we probe the ODMR photoresponse $S_s(y, df)$ of an NV ensemble with a diffraction limited laserspot, we model our observed photoresponse by convolving the individual NV ODMR response with a Gaussian point spread function,

$$S(y, df) = S_s(y, df) * \frac{1}{2\pi s} e^{-y^2/2s^2}, \quad (4.4)$$

where s is the FWHM of our optical spot size. Thus, before we can fit $S(y, df)$ to our dataset, we must first find the spot size of our laser. We do so by measuring the photoluminescence of the 1 μm -wide holding bar of the diamond membrane (Fig. 4.5a). The line trace over the holding bar is shown in Fig. 4.5b, and we extract a spot size $s = 0.52(2)$ μm by convolving a 1 micron wide step function with a Gaussian point spread function. Finally, we fit $S(y, df)$ to the photoresponse of a line-trace along y containing two magnetic signatures as indicated in Fig. (indicate). In this process, df_{ESR} , z_0 and M_s are fit parameters, and we plot the extracted $dB_{\text{NV}} = df_{\text{ESR}}/\gamma$ with the fitted ODMR response in Fig. 4.5c, to extract a saturation magnetization $M_s^{\text{I}} = 0.48(5)$ T and $M_s^{\text{II}} = 0.48(4)$ T, well in agreement with SQUID measurements on field-polarized bulk CrSBr [24]. Notably, we extract $z^{\text{I}} = 0.10(1)$ μm and $z^{\text{II}} = 0.13(7)$ μm , in accordance with previous observations that SRIM underestimates the NV implantation depth [26].

4.4. CONCLUSION

Our novel method integrates NV ensemble magnetometry with existing 2D materials assembly methods, leveraging μm -level positioning precision, rotational alignment, and direct contact of the sensing diamond with target substrates. Our method is compatible with glovebox methods, inert atmospheres, and any substrate of choice, aiding exfoliation, identification and magnetic characterization of sensitive few-layer 2D materials. Notably, we did not observe a significant difference in magnetometry signal-to-noise between PMMA-removed and PMMA-covered regions of our diamond, indicating that the PMMA removal was an unnecessary precaution and that it can be left intact to serve as a capping layer for air-sensitive materials. We demonstrated the power of our method by placing a membrane in contact with 2D interlayer antiferromagnet CrSBr. By rotationally aligning the in-plane projections of the NV-quantization axes with the easy- and hard-axes of CrSBr, we are able to perform a straightforward quantitative analysis of the CrSBr single-layer magnetization without need for monolayer exfoliation or large magnetic fields. Importantly, our method is easy, cheap, fast and sensitive, and enables high throughput magnetic characterization of 2D materials and spintronic devices.

ACKNOWLEDGEMENTS

We thank Allard J. Katan for assistance with processing of the AFM data.

FUNDING

This project has received funding from the European Union Horizon 2020 research and innovation program under grant agreement No. 863098 (SPRING), and from the Netherlands Research Council (NWO) under grants 740.018.012 (startup), 680.91.115 (Projectruimte) and 193.077 (VIDI). S.M.V. and C.B.C. acknowledge the financial support from the European Union (ERC AdG Mol-2D 788222), the Spanish MCIN (2D- HETEROS PID 2020-117152RB-100, co-financed by FEDER, and Excellence Unit "María de Maeztu" CEX 2019-000919-M) and the Advanced Materials program, supported by MCIN with funding from European Union NextGenerationEU (PRTR-C17.I1) and by Generalitat Valenciana.

4

AUTHOR CONTRIBUTIONS STATEMENT

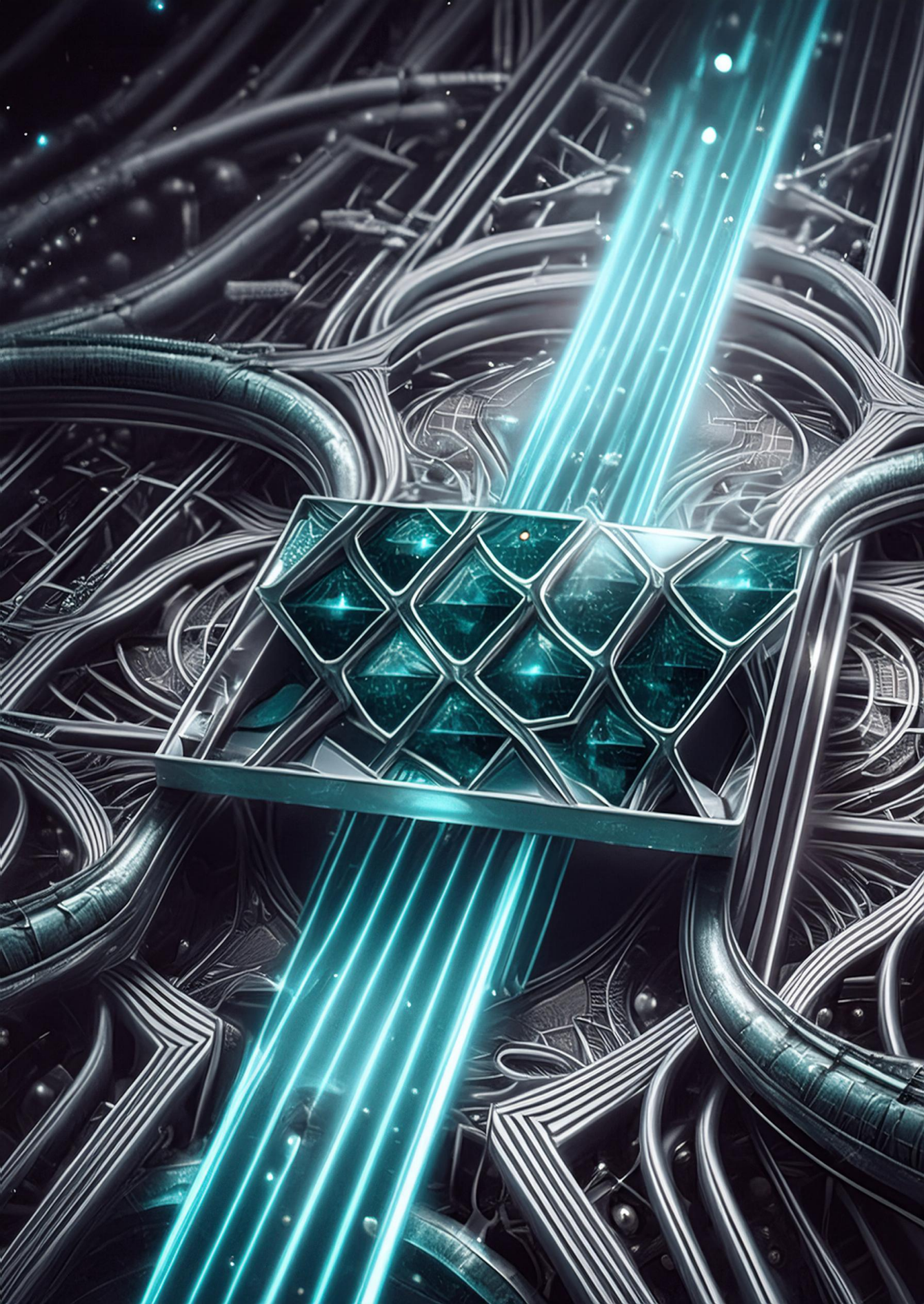
T.S.G., **S.K.**, **M.B.**, **H.S.J.v.d.Z.** and **T.v.d.S.** conceived and designed the experiment. **M.B.** and **B.G.S.** fabricated the diamond membranes. **S.K.** fabricated the stripline and developed the diamond tipping process. **T.S.G.** developed the diamond membrane transfer process, performed AFM characterizations, fabricated the CrSBr-diamond sample, and created the visuals of Fig. 4.1. **C.B.** and **S.M.** synthesized the CrSBr crystals. **M.B.** performed the NV ESR measurements with input of **S.K.** and **I.B.**. **M.B.** created the figures. **M.B.** and **T.v.d.S.** analyzed the ESR data.

REFERENCES

- [1] M. Gibertini *et al.* “Magnetic 2D materials and heterostructures”. *Nature Nanotechnology* 14.5 (2019), pp. 408–419. ISSN: 17483395. DOI: [10.1038/s41565-019-0438-6](https://doi.org/10.1038/s41565-019-0438-6).
- [2] B. Huang *et al.* “Layer-dependent ferromagnetism in a van der Waals crystal down to the monolayer limit”. *Nature* 546.7657 (2017), pp. 270–273. ISSN: 14764687. DOI: [10.1038/nature22391](https://doi.org/10.1038/nature22391). arXiv: [1703.05892](https://arxiv.org/abs/1703.05892).
- [3] C. Gong *et al.* “Discovery of intrinsic ferromagnetism in two-dimensional van der Waals crystals”. *Nature* 546.7657 (2017), pp. 265–269. ISSN: 14764687. DOI: [10.1038/nature22060](https://doi.org/10.1038/nature22060).
- [4] Z. Fei *et al.* “Two-dimensional itinerant ferromagnetism in atomically thin Fe₃GeTe₂”. *Nature Materials* 17.9 (2018), pp. 778–782. ISSN: 14764660. DOI: [10.1038/s41563-018-0149-7](https://doi.org/10.1038/s41563-018-0149-7). arXiv: [1803.02559](https://arxiv.org/abs/1803.02559).
- [5] Z. Sun *et al.* “Giant nonreciprocal second-harmonic generation from antiferromagnetic bilayer CrI₃”. *Nature* 572.7770 (2019), pp. 497–501. ISSN: 14764687. DOI: [10.1038/s41586-019-1445-3](https://doi.org/10.1038/s41586-019-1445-3).
- [6] H. Chu *et al.* “Linear Magnetoelectric Phase in Ultrathin MnPS₃ Probed by Optical Second Harmonic Generation”. *Physical Review Letters* 124.2 (2020), p. 27601. ISSN: 10797114. DOI: [10.1103/PhysRevLett.124.027601](https://doi.org/10.1103/PhysRevLett.124.027601). arXiv: [2001.07219](https://arxiv.org/abs/2001.07219).
- [7] K. Lee *et al.* “Magnetic Order and Symmetry in the 2D Semiconductor CrSBr”. *Nano Letters* 21.8 (2021), pp. 3511–3517. ISSN: 15306992. DOI: [10.1021/acs.nanolett.1c00219](https://doi.org/10.1021/acs.nanolett.1c00219). arXiv: [2007.10715](https://arxiv.org/abs/2007.10715).
- [8] P. Maletinsky *et al.* “A robust scanning diamond sensor for nanoscale imaging with single nitrogen-vacancy centres”. *Nature Nanotechnology* 7.5 (2012), pp. 320–324. ISSN: 17483395. DOI: [10.1038/nnano.2012.50](https://doi.org/10.1038/nnano.2012.50).
- [9] D. A. Simpson *et al.* “Magneto-optical imaging of thin magnetic films using spins in diamond”. *Scientific Reports* 6. February (2016), pp. 1–8. ISSN: 20452322. DOI: [10.1038/srep22797](https://doi.org/10.1038/srep22797).
- [10] F. Casola *et al.* “Probing condensed matter physics with magnetometry based on nitrogen-vacancy centres in diamond”. *Nature Reviews Materials* 3 (2018). ISSN: 20588437. DOI: [10.1038/natrevmats.2017.88](https://doi.org/10.1038/natrevmats.2017.88).
- [11] L. Thiel *et al.* “Probing magnetism in 2D materials at the nanoscale with single-spin microscopy”. *Science* 364.6444 (2019), pp. 973–976. ISSN: 10959203. DOI: [10.1126/science.aav6926](https://doi.org/10.1126/science.aav6926). arXiv: [1902.01406](https://arxiv.org/abs/1902.01406).

- [12] D. A. Broadway *et al.* “Imaging Domain Reversal in an Ultrathin Van der Waals Ferromagnet”. *Advanced Materials* 32.39 (2020), pp. 1–6. ISSN: 15214095. DOI: [10.1002/adma.202003314](https://doi.org/10.1002/adma.202003314). arXiv: [2003.08470](https://arxiv.org/abs/2003.08470).
- [13] Q. C. Sun *et al.* “Magnetic domains and domain wall pinning in atomically thin CrBr₃ revealed by nanoscale imaging”. *Nature Communications* 12.1 (2021), pp. 1–7. ISSN: 20411723. DOI: [10.1038/s41467-021-22239-4](https://doi.org/10.1038/s41467-021-22239-4).
- [14] F. Fabre *et al.* “Characterization of room-temperature in-plane magnetization in thin flakes of CrTe₂ with a single-spin magnetometer”. *Physical Review Materials* 5.3 (2021), p. 34008. ISSN: 24759953. DOI: [10.1103/PhysRevMaterials.5.034008](https://doi.org/10.1103/PhysRevMaterials.5.034008). arXiv: [2011.05722](https://arxiv.org/abs/2011.05722).
- [15] T. Song *et al.* “Direct visualization of magnetic domains and moiré magnetism in twisted 2D magnets”. *Science* 374.6571 (2021), pp. 1140–1144. ISSN: 10959203. DOI: [10.1126/science.abj7478](https://doi.org/10.1126/science.abj7478).
- [16] A. Laraoui *et al.* “Opportunities for nitrogen-vacancy-Assisted magnetometry to study magnetism in 2D van der Waals magnets”. *Applied Physics Letters* 121.6 (2022), pp. 0–9. ISSN: 00036951. DOI: [10.1063/5.0091931](https://doi.org/10.1063/5.0091931).
- [17] I. O. Robertson *et al.* “Imaging current control of magnetization in Fe₃GeTe₂ with a widefield nitrogen-vacancy microscope”. *2D Materials* 10.1 (2023). ISSN: 20531583. DOI: [10.1088/2053-1583/acab73](https://doi.org/10.1088/2053-1583/acab73). arXiv: [2207.10329](https://arxiv.org/abs/2207.10329).
- [18] P. J. Scheidegger *et al.* “Scanning nitrogen-vacancy magnetometry down to 350 mK”. *Applied Physics Letters* 120.22 (2022). ISSN: 00036951. DOI: [10.1063/5.0093548](https://doi.org/10.1063/5.0093548). arXiv: [2203.15527](https://arxiv.org/abs/2203.15527).
- [19] D. M. Toyli *et al.* “Measurement and control of single nitrogen-vacancy center spins above 600 K”. *Physical Review X* 2.3 (2012), pp. 1–7. ISSN: 21603308. DOI: [10.1103/PhysRevX.2.031001](https://doi.org/10.1103/PhysRevX.2.031001). arXiv: [1201.4420](https://arxiv.org/abs/1201.4420).
- [20] I. Bertelli *et al.* “Magnetic resonance imaging of spin-wave transport and interference in a magnetic insulator”. *Science Advances* 6.46 (2020), pp. 1–8. ISSN: 23752548. DOI: [10.1126/sciadv.abd3556](https://doi.org/10.1126/sciadv.abd3556). arXiv: [2004.07746](https://arxiv.org/abs/2004.07746).
- [21] P. J. Zomer *et al.* “Fast pick up technique for high quality heterostructures of bilayer graphene and hexagonal boron nitride”. *Applied Physics Letters* 105.1 (2014). ISSN: 00036951. DOI: [10.1063/1.4886096](https://doi.org/10.1063/1.4886096). arXiv: [1403.0399](https://arxiv.org/abs/1403.0399).
- [22] Y. Schlüssel *et al.* “Wide-Field Imaging of Superconductor Vortices with Electron Spins in Diamond”. *Physical Review Applied* 10.3 (2018), p. 1. ISSN: 23317019. DOI: [10.1103/PhysRevApplied.10.034032](https://doi.org/10.1103/PhysRevApplied.10.034032). arXiv: [1803.01957](https://arxiv.org/abs/1803.01957).
- [23] E. J. Telford *et al.* “Layered Antiferromagnetism Induces Large Negative Magnetoresistance in the van der Waals Semiconductor CrSBr”. *Advanced Materials* 32.37 (2020), pp. 1–7. ISSN: 15214095. DOI: [10.1002/adma.202003240](https://doi.org/10.1002/adma.202003240). arXiv: [2005.06110](https://arxiv.org/abs/2005.06110).
- [24] O. Göser *et al.* “Magnetic properties of CrSBr”. *Journal of Magnetism and Magnetic Materials* 92.1 (1990), pp. 129–136. ISSN: 03048853. DOI: [10.1016/0304-8853\(90\)90689-N](https://doi.org/10.1016/0304-8853(90)90689-N).

- [25] S. Pezzagna *et al.* “Creation efficiency of nitrogen-vacancy centres in diamond”. *New Journal of Physics* 12 (2010). ISSN: 13672630. DOI: [10.1088/1367-2630/12/6/065017](https://doi.org/10.1088/1367-2630/12/6/065017).
- [26] D. M. Toyli *et al.* “Chip-scale nanofabrication of single spins and spin arrays in diamond”. *Nano Letters* 10.8 (2010), pp. 3168–3172. ISSN: 15306984. DOI: [10.1021/nl102066q](https://doi.org/10.1021/nl102066q).



5

OBSERVATION OF HYBRID SPIN-WAVE–MEISSNER-CURRENT TRANSPORT MODES

*"Nanofabrication is best performed
on the correct side of your sample."*

Superconductors are materials with zero electrical resistivity and the ability to expel magnetic fields known as the Meissner effect. Their dissipationless diamagnetic response is central to magnetic levitation and circuits such as quantum interference devices. Here, we use superconducting diamagnetism to shape the magnetic environment governing the transport of spin waves – collective spin excitations in magnets that are promising on-chip signal carriers – in a thin-film magnet. Using diamond-based magnetic imaging, we observe hybridized spin-wave–Meissner-current transport modes with strongly altered, temperature-tunable wavelengths, and then demonstrate local control of spin-wave refraction using a focused laser. Our results illustrate the versatility of superconductor-manipulated spin-wave transport and have potential applications in spin-wave gratings, filters, crystals and cavities.

This chapter has been published in *Science* **382**, 430-434 (2023), by **M. Borst**, P.H. Vree, A. Lowther, A. Teepe, S. Kurdi, I. Bertelli, B.G. Simon, Y.M. Blanter, and T. van der Sar

5.1. INTRODUCTION

The ability to control the transport of spins and charges using metal electrodes is fundamental to information processing devices and an indispensable tool in quantum and condensed matter physics. While devices such as spin valves and transistors are based on transport of uncorrelated particles [1], the excitations of magnetic materials known as spin waves are emerging as promising alternative information carriers [2]. These collective spin excitations provide new opportunities for realizing analog or binary device functionality based on their wave nature, non-reciprocal transport properties, and low intrinsic damping [3]. Control of spin-wave transport is possible by heavy-metal electrodes that enable modulation via the spin-Hall effect [4–6] or by auxiliary magnetic materials that modify the spin-wave spectrum [7, 8]. However, metallic gates can also introduce additional spin-wave damping because of uncontrolled spin pumping or spin-wave-induced eddy currents [6, 9, 10]. Furthermore, the diamagnetic response of normal metals is dominated by ohmic resistance, precluding effective stray-field control of the spin-wave spectrum. An attractive approach for strong, low-damping spin-wave modulation is to use superconducting electrodes. Superconductors are materials with zero electrical resistivity and a strong diamagnetic response that enables creating magnetic shields, magnetic lenses, and circuits such as quantum bits and quantum interference devices [11, 12]. Spin-wave spectroscopy measurements have demonstrated that superconducting strips on magnetic films can alter the spin-wave spectrum through the backaction of induced currents [13] or the interaction with Abrikosov vortices [14]. Recently, it was proposed to harness the diamagnetism of a superconductor to create the spin-wave equivalents of optical mirrors and cavities [15]. Being able to image and control spin waves as they travel underneath superconducting electrodes would enable insight into the nature of the spin wave–superconductor interaction and unlock opportunities to control the propagation, dispersion, and refraction of spin waves. In this work, we develop, image, and study temperature-, field-, and laser-tunable spin-wave transport enabled by a superconducting strip on a thin-film magnetic insulator (Fig. 1A). We use magnetic resonance imaging based on nitrogen-vacancy (NV) spins in diamond [16–18] to study the spin waves as they travel underneath the optically opaque superconductor.

5.2. MAGNETIC RESONANCE IMAGING OF HYBRIDIZED SWMC TRANSPORT MODES

Our system consists of a thin film of yttrium iron garnet (YIG) — a magnetic insulator with low spin-wave damping [2] — equipped with gold microstrips for spin-wave excitation and a molybdenum-rhenium superconducting strip for spin-wave modulation (Fig. 1A). To image the spin waves, we place a diamond membrane that contains a thin layer of nitrogen vacancy (NV) sensor spins on top of the sample (Fig. 5.1, Fig. 5.2a) [18]. These spins detect the spin waves by their microwave magnetic stray fields, enabling imaging through optically opaque materials [10]. The sample is embedded in a variable temperature cryostat with a base temperature of 5.5 K and free-space optical access to read out the NV sensor spins. NV centers are atomic defects in the diamond carbon lattice with an $S = 1$ electron spin [16]. The sensitivity of the NV spin to magnetic fields, combined with

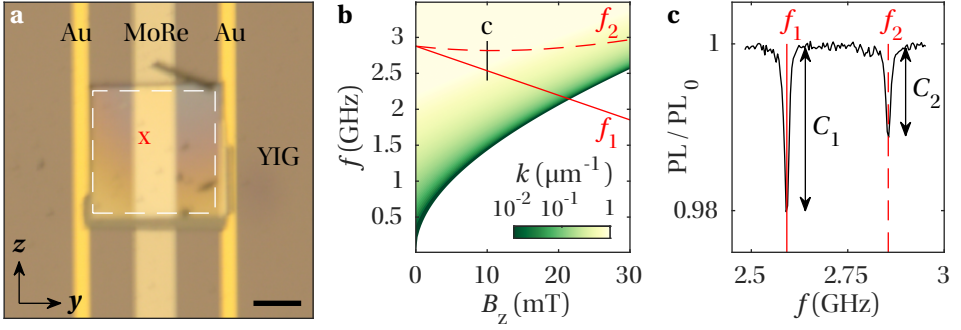


Figure 5.2. **Driving electron spin resonance of NVs with spin-wave stray fields through a MoRe strip.** (a) Optical micrograph of an NV-ensemble diamond membrane on top of a MoRe strip between Au microstrips, fabricated on a 245-nm thick YIG film. Scale bar: 30 μm . (b) YIG dispersion (color map) and NV electron spin resonance (ESR) frequencies (red lines) as a function of the in-plane field component $B_z = B_{\text{NV}} \cos(\theta)$. $f_{1(2)}$ denotes the ESR frequency of NV spins with zero-field quantization axis aligned (misaligned) with \mathbf{B}_{NV} . The intersection of the ESR frequencies with the spin-wave dispersion sets the detectable spin-wavenumbers k . (c) Optically detected NV ESR spectrum at $B_z = 10$ mT, at a location denoted by the red cross in (a). The ESR contrast $f_{1(2)}$ results from interference between the microstrip field and spin-wave field, enabling spatial mapping of the spin-wave fronts.

generate NV-resonant spin waves with wavevector $k = k \hat{y}$ by applying a microwave current at NV frequency f_1 to the gold microstrip that is located just left outside the imaging area. The interference between the microwave magnetic stray field generated by these spin waves and the direct microstrip field leads to a spatial standing-wave modulation of the NV ESR contrast [17, 18]. Crucial for our measurements, this interference effect enables a straightforward extraction of the spin-wave length. The spatial map of the ESR contrast C_1 at $T = 10.7$ K (above T_c) shows spin waves traveling towards and then underneath the MoRe strip without a change in wavelength (Fig. 5.3b). In contrast, the spin-wave length increases almost twofold when the strip is cooled into its superconducting state at $T = 5.5$ K (Fig. 5.3c). Averaging the maps along \hat{z} (Fig. 5.3e) highlights the spatial homogeneity of the wavelength change.

We explain the superconductor-induced change of the spin-wave length by developing an analytical expression for the spin-wave dispersion in a magnet-superconductor thin-film hybrid. In this model, building on the formalism developed in [15], the spin waves induce alternating Meissner currents that are governed by the London penetration depth λ_L of the superconductor. These currents, in turn, generate a magnetic field that acts back on the spin waves.

By integrating this field self-consistently into the Landau-Lifshitz-Gilbert (LLG) equation, we find that the spin-wave dispersion shifts upwards in frequency as

$$f_{\text{YIG/SC}}(k, \lambda_L) = f_{\text{YIG}}(k) + f_{\text{SC}}(k, \lambda_L), \quad (5.1)$$

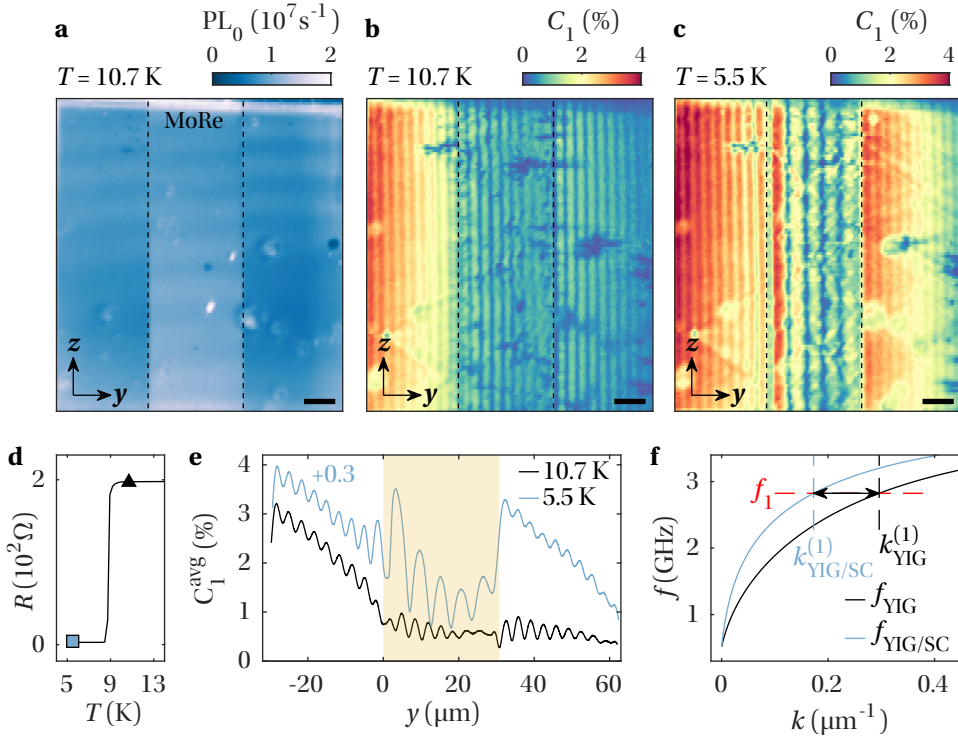


Figure 5.3. Magnetic resonance imaging of spin waves above and below the superconducting transition temperature. (a) Spatial map of the NV photoluminescence PL_0 in the absence of microwaves, showing the MoRe strip (between the vertical dashes). Scale bar: 10 μm . (b, c) Spatial maps of the NV electron spin resonance contrast C_1 above (b) and below (c) the superconducting transition temperature of $T_c = 8.7$ K, at $T = 10.7$ K and $T = 5.5$ K respectively. The Au microstripping exciting spin waves is located just outside the left edge of the imaged area. Above (below) T_c , the wavelength is unaffected (lengthened) by the interaction with the MoRe strip. (d) DC resistance R of the MoRe strip as a function of temperature T , with markers indicating the resistance of the film during the measurements of (b), triangle, and (c), square. (e) Data from (b) and (c) averaged over the z -direction, with the MoRe strip indicated by yellow shading. (f) Calculated spin-wave dispersion $f_{\text{YIG}}(k)$ for bare YIG and $f_{\text{YIG/SC}}(k, \lambda_L)$ for YIG covered by a superconducting film with London penetration depth $\lambda_L = 400$ nm. The superconductor shifts the dispersion upwards by $f_{\text{SC}}(k, \lambda_L)$, which manifests as a reduction in the wavenumber at the NV frequency f_1 from $k_{\text{YIG}}^{(1)}$ to $k_{\text{YIG/SC}}^{(1)}$ as indicated by the dashed lines.

where $f_{\text{YIG}}(k)$ is the bare-YIG spin-wave dispersion (SI) and

$$f_{\text{SC}}(k, \lambda_L) \approx \gamma \mu_0 M_s k t r \frac{1 - e^{-2h/\lambda_L}}{(k\lambda_L + 1)^2 - (k\lambda_L - 1)^2 e^{-2h/\lambda_L}} \quad (5.2)$$

is the superconductor-induced shift (Section 5.7). Here, M_s is the YIG saturation magnetization, $t = 245$ nm is the YIG thickness, $h = 140$ nm is the superconductor thickness, $\gamma = 28$ GHz/T is the electron gyromagnetic ratio, μ_0 is the vacuum permeability, and r is a

dimensionless factor associated with the YIG thickness and spin-wave ellipticity. The approximation holds when the kinetic inductance dominates the impedance, as is the case for our superconducting strip (Supplementary Sec. 5.7), and when $k^2\lambda_L^2 \ll 1$. A more general expression is given in the supplementary text. The dispersion shift $f_{\text{SC}}(k, \lambda_L)$ is maximal when $\lambda_L \rightarrow 0$, in which case the superconductor perfectly screens the spin-wave stray field. This limit was analyzed in [24, 25] by considering a magnetic film covered by a ‘perfect metal’, as defined by a perfect magnetic field screening. Indeed, when we let $\lambda_L \rightarrow 0$, the shift calculated by our model approaches the shift predicted in [24, 25]. The calculated bare-YIG and hybridized YIG/MoRe spin-wave dispersions are compared in 5.3e. The upwards frequency shift underneath the superconductor manifests as a reduction in wavenumber of the NV-resonant spin waves detected in our experiments (Fig. 5.3f).

We observe that the ESR contrast just to the right of the MoRe strip is higher than that in the MoRe-strip region (Fig. 5.3c), consistent with the screening of the spin-wave field by the Meissner currents. In addition, we observe that the ESR contrast just to the right of the MoRe strip exceeds that just to the left of it (Fig. 5.3e), indicating the excitation of additional, secondary spin waves by the MoRe strip itself. This enhanced excitation of secondary spin waves is presumably caused by an additional microwave current in the MoRe strip that is excited via the direct geometric inductive coupling with the Au microstrip when the MoRe impedance changes as it is cooled below T_c .

5

5.3. FIELD-TUNING OF THE HYBRIDIZED MODES

We characterize the magnetic-field dependence of the spin-wave dispersion underneath the superconductor and use it to extract the London penetration depth λ_L at the $T = 5.5$ K base temperature of our cryostat. Spatial line traces of the NV photoluminescence serve as a reference image, and show increased PL on the MoRe, presumably due to additional NV excitation by the reflection of the excitation laser on the opaque MoRe film (Fig. 5.4a-b). For each value of y and B_z a full ESR spectrum is taken, which is fitted with a Lorentzian to extract ESR frequency and contrast. The fitted ESR frequencies f_i for field-aligned ($i = 1$) and misaligned ($i = 2$) show Meissner screening of the bias field B_{NV} , along with spin-wavefronts, highlighted by subtracting the y -averaged frequency for each B_z (Fig. 5.4c-f). The ESR contrast across the strip shows the dependence of the spin-wave length on the applied magnetic field (Fig. 5.4g-h), along with a beating interference pattern along B_z , arising from interference between spin waves excited by the Au microstrip and those excited by the inductively coupled MoRe strip. We extract the spin-wave numbers in the bare-YIG and YIG/MoRe regions separately by Fourier transformation (Supplementary Fig. 5.8), and plot these as a function of field and frequency in Fig. 5.5a-b. A similar measurement with the bias field applied in-plane along \hat{z} shows that Meissner screening of the bias field does not play a significant role in the wavelength shift (Supplementary Fig. 5.9).

From the field-dependence of the extracted spin-wave numbers in the bare-YIG region, we extract the YIG saturation magnetization $M_s = 194(1)$ kA/m (Supplementary Sec. 5.7) in agreement with previous low-temperature measurements [26]. We then use M_s as a fixed parameter to fit the field-dependence of the spin-wave numbers under-

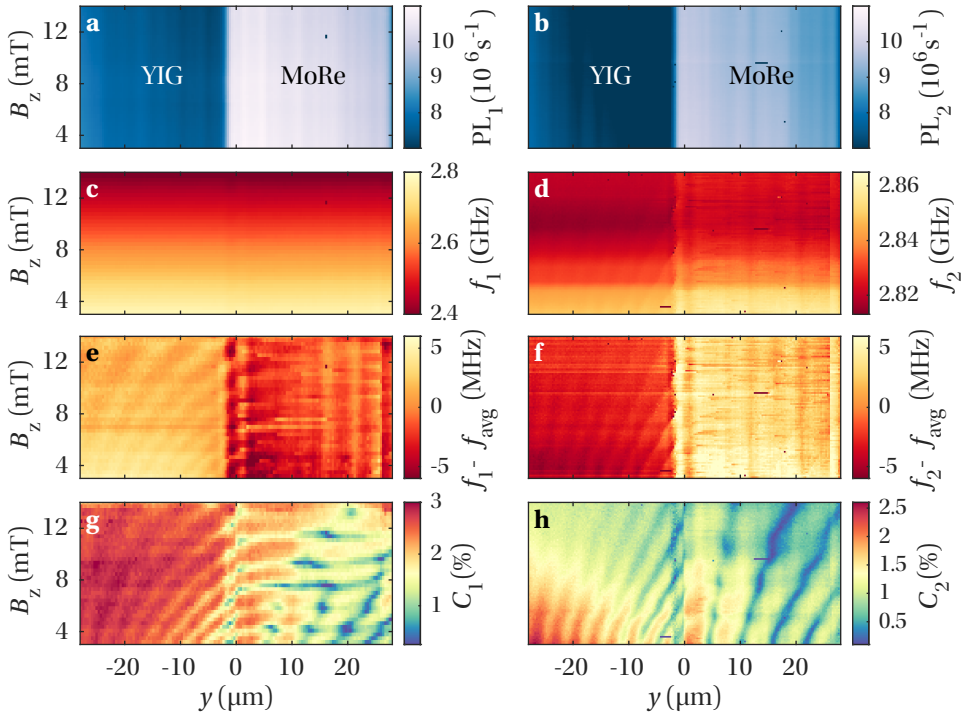


Figure 5.4. **Field-dependence of hybrid spin-wave-Meissner-current modes.** (a,b) Photoluminescence maps during resonant excitation of nitrogen vacancy electron spin resonance in bare YIG and MoRe-covered YIG for aligned (PL_1) and mis-aligned (PL_2) nitrogen vacancy center families. The NV photoluminescence is independent of field, and is higher in the MoRe region, presumably due to a higher reflection of the excitation laser on the opaque MoRe film than on largely transparent YIG. (c, d) Field-dependence of the drive frequencies $f_{1(2)}$, which are adjusted at each B_z to maintain resonance with the NV ESR transition. (e, f) Average-subtracted electron spin resonance frequencies for each value of B_z reveal spatial variations in static magnetic field due to Meissner expulsion of the bias field B_{NV} . The average value for each B_z is used for fitting data to our model. The spin-wafronts are visible in the ESR frequency, likely due to an asymmetry in the ESR dip and imperfect fitting. (g, h) Spatial linetraces of the NV ESR contrast as a function of magnetic field B_z . Underneath the superconductor, the spin-wavelength is stretched. Interference with spin waves excited at $y = 0$ due to inductive coupling between Au and MoRe microstrips results in a beating pattern along B_z for $y > 0$. Data taken at $T = 5.5$ K.

neath the superconducting strip using the hybridized YIG/MoRe spin-wave dispersion (Eq. 1). From this fit we extract a London penetration depth $\lambda_L = 405(10)$ nm at $T = 5.5$ K, which agrees well with static-field nano-squid measurements [27].

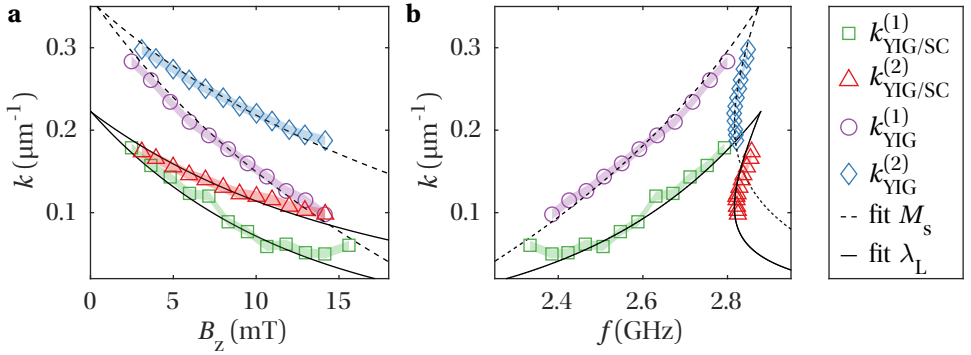


Figure 5.5. **Extraction of M_s and λ_L from field-dependence of spin-wavenumber.** (a, b) Spin-wavenumber as a function of field (a) and frequency (b), extracted from data in Fig. 5.4 through Fourier analysis. The $k^{(i)}$ are wavenumbers measured with the field-aligned ($i = 1$) and misaligned ($i = 2$) NV ensembles. The error bars (indicated by shading) are determined by the inverse of the spatial sampling range in the y -direction. We determine the saturation magnetization M_s by fitting the data in the bare YIG region $k_{\text{YIG}}^{(i)}$, and the London penetration depth by fitting the data from the superconductor-covered region $k_{\text{YIG/SC}}^{(i)}$ to our hybrid dispersion model.

5

5.4. TEMPERATURE-TUNING OF THE HYBRIDIZED MODES

The temperature dependence of the London penetration depth provides a powerful tool for tuning the spin-wave length. To demonstrate this, we image the spin waves in the YIG/MoRe region while stepping through T_c at different magnetic fields (Fig. 5.6). The extracted spin-wave number k is shown in Fig. 5.6, with the color indicating the in-plane component B_z of the magnetic bias field B_{NV} . We observe that k changes continuously with temperature over the superconducting phase transition in the YIG/MoRe region while remaining unchanged in the YIG region (Supplementary Fig. 5.11). We note that we do not observe global heating of the superconductor due to our excitation laser (Supplementary Fig. 5.10). Using our model, we extract the London penetration depth $\lambda_L(T)$ for every observed value of k (Fig. 5.6b, Supplementary Sec. 5.7). We find that almost all data collapse onto a single curve described by

$$\lambda_L = \lambda_L^0 [1 - (T/T_c)^4]^{-1/2}, \quad (5.3)$$

with $T_c = 8.7$ K and $\lambda_L^0 = 380$ nm [28]. The exceptions occur when the spin-wave length $\lambda_{\text{sw}} = 2\pi/k$ becomes comparable to the width of the MoRe strip. Here, our approximation of the superconducting strip by an infinite film breaks down. These results highlight that imaging the hybridized spin-wave–Meissner-current transport modes is a powerful tool for extracting the temperature dependence of the London penetration depth.

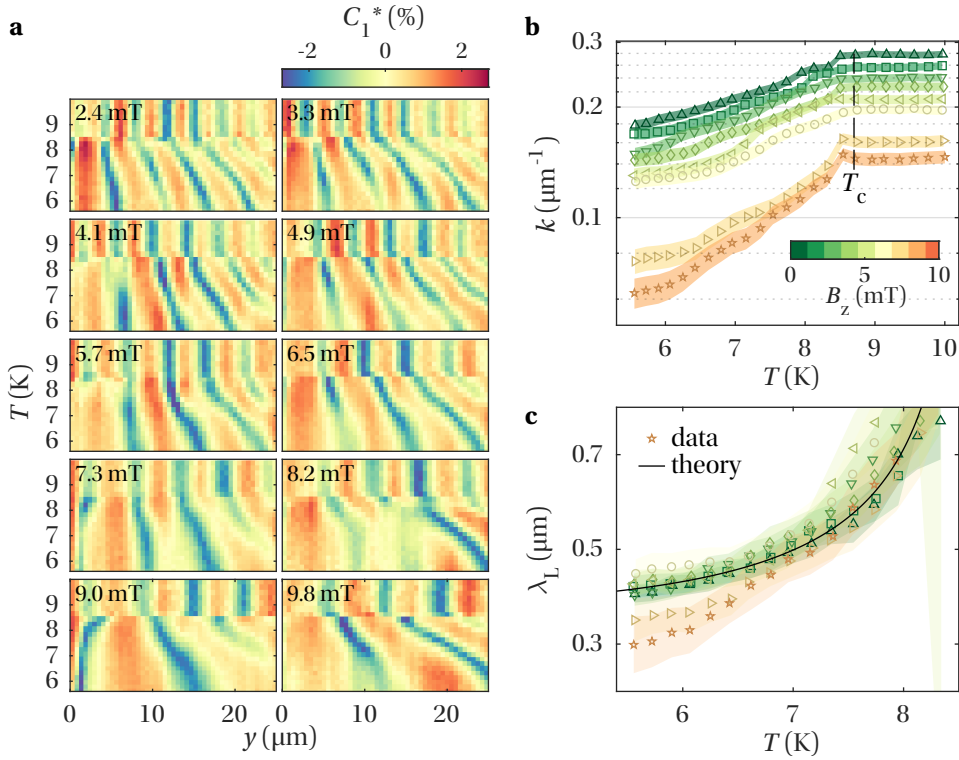


Figure 5.6. **Spin-wave manipulation through temperature control of the superconducting gate.** (a) Spatial line traces of the linearly detrended and renormalized NV ESR contrast C_1^* over the MoRe-covered YIG region, as a function of temperature, showing a continuous change of the spin wavelength underneath the MoRe strip, for different in-plane magnetic fields B_z . Above the superconducting phase transition at $T_c = 8.7$ K, there is no temperature dependence of the wavelength, indicating the absence of the Meissner effect. M_s does not change significantly over the explored temperature range. A sudden phaseshift is visible at the superconducting phase transition for certain values of B_z . The ESR contrast C_1 increases below T_c , potentially due to an increase in induced RF signal in the MoRe strip. A.u., arbitrary units. (b) Spin-wave numbers k extracted from data in (a). The colors indicate the different magnetic field values B_z and each field value has a unique marker symbol. (c) London penetration depth λ_L of the MoRe film as a function of temperature, extracted from the data in (a) through our hybrid dispersion model. The black line represents the fit of the temperature dependence of $\lambda_L(T)$ from which we extract $T_c = 8.7$ K and $\lambda_L^0 = 380$ nm. The colors and markers indicate the different values of B_z as in (a).

5.5. SPIN-WAVE REFRACTION AT TARGET SITES

Thus far, we have demonstrated dispersion engineering through global control of temperature and magnetic field. We now show that the creation of a hot spot in the superconductor using a focused laser enables local manipulation of the spin-wave transport by tuning the effective refractive index (Fig. 5.7a). To do so, we couple an auxiliary, orange laser into our setup and focus it at target sites on the superconductor (Fig. 5.7b).

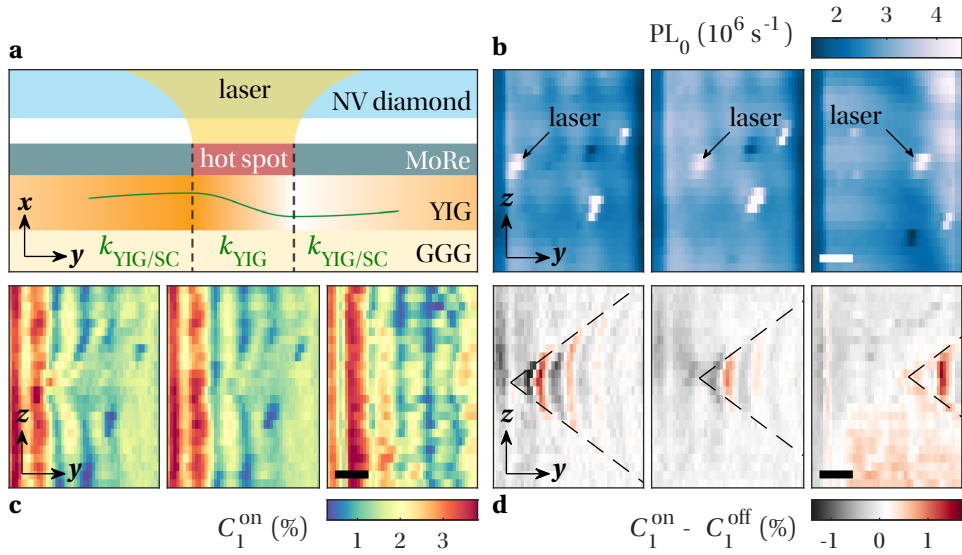


Figure 5.7. Laser induced spin-wave refraction at target locations. (a) Schematic illustration of a laser-induced scattering spot. By shining an auxiliary 594-nm laser on the sample, we create a hot spot in the MoRe strip that locally alters the effective refractive index governing the spin-wave propagation. (b) Scanning confocal microscope images of the NV photoluminescence at $T = 5.5$ K, with the auxiliary laser focused onto the MoRe strip at three different locations indicated by the arrows. Scale bar, $7.5 \mu\text{m}$. (c) Spatial maps of the NV ESR contrast with auxiliary laser turned on (C_1^{on}) showing spin waves in the YIG-MoRe region that scatter on the laser spot. (d) Background-subtracted ESR contrast highlighting the laser-induced spin-wave scattering obtained by subtracting the ESR contrast with the auxiliary laser turned off (C_1^{off}) from the measurements in (c, f, i). Data taken at $T = 5.5$ K and $B_z = 3.3$ mT.

The laser spot is visible through the locally enhanced NV photoluminescence. Spatial measurements of the NV ESR contrast C_1^{on} with the auxiliary laser on (Fig. 5.7c) show the spin-wave scattering patterns induced by the local hot spot. The reduction in amplitude behind the hot spot indicates destructive interference between the scattered and incident spin waves. Subtracting a reference measurement with the auxiliary laser turned off (Fig. 5.7d) highlights the angular profile of the scattered spin-wave patterns. The characteristic ‘caustic’ angles observed in these scattered patterns (dashed lines in Fig. 5D) result from the highly anisotropic dipolar spin-wave dispersion [29]. Tracing the patterns to their origin shows that the scattering site is tightly confined to the laser location. Presumably, the laser locally breaks the superconductivity, inducing a local change in the magnetic environment seen by the spin waves, leading to local spin-wave refraction akin to defect-controlled spin-wave scattering [29]. The ability to optically induce spin-wave refraction at target sites could be used to create devices such as gratings or magnonic crystals [30] and enable spin-wave manipulation via optical switching of flux-focusing regions in the superconducting strip.

5.6. CONCLUSION

We demonstrated local measurements of hybridized spin-wave–Meissner-current transport modes in a magnetic thin film equipped with a superconducting gate. The wavelength is tunable by temperature and field, enabling efficient phase-shifting of the spin-wavefronts and a striking in-situ visualization and quantitative extraction of the London penetration depth as a function of temperature. As MoRe is a type-2 superconductor with an estimated lower critical field of

$$H_{c1} = \frac{\phi_0}{4\pi\lambda_L^2} \left(\ln\left(\frac{\lambda_L}{\xi}\right) + 0.5 \right) \approx 4 \text{ mT} \quad (5.4)$$

at $T \approx 5 \text{ K}$ [31, 32], where $\xi \approx 0.01 \mu\text{m}$ is the coherence length [33] and ϕ_0 the superconducting flux quantum, Abrikosov vortices were expected in measurements such as those in Fig. 3B with a few-mT out-of-plane field component. We did however not identify vortex-related effects in these measurements, which look qualitatively similar to those with purely in-plane field (Supplementary Fig. 5.9). Presumably, the presence and location of vortices is strongly influenced by our focused excitation laser, as highlighted by recent magneto-optical [34] and wide-field NV-imaging experiments [35]. In particular, Ref. [34] showed that vortices can be annihilated by the laser via local heating above T_c or pushed by the laser to new pinning sites or border regions of the superconductor. The presented microwave magnetic imaging of the spin-wave transport modes in a YIG/MoRe heterostructure shows the versatility of superconducting gates for spin-wave manipulation, enables determining the temperature-dependent London penetration depth, and opens new opportunities for creating wave-based circuit elements such as filters, mirrors, and cavities.

ACKNOWLEDGEMENTS

We thank prof. A.F. Otte for commenting on the manuscript and prof. T. Yu and prof. G.E.W. Bauer for valuable discussions.

FUNDING

This work was supported by the Dutch Research Council (NWO) under awards VI.Vidi. 193.077, NGE1582.22.018, and OCENW.XL21.XL21.058. This work was also supported by the Dutch National Growth Fund (NGF) as part of the Quantum Delta NL programme.

AUTHOR CONTRIBUTIONS STATEMENT

Conceptualization: T.S. and M.B.; Sample design and fabrication: M.B.; Diamond membrane fabrication: B.S. and M.B.; Membrane placement: A.L. and S.K.; Constructing experimental setup: M.B. and A.L.; Measurements and software: M.B., P.H.V., A.L., and I.B.; Data analysis: M.B., P.H.V., and A.T.; Theory: T.S. and Y.M.B.; Figures: M.B. and P.H.V.; Funding acquisition: T.S.; Project administration: M.B. and T.S.; Supervision: T.S. and M.B.; Writing–original draft: M.B., T.S., and P.H.V.; Writing–review and editing: M.B., T.S., P.H.V., and Y.M.B.

5.7. SUPPLEMENTARY INFORMATION

DIAMOND MEMBRANE FABRICATION AND PLACEMENT

To fabricate the diamond platelet with a dense nitrogen-vacancy ensemble, we purchase $4 \times 4 \times 0.5 \text{ mm}^3$ electronic-grade diamond plates (Element 6 Inc.) and have them cut and polished into $2 \times 2 \times 0.05 \text{ mm}^3$ platelets (Almax Easylabs). Nitrogen ions are implanted at an energy of 54 keV and density of $105 \mu\text{m}^{-2}$ (Innovion), after which the diamond is annealed in vacuum, resulting in an estimated nitrogen vacancy center density of $10^3 \mu\text{m}^{-2}$ at a depth of approximately 70 nm below the surface [36].

Next, we reshape this platelet to host many $100 \times 100 \times 5 \mu\text{m}^3$ diamond membranes. To do so, we first cover the diamond with a 50 nm Ti layer by e-beam evaporation, into which the membrane pattern is etched by a SF6/He plasma following e-beam lithography. The Ti layer serves as a hard mask for the next step, in which the membrane pattern is reactive-ion etched $5 \mu\text{m}$ into the diamond by an O2 plasma. We turn the diamond over and etch the back almost all the way through with the same O2 plasma, until the diamond membranes only remain attached to the host by a small holding bar. Finally, we remove the Ti with a hydrofluoric acid dip.

PHOTOLUMINESCENCE MEASUREMENTS

We perform nitrogen vacancy center photoluminescence measurements in a closed cycle cryostat (Montana Cryostation S100) with optical access, through a room-temperature-stabilized NA = 0.85 microscope objective. We position the sample globally using slip-stick positioners (Attocube ANPx101, ANPz101), and use a fast-steering mirror (Newport FSM300) to scan a 520 nm continuous-wave laser (Coherent Obis 520LX) over our sample. We detect the corresponding NV photoluminescence by an avalanche photodiode (Excelitas SPCM-AQRH-13), after 600 nm longpass filtering the optical signal. The magnetic field used to magnetize our sample and set the NV resonance frequencies is applied by a large permanent magnet outside the sample chamber, in a home-built positioning system that has rotational (Zaber T-RS60) and translational (Zaber X-LRT0250AL-E08C) degrees of freedom. A microwave generator (Windfreak SynthHDv2) is used to apply microwave signals to the excitation stripline to excite spin waves and drive the NV center ensemble spins.

EXTRACTING M_s AND λ_L .

Here we describe the extraction of the saturation magnetization M_s of the YIG film and the London penetration depth λ_L of the MoRe strip. We determine M_s from the magnetic-field dependence of the spin-wavenumber k_{YIG} in the bare-YIG region ($y < 0$ region in Fig. 5.4 of the main text). M_s does not significantly change over the $T = 5.5\text{-}10 \text{ K}$ temperature range in our measurements such that the spin-wave length is temperature-independent in the bare-YIG region (Supplementary Fig. 5.11). Knowing M_s , we subsequently determine λ_L from the magnetic-field dependence of the spin-wavenumber $k_{\text{YIG/SC}}$ in the YIG+MoRe region ($y > 0$ region in Fig. 5.4 of the main text).

To extract the wavenumbers k_{YIG} and $k_{\text{YIG/SC}}$, we separate our spatial maps of the NV ESR contrast C into a bare-YIG and a YIG+MoRe region, and then linearly detrend the data along the y -direction (Supplementary Fig. 5.8a-b). We pad the data with zeros,

Fourier transform along y (Supplementary Fig. 5.8c), and extract k_{YIG} for the bare-YIG and $k_{\text{YIG/SC}}$ for the YIG+MoRe region by finding the FFT amplitude maximum (Supplementary Fig. 5.8d). The uncertainty $e^{(h)}$ of the extracted wavenumbers is determined by the inverse of the spatial sampling range $1/\Delta y^{(h)}$. The sampling ranges are indicated with arrows in Supplementary Fig. 5.8b.

From the field dependence of the spin-wave number in the bare-YIG region, we extract the saturation magnetization M_s via least-squares minimization of

$$\chi_j^2 = \sum_{i=1}^N (f_{sw}(B_z(i), k_{\text{YIG}}^{(j)}(i), M_s) - f_{NV_j}(i))^2. \quad (5.5)$$

Here, $f_{sw} = \omega_{sw}/2\pi$ is the spin-wave dispersion in the bare-YIG region given by 2.37, $i = 1, 2, \dots, N$ indexes the measurements at the different magnetic fields $B_z(i)$, $k_{\text{YIG}}^{(j)}(i)$ are the corresponding extracted wavenumbers (see previous subsection), M_s is a free parameter, and $j = 1$ ($j = 2$) indicates the field-aligned (misaligned) NV ensemble used in Fig. 5.4a (Fig. 5.4b) of the main text.

Having found M_s , we extract λ_L using a similar procedure, by least-squares minimization of

$$\chi_j^2 = \sum_{i=1}^N (f_{sw}(B_z(i), k_{\text{YIG/SC}}^{(j)}(i), M_s, \lambda_L) - f_{NV_j}(i))^2. \quad (5.6)$$

Here, $f_{sw} = \omega_{sw}/2\pi$ is the spin-wave dispersion in the YIG/MoRe region given by Eq. 5.41, M_s is fixed, and λ_L is a free parameter. Additional parameters we keep fixed in the fitting procedures are the thicknesses of the YIG and MoRe films.

SPIN-WAVE DISPERSION UNDERNEATH A SUPERCONDUCTING THIN FILM.

Here we derive the spin-wave dispersion for the magnet-superconductor hybrid (Eqs. 5.1-5.2 of the main text). We do so by integrating the magnetic field generated by the spin-wave-induced Meissner currents self-consistently into the linearized Landau-Lifshitz-Gilbert (LLG) equation.

We consider a superconducting film located between $0 < x < h$ on top of a magnetic film located between $-t < x < 0$, both infinite in the yz -plane. As we consider spin waves with an in-plane wavevector $\mathbf{k} = (k_y, k_z)$, we analyze the system in 2D Fourier space. Because the fields applied in our work are much smaller than $\mu_0 M_s$, where M_s is the YIG saturation magnetization, the equilibrium magnetization lies predominantly in-plane along z .

THE MAGNETIC STRAY FIELD OF SPIN WAVES IN A THIN-FILM MAGNET

The magnetic field generated by a magnetization $\mathbf{M}(\mathbf{r}) = M_s \mathbf{m}(\mathbf{r})$, where \mathbf{m} is a unit vector, is

$$\mathbf{B}(\mathbf{r}) = \mu_0 M_s \int \mathbf{m}(\mathbf{r}') \Gamma(\mathbf{r} - \mathbf{r}') d\mathbf{r}' \quad (5.7)$$

where $\Gamma(\mathbf{r})$ is the dipolar tensor [37]. Fourier transforming over the y, z coordinates yields

$$\mathbf{B}(\mathbf{k}, x) = \mu_0 M_s \int_{-t}^0 \Gamma(\mathbf{k}, x - x') \mathbf{m}(\mathbf{k}, x') dx' \quad (5.8)$$

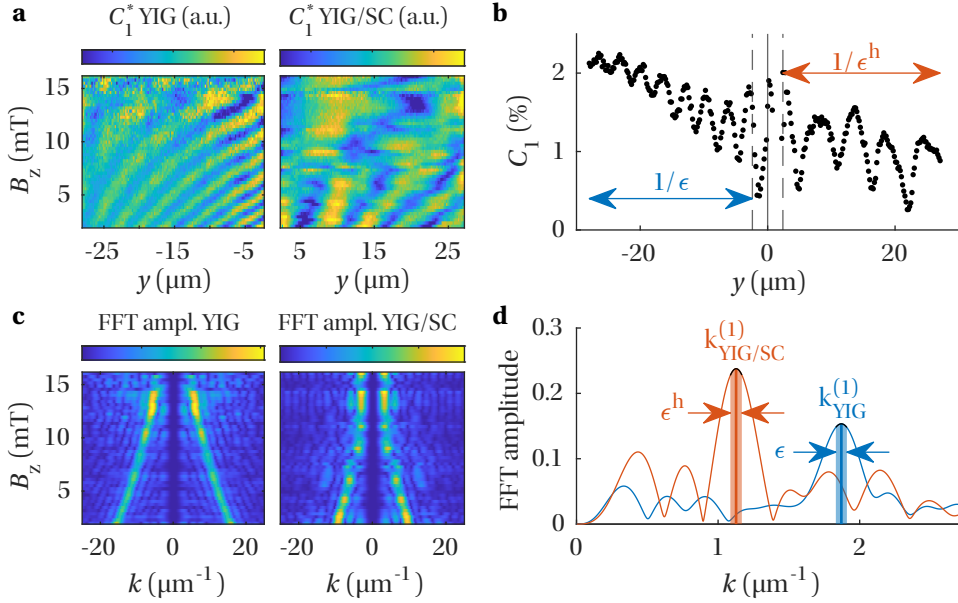


Figure 5.8. **Extracting the spin-wavenumber through Fourier analysis.** (a) Detrended and line-by-line normalized field-dependent ESR contrast for the YIG and YIG/MoRe regions. (b) ESR contrast as a function of position, example of raw data. The solid vertical line indicates the border between bare magnet ($y < 0$) and the heterostructure ($y > 0$), we ignore data between the dashed lines in our fitting process. (c) Fourier transform of data in (a) padded with zeros. (d) Fourier transform of data in (b) padded with zeros. The wavenumbers k_{YIG} and $k_{\text{YIG/SC}}$ are determined by finding the peak location in the Fourier spectrum. The uncertainty $\epsilon^{(h)}$ (indicated by the shading) is determined by the inverse of the sampling range.

with $\Gamma(\mathbf{k}, x)$ the dipolar tensor in 2D Fourier space, given by

$$\Gamma(\mathbf{k}, x) = -\frac{1}{2} k e^{-k|x|} \begin{pmatrix} 2\delta(x)/k - 1 & i\sigma_x s & i\sigma_x c \\ i\sigma_x s & s^2 & sc \\ i\sigma_x c & sc & c^2 \end{pmatrix} \quad (5.9)$$

where we defined $\sigma_x = \text{sign}(x)$, $s = k_y/k$, $c = k_z/k$, and $k = |\mathbf{k}|$.

Spin waves are described by the dynamics of the transverse magnetization components $m_{x,y}$. Because the spin-wavelengths in our work are much larger than the YIG film thickness, we are in the 2D limit such that $\mathbf{m}(\mathbf{k}, x) = \mathbf{m}(\mathbf{k})$, i.e., the magnetization dynamics are homogeneous over the film thickness. In this case, the out-of-plane component of the magnetic field above the film is

$$B_x(\mathbf{k}, x) = \frac{\mu_0 M_s}{2} (1 - e^{-kt}) (m_x - i s m_y) e^{-kx}, \quad (5.10)$$

which we write as $B_x^{sw}(\mathbf{k}, x) = B_0(\mathbf{k}) e^{-kx}$. In the following, we omit the in-plane wave vector \mathbf{k} from the argument lists for brevity.

THE MAGNETIC FIELD GENERATED BY THE SPIN-WAVE INDUCED EDDY CURRENTS

The in-plane eddy currents in the metal film are induced by the out-of-plane component of the magnetic field according to Faraday's law:

$$-[\nabla \times \mathbf{E}]_x = -\frac{\partial E_z}{\partial y} + \frac{\partial E_y}{\partial z} = \frac{\partial B_x(\mathbf{r}, t)}{\partial t}, \quad (5.11)$$

where \mathbf{E} is the electric field. In Fourier space, this yields:

$$cJ_y(x) - sJ_z(x) = \frac{\omega\sigma}{k} B_x(x) \quad (5.12)$$

where $\mathbf{J} = \sigma\mathbf{E}$ with σ the metal conductivity. We calculate the magnetic field generated by the current distribution $\mathbf{J} = (J_y, J_z)$ by expressing \mathbf{J} as an effective out-of-plane magnetization [38] using:

$$M_s^{\text{eff}} m_x^{\text{eff}}(x) = -\frac{i}{k} (cJ_y(x) - sJ_z(x)) \quad (5.13)$$

The total field $B_x(x)$ is the sum of the eddy-current field and the spin-wave drive field

$$B_x(x) = \mu_0 M_s^{\text{eff}} \int_0^h \Gamma_{xx}(x-x') m_x^{\text{eff}}(x') dx' + B_x^{sw}(x) \quad (5.14)$$

Substituting 5.12 and the expression for Γ_{xx} from 5.9 leads to the integral equation

$$B_x(x) = \frac{-i\omega\mu_0\sigma}{k^2} \int_0^h \frac{1}{2} k e^{-k|x-x'|} B_x(x') dx' + B_x^{sw}(x) \quad (5.15)$$

which needs to be solved self-consistently. Note we excluded the delta function from Γ_{xx} because we are analyzing free currents instead of spins. To solve 5.15, we use a trial solution $B_x(x) = A_1 B_0 e^{-\kappa x} + A_2 B_0 e^{\kappa x}$. This gives

$$\begin{aligned} A_1 e^{-\kappa x} + A_2 e^{\kappa x} &= \frac{-i\omega\mu_0\sigma}{2k^2} A_1 \left(\frac{k}{k-\kappa} (e^{-\kappa x} - e^{-kx}) + \frac{k}{k+\kappa} (e^{-\kappa x} - e^{-\kappa h} e^{k(x-h)}) \right) \\ &+ \frac{-i\omega\mu_0\sigma}{2k^2} A_2 \left(\frac{k}{k+\kappa} (e^{\kappa x} - e^{-kx}) + \frac{k}{k-\kappa} (e^{\kappa x} - e^{\kappa h} e^{k(x-h)}) \right) + e^{-kx} \end{aligned} \quad (5.16)$$

From equating the prefactors of the exponents with the same x -dependence, we get the solution

$$\begin{aligned} \kappa &= \sqrt{k^2 + i\omega\mu_0\sigma}, \\ A_1 &= A \frac{1}{1 - \frac{a_-^2}{a_+^2} e^{-2\kappa h}}, \\ A_2 &= -A \frac{a_-}{a_+} e^{-2\kappa h} \frac{1}{1 - \frac{a_-^2}{a_+^2} e^{-2\kappa h}}, \end{aligned} \quad (5.17)$$

where we defined $A = \frac{2ik^2 a_-}{\omega\mu_0\sigma}$ and $a_{\pm} = 1 \pm \kappa/k$.

Having solved for $B(x)$ inside the metal, we obtain the eddy currents from 5.12. As before, we calculate the field generated by the eddy currents by expressing these currents as an effective magnetization using 5.13:

$$\mu_0 M_s^{\text{eff}} m_x^{\text{eff}}(x) = 2\left(1 - \frac{\kappa}{k}\right) \frac{A_1 B_0 e^{-\kappa x} + A_2 B_0 e^{\kappa x}}{A} \quad (5.18)$$

The eddy-current field above and below the metal is given by:

$$B_x^e(x > h) = \mu_0 M_s^{\text{eff}} \int_0^h \frac{1}{2} k e^{-k(x-x')} m_x^{\text{eff}}(x') dx' \quad (5.19)$$

$$= \left(A_1 (e^{a-kh} - 1) + A_2 \frac{a_-}{a_+} (e^{a_+ kh} - 1) \right) \frac{B_0}{A} e^{-kx} \quad (5.20)$$

$$B_x^e(x < 0) = \mu_0 M_s^{\text{eff}} \int_0^h \frac{1}{2} k e^{k(x-x')} m_x^{\text{eff}}(x') dx' \quad (5.21)$$

$$= \left(A_1 \frac{a_-}{a_+} (1 - e^{-2\kappa h}) \right) \frac{B_0}{A} e^{kx} \quad (5.22)$$

$$= \frac{-i\omega\mu_0\sigma}{k^2} \frac{1 - e^{-2\kappa h}}{a_+^2 - a_-^2 e^{-2\kappa h}} B_0 e^{kx} \quad (5.23)$$

To calculate the coupling to the lowest-order perpendicular spin-wave mode studied in our work, we average 5.23 over $-t < x < 0$, which corresponds to replacing $e^{kx} \rightarrow g_t = \frac{1 - e^{-kt}}{kt}$.

In the limit $2|\kappa|h \ll 1$, 5.23 reduces to $B_x^e(x < 0) = \frac{-i\omega\mu_0\sigma h}{2k} B_0 e^{kx}$ as found in [15]. However, in our experiments we are not in this limit as $\kappa > k$ because of the superconducting penetration depth (see next section). Furthermore, we observe that the expression reduces to $B_x^e(x < 0) = -B_0 e^{kx}$ when $|\omega\mu_0\sigma| \gg k^2$. In this limit the screening exactly cancels the drive field at $x = 0$ and has become independent of σ .

DECAY OF THE MAGNETIC FIELD IN A METAL/SUPERCONDUCTOR THIN FILM

We calculate the decay constant κ for a superconducting film. Using a two-fluid model, the conductivity of the superconductor is $\sigma = \sigma' - i\frac{1}{\omega L'}$, where $\sigma' = \sigma_n n_n(T)/n$, with σ_n the normal-state conductivity of the metal, n_n/n the fraction of non-cooper pair electrons, and $L' = \mu_0 \lambda^2(T)$ is the specific kinetic inductance, with λ_L the London penetration depth. Defining the skin depth $\delta = \sqrt{\frac{2}{\sigma_n \omega \mu_0}}$, we get

$$\kappa = k \sqrt{1 + i\omega\mu_0\sigma/k^2} = k \sqrt{1 + \frac{2i}{k^2 \delta^2(T)} \frac{n_n(T)}{n} + \frac{1}{k^2 \lambda_L^2(T)}} \quad (5.24)$$

The imaginary term underneath the square root induces additional spin-wave damping [10], but this effect is small because the MoRe skin depth $\delta \approx 4\mu\text{m}$ for $\omega/2\pi = 3\text{ GHz}$ far exceeds the MoRe film thickness and because the fraction of normal electrons $n_n(T)$ decreases quickly with decreasing temperature [28]. As such, we neglect the real part of the conductivity when calculating the hybridized spin-wave dispersion below.

COMPARISON GEOMETRIC AND KINETIC INDUCTANCE

To assess the role of geometric inductance in our measurements, we first consider the energy cost of creating a sinusoidal current pattern in the superconducting strip $J_z(y) = J_0 \cos(k_0 y) \cos(\omega t)$. The kinetic energy density of the supercurrent is $\mu_0 \lambda_L^2 J_z^2 / 2$ [39]. The kinetic inductance per unit length is defined by

$$\frac{1}{2} L_k I_z^2 = \frac{1}{2} \mu_0 \lambda_L^2 \int J_z^2 dx dy \quad (5.25)$$

and depends on temperature through λ_L . The geometric inductance per unit length is defined by

$$\frac{1}{2} L_g I_z^2 = \frac{1}{2 \mu_0} \int B^2 dx dy \quad (5.26)$$

with $I_z = I_0 \cos(\omega t)$ the current running in the z direction, where $I_0 = \frac{2W J_0 h}{\pi}$. The geometric inductance is independent of temperature. Neglecting the finite thickness of the superconductor, the magnetic field generated by J_z is

$$\begin{aligned} B_x &= -\frac{\mu_0}{2} J_0 h e^{-k_0 |x|} \sin(k_0 y) \cos(\omega t) \\ B_y &= \frac{\mu_0}{2} J_0 h e^{-k_0 |x|} \cos(k_0 y) \cos(\omega t). \end{aligned} \quad (5.27)$$

It follows that the ratio of the kinetic and geometric inductance is

$$\frac{L_k}{L_g} = \mu_0^2 \lambda_L^2 \frac{\int J_z^2 dx dy}{\int B^2 dx dy} = k_0 \Lambda \quad (5.28)$$

where we assumed $k_0 W \gg 1$ so that we can neglect edge effects and where $\Lambda = 2\lambda_L^2/h$ is the Pearl length [40]. Considering $\lambda_L > 0.4 \mu\text{m}$ and spin-wavenumbers $k_0 > 0.8 \mu\text{m}^{-1}$ (c.f. Fig. 5.6b and black line in Fig. 5.6c of the main text), we get $k_0 \Lambda > 2$. We observe that the kinetic inductance dominates.

To assess the inductance for the eddy-current pattern excited by the spin waves, we now consider the traveling-wave eddy-current pattern $J_z(y, t) = J_0 \cos(ky - \omega t)$ running in an infinite metal film. In this case, the total current running in the $+z$ direction is independent of time, as is the energy density of the associated magnetic field:

$$\frac{1}{2\mu_0} (B_x^2 + B_y^2) = \frac{\mu_0 (J_0 h)^2}{2 \cdot 4} e^{-2k_0 |x|} \quad (5.29)$$

This situation resembles the time-independent magnetic field generated by a DC current in a wire: the geometric inductance does not impede the motion of the eddy current pattern. However, at the edges of the superconducting strip, this does not hold and both the current and the magnetic-field energy density vary in time. Considering the effect of the edges only, the time-dependent part of the total current is, at most, $I(t) = I_1 \cos(\omega t)$, with $I_1 = J_0 h \frac{2}{k_0}$. Considering the $W = 30 \mu\text{m}$ width of the superconducting strip, we thus expect the role of L_g to be suppressed by a factor $I_1/I_0 = k_0 W/\pi \gg 1$, and the kinetic inductance to dominate by a factor $k_0^2 \Lambda W \gg 1$.

MEISSNER CURRENT CONTRIBUTION TO THE LLG-EQUATION

To calculate the spin-wave dispersion in our YIG-superconductor hybrid, we incorporate the magnetic field generated by the spin-wave induced eddy currents into the LLG equation. The spin waves generate a magnetic field $B_x = B_0 e^{-kx}$, with (see 5.10)

$$B_0 = \frac{\mu_0 M_s k t}{2} g_t (m_x - i s m_y) \quad (5.30)$$

Substituting into 5.23 yields the eddy-current-generated field in the magnetic film. Averaging this field over $-t < x < 0$ to calculate the coupling to the lowest-order perpendicular spin-wave mode leads to

$$\begin{aligned} \gamma \bar{B}_{e,x} &= i \omega \alpha_m (m_x - i s m_y), \\ \gamma \bar{B}_{e,y} &= -\alpha_m \omega s (m_x - i s m_y), \end{aligned} \quad (5.31)$$

where

$$\alpha_m = -\frac{\gamma \mu_0^2 M_s \sigma k t}{2k^2} g_t^2 \frac{1 - e^{-2\kappa h}}{a_+^2 - a_-^2 e^{-2\kappa h}} \quad (5.32)$$

is a dimensionless factor that alters the spin-wave dispersion as discussed in the next section. Assuming the kinetic inductance to dominate (see section above), we have $\sigma = \frac{-i}{\omega \mu_0 \lambda_L^2}$ so that

$$\alpha_m = i \frac{\omega_L}{\omega} \quad \text{with} \quad \omega_L = \frac{\gamma \mu_0 M_s k t}{2k^2 \lambda_L^2} g_t^2 \frac{1 - e^{-2\kappa h}}{a_+^2 - a_-^2 e^{-2\kappa h}} \quad (5.33)$$

We note that $\omega_L \rightarrow 0$ for both $k \rightarrow 0$ and $k \rightarrow \infty$ as the spin-wave stray field vanishes in this limit.

SPIN-WAVE DISPERSION UNDERNEATH THE SUPERCONDUCTOR

To derive the spin-wave dispersion underneath the superconductor, we add the eddy-current field of 5.31 to the effective magnetic field

$$\begin{aligned} \gamma B_x &= -(\omega_M(1-f) + \omega_D k^2) m_x + i \omega \alpha_m (m_x - i s m_y) + \gamma B_{AC,x}, \\ \gamma B_y &= -(\omega_M f + \omega_D k^2) m_y - \alpha_m \omega s (m_x - i s m_y) + \gamma B_{AC,y}, \end{aligned} \quad (5.34)$$

such that the linearized LLG equation 2.10 becomes

$$\begin{aligned} -i \omega m_x &= -(\omega_3 - i(s^2 \alpha_m + \alpha) \omega) m_y - \alpha_m s \omega m_x + \gamma B_{AC,y}, \\ -i \omega m_y &= (\omega_2 - i(\alpha_m + \alpha) \omega) m_x - \alpha_m \omega s m_y - \gamma B_{AC,x}, \end{aligned} \quad (5.35)$$

where ω_2 and ω_3 are given in Eq. 2.34. In matrix form:

$$\begin{pmatrix} \omega_2 - i(\alpha + \alpha_m) \omega & (i - \alpha_m s) \omega \\ -(i - \alpha_m s) \omega & \omega_3 - i(\alpha + \alpha_m s^2) \omega \end{pmatrix} \begin{pmatrix} m_x \\ m_y \end{pmatrix} = \gamma \begin{pmatrix} B_{AC,x} \\ B_{AC,y} \end{pmatrix}. \quad (5.36)$$

The resulting susceptibility is singular when

$$(\omega_2 - i(\alpha + \alpha_m) \omega)(\omega_3 - i(\alpha + s^2 \alpha_m) \omega) + (i - s \alpha_m)^2 \omega^2 = 0. \quad (5.37)$$

Splitting α_m into its real and imaginary parts via $\alpha_m = \beta + i\zeta$ and disregarding 2nd-order terms in α and β , we get

$$\omega_2\omega_3 + \omega\zeta(\omega_2s^2 + \omega_3) - \omega^2(1 - 2s\zeta) = 0 \quad (5.38)$$

We recall that $\alpha_m \approx i\zeta = i\omega_L/\omega$, with ω_L given by 5.33. Substituting into 5.38, we get

$$\omega_2\omega_3 + \omega_L(\omega_2s^2 + \omega_3) - \omega^2 + 2s\omega_L\omega = 0 \quad (5.39)$$

where we disregarded 2nd-order terms in α . Solving this equation leads to

$$\omega_{sw} = s\omega_L \pm \sqrt{\omega_2\omega_3} \sqrt{1 + \frac{\eta^2s^2 + 1}{\eta} \frac{\omega_L}{\sqrt{\omega_2\omega_3}} + \frac{s^2\omega_L^2}{\omega_2\omega_3}} \quad (5.40)$$

where $\eta = \sqrt{\omega_3/\omega_2}$. Neglecting terms of order $\omega_L^2/\omega_2\omega_3$ and disregarding the negative-frequency solution leads to

$$\omega_{sw} = \sqrt{\omega_2\omega_3} + \omega_L \frac{(\eta s + 1)^2}{2\eta} \quad (5.41)$$

which yields Eq. 5.1 of the main text $f_{YIG/SC} = f_{YIG} + f_{SC}$, where $f_{YIG} = \sqrt{\omega_2\omega_3}/2\pi$ is the bare-YIG dispersion and

$$f_{SC} = \frac{\gamma\mu_0 M_s k t}{2k^2\lambda_L^2} g_t^2 \frac{1 - e^{-2\kappa h}}{a_+^2 - a_-^2 e^{-2\kappa h}} \frac{(\eta s + 1)^2}{2\eta} \approx \gamma\mu_0 M_s k t r \frac{1 - e^{-2h/\lambda_L}}{(k\lambda_L + 1)^2 - (k\lambda_L - 1)^2 e^{-2h/\lambda_L}} \quad (5.42)$$

is the superconductor-induced shift, where we defined the dimensionless geometrical factor $r = \frac{g_t^2 (\eta s + 1)^2}{2}$, and where the approximation holds when the kinetic inductance dominates the impedance and when $k^2\lambda_L^2 \ll 1$ (c.f. 5.24 and Fig. 5.6b-c of the main text).

SUPPORTING DATA

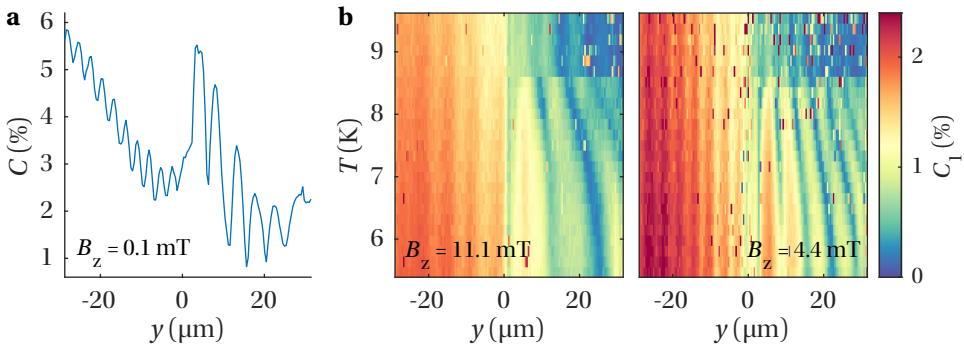


Figure 5.9. **Temperature tunable wavelength change with purely in-plane magnetic fields.** (a) ESR contrast as a function of position at $B_z = 0.1 \text{ mT}$, $f = 2.874 \text{ GHz}$ and $T = 5.5 \text{ K}$, showing hybrid modes with stretched wavelength for $y > 0$. Measurements are taken with a field applied in-plane, $\theta = 0 \text{ deg.}$, such that $B_z = B_{\text{NV}}$. (b) Spin waves in YIG and YIG/MoRe for two different, purely in-plane fields $B_z = 11.1 \text{ mT}$ and 4.4 mT with stretched-wavelength modes for $y > 0$ and $T < T_c$. As the applied field is in-plane, Meissner screening of the bias field B_{NV} is negligible and does not introduce a static field inhomogeneity that affects the spin-wave dispersion.

5

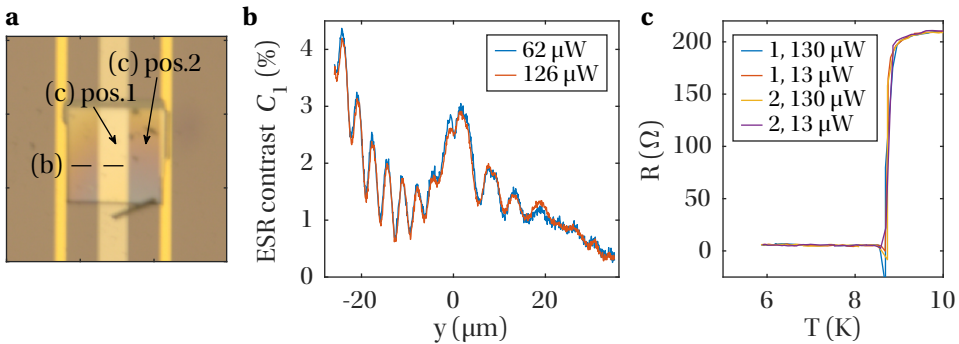


Figure 5.10. **Excluding global heating of the superconductor due to NV excitation laser.** (a) To exclude the possible influence of laser heating on the extracted spin-wave lengths, we image the spin wavelength and measure the DC resistance of the MoRe strip as different laser powers and laser positions. The dashed line in the microscope image indicates the location of the ESR linetraces in panel (b). The arrows indicate the laser location in the resistance measurements of panel (c). (b) Spatial line trace of the NV ESR contrast at $T = 5.5 \text{ K}$ with the power of our 520 nm NV excitation laser set at 62 μW and 126 μW . We do not observe a significant difference in spin-wave lengths (c) DC resistance of the MoRe strip with the laser focused at the two locations indicated in (a), for various laser powers. We do not observe a significant difference in $R|_{T < T_c}$ and T_c between the measurements.

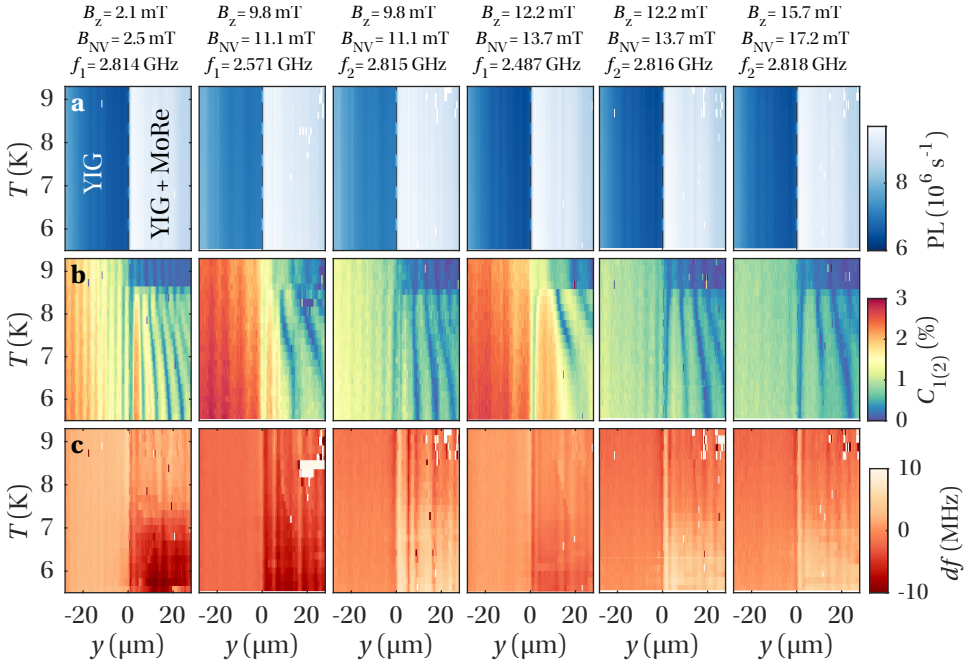


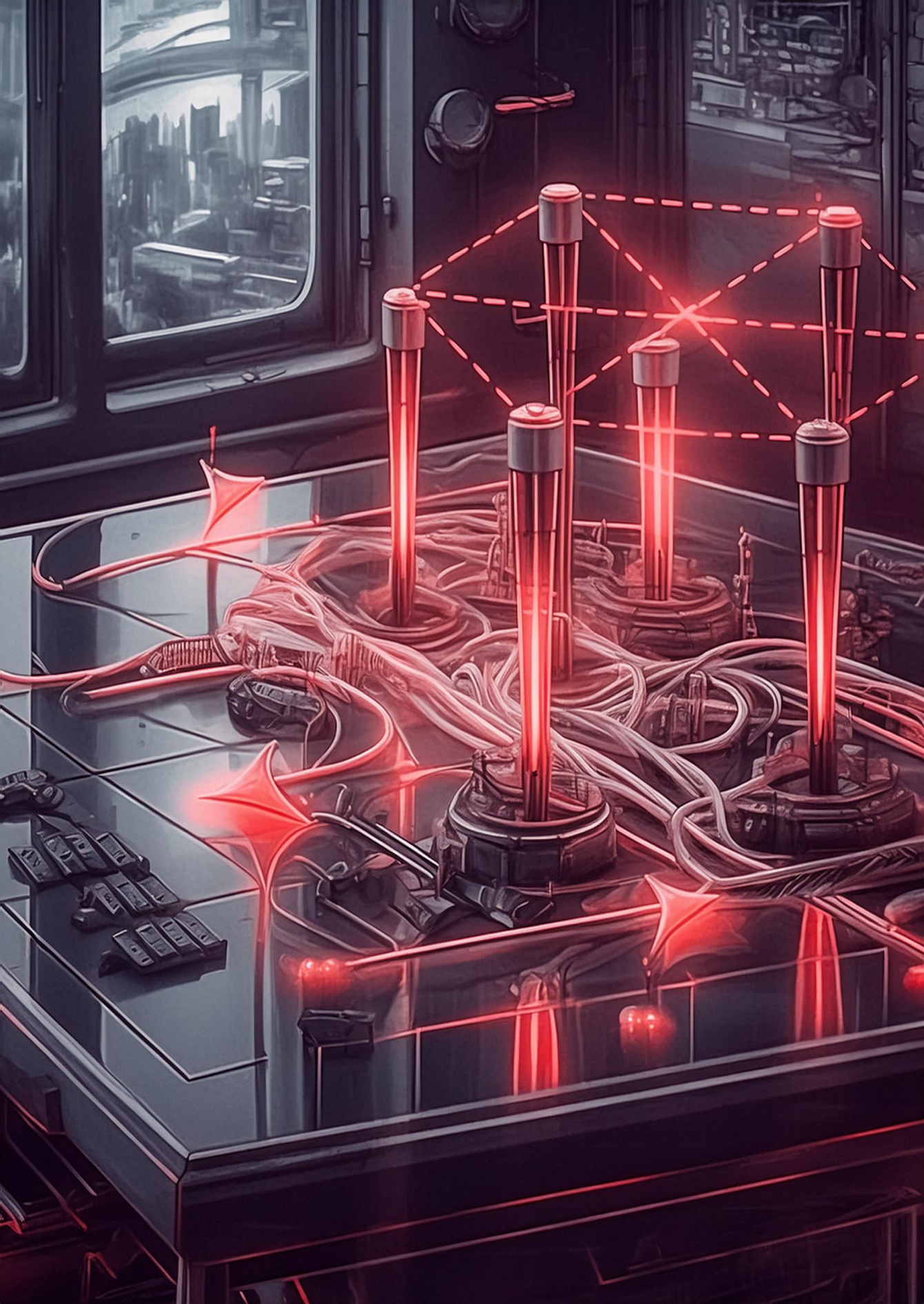
Figure 5.11. **Spin-wave length as a function of temperature for various magnetic fields.** (a) Spatial linetraces of the NV photoluminescence (PL) while cooling through the superconducting phase transition with $T_c = 8.7 \text{ K}$, showing the location of the MoRe strip at $y > 0$. (b) NV ESR contrast $C_{1(2)}$, showing the temperature-dependent shift in wavenumber in the YIG/MoRe region ($y > 0, T < T_c$) while the wavenumber in the bare-YIG region ($y < 0$) remains unchanged. (c) ESR frequency shift df as a function of position and temperature. Below T_c , the field along the NV axis increases (decreases) for field-aligned (misaligned) NV ensembles, due to flux focusing of the magnetic bias field B_{NV} through the hot spot created by the NV-excitation laser. Data are measured for various fields and NV ensembles, indicated at the top of the figure, where the subscript 1(2) indicates field-aligned (misaligned) NV ensembles.

REFERENCES

- [1] S. A. Wolf *et al.* “Spintronics: A spin-based electronics vision for the future”. *Science* 294.5546 (2001), pp. 1488–1495. ISSN: 00368075. DOI: [10.1126/science.1065389](https://doi.org/10.1126/science.1065389).
- [2] A. V. Chumak *et al.* “Magnon spintronics”. *Nature Physics* 11.6 (2015), pp. 453–461. ISSN: 17452481. DOI: [10.1038/nphys3347](https://doi.org/10.1038/nphys3347).
- [3] A. Barman *et al.* “The 2021 Magnonics Roadmap”. *Journal of Physics Condensed Matter* 33.41 (2021). ISSN: 1361648X. DOI: [10.1088/1361-648X/abec1a](https://doi.org/10.1088/1361-648X/abec1a).
- [4] J. Sinova *et al.* “Spin Hall effects”. *Reviews of Modern Physics* 87.4 (2015), pp. 1213–1260. ISSN: 15390756. DOI: [10.1103/RevModPhys.87.1213](https://doi.org/10.1103/RevModPhys.87.1213).
- [5] L. J. Cornelissen *et al.* “Long-distance transport of magnon spin information in a magnetic insulator at room temperature”. *Nature Physics* 11.12 (2015), pp. 1022–1026. ISSN: 17452481. DOI: [10.1038/nphys3465](https://doi.org/10.1038/nphys3465).
- [6] A. Hamaddeh *et al.* “Full control of the spin-wave damping in a magnetic insulator using spin-orbit torque”. *Physical Review Letters* 113.19 (2014), pp. 1–5. ISSN: 10797114. DOI: [10.1103/PhysRevLett.113.197203](https://doi.org/10.1103/PhysRevLett.113.197203).
- [7] T. Yu *et al.* “Chiral excitation of spin waves in ferromagnetic films by magnetic nanowire gratings”. *Physical Review B* 99.13 (2019), pp. 1–12. ISSN: 24699969. DOI: [10.1103/PhysRevB.99.134424](https://doi.org/10.1103/PhysRevB.99.134424).
- [8] J. Chen *et al.* “Strong Interlayer Magnon-Magnon Coupling in Magnetic Metal-Insulator Hybrid Nanostructures”. *Physical Review Letters* 120.21 (2018), p. 217202. ISSN: 10797114. DOI: [10.1103/PhysRevLett.120.217202](https://doi.org/10.1103/PhysRevLett.120.217202).
- [9] Y. Sun *et al.* “Damping in yttrium iron garnet nanoscale films capped by platinum”. *Physical Review Letters* 111.10 (2013), pp. 1–5. ISSN: 00319007. DOI: [10.1103/PhysRevLett.111.106601](https://doi.org/10.1103/PhysRevLett.111.106601).
- [10] I. Bertelli *et al.* “Imaging Spin-Wave Damping Underneath Metals Using Electron Spins in Diamond”. *Advanced Quantum Technologies* 4.12 (2021), pp. 1–6. ISSN: 25119044. DOI: [10.1002/qute.202100094](https://doi.org/10.1002/qute.202100094). arXiv: [2106.02508](https://arxiv.org/abs/2106.02508).
- [11] Z. Y. Zhang *et al.* “Magnetic lenses using different MgB₂ bulk superconductors”. *Superconductor Science and Technology* 25.2 (2012). ISSN: 09532048. DOI: [10.1088/0953-2048/25/2/025009](https://doi.org/10.1088/0953-2048/25/2/025009).
- [12] A. Blais *et al.* “Circuit quantum electrodynamics”. *Reviews of Modern Physics* 93.2 (2021), p. 25005. ISSN: 15390756. DOI: [10.1103/RevModPhys.93.025005](https://doi.org/10.1103/RevModPhys.93.025005). arXiv: [2005.12667](https://arxiv.org/abs/2005.12667).

- [13] I. A. Golovchanskiy *et al.* “Nonlinear spin waves in ferromagnetic/superconductor hybrids”. *Journal of Applied Physics* 127.9 (2020). ISSN: 10897550. DOI: [10.1063/1.5141793](https://doi.org/10.1063/1.5141793).
- [14] O. V. Dobrovolskiy *et al.* “Magnon–fluxon interaction in a ferromagnet/superconductor heterostructure”. *Nature Physics* 15.5 (2019), pp. 477–482. ISSN: 17452481. DOI: [10.1038/s41567-019-0428-5](https://doi.org/10.1038/s41567-019-0428-5). arXiv: [1901.06156](https://arxiv.org/abs/1901.06156).
- [15] T. Yu *et al.* “Efficient Gating of Magnons by Proximity Superconductors”. *Physical Review Letters* 129.11 (2022), p. 117201. ISSN: 10797114. DOI: [10.1103/PhysRevLett.129.117201](https://doi.org/10.1103/PhysRevLett.129.117201). arXiv: [2201.09532](https://arxiv.org/abs/2201.09532).
- [16] L. Rondin *et al.* “Magnetometry with nitrogen-vacancy defects in diamond”. *Reports on Progress in Physics* 77.5 (2014). ISSN: 00344885. DOI: [10.1088/0034-4885/77/5/056503](https://doi.org/10.1088/0034-4885/77/5/056503). arXiv: [1311.5214](https://arxiv.org/abs/1311.5214).
- [17] T. X. Zhou *et al.* “A magnon scattering platform”. *Proceedings of the National Academy of Sciences of the United States of America* 118.25 (2021), pp. 1–6. ISSN: 10916490. DOI: [10.1073/pnas.2019473118](https://doi.org/10.1073/pnas.2019473118). arXiv: [2004.07763](https://arxiv.org/abs/2004.07763).
- [18] I. Bertelli *et al.* “Magnetic resonance imaging of spin-wave transport and interference in a magnetic insulator”. *Science Advances* 6.46 (2020), pp. 1–8. ISSN: 23752548. DOI: [10.1126/sciadv.abd3556](https://doi.org/10.1126/sciadv.abd3556). arXiv: [2004.07746](https://arxiv.org/abs/2004.07746).
- [19] F. Casola *et al.* “Probing condensed matter physics with magnetometry based on nitrogen-vacancy centres in diamond”. *Nature Reviews Materials* 3 (2018). ISSN: 20588437. DOI: [10.1038/natrevmats.2017.88](https://doi.org/10.1038/natrevmats.2017.88).
- [20] R. Schirhagl *et al.* “Nitrogen-vacancy centers in diamond: Nanoscale sensors for physics and biology”. *Annual Review of Physical Chemistry* 65 (2014), pp. 83–105. ISSN: 0066426X. DOI: [10.1146/annurev-physchem-040513-103659](https://doi.org/10.1146/annurev-physchem-040513-103659).
- [21] D. R. Glenn *et al.* “Micrometer-scale magnetic imaging of geological samples using a quantum diamond microscope”. *Geochemistry, Geophysics, Geosystems* 18.8 (2017), pp. 3254–3267. ISSN: 15252027. DOI: [10.1002/2017GC006946](https://doi.org/10.1002/2017GC006946). arXiv: [1707.06714](https://arxiv.org/abs/1707.06714).
- [22] P. Andrich *et al.* “Long-range spin wave mediated control of defect qubits in nanodiamonds”. *npj Quantum Information* 3.1 (2017), pp. 1–6. ISSN: 20566387. DOI: [10.1038/S41534-017-0029-Z](https://doi.org/10.1038/S41534-017-0029-Z).
- [23] C. S. Wolfe *et al.* “Off-resonant manipulation of spins in diamond via precessing magnetization of a proximal ferromagnet”. *Physical Review B - Condensed Matter and Materials Physics* 89.18 (2014), pp. 1–5. ISSN: 1550235X. DOI: [10.1103/PhysRevB.89.180406](https://doi.org/10.1103/PhysRevB.89.180406). arXiv: [1403.0656](https://arxiv.org/abs/1403.0656).
- [24] A. Gurevich *et al.* *Magnetic Oscillations and Waves*. CRC Press, Inc., 1996.
- [25] S. Seshadri. “Surface Magnetostatic Modes of a Ferrite Slab”. *Proceedings of the IEEE* (1970), pp. 506–507.
- [26] S. Knauer *et al.* “Propagating spin-wave spectroscopy in a liquid-phase epitaxial nanometer-thick YIG film at millikelvin temperatures”. *Journal of Applied Physics* 133.14 (2023). ISSN: 10897550. DOI: [10.1063/5.0137437](https://doi.org/10.1063/5.0137437).

- [27] A. G. Shishkin *et al.* “Planar MoRe-based direct current nanoSQUID”. *Superconductor Science and Technology* 33.6 (2020). ISSN: 13616668. DOI: [10.1088/1361-6668/ab877c](https://doi.org/10.1088/1361-6668/ab877c).
- [28] M. Tinkham. *Introduction to superconductivity*. 2nd. Dover Publications, 2004.
- [29] R. Gieniusz *et al.* “Single antidot as a passive way to create caustic spin-wave beams in yttrium iron garnet films”. *Applied Physics Letters* 102.10 (2013). ISSN: 00036951. DOI: [10.1063/1.4795293](https://doi.org/10.1063/1.4795293).
- [30] A. V. Chumak *et al.* “Magnonic crystals for data processing”. *Journal of Physics D: Applied Physics* 50.24 (2017). ISSN: 13616463. DOI: [10.1088/1361-6463/aa6a65](https://doi.org/10.1088/1361-6463/aa6a65). arXiv: [1702.06701](https://arxiv.org/abs/1702.06701).
- [31] W. K. Kwok *et al.* “Vortices in high-performance high-temperature superconductors”. *Reports on Progress in Physics* 79.11 (2016). ISSN: 00344885. DOI: [10.1088/0034-4885/79/11/116501](https://doi.org/10.1088/0034-4885/79/11/116501).
- [32] V. E. Calado *et al.* “Ballistic Josephson junctions in edge-contacted graphene”. *Nature Nanotechnology* 10.9 (2015), pp. 761–764. ISSN: 17483395. DOI: [10.1038/nnano.2015.156](https://doi.org/10.1038/nnano.2015.156). arXiv: [1501.06817](https://arxiv.org/abs/1501.06817).
- [33] K. Makise *et al.* “Estimations of superconducting fluctuation effects in amorphous MoRu and MoRe alloy thin films”. *Materials Research Express* 5.9 (2018). ISSN: 20531591. DOI: [10.1088/2053-1591/aad65c](https://doi.org/10.1088/2053-1591/aad65c).
- [34] I. S. Veshchunov *et al.* “Optical manipulation of single flux quanta”. *Nature Communications* 7 (2016), pp. 1–7. ISSN: 20411723. DOI: [10.1038/ncomms12801](https://doi.org/10.1038/ncomms12801).
- [35] S. E. Lillie *et al.* “Laser Modulation of Superconductivity in a Cryogenic Wide-field Nitrogen-Vacancy Microscope”. *Nano Letters* 20.3 (2020), pp. 1855–1861. ISSN: 15306992. DOI: [10.1021/acs.nanolett.9b05071](https://doi.org/10.1021/acs.nanolett.9b05071). arXiv: [1912.02936](https://arxiv.org/abs/1912.02936).
- [36] S. Pezzagna *et al.* “Creation efficiency of nitrogen-vacancy centres in diamond”. *New Journal of Physics* 12 (2010). ISSN: 13672630. DOI: [10.1088/1367-2630/12/6/065017](https://doi.org/10.1088/1367-2630/12/6/065017).
- [37] B. A. Kalinikos *et al.* “Theory of dipole-exchange spin wave spectrum for ferromagnetic films with mixed exchange boundary conditions”. *Journal of Physics C: Solid State Physics* 19.35 (1986), pp. 7013–7033. ISSN: 00223719. DOI: [10.1088/0022-3719/19/35/014](https://doi.org/10.1088/0022-3719/19/35/014).
- [38] F. Casola *et al.* “Probing condensed matter physics with magnetometry based on nitrogen-vacancy centres in diamond”. *Nature Reviews Materials* 3 (2018). ISSN: 20588437. DOI: [10.1038/natrevmats.2017.88](https://doi.org/10.1038/natrevmats.2017.88).
- [39] J. R. Clem. “Inductances and attenuation constant for a thin-film superconducting coplanar waveguide resonator”. *Journal of Applied Physics* 113.1 (2013). ISSN: 00218979. DOI: [10.1063/1.4773070](https://doi.org/10.1063/1.4773070). arXiv: [1210.5929](https://arxiv.org/abs/1210.5929).
- [40] E. H. Brandt *et al.* “Type-II-superconductor strip with current in a perpendicular magnetic field”. *Physical Review B* 48.17 (1993), pp. 12893–12906. ISSN: 01631829. DOI: [10.1103/PhysRevB.48.12893](https://doi.org/10.1103/PhysRevB.48.12893).



6

OUTLOOK

*The best way to have a good idea
is to have lots of ideas.*

Linus C. Pauling

Here, we reflect on the research presented in this dissertation, provide an outlook towards NV magnetometry of valley magnetism in few-layer TMDs and spin waves in van der Waals magnets, and suggest the realization of spin-wave optics using superconductor-magnet heterostructures.

In this dissertation we presented results on valley polarization in doped monolayers of group-IV transition metal dichalcogenide WS_2 (Chapter 3), NV magnetometry of the magnetization of Van der Waals magnet CrSBr (Chapter 4) and NV-based imaging of spin waves in a magnet-superconductor heterostructure (Chapter 5). In this Chapter, we reflect on these results and propose follow-up experiments to detect valley magnetism in TMDs and spin waves in Van der Waals magnets with NV magnetometry. Finally, we build upon the developed ability to control spin waves with a superconducting gate by proposing the creation of spin wave optics using superconductors.

6.1. PROBING THE VALLEY MAGNETIC MOMENT IN GROUP-IV TMDs WITH NV CENTERS IN DIAMOND

In Chapter 3, we have demonstrated a novel doping method for few-layer WS_2 flakes, detected its effect on the valley polarization of excitons and trions, and captured this behaviour through a rate equation model. Tuning the exciton-trion equilibrium at will is an important step in maximizing the valley magnetic moment for NV magnetometry. We have performed preliminary measurements towards this end, which remain inconclusive for three reasons that are detailed later in this section. However, they do indicate that highly electron doped monolayers at cryogenic temperatures are a promising future research direction for NV-based measurements on the valley magnetic moment. As discussed in Chapter 2, the valley magnetic moment plays a key role in the selective addressability of valley states and gives rise to magnetic fields that provide outstanding - yet unexplored - experimental opportunities for studying valley physics. Here we shortly discuss these preliminary measurements, explain how to make them conclusive, and discuss two sample layouts and detection protocols for NV magnetometry of valley magnetism.

Reversible and tunable doping is an important tool to control the valley magnetic moment through the exciton-trion equilibrium, and can be achieved through the doping method presented in Chapter 3 or by electrostatic gating (Fig. 6.1a) [1]. Monolayer WS_2 luminescence measurements at room temperature showed tuning between exciton and trion regimes through gate-controlled doping (Fig. 6.1b), reproducing similar valley polarization (Fig. 6.1c-d) as in Chapter 3. The same measurement at 30 K showed that the A-exciton blue shifts on resonance with our 594 nm excitation laser and is therefore blocked by our longpass filter at 600 nm (Fig. 6.1e, grey dashed line). For negative V_g , a bright trion emission appears, with strong circular dichroism and valley polarization (Fig. 6.1f-g). Given the higher valley magnetic moment associated with trions compared to excitons [2] and the increased trion lifetime at low temperature [3], a regime characterized by low temperature and high doping is thus a promising start for NV magnetometry measurements.

However, these preliminary measurements remain inconclusive. The blue-shift of the A-exciton hinders an analysis of its luminescence and valley polarization, and thus prevents us from applying the rate equation model developed in Chapter 3 for understanding the low-temperature WS_2 exciton-trion equilibrium. A straightforward solution to this would be excitation using a laser with shorter wavelength (~ 580 nm), however the larger the detuning between the excitation wavelength and the exciton resonance, the

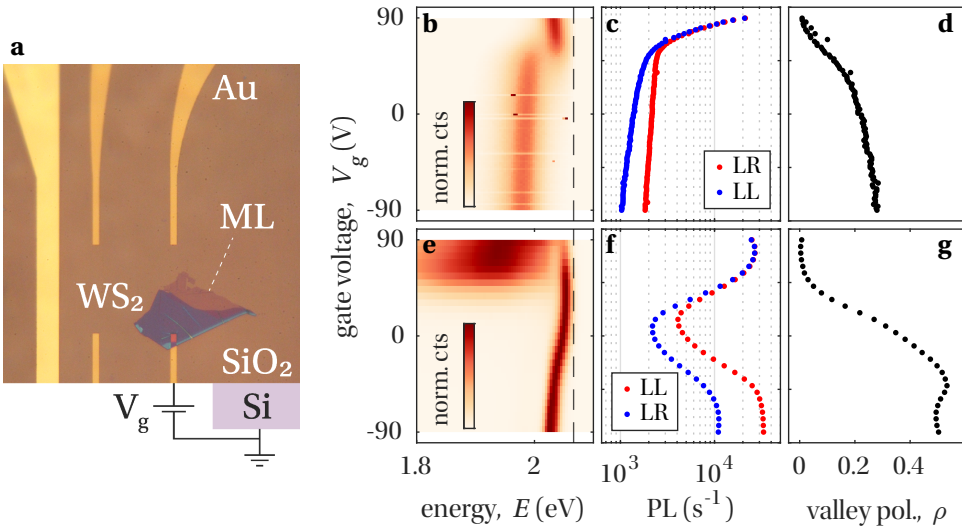


Figure 6.1. **Valley polarized trions in monolayer WS₂ at room- and cryogenic temperatures.** (a) Optical micrograph of a WS₂ flake stamped on top of a gold lead on a Si/SiO₂ substrate. A global backgate voltage V_g is applied between the lead and the silicon to control doping. The monolayer region of the flake is indicated by "ML". (b) Normalized luminescence spectra of monolayer WS₂ at room temperature as a function of gate voltage, under 594 nm (2.087 eV) laser excitation at a power of 1 μ W. The dashed line indicates the 600 nm (2.066 eV) longpass filter used to eliminate the laser reflection. (c) Circular dichroism of the photoluminescence spectra in (b) as a function of gate voltage V_g . (d) Extracted valley polarization ρ from the data in (c). (e, f, g) Same as in (b, c, d) but at $T = 30$ K.

smaller the induced valley polarization [4]. Additionally, the observed kink in the luminescence spectra and 30 K valley polarization at $V_g = -50$ V is not understood (Fig. 6.1g), but might be related to the various types of negative trions that can form [5–7]. The trion linewidth in our sample prevents spectral decomposition into inter- and intra-valley trions. This might be addressed through encapsulation of the WS₂ monolayer in hexagonal boron nitride, which has been shown to decrease exciton linewidths [8].

We now shift our attention to NV magnetometry of the valley magnetic moment. A central challenge for performing NV center measurements on WS₂ is the unwanted excitation of NV centers due to the TMD excitation laser, since its energy of 2.09 eV is higher than the NV⁻ zero phonon line at 1.94 eV. Additionally, the WS₂ excitation laser has not enough energy to excite NV centers in the NV⁰ state (ZPL at 2.16 eV), and therefore is expected to polarize NV centers to NV⁰ over time. Therefore, we next discuss several avenues that could potentially overcome this challenge.

In order to perform NV magnetometry of valley magnetism in TMDs where the A-exciton is higher in energy than the NV ZPL (WS₂ and MoS₂, Fig. 6.2d), a spatial decoupling of the NV and TMD excitation lasers might be required if even a low-power TMD laser interferes with the NV spin state. In TMD flakes on oxidized silicon, as we have presented in Chapter 3 and Fig. 6.1a, this can be achieved by placing a diamond membrane

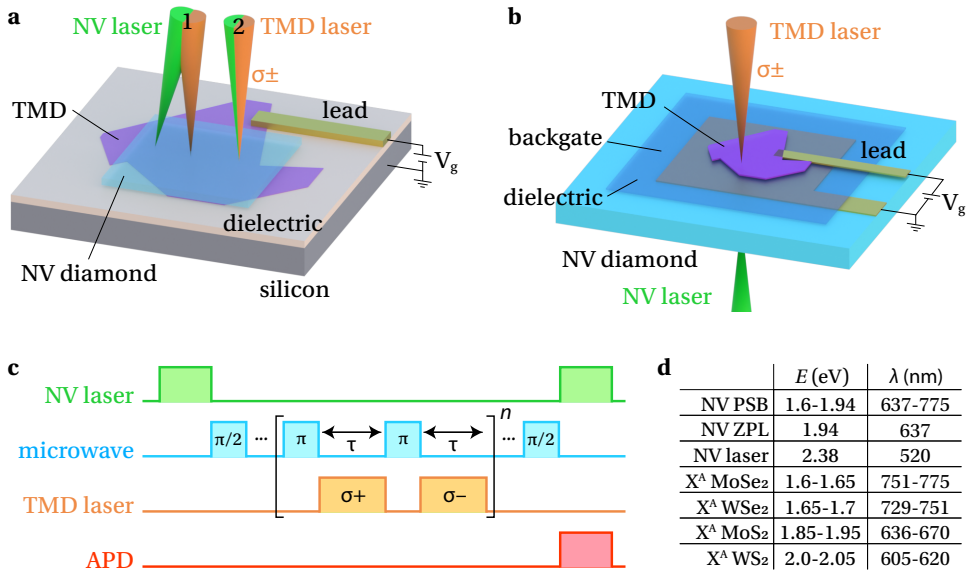


Figure 6.2. **Proposal for NV magnetometry of valley magnetism in TMDs.** (a-b) Schematics for same-side (a) and opposite-side (b) NV detection and TMD excitation, applicable when the TMD excitation laser wavelength is longer (a) or shorter (b) than the NV ZPL. (c) Proposed pulse schematic for flipping the NV spin in unison with TMD laser polarization to distinguish valley magnetic signals from photocurrents. (d) Table of relevant NV excitation and emission wavelengths [9] and A-exciton energies in group-IV TMD monolayers [10].

6

on the flake and focusing the NV and TMD lasers in adjacent but different positions (Fig. 6.2a, denoted by "1"). In this way, a non-local detection of the valley magnetic moment might be possible, which would allow insight into exciton diffusion. In order to study the magnetic moment induced at the spot location with NV and TMD laser at the same side (Fig. 6.2a, denoted "2"), the use of a TMD with an A-exciton lower in energy than the NV⁻ ZPL is suggested, such as WSe₂ and MoSe₂ (Fig. 6.2d).

Another promising approach would be to fabricate a device directly on diamond and illuminate the sample from both sides simultaneously (Fig. 6.2b). For example, a metal pad placed directly on diamond, followed by a dielectric, TMD and lead on top, will allow gating of the TMD while simultaneously serving as a mirror that optically decouples the TMD and NV layer. As magnetic sensing through optically opaque metals using NV centers was demonstrated [11], this might form a promising avenue for detecting valley magnetism.

Finally, we discuss an NV sensing protocol suitable for detecting the valley magnetic moment (Fig. 6.2c). Previous NV center measurements on MoS₂ have revealed circulating photo-Nernst currents induced by the TMD excitation laser [12]. In order to distinguish between these photocurrents and valley magnetism, we propose to employ fast σ^+/σ^- polarization switching of the TMD laser in unison with the NV spin. After initializing the NV centers with a green 520 nm pulse, a $\pi/2$ microwave pulse brings the NV in

a superposition of $|0\rangle$ and $|-1\rangle$. Then, in between a sequence of microwave π -pulses, the TMD is illuminated with σ^+ and σ^- for a time τ , which leads to a phase buildup proportional to the valley magnetic moment. Projecting the NV center back onto $|0\rangle$ and $|1\rangle$ with another $\pi/2$ pulse allows extraction of the obtained phase through a green readout pulse. By demonstrating gate-controlled and highly valley-polarized trions in WS₂ at low temperatures, and proposing an NV detection protocol applicable to all group-IV TMDs, we pave the way for detecting the valley magnetic moment with NV magnetometry.

6.2. DETECTING SPIN-WAVE EXCITATIONS IN VAN DER WAALS MAGNETS WITH NV MAGNETOMETRY

In Chapter 4, we have demonstrated NV magnetometry of van der Waals magnet CrSBr, through which we extract the CrSBr magnetization. These measurements are an important first step towards NV-based detection of spin waves in van der Waals magnets. A central challenge is the frequency mismatch between the spin wave dispersion (>10 s of GHz) and NV ESR (few GHz), which seems to eliminate established magnetic resonance methods for spin wave imaging [13]. Here, we introduce two methods that could potentially overcome this challenge.

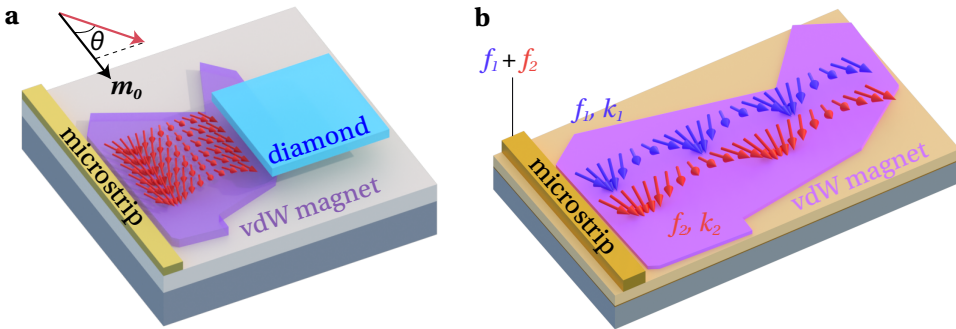


Figure 6.3. **NV magnetometry of spin waves in van der Waals magnets.** (a) Schematic of spin waves in a van der Waals magnet. A microstrip provides a drive field, causing oscillations in the transverse magnetization of a Van der Waals magnet that reduce the longitudinal magnetization from \mathbf{m}_0 to \mathbf{m}' . NV centers in a nearby diamond detect the magnetization change, which will be largest near steps and edges of the flake. (b) Schematic of two-tone excitation of spin waves in a van der Waals magnet. A microstrip provides a two-tone drive field with frequencies f_1 and f_2 , which excites two modes in the magnet simultaneously. Their interference causes the longitudinal component of the magnetization to oscillate at the difference frequency $f_1 - f_2$, which can be detected by NV centers.

The first method relies on detecting a reduction in the magnetization when spin waves are present in the magnet. In our thought experiment, spin waves in a van der Waals magnet are excited through a microstrip (Fig. 6.3a). The magnetization precesses around the equilibrium magnetization \mathbf{m}_0 at an angle θ . Since the perturbation is transverse, the static longitudinal component is reduced to $m' = \cos(\theta)m_0$. This reduction might be detected by NV centers in diamond, at edges or steps in a Van der Waals magnet flake,

through a similar experiment as presented in Chapter 4, or via an AC NV magnetometry protocol where the excitation drive is switched on and off to create an AC magnetization reduction.

The second method aims to employ difference-frequency generation to create an NV-resonant oscillation in the magnetization, as recently demonstrated in YIG [14]. By providing a two-tone drive field with frequencies f_1 and f_2 to the excitation line, two modes within the spin wave band with wavevector $k_1(y)$ and $k_2(y)$ are simultaneously excited (Fig. 6.3b). The resulting oscillation in the transverse magnetization is an interference of the individual modes,

$$m_T = a_1 e^{i(k_1 y - 2\pi f_1 t)} + a_2 e^{i(k_2 y - 2\pi f_2 t)}. \quad (6.1)$$

For a small transverse perturbation, the normalized longitudinal component of the magnetization is given by

$$m_L = \sqrt{1 - |m_T|^2} \approx 1 - \frac{|m_T|^2}{2}. \quad (6.2)$$

While for a spin wave of single frequency the longitudinal magnetization is reduced yet static, for a two-tone spin wave it will oscillate at the difference frequency $f_1 - f_2$ with spatial periodicity set by the wavenumber difference $k_1 - k_2$ [14],

$$m_L \approx 1 - \frac{a_1^2 + a_2^2}{2} - a_1 a_2 \cos((k_1 - k_2)y - 2\pi(f_1 - f_2)t). \quad (6.3)$$

The frequency difference $\delta f = f_1 - f_2$ can be detected through two methods: 1) tuning δf into resonance with the NV ESR frequency, and 2) performing AC magnetometry on the δf signal. We expect that these methods might enable spatial spin-wave imaging and probing of the spin-wave band structure in Van der Waals magnets. The signal amplitude will be limited by spin-wave damping, which is currently an unknown parameter, and therefore it is an open question whether this signal will be detectable. Additionally, it is unclear how strongly non-linear effects such as magnon-magnon interactions will limit the spin-wave amplitude.

Looking back, we employed NV centers in diamond to measure the magnetization of van der Waals magnet CrSBr, an important step towards probing spin-wave excitations. We proposed to measure spin waves in van der Waals magnets through 1) the reduction of the magnetization along the equilibrium direction and 2) the oscillations in the longitudinal magnetization in a magnet subject to a two-tone drive field. By doing so, we circumvent the frequency mismatch between NV ESR and spin wave dispersion, and set the stage for NV magnetometry of spin waves in Van der Waals magnets.

6.3. CREATING SPIN-WAVE OPTICS WITH SUPERCONDUCTOR-MAGNET HETEROSTRUCTURES

In Chapter 5, we have developed the ability to control spin waves with a superconducting gate, which opens new avenues for magnonic device applications. We showed that changing the global temperature of the superconductor allows for dispersion engineering, while local gradients in temperature allow for propagation engineering. Here,

we combine these concepts with theoretical predictions of our hybrid superconductor-magnet dispersion model, and propose novel device applications and research directions.

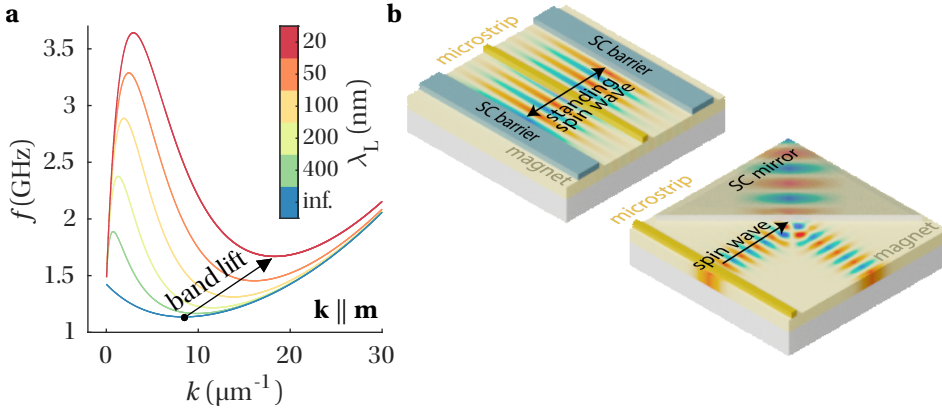


Figure 6.4. **Band lifting of the YIG-superconductor dispersion for cavities and mirrors.** (a) Dispersion for backward volume spin waves in YIG covered with a superconducting film of thickness $t = 200$ nm at $T = 0$ K and $B_z = 10$ mT, for various London penetration depths λ_L . The bottom of the band is lifted with decreasing penetration depth, creating a barrier for spin waves in the frequency gap. (b) Two parallel superconducting barriers form a cavity for spin-wave modes with $\mathbf{k} \parallel \mathbf{m}$ (left). Refraction and reflection governed by Snell's law for spin waves can be studied by non-perpendicular incidence of spin waves on a superconductor-covered region (right). The transparency of superconductor-enabled spin-wave beam splitters, mirrors and barriers is tunable by temperature.

One such direction is the realization of spin-wave barriers/mirrors and the spin-wave analogy to optical beam splitters, which might enable strong coupling between magnons and auxiliary systems integrated in the cavity, give access to nonlinear magnonics, and the study of Snell's law for spin waves [15–17]. The experimental study in Chapter 5 has focused on magnetostatic Damon-Eshbach spin waves (DESW) with $\mathbf{k} \perp \mathbf{m}$, of which the dispersion is shifted upwards by the superconductor. However, for backward volume spin waves (BVSU) with $\mathbf{k} \parallel \mathbf{m}$, the upwards frequency shift predicted by our hybrid dispersion model lifts the bottom of the spin-wave band (Fig. 6.4a). For certain frequencies f in the range $f_0 < f < f_{\text{FMR}}$, where f_0 is the bottom of the BSVW band in bare YIG, there are no longer any resonant modes in the hybrid YIG-SC system. This creates an effective barrier for backward volume spin waves as predicted in [18], potentially enabling magnonic cavities (Fig. 6.4b).

Of specific interest is the scenario where the spin-wave induced Meissner current density will exceed the critical current density of the superconductor. We predict that a constant RF signal on an excitation strip in the cavity will result in pulsed spin-wave emission from the cavity. Furthermore, due to the anisotropic dispersion relation of both YIG and superconductor-covered YIG, it is of scientific interest to study the angular relation between spin-waves and barriers. We expect that the anisotropic dispersion relation that governs the reflection and refraction of spin waves travelling underneath superconduc-

tors at an angle (Fig. 6.4b), will allow a detailed study of Snell's law for spin waves [15], and enable e.g. the construction of frequency-dependent beamsplitters.

Akin to electronics and photonics, the creation of periodic distortions in the magnetic potential enables the creation of magnonic crystals - systems in which the otherwise continuous spin-wave dispersion obtains a field-tunable band structure due to coherent scattering and Bragg reflection [17, 19–23]. Here, we propose the creation of field-, temperature-, and light-tunable magnonic crystals by interfacing a thin film magnetic insulator with a superconductor.

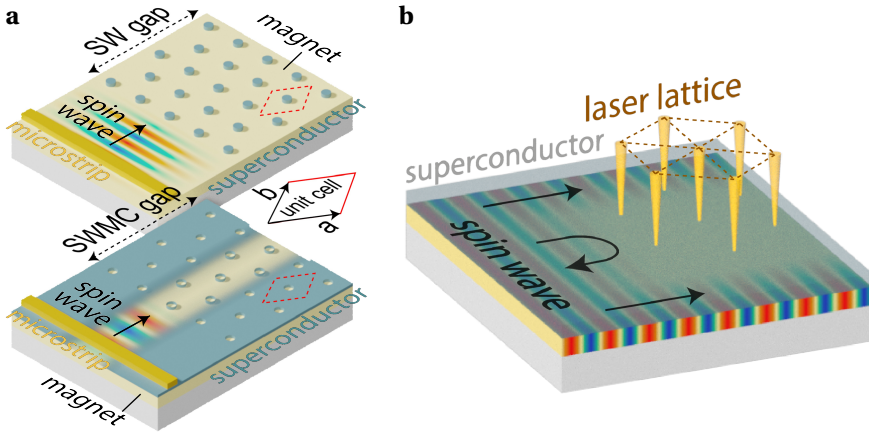


Figure 6.5. **Superconductor-enabled reconfigurable magnonic crystals.** (a) Schematic of two-dimensional magnonic crystals formed by patterning periodic superconducting structures on top of a magnetic insulator. The spin-wave (SW) dispersion of the magnetic insulator can be gapped by the periodic arrangement of superconducting islands on its surface (top). The size of the bandgap is tunable by temperature, and largest far below T_c . The hybrid spin-wave-Meissner-current (SWMC) dispersion can be gapped by periodic arrangement of holes or defects in an otherwise homogeneous superconducting film (bottom). (b) A magnonic crystal created by periodic arrangement of focused laserspots on a homogeneous superconducting film covering a magnetic insulator, enabling in-situ reconfigurable lattice parameters and coordinates through adaptation of optics.

One- and two-dimensional magnonic crystals might be realized by interfacing a magnetic insulator with periodic superconducting structures, such as superconducting islands (Fig. 6.5a, top). The islands create a periodic distortion in the magnetic environment, introducing a band gap in the spin-wave dispersion of the magnetic insulator. The distortion strength depends on the shielding capacity of the islands (parametrized by λ_L), leading to a band-gap that is temperature-tunable in size and field-tunable in energy. The inverse pattern, i.e. an otherwise homogeneous superconducting film with holes, is expected to gap the hybrid spin-wave-Meissner-current dispersion (Fig. 6.5a, bottom). The energy difference between the band gaps and the bottom of the spin-wave band depends on temperature, while flux-focusing of perpendicular fields can increase the band gap size.

Instead of etching a periodic structure of holes in the superconductor, we now con-

sider the more interesting scenario where the superconductor is illuminated by an array of tightly focused laser spots (Fig. 6.5b). As discovered in Chapter 5.5, a focused laser-spot creates a spin-wave scattering site, and a lattice of laser-spots thus constitutes a magnonic crystal, of which the lattice parameters can be tuned in situ by adaptation of optics. Similarly, the use of a spatial light modulator for widefield structural illumination might be used to create reconfigurable spin-waveguides. The ability to create magnonic crystals and waveguides in superconductor-magnet hybrids by optical illumination should enable exploration of a large variety and number of designs in quick succession, without the need for additional nanofabrication.

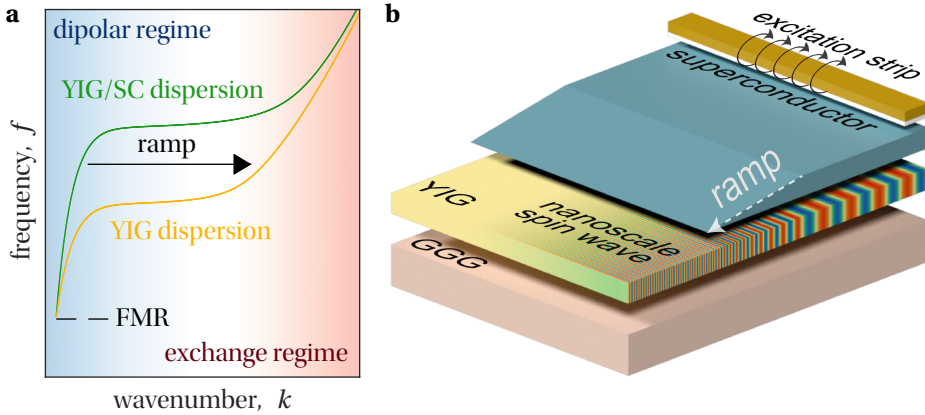


Figure 6.6. **Efficient nanoscale spin-wave excitation using superconducting ramps.** (a) Schematic of the spin-wave dispersion in yttrium iron garnet (YIG), and hybrid spin-wave-Meissner-current dispersion in a YIG-superconductor (YIG/SC) heterostructure, in the Damon-Eshbach geometry ($\mathbf{k} \perp \mathbf{B}$). Creating an adiabatic transition between these two systems might enable efficient conversion of dipolar-dominated spin waves to exchange-dominated spin waves. (b) Schematic of the proposed experiment. A micron-sized excitation strip efficiently excites dipolar spin waves underneath a superconductor, that are adiabatically transformed to short-wavelength spin waves through interaction with a superconducting ramp.

Nanoscale spin waves are attractive for magnonics due to their short wavelength and high group velocity, which enable device minimization and improved performance [17, 24]. However, efficient excitation of nanoscale exchange spin waves using transducer lines remains an outstanding technological challenge due to the required scale of fabrication and impedance mismatch to the environment [24, 25]. Alternative approaches, such as periodic patterning of auxiliary magnets on top of the spin-wave conduit [26–28] or the use of magnetic vortex cores have enabled excitation of nanoscale spin waves, yet these methods rely on complex nanofabrication and are unsuitable for planar devices that require multidirectional propagation. An attractive alternative is therefore to instead reduce the spin-wavelength only after generation [24]. Here, we propose to achieve this using a superconducting ramp to efficiently convert dipolar spin waves to nanoscale spin waves.

As demonstrated in Chapter 5, the dispersion of spin waves in a YIG-superconductor thin film hybrid shifts upwards due to the back-action of Meissner currents created by

the spin-wave stray fields. For nanoscale exchange-dominated spin waves, the stray field and Meissner shielding gradually vanish, leading to a merging of YIG and hybrid YIG-superconductor dispersions with increasing wavenumber k (Fig. 6.6a). In a frequency range above the flattening of the YIG dispersion, there are only high k modes in bare YIG, yet low k modes in the YIG-superconductor system. We propose to create an adiabatic transition between these modes by constructing a superconducting ramp (Fig. 6.6b). In the superconductor-covered YIG, a transducer will efficiently excite low k modes that propagate through a region where the thickness of the superconductor is gradually decreased. As the thickness of the superconducting film vanishes, the hybrid YIG/SC dispersion approaches the YIG dispersion. As such, the superconducting ramp should adiabatically transform long-wavelength spin waves into short-wavelength spin waves that the transducer itself can not excite. The ability to coherently excite nanoscale spin waves with transducers that are much larger than their wavelength (and thus easily fabricated) gives straightforward access to the short-wavelength regime in magnetic insulators, opening up new avenues for research and applications.

SUMMARY

In this chapter, we have proposed AC NV magnetometry experiments for detecting the valley magnetic moment of highly valley polarized trions at low temperatures in monolayers of group-IV TMDs through fast polarization switching. Additionally, we proposed NV detection of spin waves in van der Waals magnets through a reduction in the magnetization and through oscillations in the longitudinal magnetization component due to two-tone spin-wave excitation. Finally, we discussed magnonic device applications based on the hybridization of spin waves and Meissner currents in thin film magnets interfaced with a superconductor. By doing so, we have set the stage for exciting experiments that aim to detect valley magnetism and spin waves in Van der Waals semiconductors and realize magnon optics with superconductor-magnet heterostructures.

REFERENCES

- [1] B. Zhu *et al.* “Exciton binding energy of monolayer WS₂”. *Scientific Reports* 5 (2015). ISSN: 20452322. DOI: [10.1038/srep09218](https://doi.org/10.1038/srep09218). arXiv: [1403.5108](https://arxiv.org/abs/1403.5108).
- [2] A. Srivastava *et al.* “Valley Zeeman effect in elementary optical excitations of monolayer WSe₂”. *Nature Physics* 11.2 (2015), pp. 141–147. ISSN: 17452481. DOI: [10.1038/nphys3203](https://doi.org/10.1038/nphys3203). arXiv: [1407.2624](https://arxiv.org/abs/1407.2624).
- [3] H. Wang *et al.* “Radiative lifetimes of excitons and trions in monolayers of the metal dichalcogenide MoS₂”. *Physical Review B* 93.4 (2016), pp. 1–11. ISSN: 24699969. DOI: [10.1103/PhysRevB.93.045407](https://doi.org/10.1103/PhysRevB.93.045407). arXiv: [1409.3996](https://arxiv.org/abs/1409.3996).
- [4] A. T. Hanbicki *et al.* “Anomalous temperature-dependent spin-valley polarization in monolayer WS₂”. *Scientific Reports* 6.1 (2016), p. 18885. ISSN: 2045-2322. DOI: [10.1038/srep18885](https://doi.org/10.1038/srep18885).
- [5] A. Singh *et al.* “Trion formation dynamics in monolayer transition metal dichalcogenides”. *Physical Review B* 93.4 (2016), pp. 1–5. ISSN: 24699969. DOI: [10.1103/PhysRevB.93.041401](https://doi.org/10.1103/PhysRevB.93.041401). arXiv: [1507.04463](https://arxiv.org/abs/1507.04463).
- [6] T. P. Lyons *et al.* “The valley Zeeman effect in inter- and intra-valley trions in monolayer WSe₂”. *Nature Communications* 10.1 (2019), pp. 1–8. ISSN: 20411723. DOI: [10.1038/s41467-019-10228-7](https://doi.org/10.1038/s41467-019-10228-7). arXiv: [1811.08835](https://arxiv.org/abs/1811.08835).
- [7] A. M. Jones *et al.* “Optical generation of excitonic valley coherence in monolayer WSe₂”. *Nature Nanotechnology* 8.9 (2013), pp. 634–638. ISSN: 17483395. DOI: [10.1038/nnano.2013.151](https://doi.org/10.1038/nnano.2013.151).
- [8] O. A. Ajayi *et al.* “Approaching the intrinsic photoluminescence linewidth in transition metal dichalcogenide monolayers”. *2D Materials* 4.3 (2017). ISSN: 20531583. DOI: [10.1088/2053-1583/aa6aa1](https://doi.org/10.1088/2053-1583/aa6aa1). arXiv: [1702.05857](https://arxiv.org/abs/1702.05857).
- [9] A. Gruber *et al.* “Scanning confocal optical microscopy and magnetic resonance on single defect centers”. *Science* 276.5321 (1997), pp. 2012–2014. ISSN: 00368075. DOI: [10.1126/science.276.5321.2012](https://doi.org/10.1126/science.276.5321.2012).
- [10] G. Wang *et al.* “Colloquium: Excitons in atomically thin transition metal dichalcogenides”. *Reviews of Modern Physics* 90.2 (2018), p. 21001. ISSN: 15390756. DOI: [10.1103/RevModPhys.90.021001](https://doi.org/10.1103/RevModPhys.90.021001).
- [11] I. Bertelli *et al.* “Imaging Spin-Wave Damping Underneath Metals Using Electron Spins in Diamond”. *Advanced Quantum Technologies* 4.12 (2021), pp. 1–6. ISSN: 25119044. DOI: [10.1002/qute.202100094](https://doi.org/10.1002/qute.202100094). arXiv: [2106.02508](https://arxiv.org/abs/2106.02508).
- [12] B. B. Zhou *et al.* “Spatiotemporal Mapping of a Photocurrent Vortex in Monolayer MoS₂ Using Diamond Quantum Sensors”. *Physical Review X* 10.1 (2020), p. 11003. ISSN: 21603308. DOI: [10.1103/PhysRevX.10.011003](https://doi.org/10.1103/PhysRevX.10.011003).

- [13] I. Bertelli *et al.* “Magnetic resonance imaging of spin-wave transport and interference in a magnetic insulator”. *Science Advances* 6.46 (2020), pp. 1–8. ISSN: 23752548. DOI: [10.1126/sciadv.abd3556](https://doi.org/10.1126/sciadv.abd3556). arXiv: 2004.07746.
- [14] J. J. Carmiggelt *et al.* “Broadband microwave detection using electron spins in a hybrid diamond-magnet sensor chip”. *Nature Communications* 14.1 (2023), pp. 1–6. ISSN: 20411723. DOI: [10.1038/s41467-023-36146-3](https://doi.org/10.1038/s41467-023-36146-3). arXiv: 2206.07013.
- [15] J. Stigloher *et al.* “Snell’s Law for Spin Waves”. *Physical Review Letters* 117.3 (2016), pp. 1–5. ISSN: 10797114. DOI: [10.1103/PhysRevLett.117.037204](https://doi.org/10.1103/PhysRevLett.117.037204).
- [16] B. Zare Rameshti *et al.* “Cavity magnonics”. *Physics Reports* 979 (2022), pp. 1–61. ISSN: 03701573. DOI: [10.1016/j.physrep.2022.06.001](https://doi.org/10.1016/j.physrep.2022.06.001). arXiv: 2106.09312.
- [17] V. V. Kruglyak *et al.* “Magnonics”. *Journal of Physics D: Applied Physics* 43.26 (2010). ISSN: 00223727. DOI: [10.1088/0022-3727/43/26/264001](https://doi.org/10.1088/0022-3727/43/26/264001).
- [18] T. Yu *et al.* “Efficient Gating of Magnons by Proximity Superconductors”. *Physical Review Letters* 129.11 (2022), p. 117201. ISSN: 10797114. DOI: [10.1103/PhysRevLett.129.117201](https://doi.org/10.1103/PhysRevLett.129.117201). arXiv: 2201.09532.
- [19] G. Gubbiotti *et al.* “Reprogrammable magnonic band structure of layered permalloy/Cu/permalloy nanowires”. *Physical Review B* 97.13 (2018), pp. 1–6. ISSN: 24699969. DOI: [10.1103/PhysRevB.97.134428](https://doi.org/10.1103/PhysRevB.97.134428).
- [20] A. V. Chumak *et al.* “All-linear time reversal by a dynamic artificial crystal”. *Nature Communications* 1.9 (2010). ISSN: 20411723. DOI: [10.1038/ncomms1142](https://doi.org/10.1038/ncomms1142).
- [21] D. Grundler. “Reconfigurable magnonics heats up”. *Nature Physics* 11.6 (2015), pp. 438–441. ISSN: 17452481. DOI: [10.1038/nphys3349](https://doi.org/10.1038/nphys3349).
- [22] G. Gubbiotti *et al.* “Brillouin light scattering studies of planar metallic magnonic crystals”. *Journal of Physics D: Applied Physics* 43.26 (2010). ISSN: 00223727. DOI: [10.1088/0022-3727/43/26/264003](https://doi.org/10.1088/0022-3727/43/26/264003).
- [23] S. A. Nikitov *et al.* “Spin waves in periodic magnetic structures - Magnonic crystals”. *Journal of Magnetism and Magnetic Materials* 236.3 (2001), pp. 320–330. ISSN: 03048853. DOI: [10.1016/S0304-8853\(01\)00470-X](https://doi.org/10.1016/S0304-8853(01)00470-X).
- [24] V. E. Demidov *et al.* “Excitation of short-wavelength spin waves in magnonic waveguides”. *Applied Physics Letters* 99.8 (2011). ISSN: 00036951. DOI: [10.1063/1.3631756](https://doi.org/10.1063/1.3631756).
- [25] S. Wintz *et al.* “Magnetic vortex cores as tunable spin-wave emitters”. *Nature Nanotechnology* 11.11 (2016), pp. 948–953. ISSN: 17483395. DOI: [10.1038/nnano.2016.117](https://doi.org/10.1038/nnano.2016.117).
- [26] C. Liu *et al.* “Long-distance propagation of short-wavelength spin waves”. *Nature Communications* 9.1 (2018), pp. 4–11. ISSN: 20411723. DOI: [10.1038/s41467-018-03199-8](https://doi.org/10.1038/s41467-018-03199-8).
- [27] J. Chen *et al.* “Excitation of unidirectional exchange spin waves by a nanoscale magnetic grating”. *Physical Review B* 100.10 (2019), pp. 1–7. ISSN: 24699969. DOI: [10.1103/PhysRevB.100.104427](https://doi.org/10.1103/PhysRevB.100.104427). arXiv: 1903.00638.

- [28] S. J. Hämäläinen *et al.* “Tunable Short-Wavelength Spin-Wave Emission and Confinement in Anisotropy-Modulated Multiferroic Heterostructures”. *Physical Review Applied* 8.1 (2017), pp. 1–9. ISSN: 23317019. DOI: [10.1103/PhysRevApplied.8.014020](https://doi.org/10.1103/PhysRevApplied.8.014020).

ACKNOWLEDGEMENTS

The warm and radiant yes of the heart is perfect, like the sun in bringing all things to life and nourishing all that is truly human.

John Welwood

As my PhD comes to a close and I reflect on everything I have experienced and learned, I realize that for me it's not so much about the things I do, but about the people I do them with. I am extremely grateful for having met so many wonderful humans during this journey, and these words are for you!

First, I would like to express gratitude to the members of my committee, **Herre, Semonti, Marcos, Carlos, Christian** and **Sander**. Thank you for accepting my invitation, reading my thesis, and your fast communication which ensured these final stressful months went by smoothly. I am looking forward to our discussions.

Toeno, when I came by for an interview five-and-something years back, I did not expect to be hired before the day was over. Something clicked from both sides. Your enthusiasm and curiosity about physics and potential new projects was (and still is) contagious. It was also clear you were gathering a wonderful group of diverse and social people around you, so I wanted in. This section is too short to list all the things I have learned from you. Striking the right balance between getting lost in new and promising ideas, and staying focused on feasible results and projects. You always found a way to rewrite any of my sentences in something more compact and clear, and I admire your efficiency. But more importantly, I appreciate that you value the human element of the group. The yearly uitje is a great tradition, and I hope SarLab will keep it up for years to come. I am particularly grateful about the way you handled the more challenging times of my PhD, always prioritizing my wellbeing over work, even in the demanding face of high impact results. Thank you for everything, I am proud of the work we have done together. I will miss the sight of your passionate karaoke performances at random bars in foreign places. I am sure we will meet again and share a Jägermeister (Aperol Spritz is also allowed) when that time comes.

The 'downside' of having a particularly amazing supervisor, is that our yearly meetings were short and straightforward, **Gary**. Even though our interactions were limited, you helped to zoom out, put things into perspective and focus on the big picture, for which I am grateful. Your passion for good coffee has boosted the efficiency of our department. I say passion, because I do distinctly remember some all-caps-lock email about the coffee grinder settings. Thank you for being my promotor, and I'm proud we got you dancing at the last QN party.

Luuk, my bff, I'm not sure where I would be without you! Certainly not where I am right now. And I'm pretty happy with the right now. Looking back to where this journey started, I barely recognize myself and my life. You were there during all of it. Which also

means you are endowed with much material to ridicule me with at my party, I trust that you will. Thank you for your unconditional friendship throughout the rollercoaster that is life. I am honoured to have you as my paronymph, and I am looking forward to returning the favour soon. Here's to many more years of drinks, vacations, festivals, asking me what's precisely the plan, fulfilling conversations, and watching you hurt yourself in impossible ways trying to ascent the bouldering walls. Do warm ups, please!

Iacopo / Lacopo / Iacapulco (which was the right one again?), I first saw you briefly during the cleanroom intake meeting in preparation for my master's project, somewhere in the end of 2017. I thought you looked a bit grumpy. One-and-a-half year later, I got the opportunity to find out how I wrong I was. I now consider you one of my dearest friends, and I feel we are alike in many ways. Perhaps I make grumpy impressions too? You're smart, considerate and quick of mind, and I admire the perseverance you showed during the search for your next adventure – you've found a great place and I'm proud that you're doing well. Thank you for my bouldering addiction, the care-free island-hopping in Greece (I'm game for the next one), all the lovely dinners, and your unwavering dedication to capturing moments in pictures. I'm honoured to have you as my paronymph. Perhaps I can cook you that deer steak for your 60th birthday? Though my agenda is already filling up quickly. I'd also like to thank your better half, **Ana**. Thank you for your friendship, always asking me how I'm doing, your lovely dinners and our sailing adventures. See you guys at the housewarming!!

Next up, **Capitano Carmiggelt**, the legendary **JJC**, soon to be *Daddy JJC*, who would've thought?! The day of my interview, we already got lost in scientific discussions which made me excited for the idea of working together. Professionally, we struck a healthy balance between your efficiency and my organizational mindset. Socially, we seemed to amplify each other's escalating tendencies. I have fond memories of fire escapes in Chicago, that one pool in Castelldefels, and climbing to your hotel window to try and wake **Lara**; because of course you managed to lock yourself out. Your excitement for both the special and mundane things in life is really contagious, and I miss the positive energy you bring wherever you go. Thank you for all the good times, and the great conversations when either of us got our heart broken again. I am happy for you and **Lara**, and I hope to visit you guys in Munchen sometime!

Blender Guru Brechtosaurus, you and your wonderful pictures are dearly missed! I am extremely thankful for that one day where you shared your amazing diamond fabrication skills (which were established with nothing but your perseverance) to help me out with diamond membranes – looking back now, that really saved my PhD. You always do things properly, and I really like that – I'm sure that's the reason the membranes were an immediate success. I always enjoyed our conversations, whether it was about experimental frustrations, GSBS, or your secret desire to move back into nature and become a fulltime crazy catlady. I'm sure that your love for Khruangbin has helped me bring better people in my life, if you catch my drift. Finally, I'm glad you are enjoying the peace that only Oegstgeest can bring to one's soul. Let's do a market stroll or bouldering session again soon!

Dr² **Sam-Ka, Samurababy!** And soon to be **Daddy Kurdi!** For a while there, it seemed like we were the only ones left from the OG Sarlab squad, but now you have also deserted me. However, because you are such a loveable giant there really is nothing to forgive. It

feels like yesterday that we went out for dinner to see what this guy from Cambridge was all about. It turned out he is one of the most kind, modest, polite and friendly (and hustling) people I've come to know. Your journey from material scientist to physicist is hard-fought and impressive, you absorbed knowledge like a sponge. An overworked sponge, who I hope will take more vacation days. I thank you for your Jager-solidarity and the many laughs that had you (and consequently the room) shaking. Also, Nutella pizza sucks, man. I'm happy that you and **Fran** are finally united in Groningen, and I will drive my Panda up there soon. Much love!

Yufan! Our last remaining diamond wizard, thank you for transferring your book of wisdom to the next wizard generation during such a busy time for you. Thank you for keeping the Sarlab up to fashion standards over the years. But you're not only about the looks, I remember well how you surprised all of us with that amazing singing voice during karaoke. You're smart, dedicated and kind, and seem to have an eye for beauty, based on your always well framed holiday pictures and visual artistry. I have used your beautiful spin-waves-with-lab-member-heads concoction proudly during all the talks I have given since it first appeared on **Toeno's** mug. I hope that your search for a place in industry will turn out well, and good luck with the last remaining months!

Drallard! Sorry for the coffee grounds and q-tips, I hope you like practical art. I was bored and felt like some memoire to all the times your coffee cups were left about, lonely and forgotten. Somehow, we always saw and spoke eye to eye, I really appreciate that. I admire the perseverance and reflection you showed throughout your journey the last few years. I was bummed about missing the BBQ, so let's make another one happen soon. Your experience was invaluable during all the times we ran into issues with our lovely Montana, sample holders or PCBs, and you were always willing to think along, for which I'm very grateful! QN needs more people like you. Let's stay in touch!

Edouard, I like the way you work and think. Even though your time in our lab was relatively short, your cynical attitude and vast experience is missed. I hope that your academic journey is bearing the fruits it so obviously deserves. Let's make that German techno festival happen sometimes!

Pimboooo, it all started with a master's project in our group. But, when that master student has no problem climbing trees together with you, you know he's a keeper. I'm glad you felt the same way! I would have loved to write a chapter about the low-temp WS₂ results we achieved together, if only we'd had a sample thermometer. We live and learn. I'm happy about the fruitful collaborations we've had, and I have the feeling our final dance is going to yield something special as well. You have an uncompromisable work-life balance, for that you have my respect and compliments. You've got great humor (even though the age thing has really peaked some time ago!!!) and always carry positive energy with you. But besides that, you're also critical and diligent (your coding ethics are getting there). I look forward to the wide-field imaging of spin waves you'll undoubtedly realize! Thanks for all the good times amigo!

Rooowland! First of all, thank you for taking charge in organizing the Delft side of things for my defense (if I am to believe **Iacopo** – because I definitely did not see that department email recently). I think that makes you a mininymp! You have a talent for melting our hearts with pictures of your daughter, not so much for baking pasta pie. Doing a PhD while being a father to two kids (yes, **LT1** counts too), my brain does not

compute – you’re doing amazing! When your smart and stuko humour pervades the room, I’m reminded that the student part of you might actually never die. If fatherhood doesn’t do it, what will? Your Josephson projects are ambitious, and I’m sure they’ll come to fruition as soon as **LT1** matures. Have fun with that shearing interferometer in the meantime!

Annick, Sarlab’s long lost daughter. You dove headfirst into a PhD, and you were totally rocking it. You’re smart, organised and a sporty ball of energy. That energy you brought to the group dynamics, and it was exactly what we needed. That being said, I’m very happy that you chose what’s good for you, you can be proud! It looks like that lovely brain management course has completely paid off!! Perhaps next we can stop putting alarm clocks! I wish you all the best with your new adventure at CERN, and I’ll drop by for some outside climbing adventures if I’m ever in the neighbourhood!

Fabman, thank you for making sure the lab members do not get electrocuted. It’s the lab spam that should be fried, not us. You have a great taste in music, although arguably there is some bias in that statement since I chose the songs for the quiz questions with which you pulled your team from the jaws of defeat. You’re a quick and witty guy, often speak words of which I – old man – do not know the meaning, and your sarcasm is unrivalled. I look forward to the next instances in which innocent bystanders are dubbed ‘idiot’ in deadpan delivery, whether they be fishermen or not.

Samuel, it’s clear you have a passion for physics and its history, I’m amazed by all the small facts you keep coughing up and the beautiful analogies during your data meeting slides. You’ve been hard at work developing your cute but lazy sloth, and I hope you’ll be rewarded with some well-earned results. Wherever your journey takes you next, I’m sure it’ll end in **Prof. Manas-Valero**.

Gesa, thank you for the social boost and kind care you give to everyone in the group. You always propose breaks together, help organising uitjes, BBQs, spoil us with delicious lemon cake, and much more. Now, let the universe return the favour and present you with some tin vacancies soon! I hope you’ll achieve the learning goals you’ve set for yourself, and I’m sure your recently gained experience will prove very useful for your next steps. You know the idea of the QN pastabar scares me, but let’s hope I’m around long enough to participate at least once.

And finally, with **Yasmin**, we have our very first witch, complete with cauldron and all! You had me a bit surprised because I thought witches weren’t supposed to be fashionable. You’re curious and ask a lot of questions, I like that a lot, it’s the best way to learn and get to know people. It’s easy to talk with you about anything, whether it’s physics, societal constructs, moral philosophy, or the best way to eat a kilogram of Milner cheese. You’re a great addition to the group and I’m sure you’re going to do very well!

A deep and humble thank you goes to our secretaries, **Marijke** and **Lizzy**, and the rest of the team. You have been vital throughout the years in ensuring that we survive. None of the things we achieved would be possible without your hard work. Thank you for consistently solving all the difficult puzzles I have presented you with over the last years.

I’ve had the pleasure to supervise various bachelor and master students! **Sibren**, you did an awesome BEP developing a fast polarization switching setup, that was integrated into our low-temp setup later on. Given that you chose to do a theory MEP afterwards, I can only hope we didn’t scare you too much!

Michiel, due to Covid you did a BEP while we only communicated through Zoom. You did a great job in exploring how Josephson junctions could be interfaced with NVs, and Roland is hard at work to realize the experiments that you modelled! I remember thinking “wow, this guy is way taller than I expected” when we met in person at a QN party later. I’m glad you chose to pursue a PhD, because now we can actually talk in real-life.

Next in line was my great master student **Pim**, but since you stuck around, you already have your own dedicated paragraph.

Then, my last (or so I thought) student for a MEP was **Andrew**. I am still amazed at the amount work we did in only 9 months. We started without a proper PCB, without magnet, without samples, without a way to put membranes on our sample, without code. 9 months later, we had our first images of stretched wavelengths underneath the superconductor. We had a very efficient task distribution, and I’m still often impressed by the quality of the work you delivered in designing the magnet stage, developing calibration routines, placing membranes on our chips, and your very efficient coding. I hope you learned as much from me as I did from you, you have a bright future ahead, and I hope you’re enjoying bringing NVs into space!

And then I stumbled in some shared supervision of **Merel**. Your enthusiasm made it a lot of fun helping you out with the optics of LT2. You pick things up quickly, and I’m sure you’ll gather interesting results when you’re back from your five-year hiatus. Also, stop pretending I’m a grandpa!

Many more people have carried the wonderful spirit of Van der Sar Lab over the years, thank you for all the interactions: **Ilse** (your Nessies are a work of art!), **Tim** (I didn’t see you at DTRH, were you really there?!), **Tijmen**, **Helena**, **Pepijn**, **Guillermo**, **Siham**, **Angela**, **Kaveh**, **Coosje**, **Olaf**, **Guido**, **Tjipke**, **Klaas** and **Nikolaj**.

Having fun officemates is a central factor in day-to-day pleasure in work, and I consider myself lucky in that regard so let me thank you next! **Moritz**, thanks for the good times in the old ages of D113, I always enjoyed our conversations. Thanks for hosting us back on the way from Austria. Every time I open Strava, I’m impressed by your discipline!

Claus, I’m glad we became friends. Upon first impression you seemed a bit distant, maybe because I kicked your friend out of the office. At some point we figured out we both have an affinity for chess, and that we’re on similar wavelengths about introspections and self-development. For reasons, our paths intertwined afterwards, and I’m grateful for your attitude during that time. When you first shared Welwood with me, little did I know his quotes would make my thesis. I’m looking forward to our next meetup, wherever and whenever that may be.

Jin, you’re an enthusiastic and fun guy to be around. I admire your always positive attitude. I hope you’ll succeed in designing that PCB at some point in time, and I wish you all the best in your next steps.

Evert, whenever we strike some (physics) topic, the conversation turns into a fun and elaborate discussion. You’re smart, curious and passionate about what you do, I’m sure your PhD will be fruitful. Thanks for your efforts in the QN Culture & Community Committee, the QN events rocked!

Finally, **Fatemeh**, **Alex**, **Yong**, I thank you all for making D113 a comfortable, friendly and relaxed environment.

The department of Quantum Nanoscience has seen many amazing people come and go over the years. I can not possibly thank everyone who I'm grateful to, but let me give it my best attempt anyway!

Rasa, my fellow nymphoo, your loud laughter echoing in the hallways is missed greatly! Thank you for my newly established title based on your first impressions, I wear it with grace. Thanks for all the small chats and good vibes over the years, you're a great listener and I've always found comfort in sharing with you, whatever the topic. I hope you'll be happy in Norway!

Lukas, one of the three very tired boys. Our musical endeavours were like some of the best hits: a one day fly. Only we didn't even really fly, I guess. We started our PhD on the exact same day, in some way it always felt like we were in it together. I understand that's exactly why the brain management betrayal hurts, but hey, we all got our credits now! Who would've thought! I admire the perseverance you've shown in your journey, and thank you for all the good times. One day we will play Madonna covers on a stage somewhere.

Uldipuldiii, the bouldering beast. We seem to have a similar taste in dark humour, I always laugh a lot when you're around. I'm saddened that Il Peperoncino does not have your Italian seal of approval it so deserves. Thanks for all the times you helped out with wirebonding, you carry an important torch in the department. I'm sure we'll meet in the bouldering halls from time to time.

Mattias, there's some magic in the way your stern and dry sarcastic attitude makes people laugh. I'm happy you're all set for a renewed adventure in Norway together. Thanks for all the laughs, and good luck with the last few moments of being a freelance writer. See you in Delft when you defend!

Parsa, you're a great guy. Kind, compassionate and a great listener. I much enjoyed our chats about life and love. It was fun to find out there are Opeth fans in this department, and as it turns out we have quite a bit in common, both in terms of music and our recent journeys in life. Let's combine our guitar skills and jam out some time! I'm looking forward to see how you will shape your next journey, and I'm sure we'll chat about that in the meantime.

Hester, I appreciate the dryness of your humour. In some ways we share a similar journey, and I value the few moments we shared about that. I'm sure that when we look back in a few years, we see how far we've come.

Sonakshi, thanks for the good times at the QN parties over the years, and the efforts you put into realizing those! Your thesis cover series was a work of art, and I hope life in consultancy is treating you well!

Luigi, the last tired boy! Thanks for all the fun conversations about TMDs, and I'm curious how your Madonna drumming skills have evolved.

Niccolo, I always enjoyed your positive and free mindset, and I enjoyed the valuable conversations about love and life we've had over the years. All the best on your new adventures in California!

Thierry, soon to be father! You always struck me as a stable, smart and capable guy, so I'm sure you'll do well in fatherhood. I hope everything will go well in the upcoming exciting times. I'm sure we'll meet in the bouldering halls again to score some drinks on **Iacopo's** money.

Nikos, stamping magician, thanks for showing me around on 2D materials and ironing them with an AFM in the early times of my PhD. I enjoyed our moments on the football fields together, and I'm happy you've found a place at TNO!

Martin, I was in awe at the 30 publications at the back of your PhD. You know how to collaborate and work hard. Thanks for the countless times you helped out with 2D materials.

Houssam, amigooo, you're very chill and laid back, and it felt natural to connect with you. I enjoy our small breaks and conversations, whether it's about physics, techno parties or the struggles of life. We share a similar affinity for partying, and I'm sure we'll repeat that Awakenings meetup sometime soon. See you in the sun!

Nina, it's been some time since we caught up, but I always enjoyed our TPKV sessions and our times at parties. Hope you're well, and that doctorate will be yours soon!

Laeti, I've always enjoyed your puristic French behaviour. Thanks for the introduction to (way too much) Berliner Luft!

Talieh, thank you for pushing our collaboration when I didn't have the capacity to do so. Your determination and ethics are inspiring, and I'm very sure **Prof. Ghiasi** is only a matter of time. Until we meet again!

Alvaro, your dancing skills are unmatched in the department! Together with **Linde**, **Maurits**, **Ritesh**, thanks for the good times in Bologna!

Bow and **Kostas**, thanks for making a very good Solid State Squad!

Adrian, thanks for all our talks about chess, I wonder how your journey to FIDE Master is coming along.

Clinton, you really have to explain to me again sometime how that phonon laser works! It sure sounds cool.

Alex, I'm glad you found a position to pursue your passion for teaching, maybe I'll sit in on one of your lectures for a recap sometime!

Jorrit, you were always helpful, thanks for sparring about the Montana over the years, lending out filters, and giving us the visual pleasure of your beautiful PhD thesis cover.

Irina, thank you for helping out with the early experimental stages of our work on tungsten disulfide, you saved us months of time by lending us that laser!

Emanuele, you're cut out for the Quantum Warriors, I hope we get to play a football match together!

Christos, I still chuckle when I think back to us trying to explain our research in 5 words or gestures with **Gerben** observing closely.

Valentina, that coffee after our Public Speaking Training (and staring awkwardly) is a year in the making, but I'm sure we'll manage at some point!

Patrick, my brain really had a does-not-compute when I walked in the hallway of my house and looked through the door. See you at **Marit's** next BBQ or house party!

Yaroslav, thank you for our collaborations, and the advice you gave early in my PhD journey.

Tino, you're juggling 15 jobs (including being a Feyenoord video-model), it seems. Still, you always were helpful and willing to make time to help us out. Whether that's drilling holes in walls or metals, installing water pumps or importing chemicals or desiccators. Thank you for all your efforts, little would have been possible without them.

Tom, even though you recently retired and probably will not read this, I am grateful for all the times you helped out with milling and drilling advice in the workshop.

I can't keep on writing pages forever, so let me take the easy way out and give a very warm thank you to all people in **QN** who I've interacted with over the years. A special thanks to all past, current, and future members of the **QN C&C Committee**, who made determined efforts to increase social cohesion and togetherness in our department in the wake of Covid. I hope you'll continue these efforts in years to come; they are dearly appreciated and a lot of fun!

The cleanroom facilities in Delft are among the best, and that is for a large part due to the full-time dedication of a wonderful team of helpful people that teach, maintain, and organize everything related to the cleanroom facilities. **Marc, Eugene, Arnold, Anja, Lodi, Hozanna, Charles, Pauline, Ewan, Marco** (x2!), **Bas, Roald, Marinus, Ron, Brian, Loic, Esther**. Your work is at the center of so many experiments done here, thank you for all your efforts over the years that I've had the pleasure to work in the CR. Without you, none of the contents in this thesis would have been realized! And not to forget, thanks for all the patience with missing cleanroom suits and test deadlines. I can't promise that won't happen again, but I will definitely try.

To realize the experimental setups with which we studied the samples created in the beautiful cleanroom mentioned above, I've had a lot of support from our mechanical support team. **Ronald, Nico, and Tim**, thank you for all the times I dropped in with (of course very urgent) requests to realize sample holders, shape pieces of metal, or mechanical design advice in general. You've always been helpful and delivered high-quality work in a very timely fashion.

I would also like to thank our electronics support team, who have lent a helping hand from designing PCBs, applying proper soldering techniques, repairing cables and solder joints, to searching for that one RF connector with the right footprint. You're a vital part in the efficient functioning of the experiments in this building, thank you for all the help!

Srijit, if it was not for the great experience in your lab, I would not have chosen to pursue a PhD. I'm very glad you found the winning recipe, congrats on the recent Nature publication! I always enjoyed our conversations over drinks, chess matches, and darts faceoffs, let's repeat that again sometime soon (I know, I actually have to visit TPKV for that. I'll try to better my life).

During the homebound isolation that was Covid, we occasionally gathered for online chess tournaments over Zoom, all cameras on with beers on the side. Thanks, **Srijit, Claus, Michiel, Adrian, Fokko**, for providing a much-needed escape during those dark times! We should continue that endeavor in person!

Christian, you definitely played a big role in my decision to undertake a PhD. Thanks for the football matches with the Quantum Warriors and all the party nights. I hope you're having a great time in Australia with **Ellie**, let's catch up soon.

DVD! I'm sorry for being on vacation during your upcoming defense, I hope it won't stop you from attending my party! I admire that you were not scared to shape your own vision and projects during your PhD. It was always fun to catch up, and your wedding party was amazing. I hope it will be smooth sailing during the upcoming months.

An important part in maintaining clarity of thought is doing some fun sports to work out all that stress. This is precisely what we did with the Quantum Warriors! **Gustavo**,

Christian, Thijs, Maarten, Francesco, Stefano, Jorge, Alberto, Anta, Mark, Sjoerd, Bas, and Valentin, thanks for all the matches, drinks, and karting together. Though my participation during my PhD was intermittent at best because of health-related situations, I had loads of fun with you guys, for which I'm very grateful! I just might buy some shoes and drop by for some matches next season.

Even though all the work was accomplished in Delft, I want to thank the people outside of Delft and work who had a significant indirect impact on this thesis: your love, support, and friendship helped keep me sane, and I couldn't have survived this without you! So, here goes!

First off, **Marit, Teun, Saskia, Annemieke, Joana**, thank you for making the Lombokstraat such a chill and fun place to live! I still owe you some cooking, **Marit**. Thanks for all the nice conversations we've had over the last years. With BBQs it seems third time's the charm, I'll come grab a beer at the next one.

Willeke, thank you for the unwavering support during the first years of my PhD. In many ways, you enabled me to give it my all, and for that, I'm very grateful.

BoZo Productions, thanks for being there during all the changes my life saw during the years of my PhD. You guys always felt like a grounded and sane safe space, your friendship and #Patatdag has helped me stay in touch with myself! I admire the courage it took to leave everything behind for your travels, but secretly I'm very happy that you guys are back. Congrats on your newly obtained house, I'm looking forward to demolishing that ugly brown floor soon.

Rob, Li, Seb, Roos, thank you for organizing our yearly skiing adventures and the summer vacations. Though I always returned physically exhausted, they recharged me mentally and really were some of the best carefree escapes I've had over the years. Thanks for your friendship, and all the patience while I've been finishing this demanding adventure in Delft. I look forward to spending more time together again afterward!

Annika, thanks for the Mozartkugels! They were delightful company while designing my thesis cover.

Naomi, thanks for all the good times, the crazy police stories (they made me very glad I'm doing what I'm doing) and the Christmas dinners with my new family! I'm glad you and **Lukas** (die integere vent) are doing well, and I can't wait to fly the sun in October!

Evan and Gijs, I really enjoyed connecting over bouldering (and the occasional party, ABL <3). Whenever you guys are on the sidelines I seem to climb five grades higher!

Aline, I enjoyed pretending we've known each other for years to our innocent AirBnB friends. Let's go on more adventures!

Liesjeee, international field-hockey referee powerwoman! It's always a highlight when we catch up, thanks for your support over the years. **Maeve** is lucky to have you and **Vincent** as parents!

Fleur, you're a kind soul. Thanks for the adventures, fulfilling conversations and your spraakmakende verjaardagcadeautjes. Your radical honesty is delightful (even when I totally disagree with you), and I'm curious to meet that **V** of you.

Rey, you chase adventure, freedom and heart, and it's wonderful to see. Your stories always make me feel like I'm the ANWB-couple guy, I'm curious where life takes you!

Natas en Mar, thanks for letting me be your kind-aan-huis over the years (even allowing your kid to take the car for a weekend). I think I'll have to grow up now and move

out, since a *real kid* is on the way. I'm so happy for you guys!

Marije, thank you for the good times, the 'fresh air videochats', the personalized song(s?), and our conversations. I'm curious where your singer-songwriter journey is going to take you, keep at it! But who knows, you might want to become an airfryer-masterchef next year.

Mikeyyy, my oldest friend (not in age, but in time) and our crypto-influencer-celebrity! You're not scared to create your own path in life and it's always enjoyable being on the sidelines and catching up. I've enjoyed our nights that ended in taxi Matthijs, if you catch my drift - let's go again sometime.

Ties, keeeerel. I miss hanging out with you. Thanks for always being there when I really needed you and your amazing capacity to make one feel heard. Also, thanks for dragging me back home in a neck brace in Saalbach when I really did not feel like it, hahahaha. I'm glad we're going to the sun in October, it's about time our party endeavors are united once more!

Willemijn, looking back, we kicked off a whole lot of changes in my life. I have fond memories of drinking glacier water, crowing roosters, becoming hypothermic after a dive in the Delftse Hout, and obtaining tunnel vision on bridges. We're very much alike, yet we learned many things together. I grew a lot because of our interactions and for that I'll always be grateful.

Robinnn, I remember us chatting about how it can be hard to build new friendships at our age, before realizing that's actually what we did together, and then laughing out loud. Our weekly salsa-and-wine evenings were a lot of fun, and they always helped me detach from work and personal matters. We have more in common than I initially thought, and I'm thankful for our friendship, the good times, and deep conversations. On to many more! Let's finally go bar hopping in Amsterdam to celebrate!

Anna, when we met I wasn't having the greatest time. It turned out we shared similar struggles, and we bonded quickly. Our many conversations helped me in picking up the pieces, standing up for myself, and shaping healthy boundaries – which were instrumental in finishing last year's publication and writing my thesis (though the role of all the great music you introduced me to can't be underestimated). The freedom, peace, and calm we felt during our vanlife escape serves as a guide for redesigning my life towards living in the moment and just simply being. I'm thankful that we met, I'm proud of how we've both grown since then, and I admire your courage for taking the leap with Rudi and leaving everything behind. See you when I see you.

Bor, Lexington (Music League overlord), **Murfiee**, **Chris, JP**, thanks for the recent jam sessions. It's been a blast getting back in a group to play some music, and it's really helped me find pleasure in playing guitar again, something which has been completely drowned out during my PhD. I'm looking forward to picking my Tele up again after my defense.

Sannee, my boulderwife!! It feels like we've known each other for years, but the opposite is true. You're smart, sensitive, driven, a great listener, and somehow we just get along very well. I'm happy that you chose to be with my bestie, and the process of sharing (or ridiculing) him is going quite smoothly I'd say. Thank you for the countless times you've been there for me over the last years, all the bouldering sessions, parties, and Plantsoen-chillings. And not to forget, the amazing friends that have come into my life

through you. I'm looking forward to my guest talk at the LUMC! Also a shoutout to your caring parents, I appreciate them asking about me, and you can definitely hand them a copy.

Patrick, my brooooo!! Ik heb echt genoten van onze escape in Kroatië, en het lijkt me tof om weer zoiets te doen als ik aan de andere zijde van de PhD ben beland. Wat mij betreft dit keer zonder dat onze huurauto tot op het laatste element in de toiletas wordt leeggegooid bij grenscontroles. Je bloeit op sinds je in je nieuwe huis bent ingetrokken en het maakt me blij en trots dat te zien!

Als laatste, **Pap** en **Mam**. De academische wereld is jullie volledig vreemd, maar dat heeft jullie nooit tegengehouden om me te steunen en vertrouwen op elke stap van de weg. Ik kijk er naar uit om jullie een kijkje in mijn wereld te geven op de dag van de verdediging. Dankjulliewel voor alles.

Michael Borst
July 2024, Delft

CURRICULUM VITÆ

Michael BORST

- 2019-2024 **PhD in Physics**
Delft University of Technology, The Netherlands
Department of Quantum Nanoscience
Thesis: Control and imaging of excitons, spins and spin dynamics in Van der Waals semiconductors and superconductor-magnet hybrids
Promotors: Dr. Ir. Toeno van der Sar
 Prof. Dr. Gary Steele
- 2018-2019 **Tutor**
Lyceo, The Netherlands
Role: After-hours lecturing, tutoring and supervision of secondary school students
- 2016-2018 **MSc in Applied Physics**
Delft University of Technology, The Netherlands
Quantum Nanoscience track
Thesis: Developing InSb 2DEGs as a platform for topological superconductivity
Supervisor: Dr. Srijit Goswami
- 2016-2018 **Teaching assistant**
The Hague University of Applied Sciences, The Netherlands
Role: Supervising photonics practicals, creating and writing an optics tutorial, homework and exam grading
Supervisor: Dr. Ir. Roel Smit
- 2015-2016 **Pre-master in Applied Physics**
Delft University of Technology, The Netherlands
- 2014 **Internship**
European Space Agency
European Space Research and Technology Centre (ESTEC), The Netherlands

- Project:* Image processing software for the descent camera of the Exomars 2016 entry, decent and landing demonstrator module
Supervisor: Prof. Dr. Detlef Koschny
- 2014 **Internship**
Airbus Defence and Space Netherlands
Project: Optical design of a spectrometer for the purpose of air quality measurements
Supervisor: Ir. Barend Ording
- 2010-2015 **BSc in Applied Physics**
The Hague University of Applied Sciences, The Netherlands
Photonics track
Thesis: Existential conditions for surface plasmon excitation in the Kretschmann-Raether configuration
Supervisors: Dr. Aurèle Adam
Ir. Jan Lambers
- 2003-2009 **Secondary school**
Gymnasium Bonaventuracollege, Leiden, The Netherlands
- 31-03-1992 Born in Rijpwetering, The Netherlands.

LIST OF PUBLICATIONS

4. **M. Borst**, P.H. Vree, A. Lowther, A. Teepe, S. Kurdi, I. Bertelli, B.G. Simon, Y.M. Blanter and T. van der Sar. Observation and control of hybrid spin-wave–Meissner-current transport modes. *Science* **382**, 430-434 (2023). DOI: 10.1126/science.adj7576
3. T.S. Ghiasi, **M. Borst**, S. Kurdi, B.G. Simon, I. Bertelli, C. Boix-Constant, S. Mañas-Valero, H.S.J. van der Zant and T. van der Sar. Nitrogen-vacancy magnetometry of CrSBr by diamond membrane transfer. *npj 2D Mater Appl* **7**, 62 (2023). DOI: 10.1038/s41699-023-00423-y
2. B.G. Simon, S. Kurdi, J.J. Carmiggelt, **M. Borst**, A.J. Katan and T. van der Sar. Filtering and Imaging of Frequency-Degenerate Spin Waves Using Nanopositioning of a Single-Spin Sensor. *Nano Letters* **2022** 22(22), 9198-9204. DOI: 10.1021/acs.nanolett.2c02791
1. J.J. Carmiggelt*, **M. Borst*** and T. van der Sar. Exciton-to-trion conversion as a control mechanism for valley polarization in room-temperature monolayer WS₂. *Sci Rep* **10**, 17389 (2020). DOI: 10.1038/s41598-020-74376-3

* indicates equal contributions.

